**GEO 511: Master's Thesis**

# Biomass estimation from polarimetric L-band SAR data over Swiss temperate forests

**Remote Sensing Laboratories (RSL)**
**Department of Geography**
**University of Zurich**

| | |
|---|---|
| Author: | Daniel Kükenbrink |
| Matriculation number: | 08-702-623 |
| Supervisor: | Dr. David Small (RSL) |
| Co-Supervisor: | Dr. Felix Morsdorf (RSL) |
| Faculty Member: | Prof. Dr. Michael E. Schaepman (RSL) |


June 27th, 2014

# Abstract

In the face of the continued threat of global warming, better understanding and modeling the climate is becoming more urgent. A major concern is the global carbon cycle, as the largest single source of uncertainty in the global carbon budget lies in the terrestrial ecosystem. The world's forests act as a major carbon sink and therefore play an important role in the terrestrial carbon cycle. In order to improve global climate models, accurate and repeated estimates of the distribution and changes in forest biomass are needed. Most promising methods to meet this requirement are found in remote sensing with Airborne Laser Scanning (ALS) and Synthetic Aperture Radar (SAR) measurement techniques. In this thesis, the biomass estimation capability of fully polarimetric air- and spaceborne L-Band SAR data over heterogenous, temperate forests in north-eastern Switzerland is analyzed. Multiple techniques are evaluated, including use of backscatter and Polarimetric Interferometric SAR (PolInSAR). SAR data were available from ALOS PALSAR and DLR's airborne E-SAR instruments, both operated in fully polarimetric mode. As a biomass reference, forestry field measurements as well as ALS derived biomass estimates were available. The results showed that no single polarization, neither from space nor from airborne backscatter data, had sufficient sensitivity to biomass in order to accurately estimate biomass for the selected study sites. Only by combining backscatter data from the full set of polarimetric channels and focusing on the stand-level, more accurate biomass estimates were possible with an $R^2$ of 0.4 and an RMSE of 74.3 t ha$^{-1}$ when using airborne SAR data. The weak performance of backscatter based approaches in estimating biomass could be related to the high noise level and the saturation of the L-band backscatter values already at relatively low biomass levels. The high biomass regime found in the analyzed study sites therefore hindered an accurate biomass estimation from backscatter data. Yet, it was shown that geometric and radiometric normalizations using high resolved Digital Elevation Models (DEMs) can improve biomass estimation performance. It was shown that forest height and biomass estimation at the stand level from PolInSAR measurements taken from the airborne E-SAR instrument were less limited by saturation. The biomass estimates from PolInSAR showed high uncertainties with a relative RMSE of over 100% of the observed average stand biomass. The low coherence due to temporal decorrelation found in the ALOS PALSAR acquisitions over the analyzed study sites hindered forest height inversion using the available spaceborne polarimetric SAR data. The results achieved in this thesis suggest that for accurate biomass estimation in the high biomass regime, alternatives are called for to improve upon common approaches based on fully polarimetric L-Band backscatter and PolInSAR techniques.

# Zusammenfassung

Angesichts der stetigen Bedrohung durch die globale Erwärmung wird ein besseres Verständnis und eine bessere Modellierung des Klimas immer wichtiger. Ein Hauptaugenmerk ist auf den globalen Kohlenstoffkreislauf gerichtet, da die grösste Einzelquelle an Unsicherheit im globalen Kohlenstoff-Budget im terrestrischen Ökosystem zu finden ist. Die globale Waldfläche, als eine Hauptsenke für Kohlenstoff, nimmt eine besondere Rolle im terrestrischen Kohlenstoffkreislauf ein. Um globale Klimamodelle zu verbessern, sind genaue und repetitive Schätzungen zur Verteilung und Veränderung der Waldbiomasse von Nöten. Vielversprechende Ansätze, um diesen Anforderungen genüge zu leisten, können in der Fernerkundung mit den Messtechniken des *Airborne Laser Scannings* (ALS) und *Synthetic Aperture Radar* (SAR) gefunden werden. In dieser Masterarbeit wird die Fähigkeit zur Waldbiomassenabschätzung von voll polarimetrischen L-Band SAR Daten (flugzeug- und satellitengestützt) über heterogenem, temperiertem Wald in der Nord-Ost Schweiz analysiert. Dabei wurden sowohl Rückstreuungs- als auch polarimetrisch-interferometrisches SAR (PolInSAR) basierte Techniken verwendet. Satellitengestützte ALOS PALSAR und flugzeuggestützte E-SAR Daten der DLR standen zur Verfügung, beide in voll polarimetrischem Aufnahmemodus. Als Biomassen-Referenz konnten Feldmessungen sowie LiDAR basierte Biomassenabschätzungen beigezogen werden. Die erhaltenen Resultate zeigten, dass kein einzelner Polarisationskanal eine ausreichende Sensitivität gegenüber Waldbiomasse aufwies, um diese akkurat abzuschätzen, weder von satelliten- noch von flugzeuggestützten Rückstreuungsdaten. Nur wenn die Rückstreuungswerte des vollen Satzes der polarimetrischen Kanäle kombiniert wurden und die Messskala auf einen ganzen Waldbestand erweitert wurde, war es möglich, die Waldbiomasse mit 40% Genauigkeit gegenüber der Referenzbiomassenmessung und einem RMSE von 74.3 t $ha^{-1}$ zu erreichen. Jedoch nur, wenn flugzeuggestützte Daten analysiert wurden. Die schlechte Biomassenabschätzung der rückstreuungsbasierten Methoden können durch das hohe Rauschen und die Saturierung der L-Band Rückstreuungswerte bei relativ niedriger Biomasse erklärt werden. Die hohen Biomassenwerte, welche in den analysierten Testgebieten zu finden sind, verhindern somit eine akkurate Abschätzung der Biomasse. Es wurde aber gezeigt, dass geometrische sowie radiometrische Normalisierungen bei Verwendung hochaufgelöster Digitaler Höhen-Modellen (DHMs) die Biomassenabschätzung verbessern können.

Es hat sich erwiesen, dass flugzeuggestützte Waldhöhen- und Biomassenabschätzungen auf Waldbestandesebene basierend auf PolInSAR Techniken weniger von Sättigungseffekten beeinflusst waren. Die Biomassen-Abschätzungen durch PolInSAR wiesen jedoch hohe Unsicherheiten auf, mit einem relativen RMSE von über 100% der mittleren Referenzbiomasse. Die niedrige Kohärenz aufgrund temporaler Dekorrelation in den ALOS PALSAR Daten über den Studiengebieten verunmöglichten eine Waldhöhen-Abschätzung mit diesen satellitengestützten Daten.

Die in dieser Arbeit erhaltenen Resultate zeigten auf, dass es nötig ist, Alternativen zu den oft verwendeten Techniken basierend auf voll polarimetrischen L-Band Rückstreuungs- und PolInSAR-Techniken zu entwickeln, um eine akkurate Biomassenabschätzung in Gebieten mit hohem Biomassenvorkommen zu erhalten.

# Contents

# List of Figures

# List of Tables

# Acronyms

**a.s.l.** above sea level

**AGB** Above Ground Biomass

**ALOS** Advanced Land Observing Satellite

**ALS** Airborne Laser Scanning

**ASAR** Advanced Synthetic Aperture Radar

**CHM** Canopy Height Model

**DBH** Diameter At Breast Height

**DEM** Digital Elevation Model

**DESDynI** Deformation, Ecosystem Structure, and Dynamics of Ice

**DHM** Digital Height Model

**DLR** German Aerospace Center

**DSM** Digital Surface Model

**DTM** Digital Terrain Model

**E-SAR** Experimental SAR

**ENVISAT** Environmental Satellite

**ESA** European Space Agency

**FBD** Fine Beam Dual-Polarization

**FGI** Finnish Geodetic Institute

**GPS** Global Positioning System

**GTC** Geometric Terrain Corrected

**INS** Inertial Navigation System

**InSAR** Interferometric SAR

**ISRO** Indian Space Research Organisation

**JAXA** Japanese Space Exploration Agency

**JERS-1** Japanese Earth Resources Satellite 1

**KSP** *Kantonales Stichproben Inventar*

**LAI** Leaf Area Index

**LFI** *Landes Forst Inventar*, Swiss Forest Inventory

**LiDAR** Light Detection and Ranging

**LOS** Line Of Sight

**LRW** Local Resolution Weighting

**MODIS** Moderate Resolution Imaging Spectroradiometer

**NASA** National Aeronautics and Space Administration

**NDVI** Normalized Difference Vegetation Index

**NESZ** Noise Equivalent Sigma Zero

**PALSAR** Phased Array L-Band Synthetic Aperture Radar

**PCI** Phase and Coherence Inversion

**PK25** *Pixelkarte 1:25'000*

**POA** Polarization Orientation Angle

**PolInSAR** Polarimetric Interferometric SAR

**RMSE** Root Mean Square Error

**RPI** Random Volume over Ground Phase Inversion

**RSL** Remote Sensing Laboratories

**RTC** Radiometric Terrain Corrected

**RVoG** Random Volume over Ground

**SAR** Synthetic Aperture Radar

**SIR-C** Spaceborne Imaging Radar at C-band

**SLC** Single Look Complex

**SRTM** Shuttle Radar Topography Mission

**TanDEM-X** TerraSAR-X add-on for Digital Elevation Measurements

**TerraSAR-X** German Earth observation satellite at X-Band

**WMG92** *Waldmischungsgrad 1992*

# 1. Introduction

Forest biomass estimation on regional and global scales is attracting more and more attention (Koch, 2010; Saatchi & Moghaddam, 2000). The world's total forest area in 2010 was estimated to be just over 4 billion hectares, corresponding to 31 percent of total land area (FAO, 2010). The world's forests store - with over 650 billion tonnes - more carbon than the entire atmosphere and are therefore a major carbon sink in the terrestrial carbon cycle (FAO, 2010; Koch, 2010). Yet for the world as a whole, carbon stocks in forest biomass decreased by an estimated 0.5 Gt annually during the period 2005-2010, mainly due to a reduction in the global forest area (FAO, 2010). Global and regional forest monitoring has become essential and is gaining in importance, as the greatest source of uncertainty in the global carbon cycle lies in terrestrial ecosystems (IPCC, 2007; Sandberg et al., 2011). In order to overcome these uncertainties and to improve global climate models, more accurate biomass estimation approaches are needed at global and regional scales.

In more regional applications, biomass estimation is essential for forest fuel load quantification in fire management (Saatchi et al., 2007a). Furthermore, the rising market demand for wood products and especially for wood-based bioenergy grants economic importance to biomass estimation. The economic importance of accurate biomass estimation and repeated monitoring also at global scales arose with the introduction of emission trading through articles 4 and 12 of the Kyoto Protocol to the United Nations Framework Convention on Climate Change (UNFCCC) (Rosenqvist et al., 2003).

Remote sensing technologies play an important role in the estimation of global and local biomass levels. With remote sensing, we are able to estimate biomass in a repetitive manner, allowing for multi-temporal analysis and monitoring applications, at steadily increasing resolution and quality. While the high costs associated with *in situ* measurements, the scarcity of resources, and the large extent of the areas to be mapped hinder an accurate and complete inventory of forest resources with frequent updates (Santoro et al., 2011; Saatchi et al., 2007b), remote sensing approaches are clearly a viable alternative. Koch (2010) identified imaging radar and Light Detection and Ranging (LiDAR) as essential data sets for biomass mapping, where low-frequency Synthetic Aperture Radar (SAR), polarimetric SAR and profiling LiDAR are the most requested future systems for vegetation canopy characterization and biomass estimation.

In remote sensing approaches, biomass is normally defined as the above-ground phytobiomass (organic mass of plants) (Koch, 2010). Biomass level estimation through remote sensing can be divided into direct and indirect methods. While in direct approaches, a relationship between the signal response registered by the sensor and the biomass is determined using mostly statistical approaches, indirect methods are based on measuring a biomass proxy first (e.g. tree height, crown closure etc.) which is then used as an input to estimate wood volume, biomass or other forest structural variables (Koch, 2010). In this thesis, both approaches are investigated using LiDAR and SAR sensors.

## 1.1. Biomass estimation through LiDAR

There are numerous approaches reported in literature that use LiDAR metrics to retrieve biomass information mostly at the regional level.

Nelson et al. (1988) published one of the pioneering studies where mean canopy height was linked to above-ground biomass at a plot level. They were able to explain 53-65% of the variability noted in ground measurements of forest biomass. In later studies, mean canopy height as well as canopy vertical structure measures, such as height percentiles, were used to predict biomass through regression analysis (Lefsky et al., 1999; Lefsky & Cohen, 2002; Lim & Treitz, 2004). Lefsky & Cohen (2002) were able to explain 84% of the observed variance in above-ground biomass at different sites in the temperate deciduous, temperate coniferous, and boreal coniferous biomes. Lim & Treitz (2004) were able to explain over 80% of the observed variance in above-ground biomass with regressional models from different height percentile measurements.

Most of the more recent studies focus on indirect approaches, trying to detect single trees from LiDAR products and measure their height and crown dimensions to infer biomass information at the single tree level. Popescu et al. (2003) introduced an algorithm that is able to detect single trees and their crown diameters from a Canopy Height Model (CHM) over deciduous, coniferous, and mixed stands in the southeastern United States. They identified the tree location using a local maximum filter. The crown dimensions were then derived by fitting a fourth degree polynomial over two profiles of the CHM around the detected tree. Popescu et al. (2003) achieved with this algorithm a standard error of estimate for the crown diameter of 1.36-1.41 m for dominant trees. Difficulties were identified where the crowns of several trees overlapped.

In a later study over the same study site as in Popescu et al. (2003), Popescu (2007) used the LiDAR software TreeVaW to detect single pine trees and retrieve their heights and crown dimensions from a CHM. He established a regression model that relates the derived tree heights and crown diameters with the Diameter At Breast Height (DBH) measured in the field. Even though DBH is a tree dimension that is not directly visible on CHMs derived from Airborne Laser Scanning (ALS) data, several studies reported that LiDAR metrics correlated well with the DBH (Popescu, 2007; Persson et al., 2002). With the derived DBH, Popescu (2007) was able to estimate the biomass of 43 pine trees via allometric equations with an RMSE of 169 kg. The estimated biomass explained 87% of the variance associated with the field-measured Above Ground Biomass (AGB) of all 43 trees.

A slightly different approach, still using the CHM, is to apply a watershed algorithm to delineate the crown dimensions (Pyysalo & Hyyppä, 2002; Pitkänen & Maltamo, 2004; Kaartinen et al., 2012). This kind of approach reported good results in an international comparison of several tree detection algorithms conducted by the Finnish Geodetic Institute (FGI) (Kaartinen et al., 2012).

Approaches using point cloud data instead of the CHM to detect single trees and delineate the crown diameter are also found in the literature. Morsdorf et al. (2004) detected tree locations in a boreal like forest in the Swiss National Park with a local maximum search algorithm. The detected tree locations were then used as a seed-point for clustering analysis of the point cloud data. The height of the highest laser point of each cluster was defined as the tree height and the crown diameter could be derived considering the shape of the cluster. With this approach, Morsdorf et al. (2004) achieved an $R^2$ of 0.92 for the linear regression between estimated and field measured tree heights. The performance of the crown diameter estimation with an $R^2$ of just 0.2 was not as good.

Although good results are reported from using LiDAR metrics to derive biomass information at different scales, hardly any investigations exist on temperate, dry or tropical forests. Most studies are focused on sub-boreal forest systems such as Scandinavian forest types dominated by spruce and pine (Koch, 2010). Nevertheless, LiDAR turned out to be one of the most applicable remote sensing techniques for forest monitoring (Hyyppä et al., 2009) due to the information that can be obtained on the vertical structure of the forest canopy (Koch, 2010).

## 1.2. Biomass estimation through SAR

Biomass estimation with SAR instruments are of particular interest, especially due to their relative robustness in diverse weather conditions (Koch, 2010). There are three basic approaches based on SAR data used for biomass estimations: backscatter, coherence and phase-based approaches.

For backscatter approaches, low frequency instruments (L- and P-band) are typically used. Numerous studies have been published on the relationship of single polarization backscatter data to biomass (Dobson et al., 1992; Le Toan et al., 1992; Baker & Luckman, 1999; Mitchard et al., 2009, 2011; Sandberg et al., 2011; He et al., 2012; Kasischke et al., 1995; Peregon & Yamagata, 2013; Rahman & Tetuko Sri Sumantyo, 2013). In all of these studies, the cross-polarized channels (HV-, and VH-polarization) have been found to be most sensitive to biomass. The co-polarized channels (HH-, and VV-polarization) also showed some correlation with biomass, yet less consistent. Mitchard et al. (2009) reported that once the HV backscatter had been taken into account, no further improvement in the models were observed when adding data from the HH-polarization channel. The studies agree that P-band backscatter is more sensitive to biomass than backscatter at L-band. Models have been developed that incorporate the combination of HH-, HV-, and VV-polarization to estimate biomass at different biomes and with different frequencies (Saatchi & Moghaddam, 2000; Saatchi et al., 2007a, 2011). Saatchi & Moghaddam (2000) were able to explain 87% of the variance in field measured biomass for boreal forests with L-band. Even better performance were reported if P-band or a combination of P-, L- and C-band (up to 91% accuracy for biomass estimation) were taken. Saatchi et al. (2011) were also able to find a strong relationship between backscatter at L- and P-band in tropical forests. Furthermore, polarization decompositions (Pauli, Yamaguchi) have been reported to be sensitive to biomass, with best results showing in the volume scattering part followed by the double bounce (ground-trunk interaction) scattering part (Chowdhury et al., 2013). Yet, estimation approaches based on simple backscatter information exhibit clear limitations, especially for areas with higher biomass levels, as L- and P-band backscatter tend to saturate with increasing biomass. L-band reaches its saturation level already at 60-100 t $ha^{-1}$, depending upon the species type and biota (Dobson et al., 1992). Some studies also report sensitivities of L-band to backscatter up to 150 to 200 t $ha^{-1}$ (Mitchard et al., 2009). P-band tends to reach its saturation limit at higher biomass levels (Sandberg et al., 2011). Further limitation in backscatter based approaches are to be found in more rugged terrain, as topography-induced distortions (such as shadow, foreshortening and layover effects) impact on backscatter information, making a robust and reliable biomass estimation in terrains with varying topography very difficult (Small et al., 2008).

Coherence based approaches are based on estimation of the complex correlation coefficient between two SAR acquisitions (Balzter et al., 2007). In several studies, coherence is reported to decrease with increasing biomass levels due to higher volume decorrelation in denser forest areas (Thiel et al., 2009; Cartus et al., 2011; Askne et al., 2013; Chen et al., 2008). It has also been reported that coherence images acquired under winter conditions tend to estimate biomass level with higher accuracy than under summer conditions (Thiel et al., 2009). Yet, biomass retrieval based on coherence is also limited by saturation effects and by the influence of weather at different data acquisition times (Zhou et al., 2008).

An alternative to overcome the aforementioned limitation due to saturation of the backscatter and coherence based approaches is found in phase-based approaches. Phase-based interferometric SAR techniques exploit the interference patterns (so-called fringes) of two electromagnetic waves to

estimate the topographic height of the scattering phase center (Balzter et al., 2007). The scattering phase centre location depends on vegetation structure, scattering mechanisms and sensor characteristics. The part of the forest that interacts most strongly with the radar wave depends on the wavelength, the polarization, incident angle and of course on the vegetation itself, like thickness and density of the crown area (Koch, 2010). Interferometric techniques can be used to estimate forest canopy height, as the interferometric phase relates to the scattering phase center, which at suitable wavelengths and polarizations is dependent on the terrain and vegetation canopy heights (Balzter, 2001). Height is one of the important input variables when estimating biomass through indirect approaches. Methods that provide the extraction of heights from Earth observation data are therefore of high interest. In one of the first studies that used Interferometric SAR (InSAR) techniques to infer forest heights, Treuhaft et al. (1996) found an average agreement of InSAR derived vegetation layer depth with ground data of 5 m, with the error being related to stand height. In a later study, Treuhaft & Siqueira (2000) combined information from interferometry and polarimetry to retrieve vegetation height with an accuracy of better than 4.2 m. Such techniques using both information from interferometry and polarimetry are called Polarimetric Interferometric SAR (PolInSAR) techniques (Cloude & Papathanassiou, 1997). The accuracy of repeat-pass PolInSAR techniques is limited by temporal decorrelation caused by temperature, orientation angle and moisture changes between the two SAR acquisitions and depends on the wavelength used (Hagberg et al., 1995; Balzter, 2001; Zebker & Villasenor, 1992). Temporal decorrelation in interferometric SAR, especially in forestry applications, is of increasing scientific importance (Papathanassiou & Cloude, 2003; Zhou et al., 2008; Lee et al., 2009). Lee et al. (2009) reported that temporal decorrelation even within one day can lead to high overestimations of forest height. To reduce the noise level in the height extraction, many approaches found in the literature are based on stand level estimates. Kellndorfer et al. (2004) suggested that a minimum mapping unit of approximately 1.8 ha is needed to achieve acceptable estimates under repeat-pass conditions.

To infer PolInSAR data to canopy height, several models exist. The most well-known model is the Random Volume over Ground (RVoG) model (Koch, 2010), which is a two-layer model composed of a vegetation layer and a ground component (Cloude, 2005; Chen et al., 2008).

Mette et al. (2004) and Mette & Papathanassiou (2004) used the PolInSAR technique combined with the RVoG model to retrieve forest heights that were later related to biomass through allometric equations in heterogenous forest stands. Mette & Papathanassiou (2004) reported good agreement of PolInSAR derived forest height with forest height indices often used in forestry (mid height of stands, or height of the 100 trees with largest DBH in the stand) and showed that common allometric equations can be used to infer biomass at the stand level from PolInSAR derived height estimates.

A recent approach to extract forest height and stand structure from radar data is the use of radar tomography methods (Tebaldini, 2010; Tebaldini & Rocca, 2012). With this approach, a real 3D image, similar to LiDAR derived point cloud datasets, of the scene is obtained by creating an additional synthetic aperture in elevation, using a coherent combination of images acquired from multiple parallel flight tracks (Koch, 2010).

Most recent investigations of phase-based extraction of forest height used experimental airborne data, avoiding problems with temporal and atmospheric decorrelation (Balzter, 2001; Koch, 2010). Only few investigations exist for space borne data (e.g. for ALOS PALSAR data in Li & Guo, 2012). This could change with the increasing availability of TanDEM-X data (Koch, 2010), which could further improve forest height and biomass estimation due to its (unique to date) single-pass data acquisition mode.

Multi-temporal analysis reported good results in biomass estimation as well, using phase-based but also coherency and backscatter based approaches. Askne et al. (2013) were able to derive biomass from model-based forest height estimates using TanDEM-X data at the stand level over boreal forest with an RMSE of 16% with an $R^2$ of 0.93. Santoro et al. (2011) estimated growing stock volume with hyper-temporal backscatter data from the C-band ENVISAT ASAR instrument in ScanSAR mode over boreal forests with an RMSE of less than 25%. Interestingly they did not find any saturation effects in the backscatter information up to 300 $m^3$/ha, even though C-band backscatter data is known to suffer from low sensitivity to biomass or growing stock volume. Santoro et al. (2011) reported that the key for this successful biomass estimation lies in the combination and weighted averaging over multiple ASAR acquisitions with varying incident angles over the same area. They found that a stack of at least 20 ASAR images is needed to get a robust biomass estimate.

## 1.3. Research Questions

As illustrated above, numerous studies have investigated biomass estimation in forests with SAR based approaches. Yet most studies, especially for backscatter based approaches, were based in boreal or tropical forests, typically consisting of just a few dominating tree species (spruce, beech etc.). Only very few studies analyzed the backscatter behavior of polarimetric SAR in temperate forests (e.g. Dobson et al., 1992; Garestier et al., 2009; Ghasemi et al., 2013; Le Toan et al., 1992). Yet these studies were usually undertaken in monoculture forests (e.g. pine forests) or forests dominated by just one tree species. This was typically not the case for studies using PolInSAR techniques, where already numerous studies of temperate forests exist, e.g. at the DLR (German Aerospace Center) Oberpfaffenhofen study site (e.g. Mette et al., 2004; Papathanassiou & Cloude, 2001).

Studies concerning biomass estimation in areas with highly variable topography are not that common. Most of the mentioned studies were undertaken in rather flat areas, to reduce the known effects due to geometric and radiometric distortions in more rugged terrain. Yet, with radiometric normalization using a Digital Elevation Model (DEM) instead of an ellipsoid model as proposed in Small et al. (2009) or Small (2011), such topographic effects could be largely corrected, allowing for land cover analysis and classification in hilly areas as found for example in Switzerland.

This thesis assesses the feasibility of using fully polarimetric SAR data over heterogenous, temperate mixed-forests in northeastern Switzerland using different approaches (backscatter, coherence and phase based approaches). Differences between airborne vs. spaceborne SAR data are analysed. For the airborne case, fully polarimetric SAR data acquired by the Experimental SAR (E-SAR) system operated by the German Aerospace Center (DLR) over Hinwil was investigated. For the spaceborne case, fully polarimetric ALOS PALSAR acquisitions covering the whole north-eastern part of Switzerland in the time period between 2006 and 2009 were available. In the course of this thesis, the following research questions were evaluated and assessed:

1 *How sensitive are airborne and spaceborne fully polarimetric L-band SAR backscatter and Pauli decomposition data to biomass in heterogenous temperate mixed-forests found in the Swiss north-eastern midlands?*

2 *How do different SAR backscatter terrain normalization products impact on biomass estimation approaches?*

3 *Does the more complex approach of forest structure retrieval from PolInSAR measurements deliver more reliable biomass estimation in heterogenous temperate forests compared to backscatter based approaches?*

4 *How can LiDAR derived products improve biomass retrieval from SAR data?*

To answer these research questions, this thesis is structured as following: First, a short theoretical background is given in Section 2. Afterwards, the analyzed study sites and the used datasets are introduced in Section 3. In Section 4, the methodological approach for answering the earlier stated research questions is outlined. The results of the different methods are shown in Section 5. In Section 6, the obtained results and the methodological approach used in this thesis are discussed. Finally, a conclusion and an outlook are given in Sections 7 and 8.

# 2. Theoretical Background

## 2.1. Normalization of SAR Backscatter Data

Variability in terrain height within a SAR image causes several geometric and radiometric distortions within most slant or ground range image products (Small et al., 2008). These distortions mainly stem from fore-shortening, layover or shadowing effects within the SAR image. For accurate retrieval of information from SAR images, e.g. biophysical properties such as biomass, a normalization to reduce such distortions is necessary, especially in rugged terrain that can be found in Switzerland. Such normalization products are explained in the subsequent subsections. To fully understand these kinds of normalization, we first need to go back to radar basics with the radar equation.

### 2.1.1. Radar equation

The radar equation explains the relationship between the power of the transmitted pulse $P_t$ and the average received power $\overline{P}_r$:

$$\overline{P}_r = \frac{\lambda^2}{(4\pi)^3} * \int\limits_{Area} \frac{P_t G^2 \sigma^0}{R^4} \, \mathrm{d}A. \tag{2.1}$$

where $\lambda$ is the radar wavelength, $G^2$ the two-way antenna gain, $R$ the slant range, and $\sigma^0$ the backscattering coefficient (Ulaby et al., 1982).

There are three well-known conventions used for the backscattering coefficient in Equation 2.1: $\beta^0$, $\sigma^0$, and $\gamma^0$. They differ in their choice of definition of a standard reference area $A$ in the radar equation (Small et al., 2009, refer also to Figure 2.1). The $\beta^0$ convention provides the natural radar observable (Raney & Freeman, 1994) and is simply normalized by the areal sample interval in the slant range plane ($A_\beta$). For the $\sigma^0$ convention, the conventional «flat Earth» reference area $A_\sigma$ is defined to be in the plane built up by the local ellipsoidal Earth normal vector. For the $\gamma^0$ convention, the normalizing area $A_\gamma$ is defined to be in the projection in the plane perpendicular to the slant range direction (Small et al., 2009). For radiometric correction of SAR images, either an ellipsoid or a Digital Elevation Model (DEM) can be utilized, resulting in either Geometric Terrain Corrected (GTC) or Radiometric Terrain Corrected (RTC) SAR image products respectively (refer also to Table 2.1).

### 2.1.2. Geometric Terrain Correction

For Geometric Terrain Corrected (GTC) products, a DEM is used to geometrically transform the SAR image into a 2D map geometry. Yet, even though the *geometry* is terrain corrected in a GTC product, the *radiometry* of the $\sigma^0$ and $\gamma^0$ backscatter contents remains ellipsoid-model-based. We therefore append the subscript $E$ to the ellipsoid-model based backscatter conventions (Small et al., 2009, see also Table 2.1)

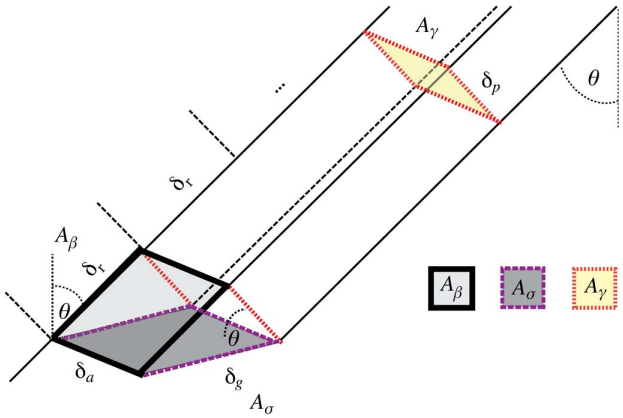


**Figure 2.1:** Backscatter convention reference areas (Small, 2011).

### 2.1.3. Radiometric Terrain Correction

Since the launch of the Environmental Satellite (ENVISAT) there is an increased availability of highly accurate information describing the acquisition geometry of spaceborne SAR imagery, enabling tie-point free orthorectification. Together with a high precision DEM, a robust radiometric calibration standard is possible (Small et al., 2009). One approach to incorporate a DEM for normalization is to use the local rather than ellipsoidal incident angle $\theta$ leading to the backscattering convention $\sigma_T^0$ with the normalization referred to as «NORLIM» in Table 2.1. Yet this angle-based normalization fails to account for many important properties of radar backscatter in regions with significant topographic variation, such as foreshortening, layover and shadowing effects (Small, 2011).

Small (2011) introduces a more complex, yet more robust approach to flatten out such radiometric effects caused by topography. In this approach, the local illuminated area for each raster pixel is integrated using the raster timing information and an accurate DEM of the imaged area. The SAR image can then be normalized with this local illuminated area map (Small, 2011). The resulting product is referred to as Radiometric Terrain Corrected (RTC) with the backscattering convention $\gamma_T^0$, where the subscript $T$ stands for terrain and signals that a DEM was used for the radiometric normalization.

With the use of RTC products, the comparability of SAR images from different sensors or also from different tracks (*ascending* and *descending*) is possible, allowing for multi-temporal analysis with short temporal baselines useful for change detection (Small, 2011). Land-cover classification in rugged terrain is improved, as landcover affected by topography induced SAR acquisition effects is normalized, becoming more comparable to landcovers not affected by such effects (Small et al., 2008).

In Figure 2.2, the two normalization products GTC (2.2a) and RTC (2.2c) for a PALSAR PLR frame at HV polarization are shown. In this scene, the Swiss mid-lands, part of lake Zurich (north) as well as the pre-alps (south) are shown. The normalization area $A_\gamma$ is shown in Figure 2.2b. It was used to radiometrically normalize the SAR image for topographic effects. In the rather flat area in the north, GTC and RTC images are similar because the different radiometric normalizations have less effect on the normalized products. Yet in the more rugged terrain of the pre-alps (in the south of this scene), topographic effects on SAR images are apparent. While topographic effects dominate in the GTC product, the RTC image appears to be relatively flat and therefore successfully radiometrically

**Table 2.1:** SAR backscatter normalization conventions (Small, 2011).

| Convention | 1 | 2 | 3 | 4 | 5 |
|---|---|---|---|---|---|
| Symbol | $\beta^0$ | $\sigma^0_E$ | $\gamma^0_E$ | $\sigma^0_T$ | $\gamma^0_T$ |
| Earth Model | None | Ellipsoid | | Terrain | |
| Reference Area | $A_\beta$ | $\underline{A}_\sigma$ | $\underline{A}_\gamma$ | $\underset{\sim}{A}_\sigma$ | $A_\gamma$ |
| Normalization | $\frac{\beta}{A_\beta}$ | $\beta^0 * \frac{A_\beta}{\underline{A}_\sigma}$ | $\beta^0 * \frac{A_\beta}{\underline{A}_\gamma}$ | $\beta^0 * \frac{A_\beta}{A_\sigma}$ | $\beta^0 * \frac{A_\beta}{\int_{DHM} A_\gamma}$ |
| Map-geometry product (when terrain-geocoded) | GTC | | | NORLIM | RTC |

corrected. Also note the black patches in the RTC image. These are areas of radar shadow, where there was no useable backscatter information. Such areas are uniquely masked. In the GTC product, such areas contain backscatter values determined by the radar system's noise floor.

### 2.1.4. Polarization Angle Orientation Correction

Several studies have reported that the polarization orientation angle of the scattering media affects the polarimetric radar signatures and that such orientation angle shifts induced by terrain azimuth slope variations should be compensated (Lee et al., 2000, 2002; Lee & Ainsworth, 2011). Lee et al. (2000) used orientation angles for polarimetric SAR data compensation, to ensure accurate estimation of geophysical parameters in rugged terrain. To successfully compensate for these effects, it is important to accurately estimate shifts in orientation angles induced by the azimuth slope variations.

The polarization orientation angle is the angle of rotation about the Line Of Sight (LOS). For flat areas, the orientation angle is zero, but when the terrain becomes rugged, the orientation angle is shifted from zero. The polarization orientation angle shifts are induced by surfaces with non-zero azimuth slopes, and by man-made targets such as buildings that are not aligned in the along-track direction and bridges with tilted linear structures (Lee et al., 2000, 2002; Schuler et al., 2000). Lee & Ainsworth (2011) reported that the orientation angle is less sensitive to the surface slopes the higher the radar frequency is.

In order to estimate the Polarization Orientation Angle (POA) from fully polarimetric SAR data, the four complex valued SAR images (SLCs for HH, HV, VH, and VV polarization) need to be converted into the coherency matrix $[T]$. The coherency matrix $[T]$ is defined as the cross-product of the Pauli scattering vector (Lee & Ainsworth, 2011):

$$[T] = \begin{bmatrix} \langle|S_{HH}+S_{VV}|^2\rangle & \langle(S_{HH}+S_{VV})(S_{HH}-S_{VV})^*\rangle & 2\langle(S_{HH}+S_{VV})S^*_{HV}\rangle \\ \langle(S_{HH}-S_{VV})(S_{HH}+S_{VV})^*\rangle & \langle|S_{HH}-S_{VV}|^2\rangle & 2\langle(S_{HH}-S_{VV})S^*_{HV}\rangle \\ 2\langle S_{HV}(S_{HH}+S_{VV})^*\rangle & 2\langle S_{HV}(S_{HH}-S_{VV})^*\rangle & 4\langle|S_{HV}|^2\rangle \end{bmatrix} \tag{2.2}$$

where $S_{tr}$ are the elements of the scattering matrix $[S]$ and the subscripts $t$ and $r$ stand for the transmitting and receiving polarization (either $H$ for horizontal or $V$ for vertical) respectively.

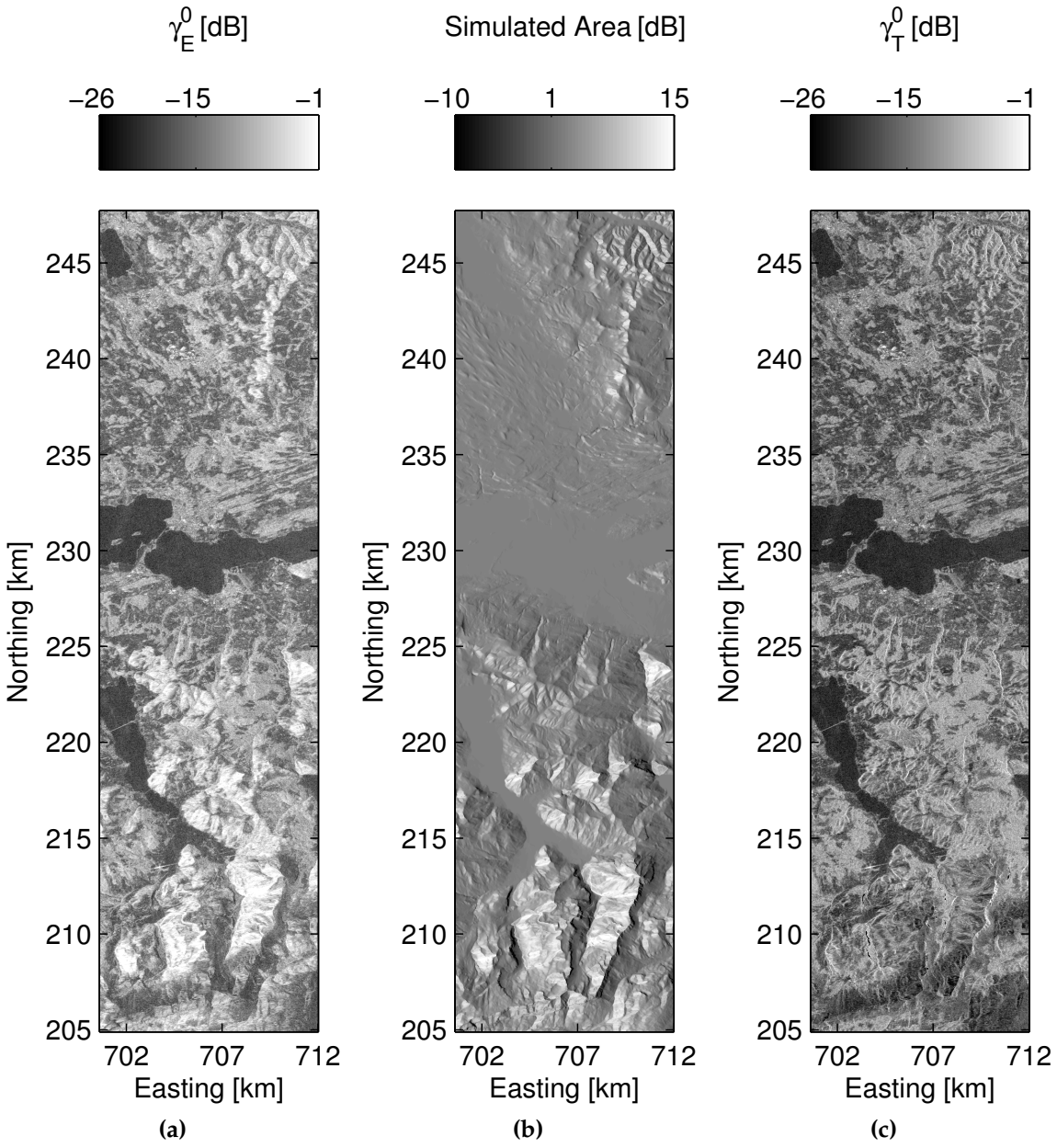


**Figure 2.2:** PALSAR PLR image products at HV-Polarisation. Subset of frame 940 of track 640 at off-nadir angle 23.1°, image acquisition on 9th of May 2009 over the Swiss pre-alps around Rapperswil. (a) GTC, (b) simulated *Area* for radiometric normalization and (c) RTC.

Note that the diagonal elements of the coherency matrix denote the scattering powers of the three decomposition bases in the Pauli decomposition (refer also to Section 2.2). The polarization orientation angle $\theta$ can then be calculated with the following equation (Lee & Ainsworth, 2011):

$$\theta = \frac{1}{4}\left[\tan^{-1}\left(\frac{-4\mathrm{Re}(\langle(S_{HH}-S_{VV})S_{HV}^{*}\rangle)}{-\langle|S_{HH}-S_{VV}|^{2}\rangle+4\langle|S_{HV}|^{2}\rangle}\right)+\pi\right] \tag{2.3}$$

In Equation 2.3, $\mathrm{Re}(A)$ denotes the real part of $A$ and the factor of 4 limits the range of $\theta$ to $[-\frac{\pi}{4}, \frac{\pi}{4}]$. It should be noted, that the orientation angle is phase wrapped just like the interferometry wrapped phase, but unlike interferometry, no fringes exist to aid phase unwrapping. To extract useful information out of this orientation angle, the phase has to be unwrapped by adding $\pi$ (Lee & Ainsworth, 2011). In order to compensate for the estimated orientation shifts, the coherency matrix $[T]$ has to be rotated by the orientation angle $\theta$:

$$[T(\theta)] = [U][T][U]^{-1}, \text{with}[U] = \begin{bmatrix} 1 & 0 & 0 \\ 0 & \cos 2\theta & \sin 2\theta \\ 0 & -\sin 2\theta & \cos 2\theta \end{bmatrix} \tag{2.4}$$

where $[T]$ and $[T(\theta)]$ are the coherency matrices before and after rotation by the orientation angle $\theta$, and $[U]$ is the unitary LOS rotation matrix (Lee & Ainsworth, 2011; Chowdhury et al., 2013). After rotation, the coherency matrix elements should be compensated for orientation angle shifts induced by the azimuth slope variations due to rugged terrain.

## 2.2. Polarimetric Target Decomposition

Polarimetric target decompositions were developed to separate polarimetric radar measurements into basic scattering mechanisms for the purpose of geophysical parameter inversion, terrain and target classification etc. (Lee & Ainsworth, 2011). The principle behind polarimetric target decomposition techniques is that a polarimetric response can be characterized by a combination of idealized scatterers (Woodhouse, 2006b). One of the frequently used polarimetric target decompositions used in remote sensing is the coherent Pauli decomposition. As opposed to the incoherent decomposition theorems such as the entropy, alpha and anisotropy decomposition introduced by Cloude & Pottier (1996) or the Yamaguchi decomposition introduced by Yamaguchi et al. (2005), the coherent Pauli decomposition preserves the amplitude and phase of the complex SAR data. A comprehensive overview of decomposition theorems is given in Cloude & Pottier (1996).

The Pauli decomposition consists of three decomposition basis, each relating to one of the three major scattering mechanisms found in SAR images: surface scattering (odd bounce), double bounce (even bounce) and volume scattering.

**Surface Scattering:** In this scattering mechanism, the backscatter in HH and VV polarizations is approximately equal and a rotation in polarization (such as in HV and VH) does not exist. It is applicable for spherical objects or an exposed flat surface. It is also called the odd bounce scattering mechanism, as it includes single reflections off tree trunks (or vertical objects in general), or multiple but odd numbered reflections, such as surface-trunk-surface reflections. Mathematically expressed it has the form $S_{HH} + S_{VV}$.

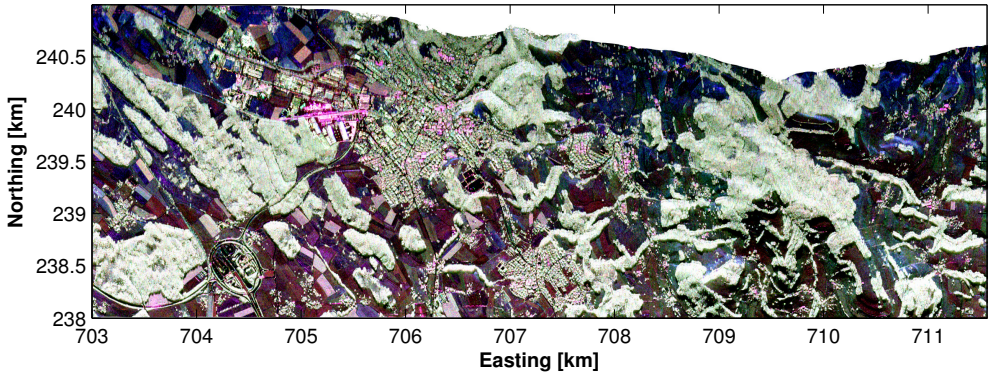


**Figure 2.3:** Pauli decomposition image over the Hinwil E-SAR test site. Red = HH - VV (-39 to -3 dB), Green = HV + VH (-46 to -5 dB) and Blue = HH + VV (-31 to 1 dB). Channels were autoscaled.

**Double Bounce:** This scattering mechanism is characterized by double reflections, usually between a horizontal and a vertical plane. The backscatter in HH and VV polarization are approximately equal, but the phase angle is shifted by 180°. Such a scattering mechanism is typically found in forests (surface-trunk interaction) or urban areas (surface-building interaction). Mathematically expressed it has the form $S_{HH} - S_{VV}$.

**Volume Scattering:** In this scattering mechanism, only cross-polar backscatter is present. The scattering in this mechanism stems from randomly oriented dipole elements, typically found in the canopy of forests (tree crowns). The mathematical term for this scattering base is $S_{HV} + S_{VH}$.

Note that these three terms $S_{HH} + S_{VV}$, $S_{HH} - S_{VV}$ and $S_{HV} + S_{VH}$ are the diagonal elements of the coherency matrix shown in Equation 2.2, which is why this coherency matrix is also known as the Pauli-based covariance matrix (Yamaguchi et al., 2005).

These three scattering mechanism terms provide a useful means for generating an RGB color composite for visualizing the data, as shown in Figure 2.3. In this RGB composite, each scattering mechanism is assigned a color. In our case, blue for surface scattering, red for double bounce scattering and green for volume scattering. We can clearly see that the surface scattering part is mainly visible in flat agricultural areas. Also visible is red double bounce scattering in the urban areas and green volumetric scattering, dominating in forest areas. Note that some urban structures show significant volume scattering terms. This is due to the alignment of the buildings relative to the SAR instrument LOS (Zuberbühler, 2012; Cloude & Pottier, 1996).

## 2.3. SAR Interferometry

Most indirect approaches to estimate biomass are based on retrieval of the canopy height. While this height retrieval is relatively simple for LiDAR acquired data, it can be a challenge in the SAR case. Height retrieval from a single SAR image is not possible. Only if we take two or more complex SAR images into account, it is possible to retrieve height information from SAR data using a technique called interferometry. While we focus just on the wave *amplitude* in the backscatter approaches, the major concern in interferometry lies on the phase of the transmitted and received wave. The

phase of a wave can be a sensitive measure of path length. A single measure of phase is not usually very useful as the exact number of absolute wave cycles is rarely known, but a comparison between two or more phase measurements can provide a measure of path length *difference* to within a fraction of wavelength (Woodhouse, 2006b). This superposition of two or multiple waves is called interference and gives us the phase difference between the two image acquisitions. This phase difference measured between the two images at a given look angle is related to the two-way (for repeat-pass interferometry) path length difference $\Delta R$ (Bamler & Hartl, 1998):

$$\delta\phi = 2\pi\frac{\Delta R}{\lambda} = k\Delta R \tag{2.5}$$

where $\delta\phi$ is the phase difference in radians, $\lambda$ is the wavelength and $k$ is the wavenumber. The SAR interferogram is generated by cross-multiplying, pixel by pixel, the first SAR image with the complex conjugate of the second (Bamler & Hartl, 1998), giving the phase difference of the two complex SAR images at each pixel. This interferogram can be used to generate a DEM. A combination of two SAR images, to retrieve further information not retrievable from a single SAR image (such as a DEM), is only possible if at least one imaging parameter is different compared with the first image. This parameter can either be the flight path, acquisition time or wavelength (Bamler & Hartl, 1998). This thesis is concerned with single baseline repeat-pass interferometry. The flight tracks between the two image acquisitions differ in time and in flight path, giving a temporal as well as spatial baseline.

One limitation of InSAR DEMs is that they have a vegetation bias, meaning that they represent a ground-plus-canopy surface and not the ground surface alone. This can be used to our advantage, as it means that InSAR may provide information on the vegetation height (Woodhouse, 2006b). This vegetation bias is highly dependent on the wavelength. While shorter wavelengths show a higher vegetation bias, larger wavelengths are less influenced by the vegetation, as they can penetrate into the canopy.

Unfortunately, not every phase difference measured gives us meaningful information about the topography. Interferograms are often affected by noise, for example in areas influenced by radar shadow. Therefore, a measure of the meaningfulness of the phase information is needed. This is found in the so called coherence, which is the complex correlation between the phase information of the two complex SAR images. The coherence tells us, how well a single phase value correlates with the neighboring phase values and gives us therefore a prediction of how consistent a phase difference in the interferogram is. This complex coherence $\gamma$ is calculated in the following way:

$$\gamma = \frac{\sum_N p_1 p_2^*}{\sqrt{\sum_N |p_1|^2 \sum_N |p_2|^2}} \tag{2.6}$$

where $p_1$ and $p_2$ are the Single Look Complex (SLC) pixel values and $N$ is the number of pixels in the $N$-sample window used to estimate the coherence. Note that $\gamma$ is a complex number, where the phase angle of $\gamma$ corresponds to the phase difference, and the amplitude $|\gamma|$ gives a measure of the meaningfulness of the measurement. The denominator normalizes the magnitude of $\gamma$ so that it ranges from 0 to 1. If the pattern of complex values over the $N$ pixels are completely correlated then they are fully coherent and $|\gamma| = 1$. If $|\gamma| = 0$ then the patterns are uncorrelated and are said to be incoherent (Bamler & Hartl, 1998; Woodhouse, 2006b).

# 3. Data

## 3.1. Study Sites

The study area of this thesis is located in the north-eastern part of Switzerland. Two locations were chosen as the primary study sites. The study site selection was based on the availability of ground truth and airborne laser scanning data. The two test sites are located on the Lägern (red rectangle in Figure 3.1) and in the greater Hinwil area (yellow rectangle in Figure 3.1). In the following subsections, each study site is characterized in depth.

As these two test sites are rather close together and both located in the *Mittelland*, the climatic conditions at each test site are very similar and can be characterized as temperate, with a mean annual temperature around 9° C and a mean annual precipitation of 1000 to 1500 mm (MeteoSwiss, 2014a,b).

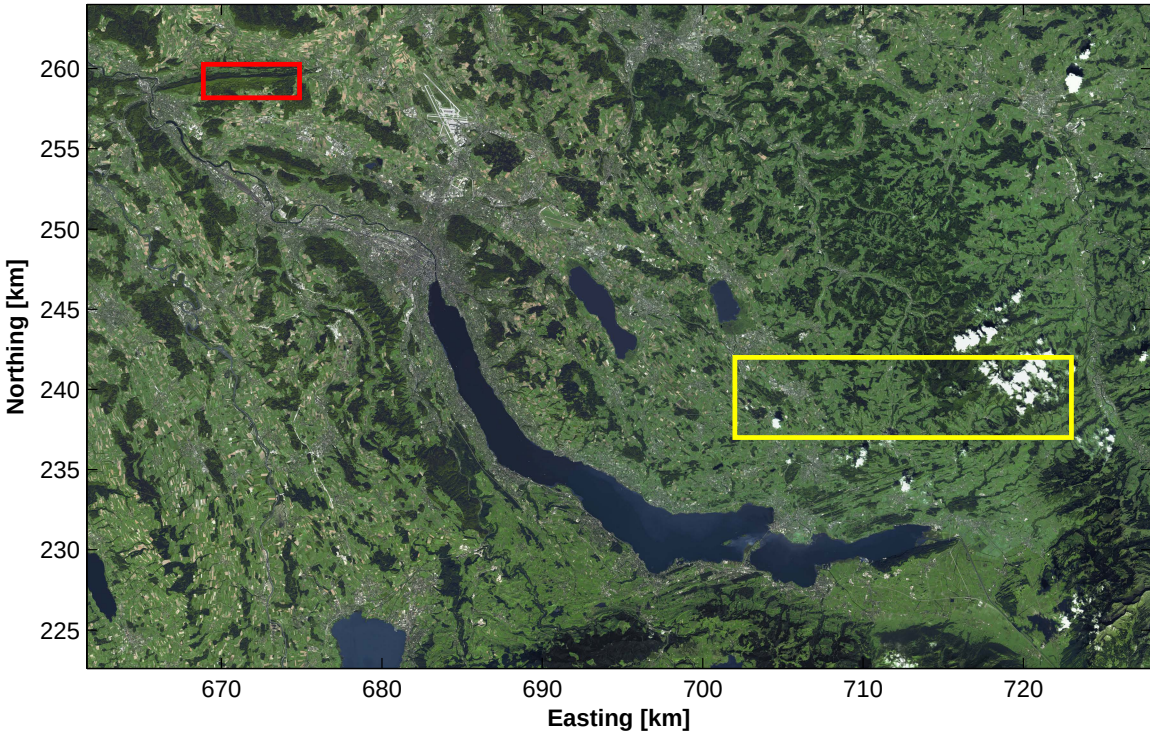


**Figure 3.1:** Study sites: Lägern (red) and Hinwil (yellow). Image taken from a SPOT mosaic provided by swisstopo (Swisstopo, 2006).

### 3.1.1. Lägern Study Site

The Lägern is a mostly forested, long and narrow hill located in the cantons of Aargau and Zurich. The altitude above sea-level ranges between 450 and 870 meters, therefore showing some topography with steep slopes on the northern and southern hill face. The dominating forest type is mixed

deciduous forest (see Table 3.1 )(Swiss Federal Statistical Office, 2004) (see Section 3.6 for further explanation of the occurring forest types). The test site covers an area of 2100 by 6000 meters (1260 ha) and is highlighted in Figure 3.2.

**Table 3.1:** Forest Types at the Lägern Test-Site (data according to *Waldmischungsgrad 92* dataset, Swiss Federal Statistical Office, 2004).

| Forest Type | Relative Occurence [%] |
|---|---|
| Coniferous | 12.4 |
| Mixed-Coniferous | 19.2 |
| Decidiuous | 33.1 |
| Mixed-Deciduous | 35.4 |

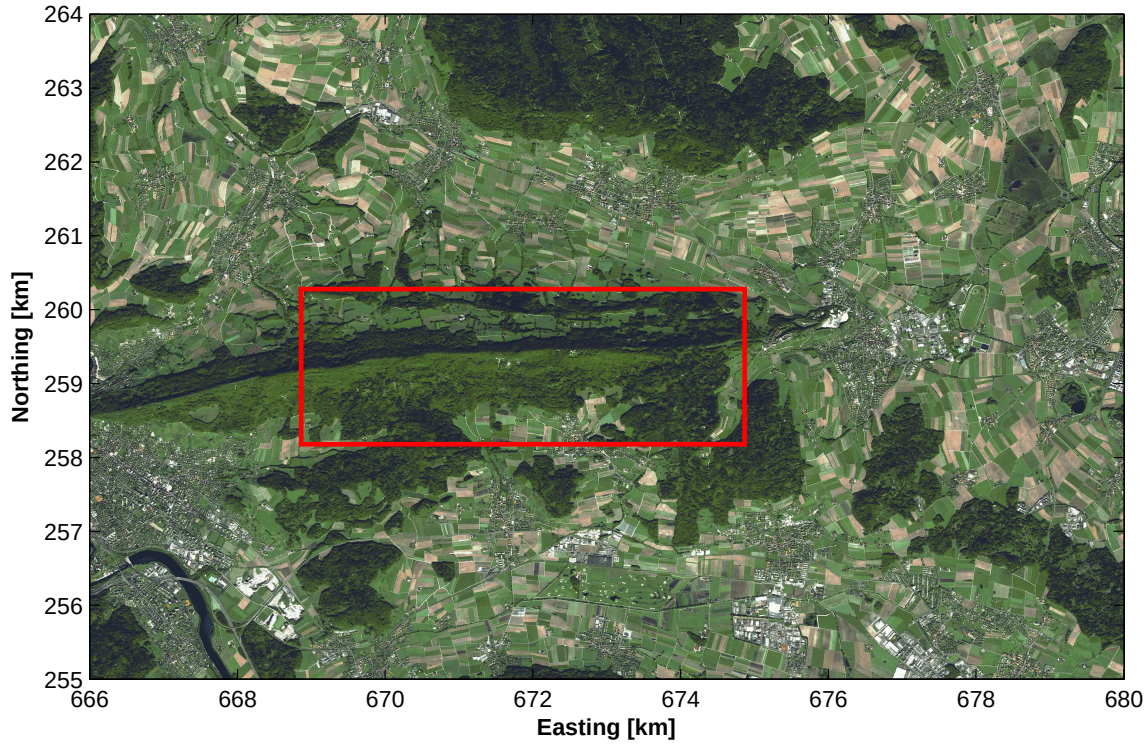


**Figure 3.2:** The Lägern test site (highlighted in red). Data taken from SPOT mosaic provided by swisstopo (Swisstopo, 2006).

### 3.1.2. Hinwil Study Site

As opposed to the Lägern test site, the Hinwil study site is not a large connected forest, but shows several smaller forest stands interspersed with agricultural areas and some villages. The western part of the test site is rather low and shows only moderate topographic variability, except for some drumlins built during the last ice-age. This changes rapidly in the eastern part of the study site, where we find some topographic features with rather steep hill faces. This study site therefore shows

the biggest topographic variability of both test-sites, with an altitude above sea-level between 520 and 1330 meters.

The extent of the study site differs depending on the methodology used for the biomass estimation and the available reference data (see Figure 3.3). The smallest extent applies to biomass estimation approaches using DLR E-SAR data (blue rectangle in Figure 3.3); it covers an area of about 3000 ha. This subset of the whole test-site extent covers the rather flat part of the Hinwil test-site. The available plot level ground truth data from the *Kantonales Stichproben Inventar* (KSP), covers the area highlighted with the yellow rectangle in Figure 3.3. When comparing ALOS PALSAR data to airborne laser scanning data, the extent shown in red in Figure 3.3 was studied, with an area of nearly 6000 ha. This extent also shows some topographic changes especially in the eastern part.

The dominating forest type for the E-SAR and the ALS data extent is mixed-coniferous forest (see Table 3.2). Thanks to the extensive forest plot data available from the KSP dataset (refer to Section 3.2), we also have a more detailed summary of the tree species occurring at the Hinwil study site. The most common tree species at the Hinwil study site are beech (*fagus silvatica*) and spruce (*picea albies*), followed by fir (*albies magnifica*) and ash (*fraxinus excelsior*), as shown in Table 3.2.

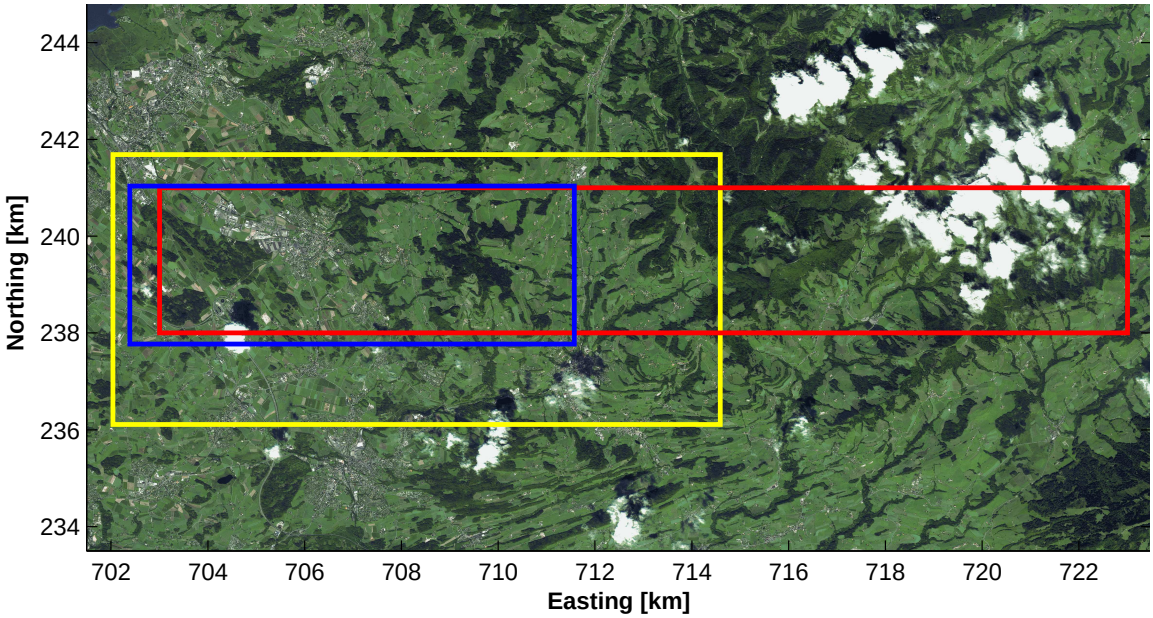


**Figure 3.3:** The Hinwil test site (yellow rectangle: KSP data bounding box, blue rectangle: ESAR data extent, red rectangle: ALS data extent). Data taken from SPOT mosaic provided by swisstopo (Swisstopo, 2006).

## 3.2. Forest Plot Survey Data

The building department of the canton of Zurich conducts extensive ground surveys (*Kantonales Stichproben Inventar* (KSP)) covering selected forested areas in the canton. In the survey available, forest plot samples were measured in a predefined grid of 80 x 300 meters in west-east (80 m) and south-north (300 m) orientation respectively. For selected areas, a denser sampling was undertaken with a grid size of 80 x 150 meters. Each sample plot comprises an area of 3 ares (horizontal radius

**Table 3.2:** Relative occurrences of forest types and tree species in the two Hinwil study site extent for E-SAR and ALS analysis according to the KSP dataset (see Section 3.2 for further explanation about KSP data).

| | Occurences [%] | |
|---|---|---|
| Forest-Type | E-SAR Extent | ALS Extent |
| Coniferous | 36.2 | 14.9 |
| Mixed-Coniferous | 44.9 | 44.1 |
| Mixed-Deciduous | 13.1 | 34.6 |
| Deciduous | 5.8 | 6.4 |
| Tree Species | | |
| Beech (*fagus silvatica*) | 15.2 | 28.1 |
| Spruce (*picea albies*) | 52.4 | 31.3 |
| Fir (*albies magnifica*) | 20.7 | 17.7 |
| Ash (*fraxinus excelsior*) | 4.4 | 9.2 |
| Maple (*acer*) | 2.2 | 5.9 |
| Rest | 5.1 | 7.8 |

of 9.77 m). Inside this area, every tree was individually assessed and measured. The assessed parameters used in this thesis are listed in Table B.1.

Inside of the three ares plot, all trees and shrubs with a diameter at breast height (DBH) larger or equal to 12 cm were measured. The breast height is defined as 1.3 meters above ground level. Dead and broken trees were measured, if they were at least 1.3 meters high. The position of each tree was surveyed in polar coordinates (azimuth and radius) relative to its center plot coordinate. Trees that lay inside of the sample plot, but have the center of the tree outside of the sample plot were not measured. Parameters describing the general neighborhood at and around the sample plot (e.g. forest mixing factor or canopy closure) were assessed in a 50x50 $m^2$ area centered at the sample plot center (Building Department Canton of Zurich, 2009).

## 3.3. Airborne Laser Scanning Data

For the two study sites Lägern and Hinwil ALS data were available. The ALS instrument measures with a laser beam the distance between the instrument and the surface. Together with exact information about the location and bearing of the airplane (Global Positioning System (GPS) and Inertial Navigation System (INS) measurements), high resolution 3D point-coordinates of the reflected ground targets can be calculated (Albertz, 2007).

Both data acquisitions were undertaken by the company TopoSys. For both test sites, raw point cloud data as well as processed and rasterized Digital Surface Model (DSM) and Digital Terrain Model (DTM) were available. Raw point cloud data includes the X-,Y- and Z-coordinates of each laser return. The DSM is a high resolution surface model that includes all visible landscape elements such as bare ground, crops, forests, buildings and infrastructure buildings such as towers, bridges

and power lines. The DTM models the bare ground topography, where surface structures such as forests, buildings, etc. are filtered out (Swisstopo, 2007).

Details of the datasets for the two study sites are listed in the following subsections. A comparison between the datasets is outlined in Table 3.3.

**Table 3.3:** Comparison between the Hinwil and Lägern ALS datasets. Information according to (TopoSys, 2003, 2010a,b).

| | ALS dataset over Hinwil | ALS dataset over Lägern |
|---|---|---|
| Acquisition date leaf-off | 01.04.2003<br>18.04.2003 | 10.04.2010 |
| Acquisition date leaf-on | - | 01.08.2010 |
| Datasets | DSM, DTM, Point Cloud | DSM, DTM, Point Cloud |
| Flight Altitude [$m.a.g.l.$] | 1400 | 500 |
| Raster resolution [$m$] | 1 | 0.5 |
| Reference Coordinate System | LV03 (CH1903) | LV95(CH1903+) |
| Positional Accuracy [$m$] | $< \pm 0.5$ | $< \pm 0.5$ |
| Vertical Accuracy [$m$] | $< \pm 0.15$ | $< \pm 0.15$ |
| Laser Mode | First-Echo / Last-Echo | Full-Waveform |
| Average Point density [$hits/m^2$] | 12 | 50 |

### 3.3.1. Hinwil Study Site

The ALS data over the Hinwil study site was acquired on the 1st and 18th of April 2003 when the vegetation was still in its leaf-off state. The flight altitude was at about 1400 meters above ground. The system was in Last-Echo and First-Echo Mode, classifying the laser returns either to last-echo or first-echo according to the amount of energy returned to the system. A full wave-form model of the laser return from the 2003 survey is therefore not available (TopoSys, 2003).

The raw point cloud data is stored flight-strip wise in an ASCII-format and contains all measured laser returns. No previous data filtering was done by TopoSys, the data therefore still contains noise such as swarm of birds or multiple reflections. The DSM and DTM were already pre-processed (filtered) and interpolated into a 1 meter resolved raster dataset. For the DSM, laser points classified as first-echo were mainly used, while for the DTM mainly last-echo points were used. Raster cells with missing data points were not filled. The reference coordinate system of the dataset was the swiss coordinate system LV03 (CH1903). The positional accuracy of the dataset is less than 0.5 meters and the height accuracy is less than 0.15 meters (TopoSys, 2003). The mean point density over the whole study site is about 12 hits per $m^2$.

### 3.3.2. Lägern Study Site

The ALS measurements covering the Lägern study site were acquired on the 10th of April 2010 and on the 1st of August 2010. For this study site, we have measurements of the leaf-off as well as the leaf-on stage of the vegetation. The flight altitude of both acquisitions was about 500 meters above

ground. The ALS system used for this dataset was in full-waveform mode, therefore delivering multiple points for each X-Y-Coordinate. For this dataset, the point cloud data containing the X-, Y- and Z-Coordinates of each echo was available in the LAS format. As for the Hinwil dataset, the DSM and DTM were filtered and interpolated into a raster with 0.5 meter pixel spacing. Pixels with missing data were not filled during this process. The reference coordinate system of the dataset was the swiss coordinate system LV95 (CH1903+). The positional accuracy of the dataset is less than 0.5 meters and the height accuracy less than 0.15 meters (TopoSys, 2010a,b). The mean point density over the whole study site was about 50 hits per $m^2$.

## 3.4. ALOS PALSAR Data

The Advanced Land Observing Satellite (ALOS) was launched with an H-IIA rocket from the Japanese Space Exploration Agency (JAXA) Tanegashima Space Center on January 24, 2006. ALOS carried three remote-sensing instruments: the along-track 2.5m resolution Panchromatic Remote-sensing Instrument for Stereo Mapping (PRISM), the 10m resolution Advanced Visible and Near-Infrared Radiometer type 2 (AVNIR-2), and the variable resolution polarimetric Phased Array L-band Synthetic Aperture Radar (PALSAR) (Rosenqvist et al., 2007; Shimada et al., 2009). ALOS orbited the earth in a sun-synchronous orbit at 691 km, passing the equator at about 10:30 and 22:30 local time in descending and ascending orbits respectively. ALOS circled the earth 14.6 times a day and needed 671 revolutions for a global coverage. ALOS therefore had a repeat cycle of 46 days (Rosenqvist et al., 2007).

For this thesis, data acquired by the Phased Array L-Band Synthetic Aperture Radar (PALSAR) were analyzed. PALSAR was an enhanced version of the JERS-1 SAR, developed jointly by JAXA and the Ministry of Economy, Trade and Industry (METI). It was a fully polarimetric instrument, operating at L-band with a 1270 MHz (23.6 cm) center frequency. PALSAR was operated in five different observation modes: Fine Beam Single polarization (FBS), Fine Beam Dual polarization (FBD), Polarimetric mode (POL or PLR), ScanSAR wide beam (WB) mode, and Direct Transmission (DT) mode (see Figure 3.4). In FBS mode, PALSAR was operated with either HH or VV polarization, in FBD mode the polarization options were HH/HV or VV/VH. The viewing angle was variable between 9.9° and 50.8° off-nadir. The fine beam modes yielded a swath width of 70 km and a ground resolution of 10 x 10 and 10 x 20 m in FBS and FBD modes respectively (Rosenqvist et al., 2007).

In this thesis, focus lies on the fully polarimetric mode (PLR) (also known as POL mode), providing full quad-pol (HH, HV, VH, VV) data with a bandwidth of 14 MHz. The default off-nadir angle for polarimetric acquisitions was 21.5°, this yielded a swath width of 30 km and a ground resolution of 30 x 10 m. The incident angle range lay between 22.8° and 25.2° from near to far range (Rosenqvist et al., 2007). A more detailed list of PALSAR characteristics is provided in Table A.1 in Appendix A.

The PALSAR data used in this thesis was provided as raw data from the European Space Agency. Five PALSAR tracks comprising three frames each at two off-nadir angles (21.5° and 23.1°) were available covering most of the north-eastern part of Switzerland and therefore covering all study sites for this thesis. For several frames, multiple acquisition dates were available, enabling the possibility of time series or interferometric studies. Overall, a total of 22 frames were available. All frames are listed in Table A.2 in the Appendix A.

Unfortunately, ALOS stopped communicating with Earth on April 22, 2011, ending its mission after five years of operation (Clark, 2011).

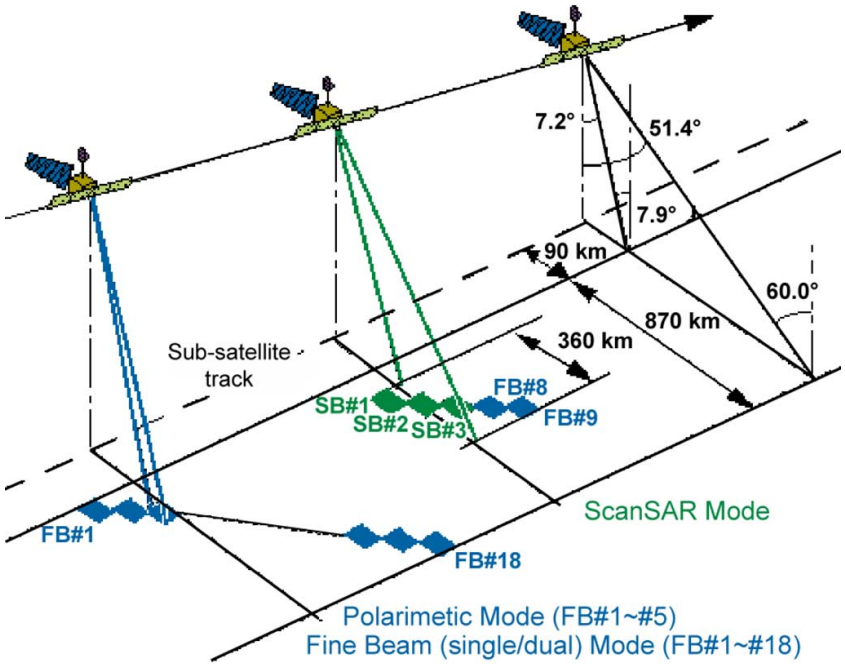


**Figure 3.4:** PALSAR observation modes (Rosenqvist et al., 2007).

## 3.5. DLR E-SAR Data

For the Hinwil study site, also airborne SAR data was available. The data was acquired with the E-SAR instrument operated by the German Aerospace Center (DLR) on the morning of the 12th of September 2006 over a narrow strip over the Hinwil study site (see blue rectangle in Figure 3.3 in Section 3.1.2). On this date, a total of 17 tracks were flown with different horizontal baselines, allowing for interferometric as well as tomographic studies. The sensor was configured to acquire fully polarimetric L-Band SAR data. A summary description of the sensor characteristics is provided in Table 3.4. As it is an experimental system, also different system setups are available in X-, C-, and P-band (DLR, 2000).

The E-SAR raw data was processed and focused to SLC products by the DLR with their internal processing facilities, whereby they already co-registered each SLC to the master-track. Further processing steps were then undertaken in the course of this thesis. They differed slightly depending on whether the data was used for backscatter sensitivity or PolInSAR analysis.These processing steps are further explained in Sections 4.1.2 and 4.1.5.

For the backscatter sensitivity analysis, the track labeled as master track by the DLR was used. A second flight track (slave) was chosen for the PolInSAR study. Its selection was based on its suitability for the later retrieval of forest height. Several studies used a short horizontal baseline (e.g. 5 m in Chen et al., 2008 or 8-10 m in Mette & Papathanassiou, 2004) paired with a short temporal baseline of a few minutes. Only two of the tracks available had a similar horizontal baseline and were therefore considered for this study. Unfortunately, these two tracks had a temporal baseline of several hours and temporal decorrelation could not be neglected. Of the two remaining candidates for the slave track the one with the straightest flight track was chosen. Further specification of the two tracks is provided in Table 3.5.

**Table 3.4:** DLR E-SAR instrument specification for the Hinwil L-Band mission.

| DLR E-SAR Instrument | |
|---|---|
| Frequency [GHz] | 1.3 (L-Band) |
| Wavelength [m] | 0.23 |
| PRF [1/s] | 400 |
| Chirp Bandwidth [MHz] | 94 |
| Sensor Mode | Fully Polarimetric (HH,HV,VH,VV) |
| Look Direction | Left |
| Pixel Spacing Azimuth (SLC) [m] | 0.455 |
| Pixel Spacing Range (SLC) [m] | 1.499 |
| Incidence Angle [deg] | 25 - 60 |

**Table 3.5:** Master and slave track specifications for PolInSAR study. The $\Delta h_{2\pi}$ calculation is referenced to a pixel in the middle of the scene.

| | 06swisar0305x1 (Master) | 06swisar0207x1 (Slave) |
|---|---|---|
| Acquisition date | 12/09/2006 | 12/09/2006 |
| Acquisition time | 10:39:27 | 7:43:26 |
| Temporal Baseline [h] | 3 | |
| Horizontal Baseline [m] | -10 | |
| Perpendicular Baseline [m] | -2.5 | |
| $\Delta h_{2\pi}$ [m] | $\pm$140 | |
| Wind speed [m/s] | 1.0 | 1.2 |
| Temperature [°C] | 19.2 | 16.3 |
| Precipitation [mm] | 0 | 0 |

The vertical wavenumber ($kz$) data used for later forest height retrieval was provided for this master-slave track combination by DLR. For height retrievals, the height of ambiguity ($h_{2\pi}$) is of importance. The height of ambiguity is defined as the altitude difference that generates an interferometric phase change of $2\pi$ after interferogram flattening (Ferretti et al., 2007). If the $\Delta h_{2\pi}$ is somewhere in the range of possible canopy heights (0 to around 35 meters), ambiguities in the height retrieval become common, especially in the case of larger perpendicular baselines ($B_n$). The height of ambiguity can be estimated with Equation 3.1 (Ferretti et al., 2007)

$$\Delta h_{2\pi} = \frac{\lambda}{2} * \frac{R * sin(\theta)}{B_n} \tag{3.1}$$

where $R$ is the range distance, $\lambda$ the wavelength, $\theta$ the incident angle and $B_n$ the perpendicular baseline. For the chosen master-slave combination, $\Delta h_{2\pi}$ was around $\pm$ 140 meters and should therefore not influence the canopy height retrieval.

The weather conditions at the time of the E-SAR campaign are listed in Table 3.5. Weather conditions such as wind and temperature can induce further decorrelation and could therefore influence the forest height retrieval negatively. The weather information was taken from the *climap* database managed by the Federal Office of Meteorology and Climatology MeteoSwiss (MeteoSwiss, 2010). The data were measured at two separate stations close to the Hinwil study site. The wind speed measurements stem from the station at Schmerikon (Coordinates: 713720 m Easting, 231500 m Northing in Swiss LV03), about 12 km south-east of the Hinwil study site. The station lies at 408 m above sea level (a.s.l.), slightly lower than the Hinwil area, but the wind conditions should not differ much between these two locations. The temperature and precipitation measurements were taken at the meteo station at Wädenswil (Coordinates: 693770 m Easting, 230780 m Northing in Swiss LV03), about 13 km south-west of the Hinwil study site. The station is at 463 m a.s.l.. The precipitation value refers to the whole day, i.e. no rain occurred there on this day.

## 3.6. Forest Mixture Data (*Waldmischungsgrad*, WMG92)

For forest, non-forest masking purposes and for specific forest type analysis, the forest mixture dataset *Waldmischungsgrad 1992* (WMG92) provided by the Swiss Federal Statistical Office (BfS) was used. This dataset is available for the whole of Switzerland at 25 meter pixel resolution, where each pixel is classified with the corresponding forest mixture. The six classes found in the dataset are listed in Table 3.6.

**Table 3.6:** Forest type classification in WMG92 dataset.

| Class | Description |
|---|---|
| 0 | Non-Forest |
| 1 | Coniferous Forest (more than 90% coniferous forest) |
| 2 | Mixed-Coniferous Forest (50 - 90% coniferous forest) |
| 3 | Mixed-Deciduous Forest (10 - 50% coniferous forest) |
| 4 | Deciduous Forest (less than 10 % coniferous forest) |
| 9 | No classification available |

For the data basis of the WMG92 dataset, 11 Landsat-5 TM-Scenes from the years 1990 to 1992, with acquisition dates between July and September, were used. First the Landsat images were geometrically and radiometrically corrected before the two classification steps leading to the final product were undertaken. The first classification step classified the whole of Switzerland into forest and non-forest areas with the help of parallelpiped and maximum-likelihood algorithms. The forest, non-forest classification reached an accuracy of 91.8% (Swiss Federal Statistical Office, 2004). Afterwards, the forest pixels were classified into forest mixture classes corresponding to the descriptions given in Table 3.6. This classification was also carried out with a parallelepiped- and maximum-likelihood-algorithm. Compared to the reference information taken from the Swiss Forest Inventory (LFI1), this classification achieved an overall accuracy of 59.8%. The coordinates were based on the Swiss LV03 (CH1903) coordinate reference system (Swiss Federal Statistical Office, 2004).

## 3.7. Forest Mask from swisstopo PK25 dataset

For a few applications in this thesis where the forest mask from the WMG92 dataset with 25 meters resolution was too coarse, the pixel map PK25 (*Pixel Karte* 25) provided by the Federal Office of Topography swisstopo with a pixel resolution of 1.25 meters was used. The PK25 raster maps are the official digital national maps of Switzerland and are based on the printed national topographic maps with scale 1:25'000. The reference coordinate system is LV03 (CH1903). The dataset consists of several layers. One of these layers is the forest area layer (so-called *wton* layer). This layer was used to mask out non-forest areas in combination with highly resolved data (i.e. ALS or E-SAR data). As this dataset covers the whole of Switzerland, the dataset was separated into several sub-parts (corresponding to the printed map sheets provided by swisstopo) with different release dates. The sub-parts of the *wton* layer used in this thesis were based on the 2007 and 2008 data acquisitions for the Swiss topographic maps provided by swisstopo (Swisstopo, 2012).

# 4. Methodology

In this section, the methodologies used in this thesis are outlined and the different approaches to extract biomass information are described. In general the workflow followed this scheme:

1. Pre-processing of the SAR-datasets
2. Establishing biomass reference information from forest inventory and ALS measurement
3. Processing and employment of auxiliary datasets for forest masking and stand retrieval
4. Establishing a backscatter and decomposition power vs. biomass relation using regressional models
5. Inverting the retrieved backscatter vs. biomass models to directly predict biomass from backscatter values
6. Retrieving forest height from PolInSAR measurements and comparing them to ALS retrieved canopy height at the stand level and using transect analysis
7. Relating PolInSAR derived canopy height to biomass via regressional analysis
8. For illustrative purposes, several mosaics of the PALSAR dataset are generated and visualized

In order to retrieve the model parameters, a free Matlab curve fitting toolbox *ezyfit* (Moisy, 2014) was used when just one independent variable was present. For multiple independent variables, the function *polyfitn* (D'Errico, 2006) was used. *Polyfitn* fits a general polynomial regression model in $n$ dimensions.

In the following sections, the processing steps outlined above are further described.

## 4.1. SAR data pre-processing

In Figure 4.1, the scheme for pre-processing the SAR data is outlined. The processing chain differs slightly depending on the SAR data (PALSAR or E-SAR) and the methodology (backscatter or PolInSAR).

### 4.1.1. PALSAR pre-processing

In order to receive focused SLC images of the raw PALSAR PLR images, the PALSAR Instrument Processing Facility (IPF) version 2.0 was used as described in Schubert & Small (2012). One difference between IPF and JAXA processed PALSAR raw data is that the IPF processor focuses the raw data to an azimuth timing convention based on zero Doppler, whereas the JAXA level 1.1 products are processed using the estimated Doppler centroid (Schubert & Small, 2012). In a later step, the focused SLCs were multi-looked (1 look in range and 6 or 5 looks in azimuth for PLR images acquired at 21.5° or 23.1° off-nadir angle respectively) and converted to detected $\beta^0$ intensity products using the software *imop2rsl* developed by David Small.

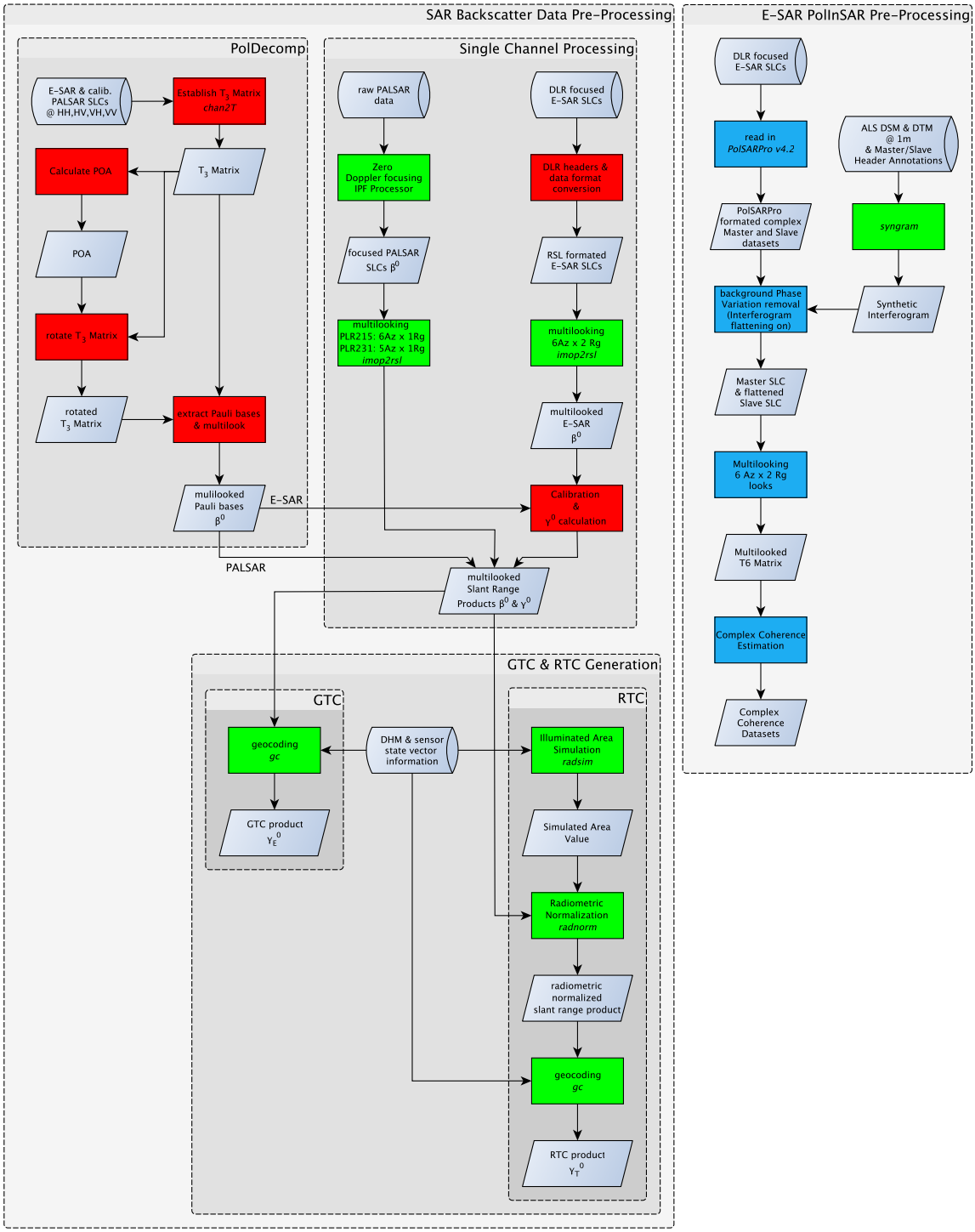


**Figure 4.1:** Workflow diagram of the processing of raw SAR data for later backscatter, polarimetric decomposition and PolInSAR analysis. Processes highlighted in red are performed in Matlab version R2013a, processes highlighted in blue are performed in PolSARPro v4.2, and processes highlighted in green are performed with scripts and software provided by the RSL (developed by David Small).

### 4.1.2. E-SAR pre-processing for Backscatter Analysis

In order to be able to use the RSL processing scripts to convert the SLC products to multi-look detected images, the SLC products delivered by DLR had to be converted into an RSL-compatible SLC format. The conversion step included a translation of the information found in the DLR headers into an RSL-formatted header.

The converted SLC products for each polarization were then multi looked (6 looks in azimuth and 2 looks in range) and converted to $\beta^0$ values. The multi-looking reduces the noise in the data and delivers a more reliable estimate of the backscatter value. The pixel spacing of the multi-looked image is 3 meters in range and in azimuth in slant-range geometry. To get calibrated $\beta^0$ values in dB, a calibration factor of -60 dB was applied according to the DLR image processing report (Horn et al., 2007). The equation to get $\beta^0$ values from E-SAR SLC products are:

$$\beta^0[dB] = 10 * log10(\langle\langle(I^2 + Q^2)\rangle\rangle) - 60dB \tag{4.1}$$

$$\beta^0 = \frac{\langle(I^2 + Q^2)\rangle}{1000000} \tag{4.2}$$

Where $I$ and $Q$ are the real and imaginary part of the complex value respectively and the $\langle\rangle$ brackets denote a spatial averaging, performed with the 6x2 multi-looking.

In order to receive GTC products in the $\gamma^0_E$ backscatter convention, the $\beta^0$ values had to be converted to $\gamma^0_E$ values first. This was done with the following equation (Small, 2011)

$$\gamma^0_E = \beta^0 * \tan\theta_E \tag{4.3}$$

where $\theta_E$ is the local incident angle on the ellipsoid.

### 4.1.3. Establish Polarimetric Decomposition Datasets

In this thesis, the well known coherent Pauli decomposition is used as a polarimetric target decomposition dataset. As described in Section 2.1.4 and seen in Equation (2.2), the three Pauli bases surface scattering (HH + VV), double bounce (HH - VV) and volume scattering (HV + VH or 2×HV if HV==VH) can be retrieved from the $T_3$ coherency matrix. The $T_3$ coherency matrix can be retrieved from SLCs by applying Equation (2.2) with the four polarization channels HH, HV, VH, and VV as input. This is processed with the help of the Matlab function *chan2T* written by Lukas Zuberbühler (RSL). This function writes each matrix element ($T_{11}$,$T_{12}$, ..., $T_{32}$, $T_{33}$) into a complex float raster file. The three Pauli bases are then retrieved from the absolute values of the diagonal matrix elements $T_{11}$, $T_{22}$, and $T_{33}$ and written into separate float raster files that are compatible with the RSL scripts used for further processing. Also note that with the established $T_3$ coherency matrix, the calculation of POA can be performed and the coherency matrix can be rotated along the LOS as described in Section 2.1.4. The rotated Pauli bases can then also be written into separate floating point raster files for further processing.

### 4.1.4. GTC and RTC Generation

The multilook detected slant range products were transformed into map geometry using the software *gc* (see Figure 4.1). Using a DEM and the exact state vector informations, *gc* maps each DEM pixel to a SAR image pixel and retrieves the local backscatter measurement. The resulting GTC product has now the same reference coordinate system as the input DEM.

To generate RTC products, the SAR image had to be radiometrically normalized in the Range-Doppler geometry first, before the image was finally transferred into map geometry. In this step, a SAR image was simulated using the state-vectors of the SAR instrument and a DEM. The simulated image was then used to radiometrically normalize the SAR backscatter image. The radiometrically normalized SAR image could then be transferred into map geometry in the same way as in the GTC case.

For the PALSAR case, the DHM25 DEM with a 25 meter pixel resolution, provided by the Swiss Federal Office of Topography swisstopo (Swisstopo, 2005), was used to geocode and normalize the SAR images. For the E-SAR case, the ALS derived DSM and DTM with a 1 meter pixel resolution described in Section 3.3.1 was used.

### 4.1.5. E-SAR pre-processing for PolInSAR Analysis

The pre-processing steps for the forest height retrieval approach was performed in ESA's open source toolbox PolSARPro version 4.2 (ESA, 2011), capable of reading E-SAR SLC data directly. As the two SLC images were already co-registered, no co-registration had to be done before further processing. As described in Chen et al. (2008) and as done with the backscatter images, the SLCs were multi-looked to 6 looks in azimuth and 2 looks in range. In order to receive the interferogram phase and coherence information, the complex coherence was estimated using a 7x7 estimation window, corresponding to the window size chosen in Chen et al. (2008). Yet, the background phase variation in the raw interferogram had to be removed first. As the DLR did not deliver a flat earth phase vector for the used master-slave combination, the background phase first had to be simulated using the RSL software *syngram*. This software uses a DEM and a header file containing all necessary information about the master and slave data acquisition geometries to generate a synthetic interferogram. The software *syngram* is able to use the DEM information directly resulting in the phase variation caused by the actual topography or to simulate the phase variation assuming a flat-earth (ellipsoid with a given reference height). By using the first case, we generate a DEM-flattened interferogram without the typical topography induced fringe pattern (see Figure 4.2a). By using the second case, we create an ellipsoid-flattened interferogram with the typical topography induced fringe pattern (see Figure 4.2b). The effects of choosing one or the other technique for forest height retrievals is analyzed in the course of this thesis. For the DEM used in the synthetic interferogram generation, the ALS derived DSM as well as the DTM described in Section 3.3.1 were used. In Figure 4.2c, the coherence image of the DSM flattened interferogram at HV polarization is shown. The forests are clearly visible due to their lower coherence caused by volume decorrelation.

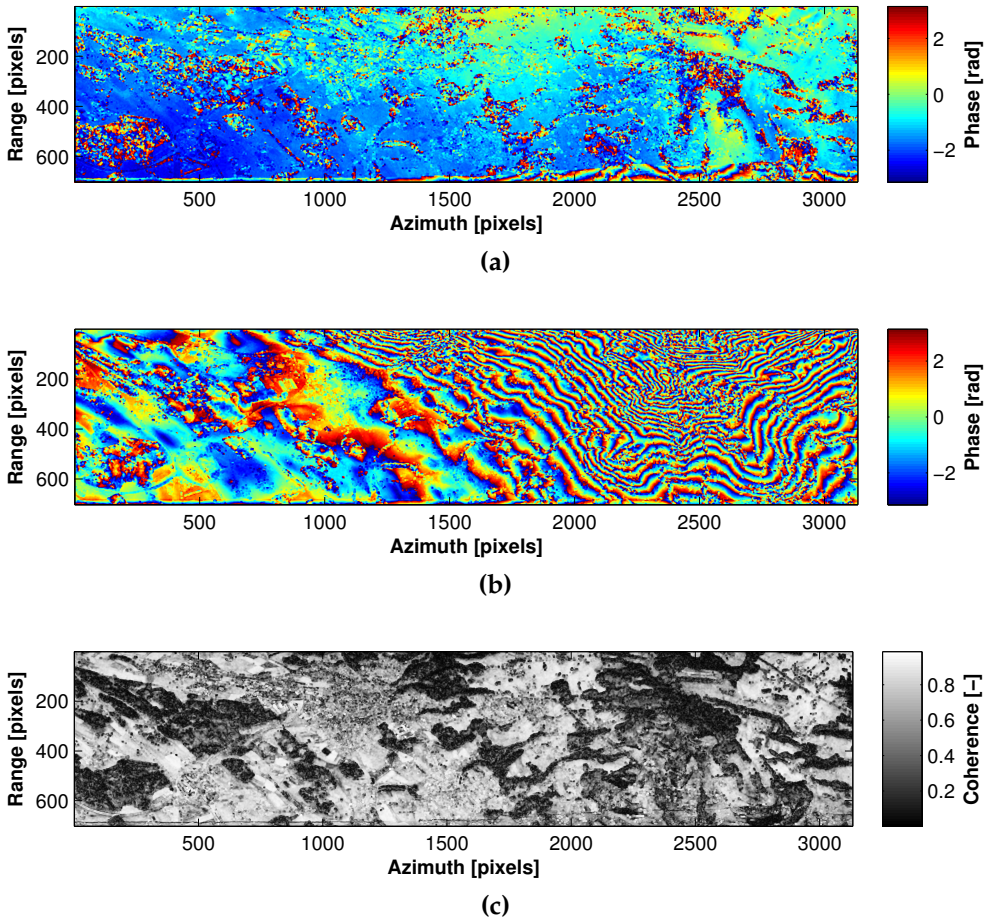


**Figure 4.2:** Interferograms and coherence image for HV-Polarisation. (a) DSM-flattened interferogram, (b) ellipsoid flattened Interferogram, (c) coherence magnitude $|\gamma|$ image of the DSM flattened interferogram.

## 4.2. Mosaic generation

As all study sites treated in this thesis were usually covered by only a single PALSAR PLR frame, no mosaic had to be generated in order to analyze the data. Yet for illustrative purposes, the available frames were combined to mosaics for each polarization, showing the whole data extent of the PLR data available. As these mosaics have only illustrative purposes, more complex approaches to combine several frames (also from two off-nadir angles) such as the Local Resolution Weighting (LRW) approach used in e.g. Small et al. (2004) or the algorithm proposed by Shimada & Ohtaki (2010) for combining PALSAR frames were not considered. Instead, a simple combination approach was chosen, where overlapping pixels were averaged by the number of frames covering that specific pixel. The conceptual work order for the mosaic generation is shown in Figure 4.3.

First, the three GTC or RTC frames (already geocoded to the LV03 coordinate system) corresponding to one track were combined together. Only frames acquired in the same overpass were combined to reduce multi temporal effects when combining frames of different acquisition dates. For the combination of the three frames, information about the coordinate of the upper-left pixel taken from an annotation header was needed. With this information and knowledge of the pixel spacing (25

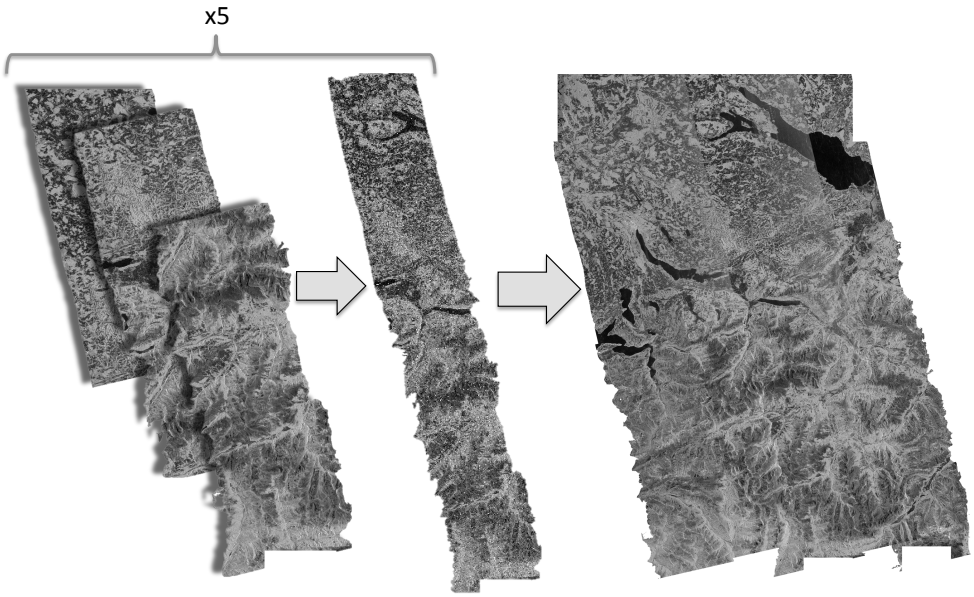


**Figure 4.3:** Conceptual work order of the mosaic generation. Three frames of one track are combined together. Afterwards all 5 tracks are combined to the resulting mosaic. Shown are RTC products at HV polarization.

meters) we know exactly the geometric location of the single frames in the tracks and ultimately also in the mosaic. To generate the whole mosaic, a total of five tracks was needed: three tracks at an off-nadir angle of 21.5° (tracks acquired on the 5th of May 2009 (T638), 17th of April 2007 (T639) and 24th of March 2009(T640)) and two tracks at an off-nadir angle of 23.1° (tracks acquired on the 7th of June 2009 (T639) and 9th of May 2009 (T640)). The generated tracks were then combined in the resulting mosaic. For this, an empty geo-referenced raster was generated first with the extent of the desired mosaic, as a place-holder for the tracks. Again using the information of the upper-left pixel of the tracks, each track was placed exactly into the mosaic. As an auxiliary output, a coverage file was generated that counted the number of frames covering each pixel (see Figure E.1 in Appendix E). For pixels covered multiple times, the backscatter values were summed up. By dividing the output mosaic by the auxiliary coverage dataset, the average backscatter of each pixel was calculated.

For the generation of the Pauli mosaics, a mosaic for each Pauli base was generated first, before combining them into an RGB composite. In order to receive an RGB composite with sufficient contrast between the three channels, the dynamic range of each channel was set individually. This was done based on the program *poldecomp* written by Lukas Zuberbühler. All final mosaic products are shown in Appendix E.

## 4.3. Establishing Biomass Reference Information

### 4.3.1. Biomass Reference from Field Measurements

Most accurate biomass estimation can be achieved from field measurements. Such field measurements were available for the Hinwil study site. As shown in Section 3.2, no direct measure of biomass

was given by the KSP, yet a biomass proxy was provided with the diameter at breast height (DBH) measurement. Several studies reported that DBH is the best proxy for estimating bole volume and biomass (Kaufmann, 2001; Popescu, 2007). Kaufmann (2001) estimated bole volume from DBH with the help of tariff functions in the course of the second assessment of the Swiss National Forest Inventory (NFI). The following basic form of an exponential model for the bole volume $Y_i$ of a single tree was developed by Hoffmann (1982) for employment in Swiss enterprise inventories:

$$Y_i = exp(b_0 + b_1 * ln(d_{1.3i}) + b2 * ln^4(d_{1.3i})) \tag{4.4}$$

Where the subscript $i$ stands for the individual tree, $d_{1.3i}$ stands for the DBH and the parameters $b_0$, $b_1$ and $b_2$ are the model coefficients. These coefficients are species specific and are also listed in Kaufmann (2001). With the application of tariff functions, the rather high inaccuracies of bole volume estimation by just using the DBH, were reduced. With the use of the above model, the standard deviation of the residuals amounts to 26.3% of the mean bole volume (Kaufmann, 2001). An even better estimation of the bole volume could be established if further explanatory variables were used, such as the tree height or the diameter at 7 meters above ground. Yet these measurements were not provided by the KSP, and the bole volume estimation was therefore based on the above stated Equation (4.4).

With the estimated bole volume, biomass can be inferred. Thürig & Schmid (2008) calculated the wood mass by multiplying the bole volume by the tree type specific wood density. Afterwards they multiplied the wood mass by the biomass expansion factor ($BEF$) to obtain biomass values of each tree:

$$Biomass = Y_i * \rho * BEF \tag{4.5}$$

Where $Y_i$ is the bole volume, $\rho$ is the tree type specific wood density and $BEF$ is the tree type specific biomass expansion factor. The specific values for $\rho$ and $BEF$ are listed in Table 4.1. To retrieve the total biomass in tonnes for each plot, the biomass of each tree inside the plot is summed up. To calculate a relative measure in tonnes per hectare, this sum is divided by 3, as each KSP plot represents an area of 3 ares, and multiplied by 100.

**Table 4.1:** Wood density and Biomass Expansion Factor for the two tree types (BEF values from Thürig & Schmid (2008), density values in tonnes dry matter/$m^3$ from Penman et al. (2000)).

| | Deciduous Trees | Coniferous Trees |
|---|---|---|
| $\rho[t/m^3]$ | 0.54 | 0.44 |
| $BEF[-]$ | 1.55 | 1.47 |

## 4.3.2. Biomass Reference from ALS Measurements

As one KSP plot covers a circular area of three ares (circle with 10 meter radius), roughly the same as a square with border length of 18 meters, the biomass information from KSP plots has a different spatial scale than the ALOS PALSAR PLR backscatter data with pixel spacing of 25 meters. The comparison of ALOS PALSAR data to KSP plots was difficult, further hampered by unlucky

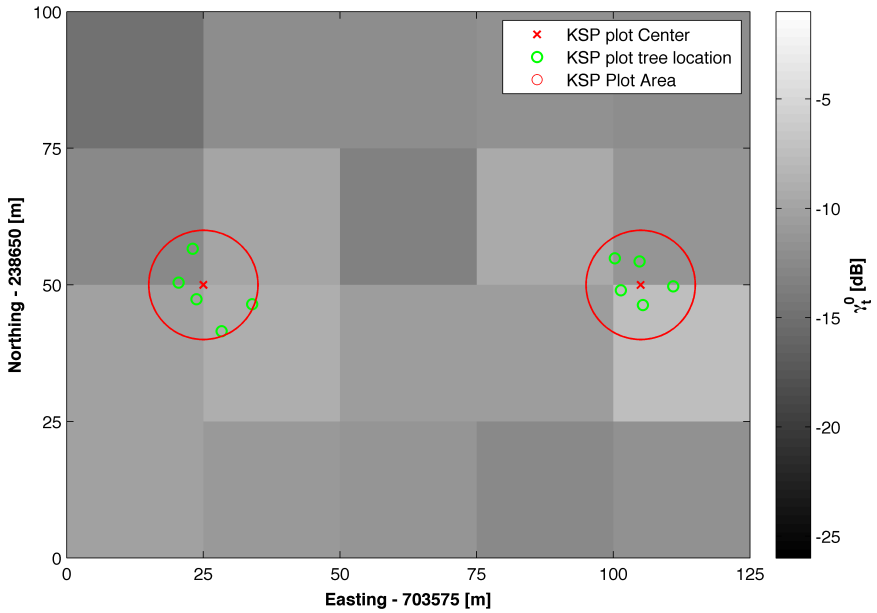


**Figure 4.4:** Relative location of KSP plots compared to geocoded PLR pixels. The red crosses denote the KSP plot center, the green circle the corresponding measured trees and the red circle the assessed plot area.

placement of the KSP plots relative to the geocoded PALSAR pixels (see Figure 4.4). Here it is shown that the plot center lies exactly on the border between two pixels and the whole plot area includes information from up to four pixels. Unfortunately, as the KSP plot locations were assigned systematically in a fixed, pre-defined grid, the relative positions of the plots compared to the PLR pixels was consistent throughout the whole KSP dataset. Furthermore, there are too few KSP plots available for each forest stand to have a reliable biomass estimation at the stand level. For these reasons, an alternative biomass reference was needed. As shown in the introduction, LiDAR metrics have proven useful in delivering biomass information at reasonable accuracy.

Even though the estimation of AGB at single-tree level showed promising results (Popescu, 2007), a single-tree detection based biomass reference generation was not performed due to the following reasons: i) A single tree detection from the point cloud data as described in Morsdorf et al. (2004) was not possible due to some corrupt raw point cloud datasets and the rather low point density of just 12 points per $m^2$. ii) For the estimation of DBH from the tree height and crown dimensions as described in Popescu (2007), an exact matching of detected and field measured trees is important. Yet, due to missing tree height information in the inventory data, an accurate matching was difficult, leading to high inaccuracies for the later biomass estimation. iii) The analyzed heterogenous and mostly dense forests could hinder an accurate detection of trees, leading to further inaccuracies.

For these reasons, a simpler prediction of AGB based on plot level mean canopy height proposed by Nelson et al. (1988) was used in the course of this thesis. Nelson et al. (1988) predicted biomass in his pioneer study using the following model:

$$ln(TTGW) = m * (LHT) + n * (ln(LHT) + b) \tag{4.6}$$

where $TTGW$ is the total tree green weight, $LHT$ is the laser height and the model parameters $m$, $n$ and $b$ were derived by a regression analysis of the mean height of each plot against the AGB measured inside the plot. Lim & Treitz (2004) used a similar approach to relate laser height quartiles to AGB but used a slightly different model. It was used successfully by others to model various forest biophysical properties (e.g. Means et al., 1999, Naesset, 2002 or Lim et al., 2003):

$$ln(M) = ln(\beta_0) + \beta_1 * ln(L) \tag{4.7}$$

where $M$ is the forest metric of interest (i.e. in our case AGB), $L$ is the laser height and $\beta_0$ and $\beta_1$ are model coefficients derived from regression analysis. Both models were analyzed before choosing one of these models for generating a reference biomass map.

For the regression analysis, the procedure proposed by Nelson et al. (1988) was followed. The outline of this is shown in Figure 4.5. First, a CHM was calculated. This was done by simply subtracting the LiDAR DTM from the DSM (refer to Figure 4.6).

In the generated CHM, objects not related to forest or vegetation in general were still visible, such as buildings or power lines. The CHM was therefore filtered first with a forest mask. As the WMG92 dataset with 25 meter resolution was too coarse for use in filtering a 1 meter resolved CHM, the forest mask found in the *Pixelkarte 1:25'000* (PK25) dataset with a pixel spacing of 1.25 meters was used. In order to simply apply this forest mask, the PK25 forest mask was first clipped to the extent of the study site and then resampled to fit on top of the 1 meter resolved CHM using the software ArcGIS version 10.2 and a nearest-neighborhood resampling algorithm. To mask out non-forested areas, the CHM was then multiplied by the previously generated forest mask.

As we had field measured biomass information for the Hinwil study site at hand, a relation between mean canopy height and AGB was established for this study site. Some KSP plots were filtered out of the dataset, as they were outside of the ALS scene. Additionally, to assess the trained model, all KSP plots inside the ALS scene were split into training and validation sets. One third of all plots were randomly assigned to the validation dataset, while the rest were used to train the model and retrieve the model parameters.

To retrieve the mean height over each plot, the mean of all pixel values inside this plot was taken. Therefore, also pixels that have no laser returns from vegetation were taken into account. By doing so, the vegetation density is implicitly considered for the biomass estimation (Nelson et al., 1988).

With the mean canopy height retrieved for each KSP plot, a scatter plot of mean canopy height versus the AGB information of the KSP dataset was drawn, and a function according to the two models described in Equations (4.6) and (4.7) was fitted to the data.

A further filtering of the KSP dataset was performed before training the model, to exclude obvious outliers caused by the big time gap between the ALS and KSP data acquisitions. There are three plots that showed no AGB levels, but had a mean canopy height of more than five meters. These plots were not included in the fit as a plot with mean canopy height of five meters should clearly have some AGB present. The two other plots not included in the fit showed a largely closed canopy in the CHM, but had only one tree inside the plot (see also Figure 4.7). This suggested that a logging or storm event had changed the canopy structure of these plots between the ALS and the KSP data acquisitions.

With the models trained, they can be inverted to finally generate an estimate of the biomass at plot level. For the model introduced by Nelson et al. (1988), the inverted model was described as:

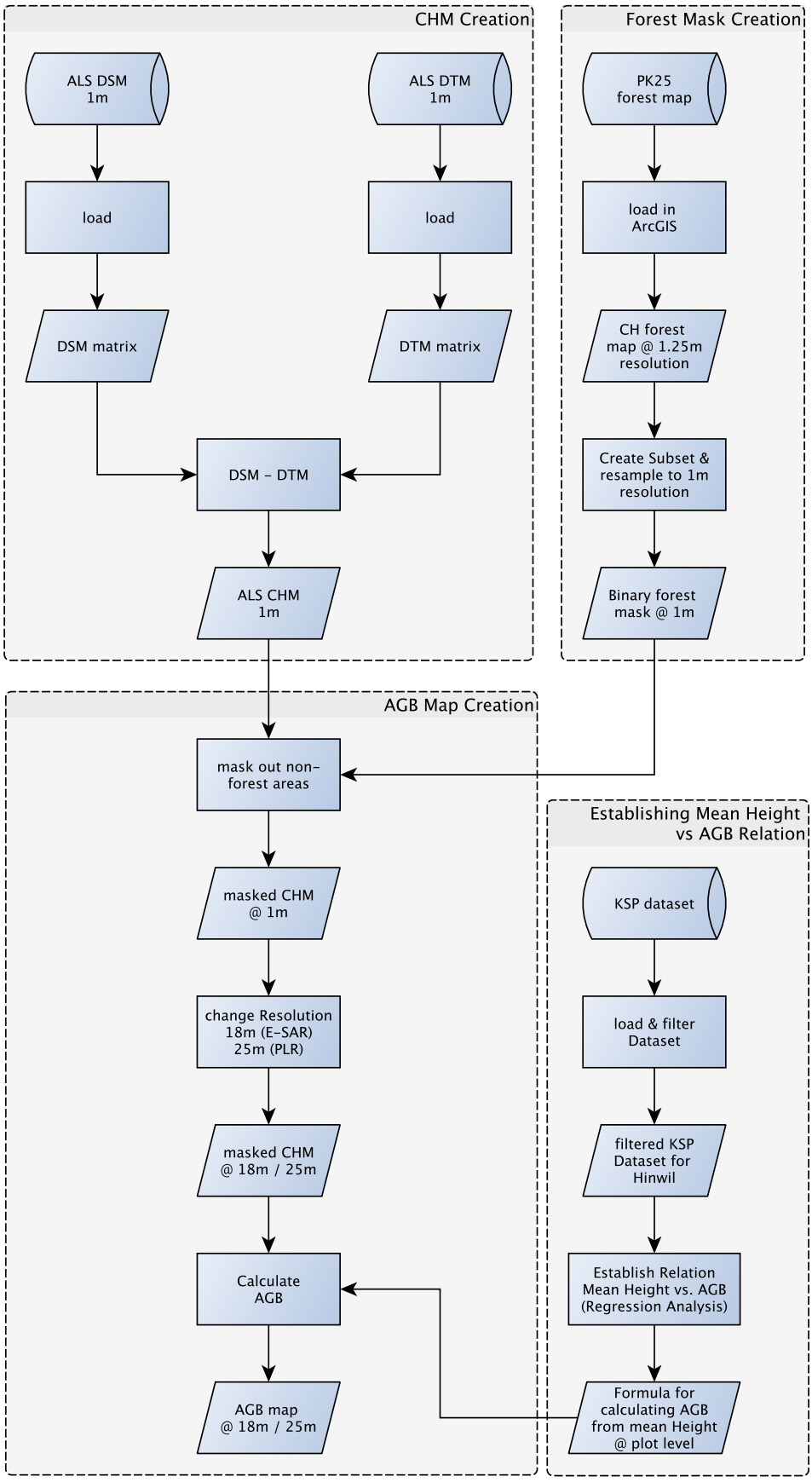


**Figure 4.5:** Workflow to generate AGB maps from ALS data at 18 and 25 meters resolution for Hinwil and Lägern study sites.

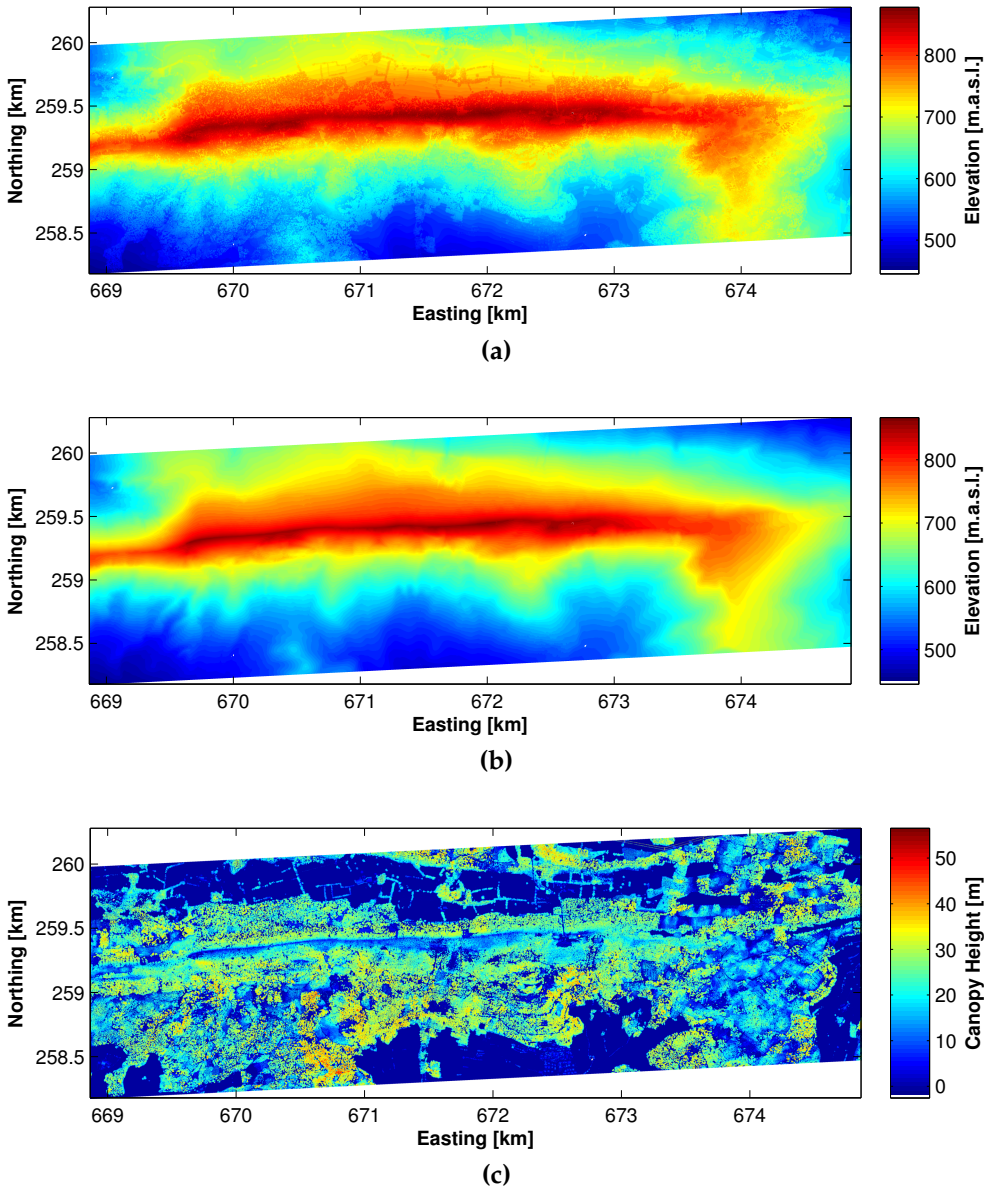


**Figure 4.6:** (a) DSM, (b) DTM and (c) CHM at Lägern study site with 1 meter pixel resolution. The laser data was acquired in spring 2010. The CHM therefore represents the *leaf-off* stage of the vegetation.

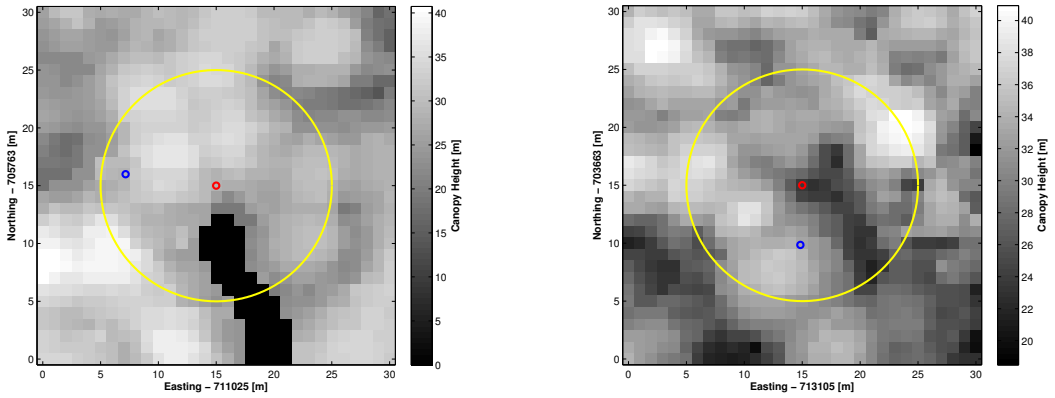


**(a)** **(b)**

**Figure 4.7:** Outlier plots with KSP plot area shown (yellow circle) around plot center (red circle) and the measured trees inside the plot (blue circle). (a) CHM subset around outlier position at 711040/238250, (b) CHM subset around outlier position at 713120/240350.

$$AGB = exp(m * (H) + n * (ln(H) + b)) \tag{4.8}$$

where $AGB$ is the biomass in tonnes per hectare, $H$ is the mean canopy height and the model parameters $m$, $n$ and $b$ are derived from the earlier regression analysis.

For the model described in Lim & Treitz (2004), the inverted model is described as:

$$AGB = exp(log(a) + b * log(H)) \tag{4.9}$$

where $AGB$ is the biomass in tonnes per hectare, $H$ the mean canopy height and the model parameters $a$ and $b$ are again derived from regression analysis. The performance of each model is shown and discussed in section 5.3 on page 59. As the model by Lim & Treitz (2004) showed better performance, all biomass maps were generated using this model.

To generate an AGB map of the study sites, the resolution of the CHM had to be changed first, before applying the chosen model to infer biomass levels from mean canopy height. The resolution of the CHM was changed to 18 meters, as this was closest to the three ares of the KSP plots. The mean value of 18x18 pixels from the CHM was calculated and assigned to the new 18x18 meter pixel. Afterwards, the biomass of each pixel could be calculated with the previously established and chosen model. The generated biomass map for the Hinwil study site as well as the generated CHM at 1 and 18 meters resolution is shown in Figure 4.8.

For establishing a biomass reference map to use with the ALOS PALSAR data, a slightly different approach was chosen. As the PALSAR data has a pixel spacing of 25 meters, a biomass reference map at 25 meters was generated first. This was done with the same method as before, but instead of resampling the CHM to 18 meters pixel size, the resolution was changed to 25 meters. During this step, it was ensured that the new pixels lay exactly on top of the PALSAR pixels (i.e. have the same pixel center coordinates). The AGB was calculated with the same model as established before. Although the model was calibrated to the Hinwil study site, the same model was used to establish the biomass reference map at the Lägern test site, as no field measurements were available

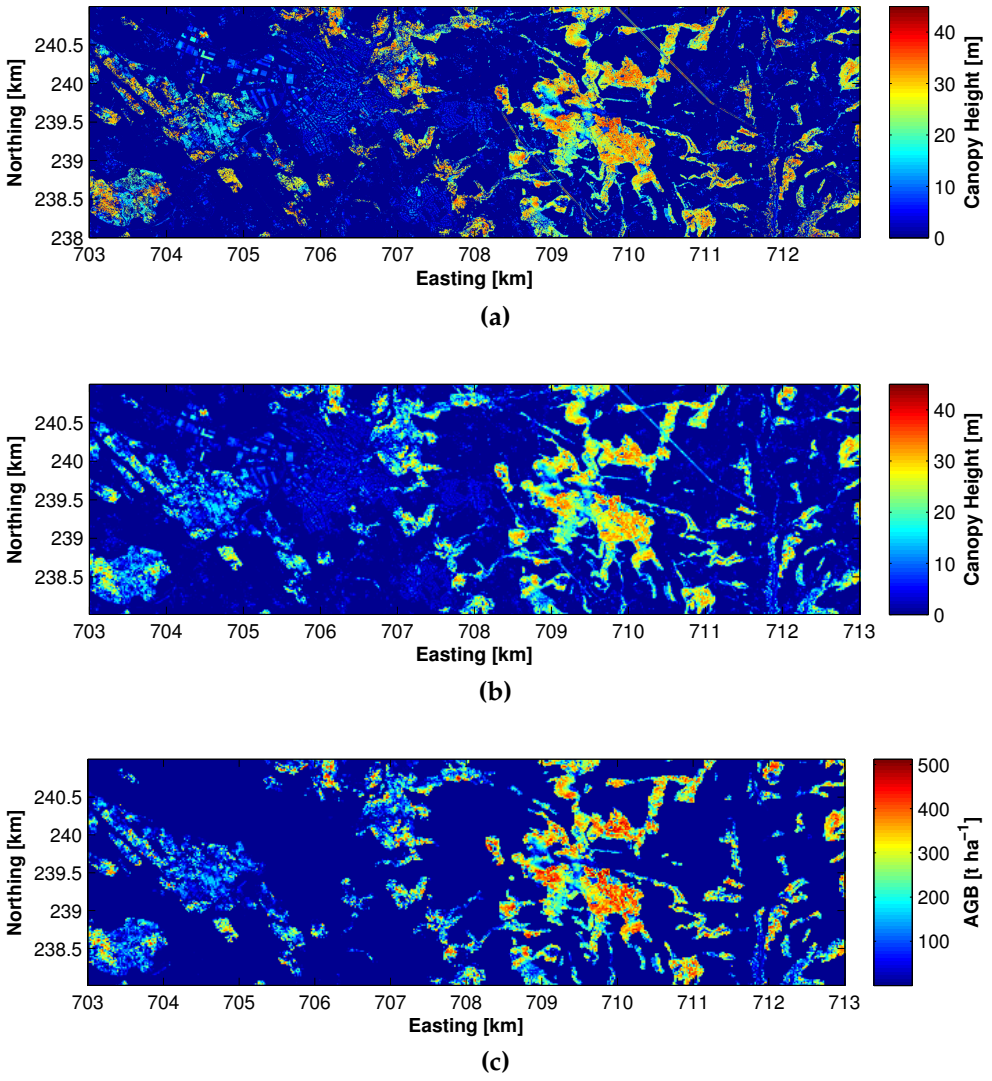


**Figure 4.8:** (a) Canopy Height Model (CHM) at 1 m resolution, (b) CHM at 18 m resolution and (c) Biomass map at 18 m resolution over Hinwil study site. Note that these images just represent a subset of the whole ALS dataset of Hinwil for illustrative purposes. Also note that non-forest areas are masked out in the biomass map.

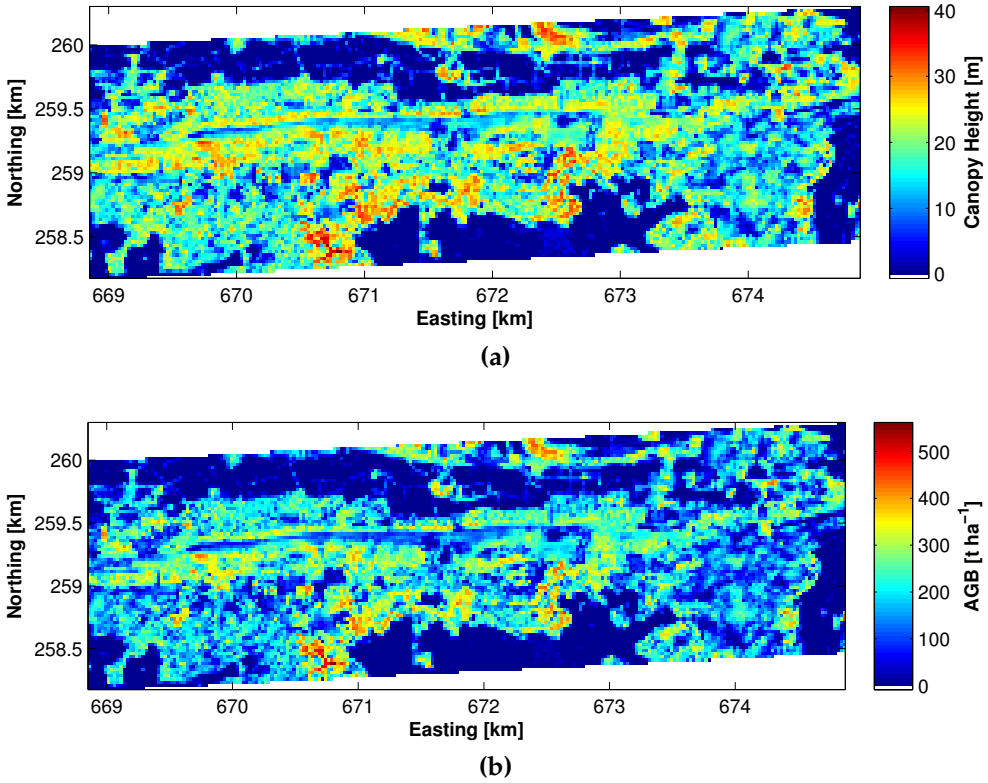


**Figure 4.9:** (a) Canopy Height Model (CHM) at 25 m resolution, (b) Biomass map at 25 m resolution over Lägern study site. Also refer to the 1 m resolved CHM for the Lägern study site shown in Figure 4.6c.

for the Lägern study site. The CHM and the derived biomass map at the Lägern test site is shown in Figure 4.9.

## 4.4. Forest stand retrieval for stand-level analysis

For the stand-level analysis, single stands had to be identified and extracted first. A forest stand is defined as a group of trees occupying a given area that is sufficiently uniform in species composition, structure, site quality and condition (He et al., 2012). As most of these descriptors were not available, a stand was redefined here as a connected forest area with the same forest type (coniferous, deciduous, mixed-deciduous or -coniferous). The requisite information was retrieved from the WMG92 dataset. For the stand-level analysis with E-SAR products, a combination of WMG92 and PK25 datasets was used to reduce errors due to differing spatial resolution and data acquisition time. The 25 m resolved WMG92 dataset was first resampled (nearest-neighborhood) to 1 meter pixel spacing, matching the extent of the E-SAR image. The resampled WMG92 dataset was then multiplied by the previously generated PK25 binary forest mask(refer to Section 4.3.2). Before multiplying the two datasets, the PK25 forest mask was eroded with a 10 meter buffer. This was done to ensure that the forest borders were not considered in the subsequent analysis, as these were known to have significant border effects in the SAR data (shadowing and high backscatter intensities at forest borders facing the sensor). As the PK25 dataset is more up-to date, forest areas that disappeared over the years were

masked out. As the forest mixture is less affected by rapid changes, the mixture information is assumed to be accurate.

The forest stand extraction algorithm searches for connected areas (areas with same pixel values) in a 8-pixel neighborhood and assigns a unique label to all pixels identified as connected. Each stand was then extracted by retrieving all pixels with the same label from the raster image. As the forest stands were later used to extract forest information from the 18 m resolved AGB map, the resolution of the forest stand dataset was also changed to 18 m.

In the case of stand-level analysis with PALSAR data, the original WMG92 dataset with 25 meter pixel spacing was used and no further processing with PK25 dataset was carried out. Instead of a 10 meter buffer around the forest borders, a 3x3 erosion was used to eliminate forest border effects before the forest stand extraction.

## 4.5. Biomass estimation using SAR Backscatter data

In this section, the methodologies to investigate the biomass sensitivity of airborne and spaceborne backscatter data and the biomass estimation performance using different model approaches are outlined. The general workflow for this backscatter approach is shown in Figure 4.10.

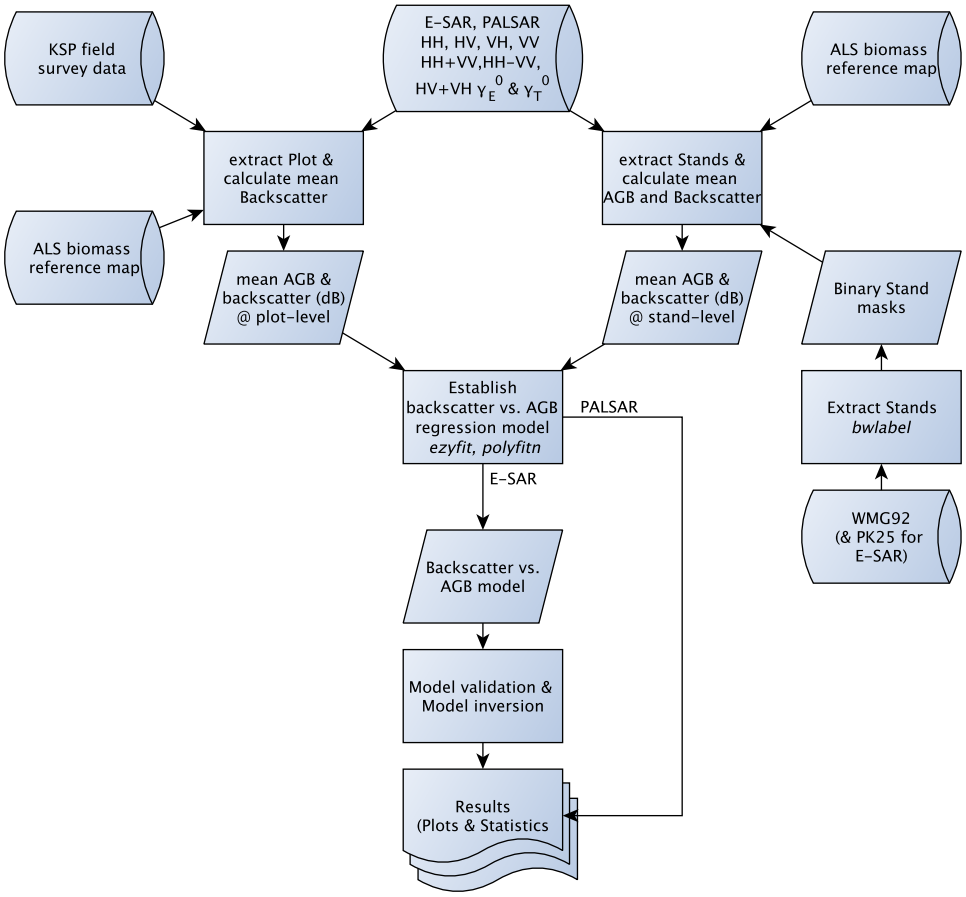


**Figure 4.10:** Workflow diagram for biomass estimation from backscatter data.

### 4.5.1. Single polarization Approach

As previously introduced in Section 1.2, many studies exist that relate L-band backscatter values at single polarization with biomass. In all of these studies, HV-polarization proved to be most sensitive to biomass (e.g. Dobson et al., 1992; Le Toan et al., 1992; Mitchard et al., 2009). One model often used in literature to relate backscatter values to biomass information is described in Mitchard et al. (2009). They modeled the backscatter behavior according to AGB derived at four different African landscapes for PALSAR Fine Beam Dual-Polarization (FBD) backscatter data (HH- and HV-polarization) at plot level. The following model was used:

$$\gamma^0 = a + b * \ln(AGB) + c * (\ln(AGB))^2 \tag{4.10}$$

where $\gamma^0$ is the mean backscatter value in the plot in decibel, $AGB$ is the biomass information retrieved from ground surveys and $a$, $b$ and $c$ are the model coefficients determined using regressions between the measured backscatter and the established AGB reference values. Note that Mitchard et al. (2009) actually used the backscatter convention $\sigma^0$ rather than $\gamma^0$ as used in this study. Also note that the regression coefficients $a$, $b$ and $c$ are dependent on polarization and have to be determined for each polarization separately. They are also highly site specific, implying that new model parameters are estimated for each study site separately.

In order to retrieve AGB information from backscatter data at single polarization channels, the model described in Equation 4.10 needed to be inverted, using the previously established model parameters $a$, $b$ and $c$. This was simply done by solving the quadratic Equation 4.10 to AGB. The inverted model is:

$$AGB = \exp\left(\frac{-b + \sqrt{b^2 - 4c(a + \gamma^0)}}{2c}\right) \tag{4.11}$$

This inverted model was used in this thesis to relate backscatter data at single polarization to AGB, either retrieved from the KSP inventory or, in the case of PLR data or for stand level analysis, retrieved from ALS measurements. Also note that the mean backscatter either at the plot level or over a whole stand was calculated in the power domain. Thus, the arithmetic, not geometric, means were used as described in Mitchard et al. (2009). Only after the average is calculated, can the decibel values of the backscatter be calculated and later related to AGB.

### 4.5.2. Multiple polarization Approach

Saatchi et al. (2007a) used a general statistical regression model that relates different biomass components (total, stem and crown biomass) to backscatter measurements at HH-, HV- and VV-polarization. This model has a quadratic form to approximately mimic the loss of sensitivity of radar backscatter at higher biomass values. The general form of the regression model can be written as

$$\ln(W) = a_0 + a_1\sigma^0_{HV} + a_2(\sigma^0_{HV})^2 + b_1\sigma^0_{HH} + b_2(\sigma^0_{HH})^2 + c_1\sigma^0_{VV} + c_2(\sigma^0_{VV})^2 \tag{4.12}$$

where $W$ is the total aboveground biomass or its components (stem, branch, and foliage), and $\sigma^0_{HV}$, $\sigma^0_{HH}$, and $\sigma^0_{VV}$, respectively, represent the radar backscatter measurements at three transmit and receive polarization configurations in decibels. Equation 4.12 can be considered a parametric equation including all scattering mechanisms represented by the radar polarimetric measurements

(Saatchi et al., 2007a). Saatchi et al. (2007a) actually related backscatter values to different biomass components in the forest (trunk, branches, foliage). As we only have *total* biomass reference values available in this thesis, the focus lies here on predicting the total biomass without distinguishing between the different components.

To retrieve the model parameters ($a_{0,1,2}$, $b_{1,2}$, and $c_{1,2}$) a regression analysis between the measured backscatter data and the reference biomass information (KSP or ALS derived) was established. The detailed methodology on establishing a plot or stand level relation is given in Section 4.5.4 and 4.5.5 respectively. With the model parameters defined, the model can be inverted and used to directly predict biomass from the backscatter data at HH-, HV-, and VV-polarizations.

### 4.5.3. Polarimetric Target Decomposition Approach

Supplementing simple use of backscatter data at different polarizations to predict biomass, polarimetric target decomposition parameters can be used instead. As opposed to using just one polarization or a combination of multiple polarization channels, the different bases of a polarimetric target decomposition relate to actual scattering mechanisms (i.e. surface scattering, volume scattering or double bounce). In this thesis, the well-known Pauli decomposition was analyzed (also refer to Section 2.2). To establish a biomass versus decomposition-power relation, an approach described in Chowdhury et al. (2013) was applied. Although Chowdhury et al. (2013) used the four component Yamaguchi decomposition, which distinguishes between surface-, double-bounce, volume-, and helix-scattering, this approach can also be used with Pauli decomposition, as Chowdhury et al. (2013) discarded the use of the helix-scattering part (this scattering mechanism is normally not found in forests). They therefore only analyzed the volume-, double-bounce-, and surface-scattering portion of the Yamaguchi decomposition.

To fit a regression line between the measured decomposition powers of all three scattering mechanisms and the reference biomass, the same model used previously in the single polarization approach (see Section 4.5.1) was used. For the decomposition power datasets, geometrically and radiometrically corrected decomposition powers (GTC and RTC) were used. The influence of POA correction on the three decomposition bases was also investigated.

Chowdhury et al. (2013) investigated several study sites in Siberia, finding that both volume and double-bounce scattering power have positive correlations and surface scattering has a negative correlation with growing stock volume at the stand level. With that background, a model could be established that describes biomass (or growing stock volume) as a function of all three scattering mechanisms, as shown in Equation 4.13

$$AGB = f\left(\frac{P_d * P_v}{P_s}\right) \tag{4.13}$$

where $AGB$ is the total above ground biomass, $P_d$, $P_v$, and $P_s$ are the double-bounce, volume and surface scattering powers respectively. This behavior can be explained as follows. If we have a dense forest with high biomass levels, the volume and double-bounce scattering return should be high, while the surface scattering part should be low, resulting in a large numerator and a small denominator in Equation 4.13. This behavior reverses if instead we have sparse forest with low biomass levels, where the surface scattering part should be dominant. The applicability of this function to predict biomass is investigated later in this thesis.

### 4.5.4. Establishing Plot Level Relations

As shown in the last three subsections, some biomass reference information is needed in order to extract the model parameters to describe the backscatter behavior with increasing biomass. For the relation of backscatter response to biomass at plot level for the E-SAR dataset, the KSP reference values described in Section 3.2 were used. Yet the whole KSP dataset includes many plots outside the E-SAR scene. Therefore an initial filtering of the dataset was performed to match the E-SAR data extent. A further filtering was performed to exclude forest borders and clear cut plots, as these plots were most likely affected by forest border effects in the SAR backscatter image. After this filtering, only 70 plots remained of the 378 available KSP plots. In a next step, the remaining dataset was divided into a training and validation dataset. All plots were first divided into 20 t ha$^{-1}$ bins according to their total biomass information. Afterwards, 2/3 of the plots in each 20 t ha$^{-1}$ bin were randomly assigned to the training dataset and the rest was assigned to the validation dataset. By doing so, we ensured that we have plots of the whole biomass range in the training dataset as well as the validation dataset. If there were fewer than three points in a 20 t ha$^{-1}$ bin, all points were assigned to the training dataset. As described in Saatchi et al. (2007a) and Askne et al. (2003), two further plots not included in the KSP dataset, representing low biomass references (near 0 t ha$^{-1}$ biomass), were included in the training and validation datasets. In Figure 4.11, the locations of the training (red crosses) and validation (green crosses) plots are shown. In Figure 4.12, histograms for the number of plots per 20 t ha$^{-1}$ bins for training and verification plots are shown, to ensure that the whole range of biomass was covered by the training and validation dataset.

With the training and validation plots established, backscatter sensitivity studies can be performed via the methods explained earlier. First of all, the mean backscatter or decomposition power over each plot was extracted from the backscatter image. Note that no forest masking was performed in this plot level analysis, as the plot locations explicitly represent forest areas (except for the two manually added low biomass reference plots). The retrieved mean backscatter could then be plotted against the total biomass in the respective plots. Afterwards, the above mentioned models could be fitted to the data points, retrieving the required model parameters. The coefficient of determination $R^2$ was calculated to give a measure of how well the model fitted the data. To validate the retrieved model, the function based on the retrieved model parameters was plotted against the validation points to see if the retrieved model accurately explained the validation points. In a further validation step, the retrieved model was inverted to estimate biomass directly from the backscatter data. The

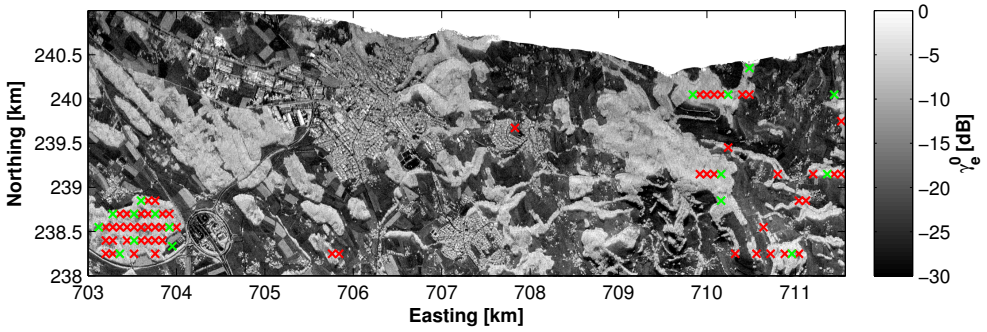


**Figure 4.11:** KSP plot locations inside the E-SAR data extent. Red crosses denote training plots and green crosses denote validation plots for the backscatter to biomass relation analysis.

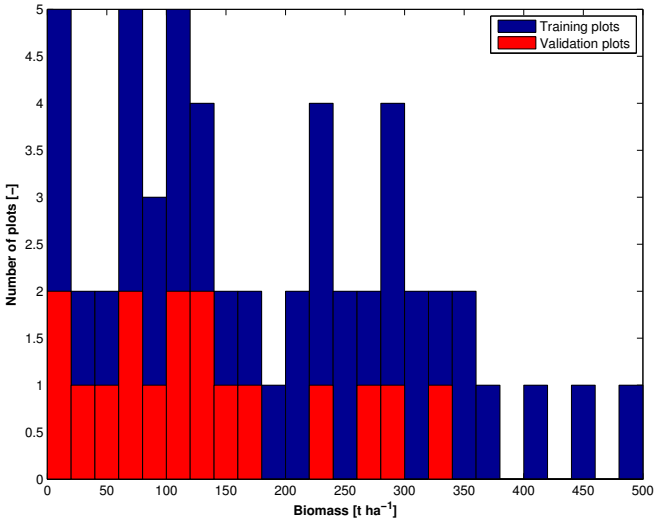


**Figure 4.12:** Histogram of number of plots per 20 t ha$^{-1}$ bin in the training (blue bars) and validation datasets (red bars).

estimated biomass for the validation points were plotted against the reference information to assess the performance of the biomass estimation.

In case of plot level analysis using PALSAR data, a slightly different approach was applied. A simple pixel-by-pixel comparison between PALSAR backscatter and the biomass reference map derived from ALS (see Section 4.3.2) was performed. In order to reduce forest border effects, the PALSAR data was masked with the 3x3 pixel eroded WMG92 forest mask at 25 m pixel resolution. The statistical evaluation of backscatter behavior against biomass is then performed in the same way as described for the E-SAR dataset. In order to reduce the noise in the PALSAR data, an analysis with 100 m resolved PALSAR backscatter data was performed. For this, the mean backscatter values of 4x4 pixels was calculated. New pixels were discarded from analysis if more than half of the 25 m pixels inside the 100 m pixel were either in the radar shadow or had been previously masked. The other datasets (biomass reference from ALS and WMG92 dataset) had to be resampled to the new pixel size as well.

### 4.5.5. Establishing Stand Level Relation

For the stand level analysis, the biomass reference values retrieved from ALS measurements were taken, as there were too few KSP plots inside the stands, and not all stands were represented by the KSP plots. As the ALS biomass reference map had a pixel spacing of 18 m, the 1 m resolved SAR datasets needed to be resampled to 18 m resolution as well. To retrieve the single stand values, the established stand dataset was taken (see Section 4.4). By retrieving a binary mask for each stand, the stand could be extracted from the SAR and biomass reference dataset by simply multiplying the mask with the datasets. Afterwards, the average of the stand's biomass and backscatter values was calculated. The previously described models could be fitted to the data to retrieve the model parameters. This was done in the same way as described in Section 4.5.4. Note also in this case: the stand datasets were divided into separate training and validation datasets. All stands were first divided into several bins according to their size (bins for stands below 0.25, between 0.25 and 0.5,

between 0.5 and 0.75, between 0.75 and 1, and above 1ha). Next, 1/3 of the stands in each bin were randomly assigned to the validation dataset, the rest to the training dataset. By doing so, we assured that the whole range of stand sizes was represented in the training stand dataset as well as the validation stand dataset. For the analysis of backscatter behavior at different minimum stand sizes, the training and validation datasets could now be filtered according to stand size.

For the 25 meter resolved PALSAR data, a similar approach was taken. Yet, as only a sensitivity analysis was performed in the PALSAR case, no separation between training and validation stands was performed. Instead, all available stands were analyzed.

## 4.6. Biomass estimation using PolInSAR techniques

In this section, we compare and contrast several different algorithms to retrieve a CHM from PolInSAR measurements and finally try to infer biomass information from these height estimates. The general workflow for the PolInSAR approach is outlined in Figure 4.13.

As is described in the introduction Section 1.2, the principle of PolInSAR derived forest height estimates relies on the separation of the scattering phase centers of different polarizations or scattering mechanisms (Pauli bases). For example, the scattering phase center of volume scattering (e.g. at HV-Polarization or from the 3rd Pauli base HV+VH) is assumed to be somewhere between half the canopy height and the top of canopy, while the surface scattering or double-bounce scattering is assumed to be close to the surface (Cloude, 2005; Saatchi et al., 2007a). This is illustrated in Figure 4.14. This assumes there is sufficient separation between the two scattering mechanisms in order to retrieve forest heights. However, this separation is not always given, causing such approaches to

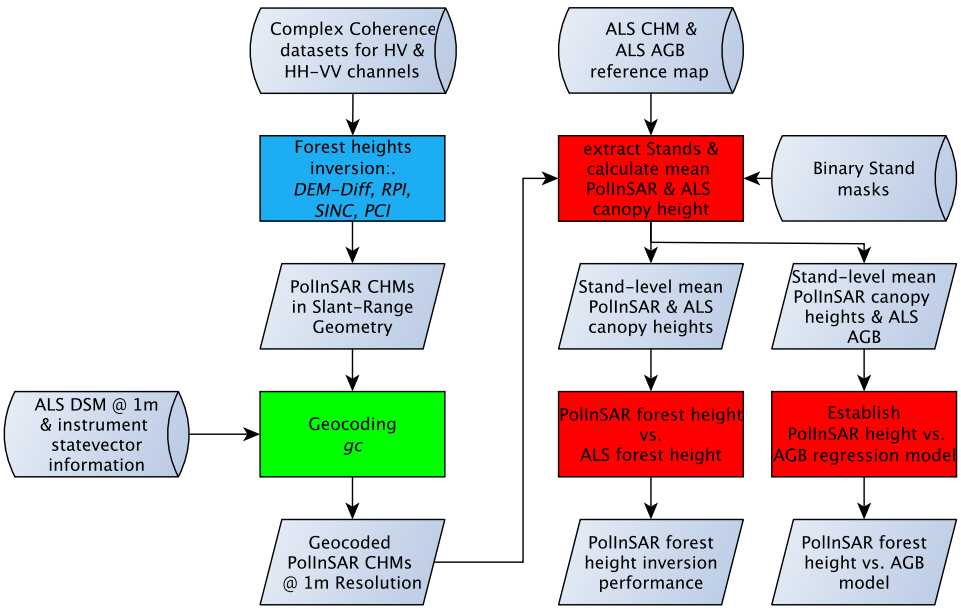


**Figure 4.13:** Workflow diagram for forest height and biomass retrieval from PolInSAR. Processes highlighted in red and blue were performed in Matlab version R2013a or PolSARPro v4.2 respectively. The geocoding process was performed with the *gc* program developed by David Small.

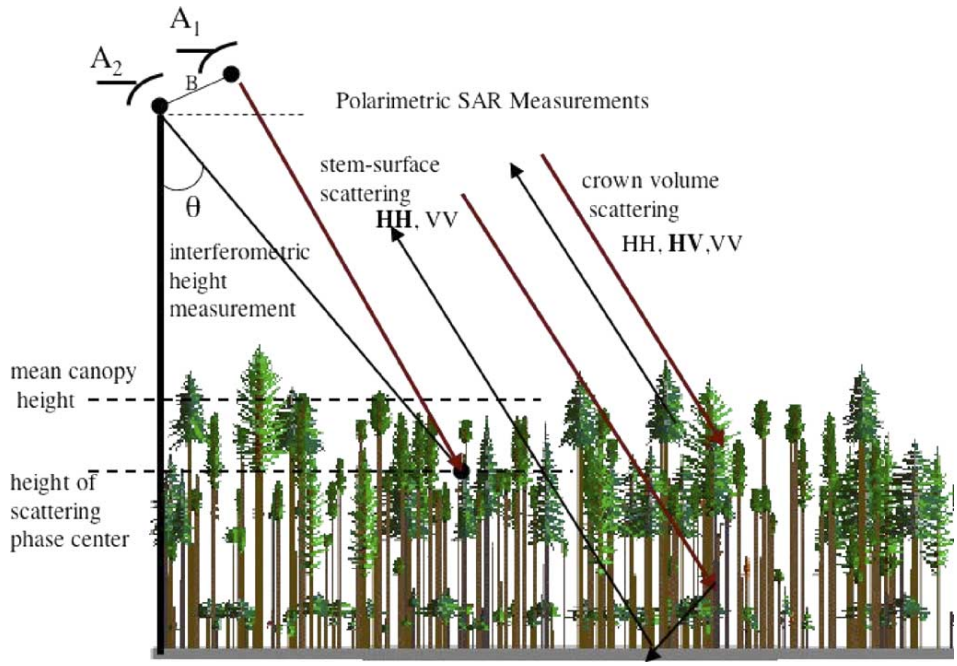


**Figure 4.14:** Polarimetric and interferometric SAR measurements of a typical forest in a flat landscape, with dominant polarizations contributing to crown and stem-surface scattering mechanisms, and interferometric measurements of the height of the scattering phase center as the height of an equivalent scatterer representing the collection of scatterers within a pixel (Saatchi et al., 2007a).

often be noisy (Cloude, 2005). This is one reason why most studies (Chen et al., 2008; Mette et al., 2004; Mette & Papathanassiou, 2004; Papathanassiou & Cloude, 2001) using PolInSAR to retrieve forest heights focus on stand-level estimates, rather than the plot-level or even single tree detection. Hence, the focus in this thesis lies on forest height and later biomass retrieval at the stand-level.

The algorithms used to retrieve forest heights are described in the following subsections. These algorithms are all implemented in the ESA's PolSARPro software package version 4.2 (ESA, 2011). The resulting CHMs from the different algorithms were geo-referenced with the *gc* program introduced in Section 4.1.4 using the 1 m resolved ALS DSM described in Section 3.3.1.

Please note that due to the large temporal baseline of 46 days of ALOS PALSAR, no meaningful PolInSAR analysis with PALSAR data could be performed. The temporal decorrelation in forested areas due to this large temporal baseline was too high to retrieve forest height at sufficient accuracy. Therefore the PolInSAR study was based on the E-SAR dataset with a temporal baseline of 3 hours.

### 4.6.1. Forest Height retrieval using DEM-Differencing

The simplest algorithm used to retrieve canopy heights via PolInSAR is known as the DEM-differencing (DEM-Diff) approach. Assuming that the scattering phase center of the volume dominated interferogram was separated from that of the surface-dominated interferogram, the canopy height $h_v$ can be extracted simply from Equation 4.14 (Cloude, 2005; Chen et al., 2008).

$$h_v = \frac{arg(\gamma_{\underline{w}_v}) - arg(\gamma_{\underline{w}_s})}{k_z} \tag{4.14}$$

where $\underline{w}_v$ is a user selected polarization assumed to be located at the top of the vegetation, $\gamma_{\underline{w}_v}$ is its complex coherence, $\underline{w}_s$ is a user selected polarization assumed to be located near the ground surface under the vegetation canopy, and $\gamma_{\underline{w}_s}$ is its complex coherence. In this thesis, HV-polarization is chosen as the the volume dominated channel $\underline{w}_v$ and HH - VV (the second Pauli base) is chosen to be the surface dominated channel $\underline{w}_s$. The $arg(...)$ function calculates the phase from the complex coherence value $\gamma$. $k_z$ is the vertical wave number, which can be estimated from the interferometric geometry using Equation 4.15 (Bamler & Hartl, 1998).

$$k_z = \frac{4\pi\Delta\theta}{\lambda \sin\theta} \approx \frac{4\pi B_n}{\lambda R \sin\theta} \tag{4.15}$$

where $\lambda$ is the radar wavelength, $\theta$ is the SAR incident angle corresponding to the master track and $\Delta\theta$ is the incident angle difference between the master and slave tracks, $B_n$ is the perpendicular baseline length, and $R$ is the slant range distance from the master to the target. As the vertical wavenumber information was delivered by the DLR for each master-slave pair, $k_z$ needed not to be calculated individually.

### 4.6.2. Forest Height retrieval using RVoG Phase Height (RPI-Inversion)

The approach described in Section 4.6.1 can be very noisy and results in negative height values, when the scattering centre of the chosen *volume dominated* channel is lower than the scattering centre of the chosen *surface dominated* channel. In the DEM-Differencing approach we assumed the second Pauli base (HH-VV) to be closest to the actual surface, with the highest ground-to-volume scattering ratio. Therefore we used this channel as an estimate for the ground phase $\hat{\phi}$. Yet extensive analysis of L- and P-band data sets have shown that in general there is no single polarization channel that yields an unbiased estimate of the ground phase (Cloude, 2005). Therefore, other types of algorithms have been developed that try to remove the residual bias. Using the well-known Random Volume over Ground (RVoG) model, one employs a pair of complex coherence values (Cloude, 2005) as outlined in the following.

One simple algorithm employs a linear fit to a pair of coherence values in the complex plane at polarizations $\underline{w}_s$ and $\underline{w}_v$, where the latter is volume dominated and the former surface dominated. The intersection of this line with the unit circle of the complex coherence plane yields two candidate points for the ground phase. In Figure 4.15, the complex coherence plane is shown with the previously mentioned linear fit between the pair of coherence values. The intersection point Q of the fitted line with the unit circle in Figure 4.15 provides an estimate of the phase of the underlying topography. The other intersection is a false solution and must be rejected by the inversion process. With the assumption that the surface dominated channel $\underline{w}_s$ is closer to the real ground phase (point Q in Figure 4.15) and that the ground-to-volume scattering ratio $\mu$ for the volume dominated channel $\underline{w}_v$ is zero, the ground phase $\hat{\phi}$ can be calculated with a quadratic equation as shown in 4.16 (Cloude, 2005; Chen et al., 2008; Cloude & Papathanassiou, 2003).

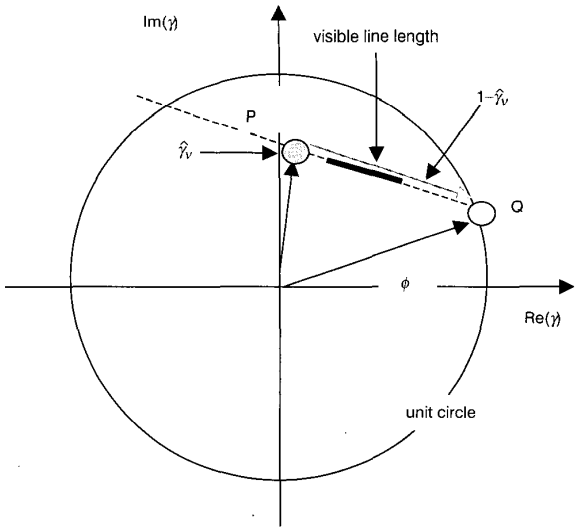


**Figure 4.15:** Linear model used to estimate ground phase $\hat{\phi}$ from two complex coherence value pairs in the complex coherence plane (Cloude & Papathanassiou, 2003).

$$\begin{aligned} &\hat{\phi} = arg\left(\gamma_{\underline{w}_v} - \gamma_{\underline{w}_s}(1 - L_{\underline{w}_s})\right) \text{ where } 0 \leq L_{\underline{w}_s} \leq 1 \\ &AL_{\underline{w}_s}^2 + BL_{\underline{w}_s} + C = 0 \Rightarrow L_{\underline{w}_s} = \frac{-B - \sqrt{B^2 - 4AC}}{2A} \\ &A = |\gamma_{\underline{w}_s}|^2 - 1 \; B = 2\text{Re}\left((\gamma_{\underline{w}_v} - \gamma_{\underline{w}_s}) * \gamma_{\underline{w}_s}^*\right) \; C = |\gamma_{\underline{w}_v} - \gamma_{\underline{w}_s}|^2 \end{aligned} \tag{4.16}$$

With the established estimate of the ground phase $\hat{\phi}$, the next step is the estimation of the scattering height. The height can be estimated using the following equation:

$$h_v = \frac{arg(\gamma_{\underline{w}_v}) - \hat{\phi}}{k_z} \tag{4.17}$$

where $\gamma_{\underline{w}_v}$ is the complex coherence of the user selected volume dominated channel, $\hat{\phi}$ is the previously estimated ground phase, and $k_z$ is the vertical wavenumber (see Equation 4.15).

As previously stated, the phase center of the *volume dominated* channel can lie anywhere between half the tree height and the top of the canopy itself. Apart from the system's wavelength, the exact location depends on two properties of the vegetation, namely the mean wave extinction and vertical canopy structure variation. For trees with a high thin canopy, the extinction is small but the phase centre is high due to the structure. If the canopy extends over the full tree height, the phase centre can be at half the true height for low density (small extinction) through to the top of the canopy for dense vegetation (high extinction) (Cloude, 2005). These vegetation structural influences need to be corrected in order to achieve more accurate height estimates. This outlined algorithm is referenced as Random Volume over Ground Phase Inversion (RPI) in the following.

### 4.6.3. Forest Height retrieval using Coherence Amplitude Inversion (SINC-Inversion)

Another possibility to retrieve canopy height would be to ignore the phase of the coherence completely, accounting only for the coherence amplitude. This approach remains sensitive to density and vertical structure variations. To overcome this limitation, a commonly applied approach is to set the wave extinction to zero, obtaining the simple «sinc» coherence model (Cloude, 2005). This model assumes that the canopy height $h_v$ is closely related to the coherence amplitude of the volume dominated channel (HV-polarization) and follows a truncated sinc function, as shown in Figure 4.16. This assumption is based on the reasoning that larger trees show more volume decorrelation, decreasing the coherence amplitude. Therefore the lower the coherence, the higher the canopy.

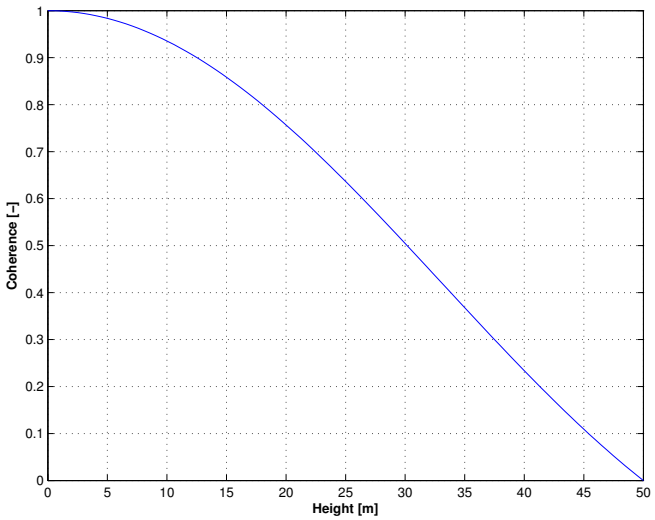


**Figure 4.16:** Example for height estimation from coherence amplitude only.

If we know the volumetric coherence $\gamma_{\underline{w}_v}$, the forest height can be estimated following Cloude (2005)

$$h_v = \frac{2 * sinc^{-1}\left(|\gamma_{\underline{w}_v}|\right)}{k_z} \tag{4.18}$$

where $|\gamma_{\underline{w}_v}|$ is the coherence amplitude of the volume dominated channel (HV-polarization) and $k_z$ is again the vertical wavenumber. Note that the inverse *sinc* function is used to match the coherence amplitude to the simple zero extinction «sinc» model. This is done via a 1-D look-up-table.

As this approach ignores the phase and remains sensitive to extinction and structure variations, it is the least robust of the algorithms, but can serve as a back-up algorithm if the other phase-based approaches fail (Cloude, 2005).

### 4.6.4. Forest Height retrieval using RVoG Phase and Coherence Inversion (PCI-Inversion)

By combining the RVoG phase inversion (Section 4.6.2) and the coherence amplitude inversion (Section 4.6.3) one can build an inversion algorithm that is robust to variations in extinction or vertical structure. Although it is based on assumptions (user selected polarizations for volume dominated and surface dominated channels, ground-to-volume scattering ratio set to zero for volume dominated channel etc.), this algorithm is expected to give height estimates within 10% accuracy, matching the bounds achievable with current air and space borne sensors (Cloude, 2005). Moreover, it is faster and easier to implement than the three stage full model inversion proposed by Cloude & Papathanassiou (2003).

The Phase and Coherence Inversion (PCI) algorithm requires a user selection of two interferograms, one for a surface dominated channel $\underline{w}_s$ and the second for a volume dominated channel $\underline{w}_v$. The canopy height can then be calculated using

$$h_v = \frac{arg(\gamma_{\underline{w}_v}) - \hat{\phi}}{k_z} + \epsilon \frac{2sinc^{-1}\left(|\gamma_{\underline{w}_v}|\right)}{k_z} \tag{4.19}$$

The height is retrieved as a sum of two components. The first is the height retrieved from the RVoG phase inversion (Section 4.6.2). To repeat, the chosen volume dominated channel does not have to be on top of the canopy due to vertical structure variations and wave extinction. To compensate for these effects, the RVoG phase inversion is augmented by the second coherence amplitude term (see Section 4.6.3). The factor $\epsilon$ weighs the two components and should be chosen to provide robustness in the face of extinction variations. In the zero extinction case, $\epsilon$ should be set to 0.5, in which case Equation 4.19 gives the exact result for height, regardless of canopy offset structure. But in the more general non-zero extinction case $\epsilon$ should be reduced. In the extreme case of infinite extinction, $\epsilon$ tends to zero and the phase centre term tends to the true height (Cloude, 2005). Cloude (2005) reported that practical extinction levels at L-band and below are less than 1 dB/m, and that therefore the best choice for $\epsilon$ would be 0.4. This is why $\epsilon = 0.4$ was chosen when applying this forest height inversion procedure in this thesis.

Note that this approach is simplified in comparison to the two layer RVoG full model inversion as introduced by Treuhaft et al. (1996) and Treuhaft & Siqueira (2000) and adapted by Cloude & Papathanassiou (2003). It strongly depends on the user's selection of the volume and surface dominated interferogram. Depending on the selection of the channel, the height inversion may be noisy and a full model inversion as described in Cloude & Papathanassiou (2003) would probably lead to higher accuracy and lower noise levels. Yet, as the full model is not implemented in PolSARPro version 4.2 (ESA, 2011), and the implementation of such a model would be beyond the scope of this thesis, the simplified model inversion was used. To overcome the noisiness of the ground phase estimation due to density variations in the canopy, a simple tweak was implemented in the software. To filter the phase jumps in the estimated ground phase (see Figure 4.17a) a strong 21x21 pixel median filter was applied, reducing the high frequency phase changes and providing a new, more robust estimate of the true ground phase. Figure 4.17 shows the effect of applying such a strong median filter on the retrieved ground phase estimate. One can see that the high frequent phase changes caused by vegetation density changes are eliminated.

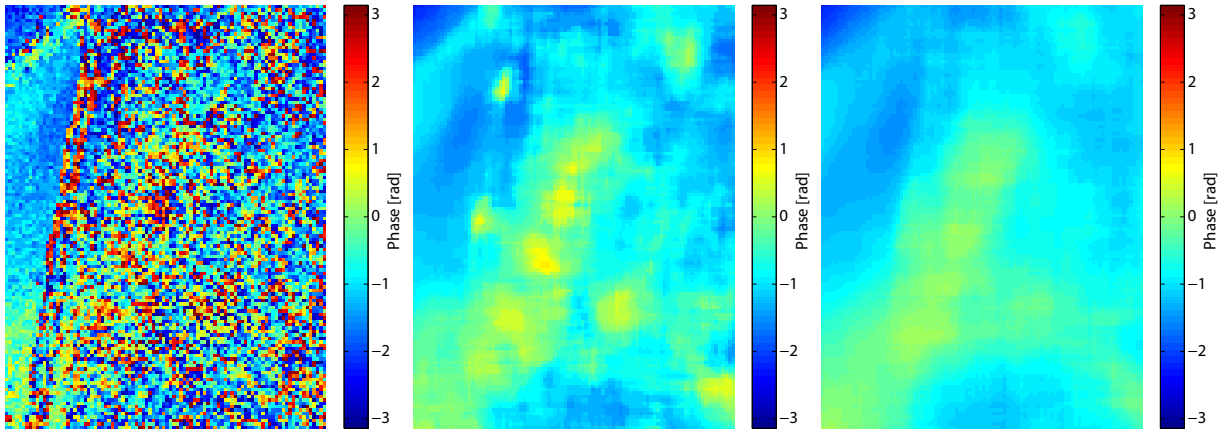


**Figure 4.17:** Ground phase estimate over vegetated area from RVoG model. a) shows the ground phase estimate without any further filtering and therefore still some vegetation induced phase changes. b) ground phase estimate with 11x11 pixel median filter, c) ground phase estimate with 21x21 pixel median filter.

### 4.6.5. PolInSAR Transect Analysis

To determine whether PolInSAR derived CHMs are capable of estimating canopy height at very small scales (up to single tree level) a transect analysis was performed. Several transects in North-South (corresponding closely to the across flight track direction of the E-SAR instrument) and East-West (corresponding closely to the along flight track direction) orientation from ALS and PolInSAR retrieved CHMs were retrieved and analyzed. Further analysis of how well PolInSAR derived CHMs fit the ALS measured canopy height was performed in the course of biomass estimation from PolInSAR canopy heights as described in the next section.

### 4.6.6. Relating PolInSAR Heights to Biomass

Due to the previously discussed close relationship between tree height and biomass, we can now establish a model that estimates biomass levels from the canopy heights estimated via PolInSAR. Mette & Papathanassiou (2004) proposed a simple allometric equation that estimates forest biomass from derived canopy height measurements:

$$Biomass_{forest} = a * height^{c} \tag{4.20}$$

where $a$ and $c$ are model parameters estimated from regression analysis between PolInSAR derived canopy height ($height$) and reference biomass information ($Biomass_{forest}$).

As previously stated, the height estimation and later biomass retrieval from PolInSAR approaches were conducted at the stand level. Before simply applying the allometric equation stated in (4.20), one should analyze how well the estimated canopy heights correspond to actual canopy heights. As a reference, the ALS-derived CHM was used. To compare these two measurements, the mean height of each stand in each PolInSAR CHM product was calculated and compared to the mean height derived from the ALS measurement. As a statistical measure of how well the estimated heights correspond

to the ALS derived measurements, the squared correlation coefficient $R^2$ (the square of the Pearson correlation coefficient) between the reference height values (ALS data) and the estimated height values (from PolInSAR) was calculated. The Root Mean Square Error (RMSE) was also calculated as a measure of the error in the forest height prediction from PolInSAR measurements.

The relation between PolInSAR heights and biomass at the stand level was then analyzed. The PolInSAR derived CHM was compared to the ALS derived biomass reference map (see Section 4.3.2). To do this, the PolInSAR CHM with 1 meter pixel spacing was first resampled to the 18 meter pixel spacing of the biomass reference map, by taking the mean height of each 18x18 pixels. The mean canopy height of each stand was then plotted against the mean biomass. The allometric equation shown in (4.20) was then fitted to the data points, retrieving the model parameters $a$ and $c$. As a measure of how well the model fits the data, the coefficient of determination $R^2$ was calculated together with the RMSE. Unfortunately, due to the small number of stands available that were big enough for PolInSAR analysis, no partition into training and validation stands was possible. There was no evaluation of how well the retrieved model estimated biomass in that case.

With the methodologies established for the backscatter as well as the PolInSAR approaches, we will now look at the retrieved results in the next section.

# 5. Results

## 5.1. Processing of E-SAR data

The processing of the E-SAR datasets was not trivial and it was the first time that RSL's software packages for radiometric and geometric normalization (see Section 4.1) were used with airborne SAR data, the results of these processing steps are described in a separate results section.

### 5.1.1. Geocoding of E-SAR data

A relatively simple way to determine the locational accuracy of the geocoded E-SAR products is by overlaying a DEM on top of the geocoded SAR backscatter image. An example of the product of such an overlay is shown in Figure 5.1, where the ALS DSM is overlaid as a color cycle on top of the geocoded E-SAR backscatter intensity image (HH-polarisation and $\gamma^0_E$ backscatter convention). Each cycle of the RGB color spectrum denotes a height change of 50 meters, visualising small changes in surface heights. Even though we see that the topographic changes visualized with the colored DSM matches the backscatter behavior quite well (lower backscatter intensities in steep hill-slopes away from the sensor), a close-up view is needed to give a better evaluation of the geolocation accuracy. Two such close-up images are shown in Figure 5.2. In Figure 5.2a we can clearly see the increase in backscatter intensity with an increase in surface height at the borders of the forest. Also in Figure 5.2b we see a relation between rapid height changes due to buildings with the characteristic increase in backscatter due to the vertical building face. A more quantitative assessment of the geolocation accuracy of the geocoded products was performed using tie-points distributed over the whole scene. This analysis showed, that the geometric accuracy of the geocoded products was around one pixel and should therefore be adequate for further analysis. Yet, some residual bias could still be present in the geocoded products.

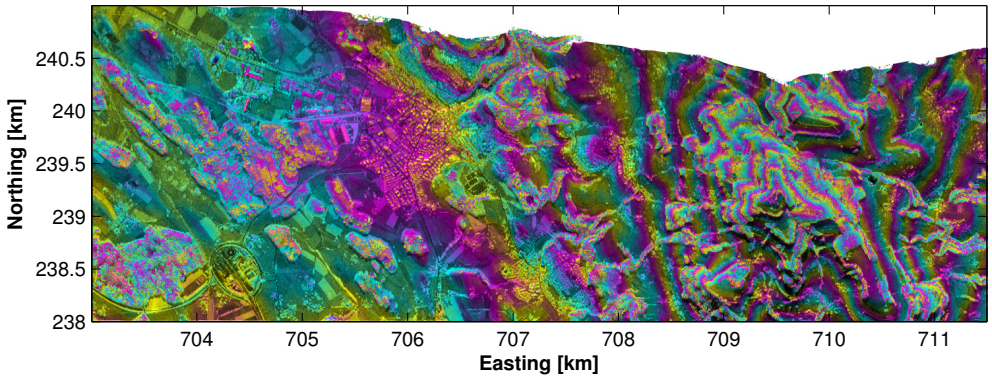


**Figure 5.1:** DSM overlaid on geocoded Backscatter image at HH-polarisation. Each cycle of color denotes a height change of 50 meters. Backscatter scaled between -30 (black) and 0 dB (white). The left-looking E-SAR Sensor flew north of the scene.

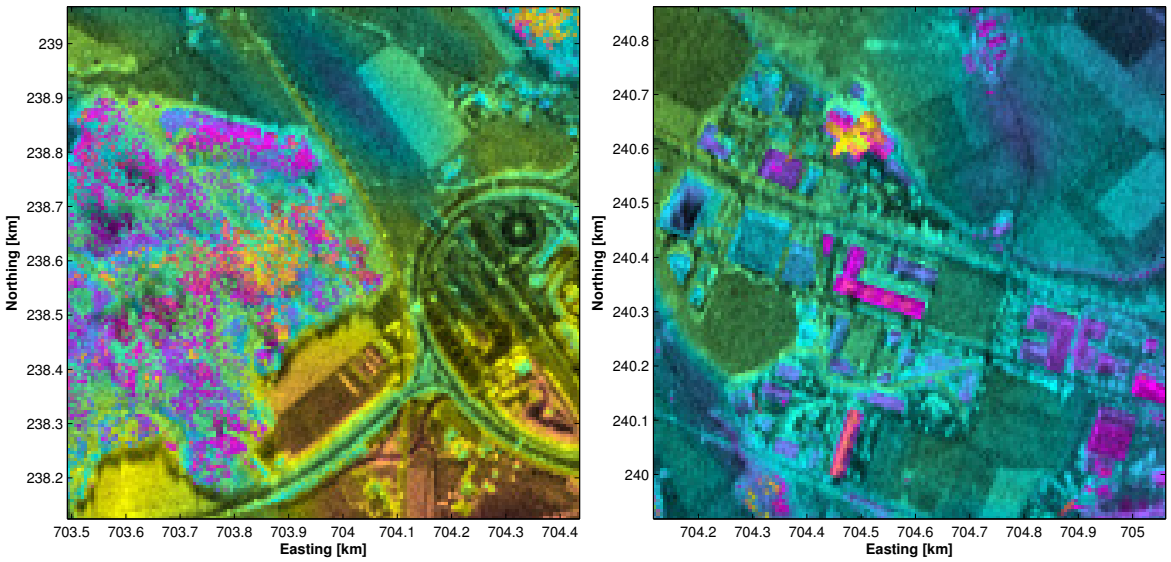


**Figure 5.2:** Two close ups from Figure 5.1. Backscatter changes clearly correlate with height changes, (a) at forest borders and (b) due to buildings.

### 5.1.2. Radiometric normalization of E-SAR data

As stated in the methodology section, both a DTM and a DSM from ALS measurements were available and used for radiometric normalization of the backscatter datasets. Until now, most radiometric normalizations are generated using a DTM, correcting for topographic effects of the terrain. Yet, depending on the wavelength used, also vegetation with significant heights, as found in forests, can affect the backscatter intensities to some extent due to shadowing, fore-shortening and layover effects. Therefore it would be also useful to normalize backscatter data for such vegetation influences. The effect of using the DSM or DTM for radiometric normalization is shown in Figure 5.3 for a small subset of the whole E-SAR scene at HV-polarization. The obvious change in these two products can be found inside the forests. During the DSM-based normalization, many shadow pixels were estimated inside the forest. A much higher variability in backscatter intensity inside the forest is visible due to the height variation of the canopy. The biggest problem here is that the normalization algorithm interprets the input DEM as a solid surface, impenetrable by the radar waves. While this is broadly true for solid objects such as buildings, this is not actually the case for forests or vegetation in general. Depending on the wavelength, the radar waves will penetrate through the canopy to a significant extent. Therefore, an assumption of an impenetrable canopy for the normalization using a DSM leads to an overcompensation of the canopy topography, causing many shadow pixels and overestimated backscatter around trees that are higher than their neighborhood. This is especially observable at forest borders or at forest clearings. Furthermore, as the ALS measurements were made in the year 2003 and the SAR images were acquired in the year 2006, the forest canopy had changed during the intervening time period. This could lead to further normalization errors in DSM-normalized RTC products.

Due to these observations, the decision was made that the DSM normalized images were not to be further used for biomass estimation, as the effects described above would most probably affect

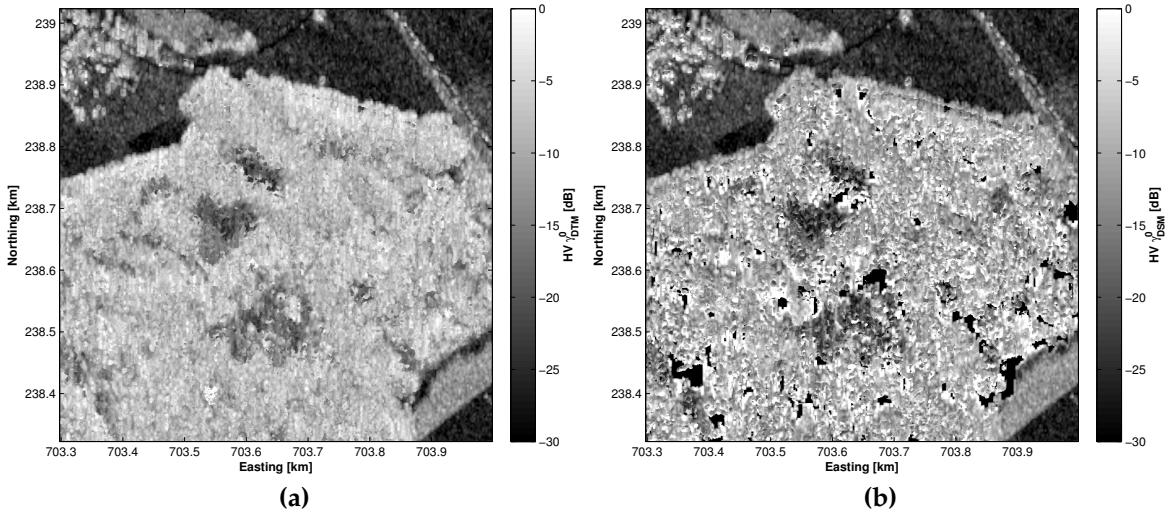


**Figure 5.3:** Radiometric normalization with DTM vs. DSM at HV polarization. (a) DTM normalized. (b) DSM normalized.

the biomass estimation accuracy. Due to the higher number of shadow pixels inside the forest, the number of available KSP inventory plots where one can retrieve realistic backscatter data decreased drastically, reducing the inventory dataset to such an extent that statistical analysis became infeasible.

### 5.1.3. E-SAR GTC vs RTC products

As the RTC product should correct for many of the distortions in more rugged terrain, there should be nearly no difference in the backscatter intensities between the GTC and RTC products in flat terrain. We already saw this in the theory section concerning radiometric normalizations in Figure 2.2. Yet, this is unfortunately not the case for the processed E-SAR GTC and RTC products as seen in Figure 5.4. Here we see that the GTC product in Figure 5.4a appears darker than the RTC product in Figure 5.4c, even in very flat terrain. This is also observable in the backscatter histogram shown in Figure 5.5. Here we see that in HV and HH polarization, the peaks of the GTC product (blue lines in histogram) are shifted by up to -5 dB from the RTC peak. Note that for the GTC products, the radiometric normalization is ellipsoid based, and no terrain information is used for the normalization. For the GTC product shown in Figure 5.4a, the reference height of the ellipsoid was set to 0 m a.s.l.. To create a better calibrated GTC product, the reference ellipsoid height was set closer to the reference elevation of the scene, i.e. 550 m a.s.l. This was done by performing a radiometric normalization using a new ellipsoid with reference height 550 m a.s.l.. The resulting GTC product (shown in Figure 5.4b) shows backscatter values more similar to the RTC product. This can also be seen in the histogram with green lines shown in Figure 5.5. The peaks are now close to those from the RTC product for HV- as well as HH-polarizations. Based on these observations, the E-SAR GTC product with 550 m a.s.l. reference height was used for further backscatter analysis unless otherwise noted. Yet, note that some differences still exist in backscatter intensity values between RTC and GTC with 550 m a.s.l. reference ellipsoid height over flat terrain (GTC image still appears darker in flat terrain located more to the east of the scene). This could be accounted to the terrain elevation changes inside the scene. The reference ellipsoid height of 550 m a.s.l. is located

at the far west of the scene. The terrain heights increase steadily from east to west (see also Figure 5.1), leading in higher differences to the ellipsoid reference height to the west. Together with the low flying altitude of the airborne SAR instrument, this could lead to highly different backscatter intensities at flat areas from different elevations.

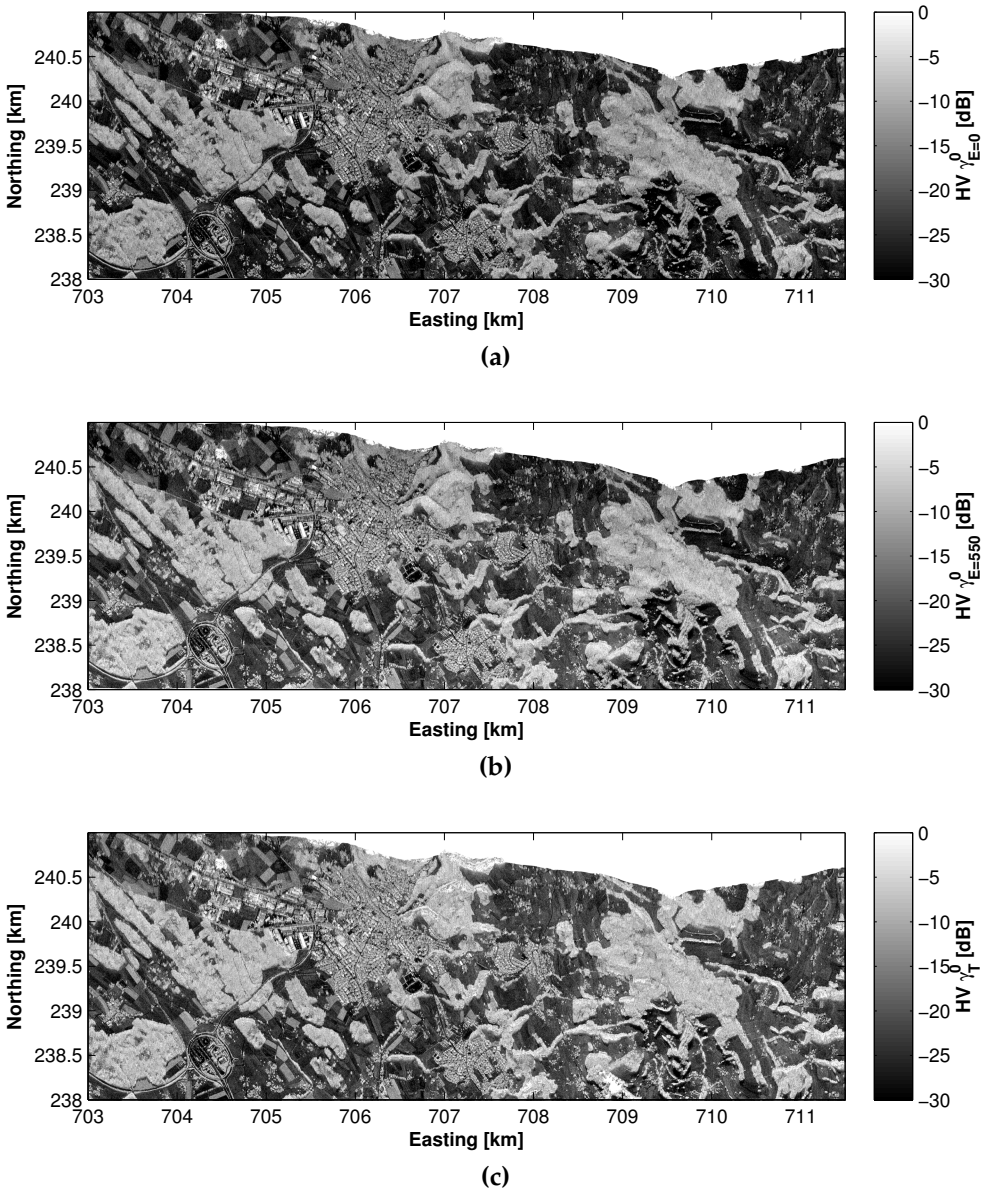


**Figure 5.4:** Processed E-SAR HV-polarization products. (a) GTC product with reference ellipsoid height of 0 m a.s.l., (b) GTC product with reference ellipsoid height of 550 m a.s.l. (c) RTC product.

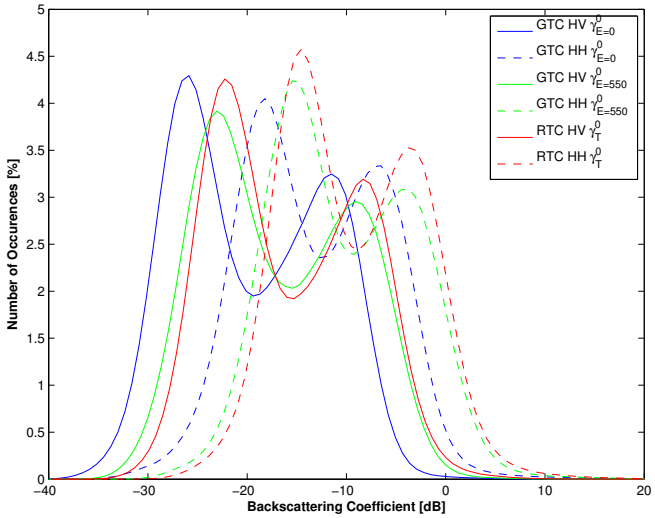


**Figure 5.5:** Backscatter Histogram of RTC products in red, GTC product with reference ellipsoid height of 0 m a.s.l. in blue and GTC product with reference ellipsoid height of 550 m in green. HV-polarization shown with solid lines; HH-polarization with dashed-lines.

## 5.2. POA estimation and Coherence matrix rotation

In Figure 5.6, the polarization orientation angle map retrieved from the fully polarimetric E-SAR acquisition using Equation (2.3) is shown. For comparison, the DTM retrieved from ALS measurements is shown. By comparing the DTM and POA, we see that there are some similarities in the images. Especially flat surfaces not covered by vegetation are clearly distinguishable. Also visible is that the hill side facing to the east shows clearly lower POA values than the hill side facing to the west. This is also visible if we zoom into the image as shown in Figure 5.7. Here we see the clear outline of the ridge of the hill, close to the middle of the scene, with low POA values to the east and higher POA values to the west. Further to the west, the POA values decrease again with increasing terrain height. Some topographic features are therefore clearly distinguishable in the POA map retrieved from E-SAR data. However, there is considerable noise in the image, especially where terrain was covered by forest. This is accountable to the wavelength of the SAR sensor. As the L-band sensor cannot penetrate through the denser canopy, other issues contaminate the POA signal.

Also for ALOS PALSAR data such POA images were calculated as shown in Figure 5.6c. Here a subset of the POA map taken from the frame PLR231-T640F940 acquired on the 9th of May 2009 over the Hinwil study site is shown. Note that while the E-SAR instrument looked roughly to the south, the PALSAR instrument was looking roughly to the E-NE. As the POA is affected by *azimuth slopes* relative to the sensor, the POA maps acquired from the different sensors are not expected to be the same. Compared to the DTM shown in Figure 5.6b not many correspondences can be found. The PALSAR POA map was far noisier, only some flat terrain can be identified. The effects of rotating the coherency matrix $T_3$ on the backscatter intensities of the three Pauli bases surface scattering, double bounce and volume scattering is shown in Figure 5.8. Here we see the three histograms of the difference between rotated and unrotated Pauli bases taken from the slant range E-SAR $\gamma^0_E$ product, where the rotated backscatter values were subtracted from the unrotated backscatter values. As expected from the coherency matrix rotation formula shown in Equation (2.4), the surface scattering channel is invariant to rotation along LOS. But the double bounce scattering channel showed a clear

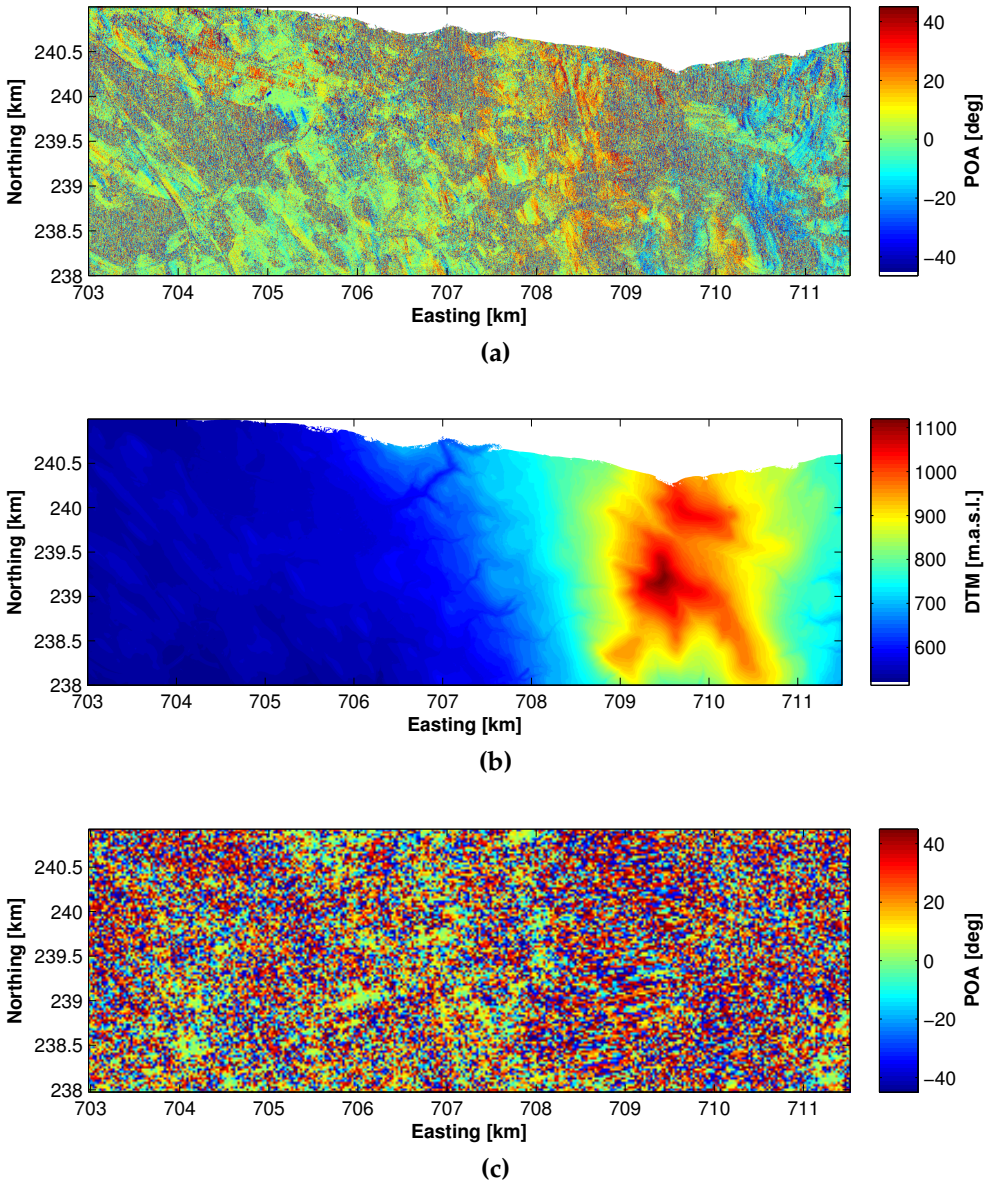


**Figure 5.6:** POA estimation over Hinwil study site. (a) POA map estimated from fully polarimetric E-SAR L-Band data. The left-looking SAR instrument flew north of the shown scene. (b) ALS measured DTM over the same extent for comparison. (c) POA map derived from PALSAR PLR data over roughly the same extent as shown in (a) and (b). The ALOS orbit was ascending and right-looking; the sensor was to the west of the scene.

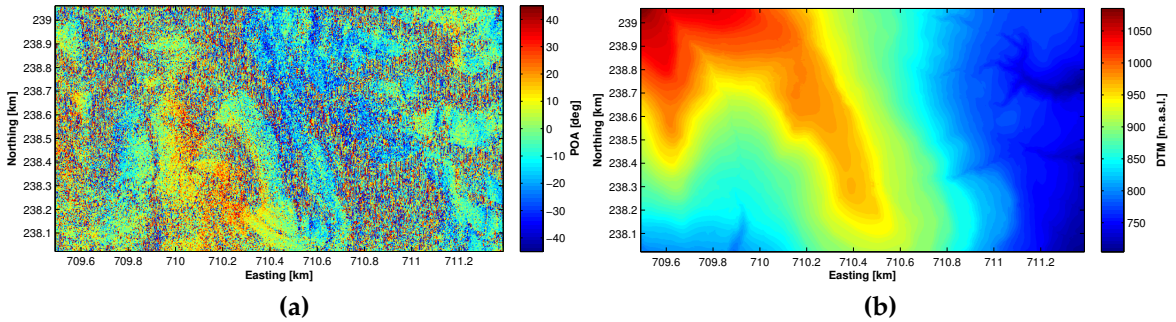


**Figure 5.7:** Close-up of Figure 5.6. (a) POA image, (b) DTM image of the same extent.

increase in backscatter, and the volume scattering channel showed a clear decrease in backscatter values due to rotation. This agrees with results published in the literature (e.g. Lee & Ainsworth, 2011).

## 5.3. Biomass reference establishment from ALS

In Figure 5.9, the scatter-plots between mean canopy heights and the logarithm of biomass are shown with the fitted models after Nelson et al. (1988) in Figure 5.9a and after Lim & Treitz (2004) in Figure 5.9b. The red crosses in the scatter plots are the obvious outliers mentioned in the methodology Section 4.3.2 and were not considered in the model fit. The model described by Nelson et al. (1988) explains the data points slightly better with an $R^2$ of 0.7, in comparison to the fitted model as described in Lim & Treitz (2004) with an $R^2$ of 0.66. In the model after Nelson et al. (1988), a clear saturation at about 15 m mean canopy height is visible. The model described in Lim & Treitz (2004) does not show such a strong saturation with increasing mean canopy height. The retrieved model parameters for each model and their respective performances ($R^2$) are listed in Table 5.1.

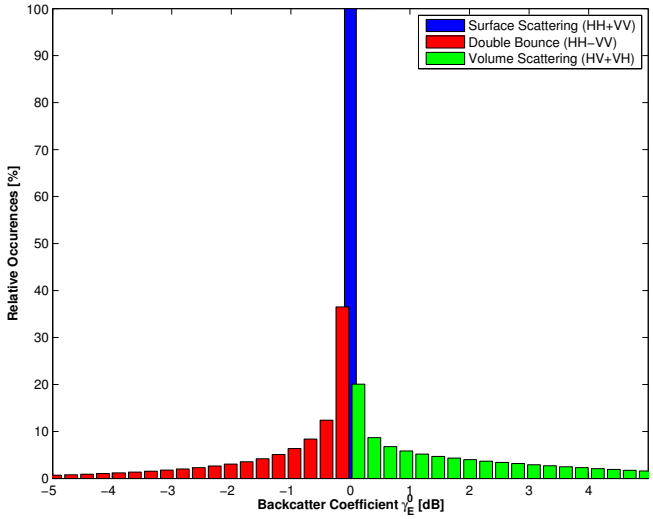


**Figure 5.8:** Histogram of the differences between *unrotated* minus *rotated* Pauli bases taken from the whole E-SAR $\gamma^0_E$ scene.

**Table 5.1:** ALS model fit performance for mean canopy height vs. logarithm of AGB relation with models after Nelson et al. (1988) and Lim & Treitz (2004).

| Model | Function | Parameters | | | $R^2$ |
|---|---|---|---|---|---|
| Nelson et al. (1988) | $ln(AGB) = m * h + n(ln(h) + b)$ | $m = -0.073$ | $n = 1.878$ | $b = 0.676$ | 0.709 |
| Lim & Treitz (2004) | $ln(AGB) = ln(a) + b * ln(h)$ | $a = 4.287$ | $b = 1.317$ | | 0.658 |

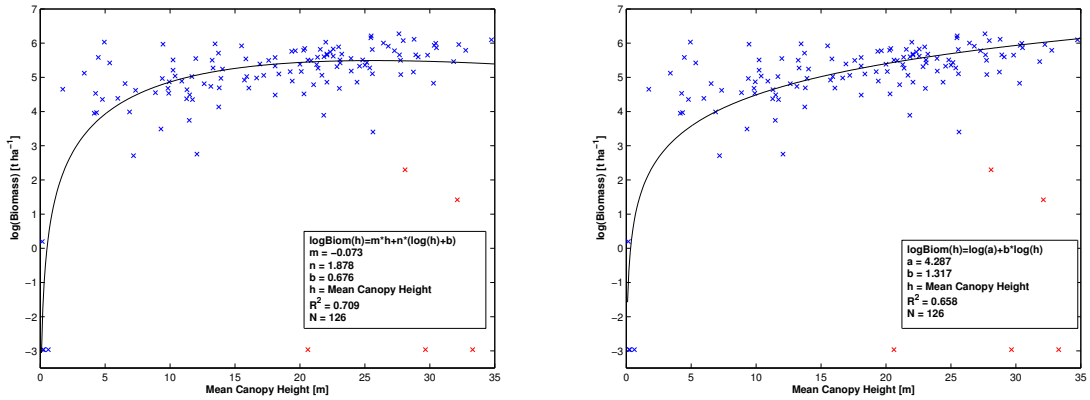


**(a)** **(b)**

**Figure 5.9:** ALS mean canopy height vs. plot level AGB(logarithmic scale) with fitted model. (a) Fitted model after Nelson et al. (1988). (b) Fitted model after Lim & Treitz (2004).

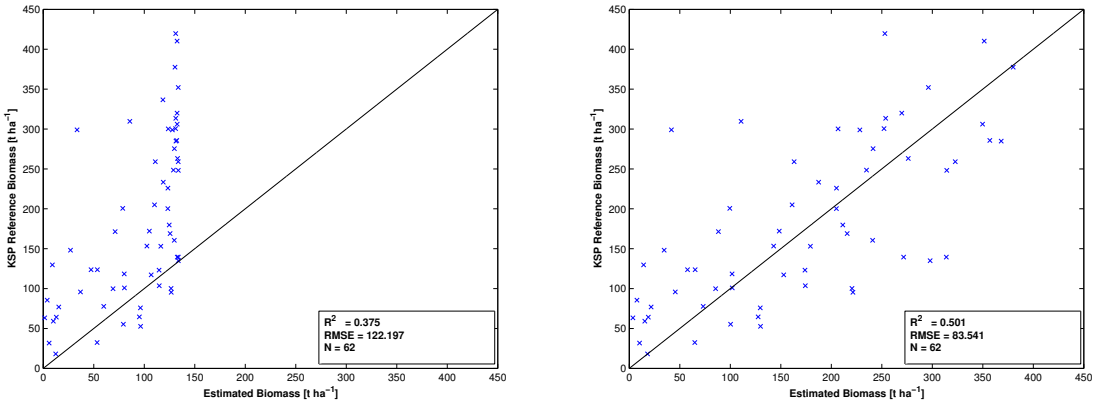


**(a)** **(b)**

**Figure 5.10:** ALS estimated AGB from ALS mean canopy height versus field measured AGB. (a) AGB estimation with model by Nelson et al. (1988), (b) AGB estimation with model by Lim & Treitz (2004).

The performance of each retrieved model can be analyzed by using the independent validation plots. The model performance in estimating biomass for the models described in Nelson et al. (1988) and Lim & Treitz (2004) are shown in Figures 5.10a and 5.10b respectively. Here we see again the saturation effect for the Nelson et al. (1988) model. While the model registers the increase in biomass up to 100 t ha$^{-1}$, a further increase in biomass was not recognized at higher biomass levels. This

was not the case for the model as described in Lim & Treitz (2004). The model was able to estimate increases in biomass over the whole biomass range without any saturation. This is also represented with the model's statistical performance. While the model after Nelson et al. (1988) achieved an $R^2$ of 0.375 with an RMSE of 122.2 t ha$^{-1}$, the model after Lim & Treitz (2004) achieved an $R^2$ of 0.5 with an RMSE of 83.5 t ha$^{-1}$. The retrieved model after Lim & Treitz (2004) was therefore selected as the reference model to predict biomass from ALS measured mean canopy height.

## 5.4. Geocoding and normalization effects on backscatter biomass sensitivity

In this section, the influence of employing a DSM or DTM for geocoding SAR products is outlined, followed by demonstrations of the consequences of using a GTC or RTC product on biomass sensitivity of airborne SAR backscatter data. PALSAR data was not analyzed in this section, as only the *DHM25* DEM was used for processing and we therefore could not analyze the consequences of using a DSM or DTM for SAR processing and later biomass estimation.

### 5.4.1. Geocoding with DTM or DSM

As we had ALS derived DSM and DTM data available, the effect of using one or the other for geocoding on retrieving biomass information was analyzed. In Figure 5.11, the $\gamma^0_E$ backscatter sensitivity at HV-polarization to biomass on a plot level using the E-SAR scene is shown. We see that sensitivity to biomass increased slightly when using the DSM instead of the DTM for geocoding the SAR image. This is consistent in all image products for all polarizations as well as Pauli bases (GTC and RTC). Due to this finding, all subsequent results from airborne SAR data were based on DSM geocoded products.

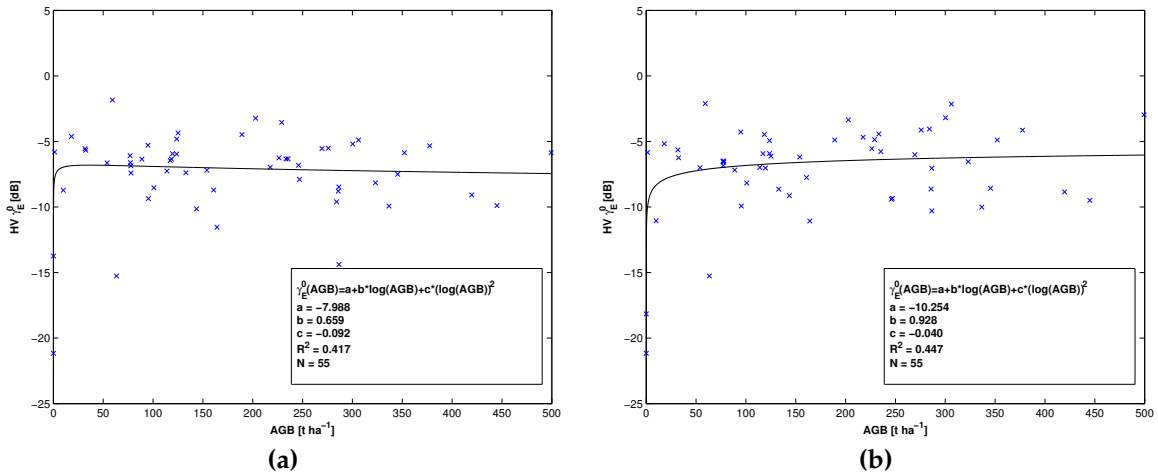


**Figure 5.11:** Backscatter sensitivity to biomass for DTM vs. DSM georeferenced E-SAR $\gamma^0_E$ backscatter products at HV-polarization. (a) DTM geocoded $\gamma^0_E$, (b) DSM geocoded $\gamma^0_E$.

### 5.4.2. GTC vs. RTC products

In Figure 5.12, the difference in backscatter sensitivity for the E-SAR HV GTC (Figure 5.12a) and the E-SAR HV RTC product (Figure 5.12b) is shown. Here we can distinguish a clear increase in sensitivity to biomass in the RTC product. The $R^2$ increased from 0.45 to 0.54. The saturation point also occured at higher biomass levels in comparison to the GTC product. The better performance of RTC over GTC images was consistent in all analyzed polarizations as well as Pauli bases.

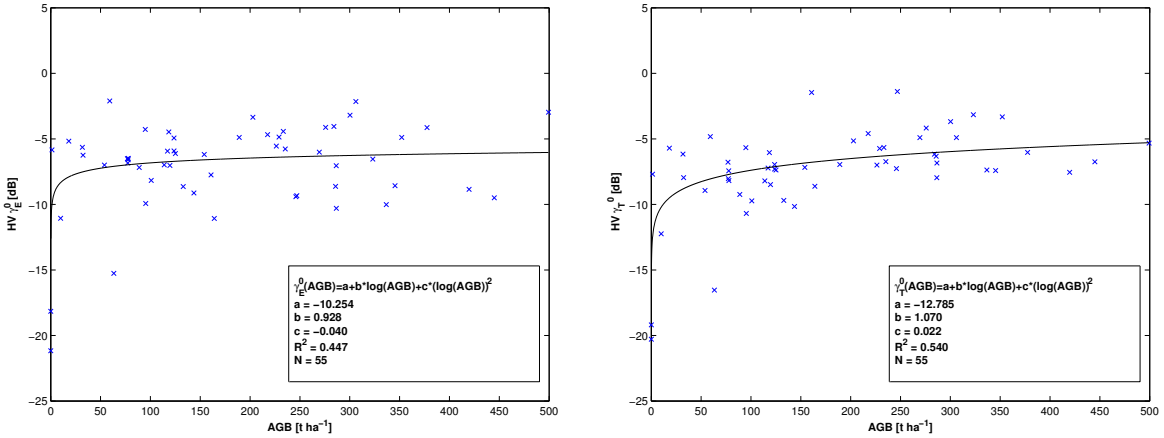


**(a)** **(b)**

**Figure 5.12:** E-SAR HV- polarization backscatter sensitivity to biomass at plot level for GTC (a) and RTC (b) product. Both products were geocoded using the DSM.

## 5.5. Biomass estimation based on airborne SAR backscatter data

In this section, three approaches to biomass estimation using backscatter data outlined in the methodology section are analyzed. First the single polarization backscatter-based approach is analyzed, where the sensitivity of the different polarizations to biomass is assessed. Afterwards, results from using multiple polarizations for estimating biomass are outlined. In the last part, the applicability of using polarimetric decompositions are assessed. As outlined in Section 5.4, only DSM geocoded RTC products are analyzed herein, as these products showed higher sensitivities to biomass compared to DTM geocoded and GTC products. An exception was made for the multiple polarization approach, where also GTC products were analyzed, as this approach behaved slightly differently to single polarization or polarimetric decomposition approaches. For all cases, first the results of the model training are outlined and afterwards the retrieved model is validated, and the performance in estimating biomass is assessed.

### 5.5.1. Single polarization approach

In Figure 5.13, the sensitivity of E-SAR RTC products to biomass at the plot level is shown for all four polarizations. The model was first fit to the KSP training plots. In this figure, it is clearly visible that the cross-polarized channels showed the highest sensitivity to biomass ($R^2$ = 0.54) followed by VV-polarization ($R^2$ = 0.46) and HH-polarization($R^2$ = 0.41). Yet in all four channels a quite high noise level was apparent, and the saturation occured already at very low biomass levels (below 50 t ha$^{-1}$).

As the cross-polarized channels showed the highest sensitivity to biomass, the HV-polarization channel was chosen for further use in direct biomass estimation. First, the retrieved model was tested against the validation points, to see if the model also described the validation points accordingly. Results are shown in Figure 5.14a. Here we see that the model fit the validation points quite well, with even a higher $R^2$ value of 0.75. Unfortunately, the performance of estimating biomass from the single HV-polarization channel based model was poor, with an $R^2$ of just 0.017 and an RMSE of 130 t ha$^{-1}$ as shown in Figure 5.14b.

As the plot level results were not satisfying, we moved on to assessing the backscatter sensitivity at the stand level. The stand level DSM geocoded $\gamma^0_T$ backscatter sensitivity to biomass at HV-polarization is shown in Figure 5.15a. At the first glimpse it seems that at least at very low biomass levels, the backscatter intensity shows some sensitivity to biomass. Yet, if we look closer into the biomass range between 0 and 25 t ha$^{-1}$, this sensitivity is less pronounced, showing nearly no increase in backscatter intensity with increasing biomass as shown in Figure 5.15b.

In order to reduce the high noise level, also a stand size based filtering was analyzed. Figure 5.16 shows the backscatter intensity to biomass at stand level for four different minimum stand sizes. Minimum stand sizes of 0.25 ha (5.16a), 0.5 ha (5.16b), 0.75 ha (5.16c), and 1 ha (5.16d) were analyzed. We see that by filtering the stand dataset, the noise level could be significantly reduced. Yet many stands were lost in the course of that, especially in the lower biomass range. Initially 641 training stands were reduced to 165, 95, 55, and 41 training stands with minimum stand sizes of 0.25, 0.5, 0.75, and 1 ha respectively. For the 1 ha case, we therefore had less than 10% from the initial number of training stands available. By filtering out the smaller stands, the data points converged to a nearly horizontal line, describing no increase in backscatter with increasing biomass. This made a reliable biomass estimate from backscatter data also at stand level impossible, as illustrated clearly in Figure 5.17. For both cases shown in Figure 5.17, no clear correlation between estimated and reference biomass was visible.

The influence of different forest types (coniferous, mixed-coniferous, mixed-deciduous, and deciduous) on backscatter sensitivity was also analyzed. Results are shown in Figure 5.18 for HV-polarized $\gamma^0_T$ backscatter data. This result showed that an individual analysis for each forest type did not lead to improved results, as no clear forest type specific backscatter behavior was visible in the plot. Interestingly though, mixed coniferous forest stands showed a much higher variability in backscatter, compared to the other forest types. This could be due to the number of stands in this forest type, as the mixed-coniferous class is the dominant forest type at the Hinwil study site. They also seem to be rather small stands, as many of the outliers labeled as mixed-coniferous shown in Figure 5.18 disappear when we increased the minimal stand size, as shown in Figure 5.16.

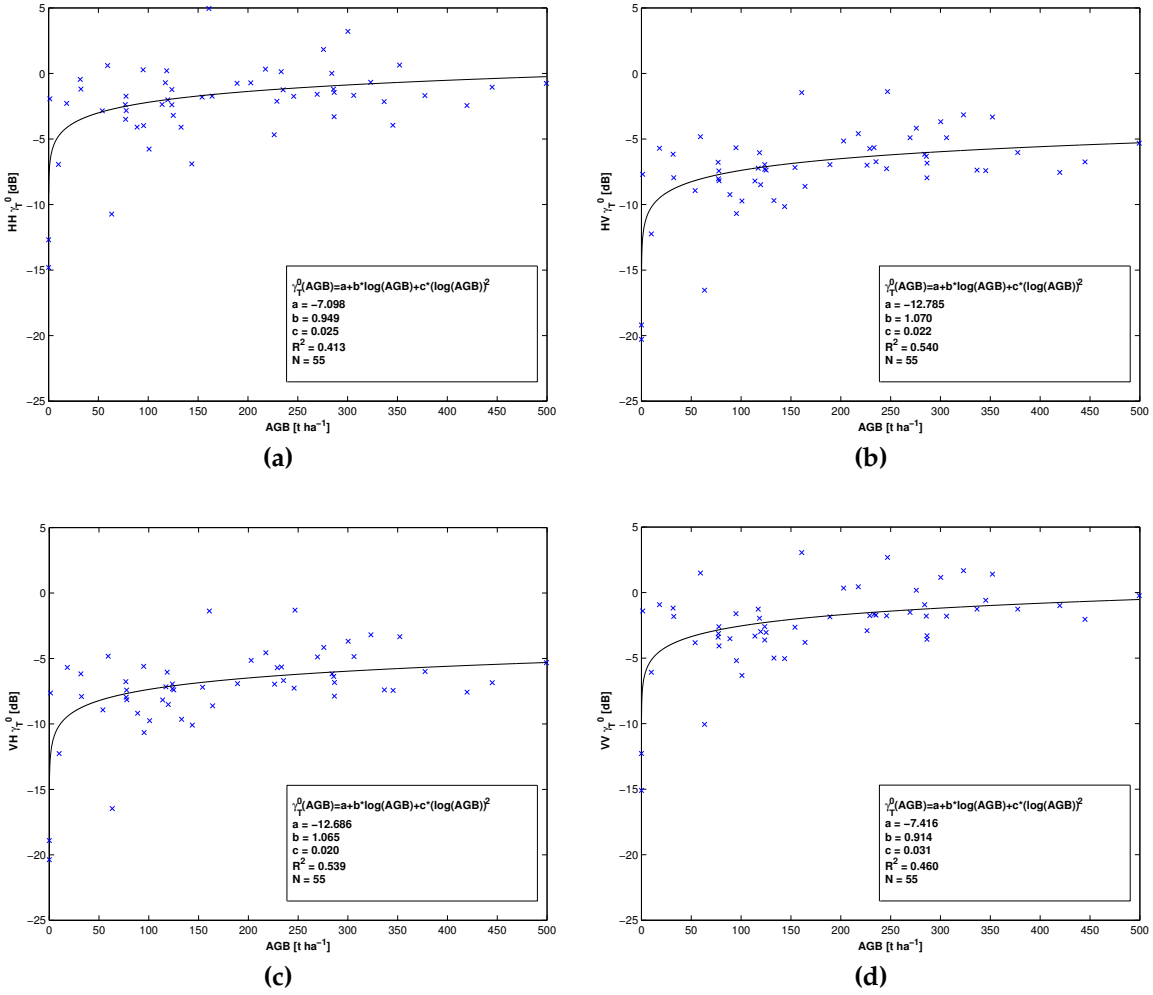


**Figure 5.13:** E-SAR RTC backscatter sensitivity to biomass for all four polarization channels at plot level. (a) HH, (b) HV, (c) VH, (d) VV.

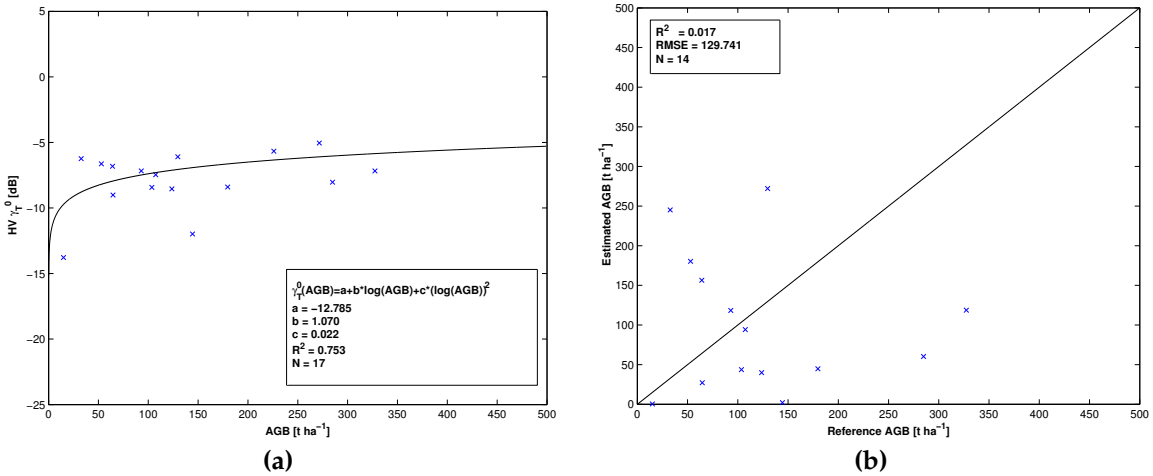


**Figure 5.14:** Model validation and biomass prediction from E-SAR $\gamma_T^0$ backscatter data at HV-polarisation at plot level. (a) Validation of retrieved backscatter-biomass model. (b) performance of model to estimate biomass of the KSP validation plots.

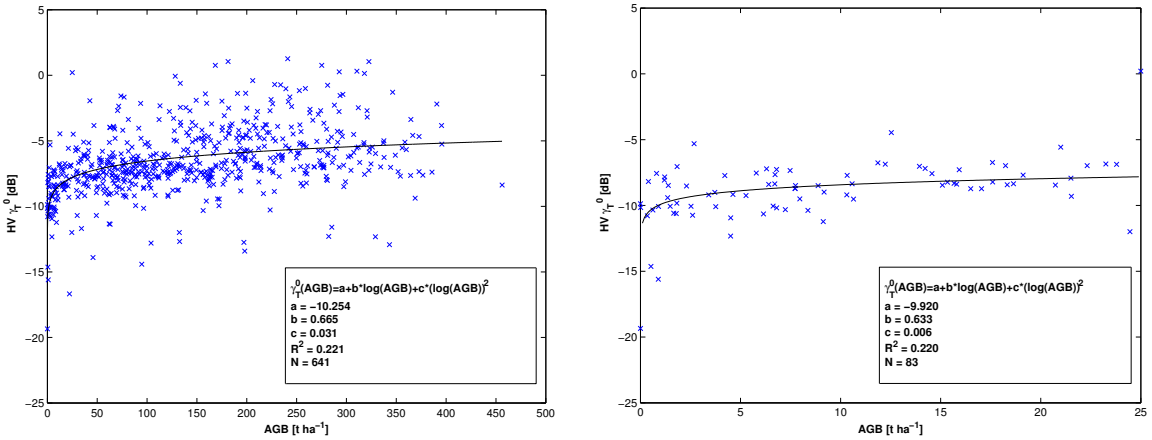


**(a)** **(b)**

**Figure 5.15:** E-SAR RTC stand level backscatter sensitivity to biomass at HV-polarization; (a) for the full biomass range and (b) for biomass levels below 25 t ha$^{-1}$.

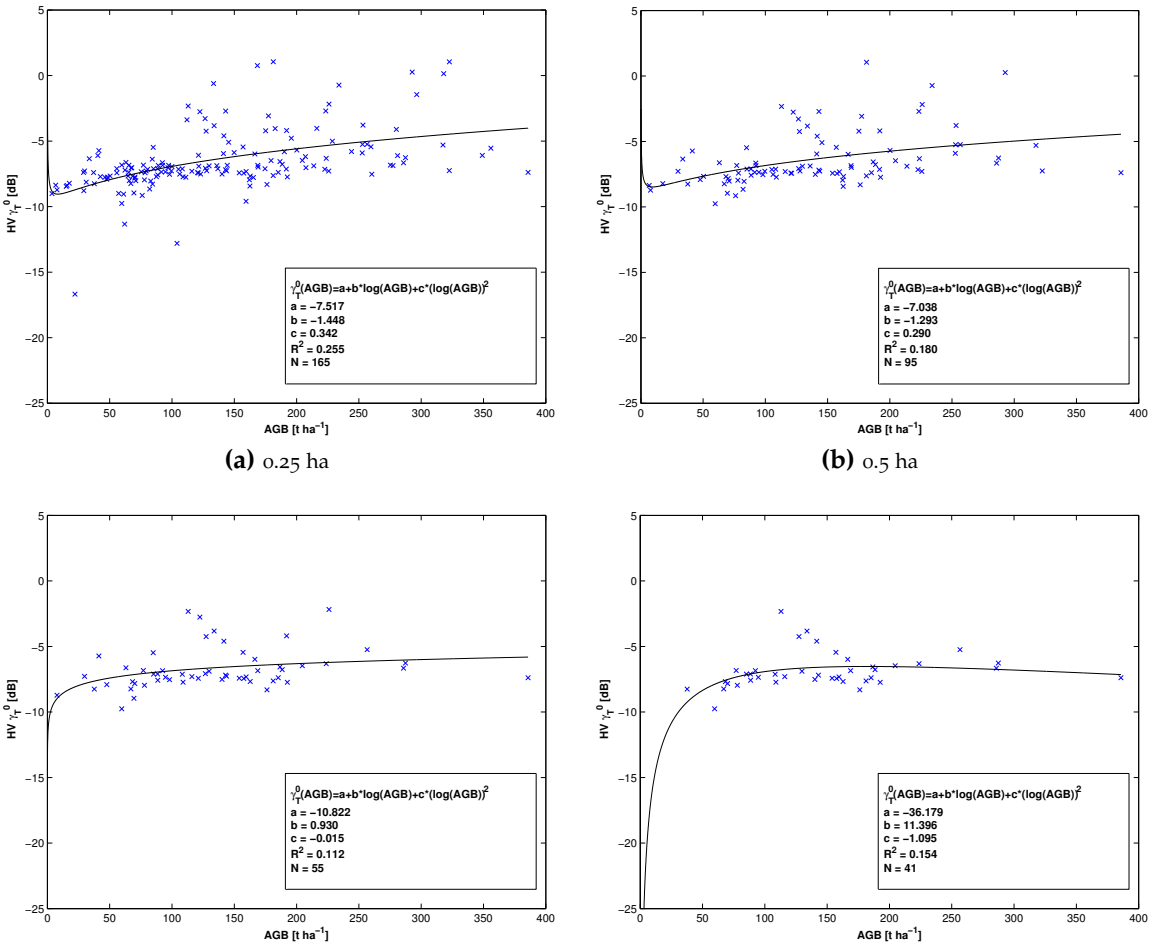


**(a)** 0.25 ha **(b)** 0.5 ha

**(c)** 0.75 ha **(d)** 1 ha

**Figure 5.16:** Relation between E-SAR DSM geocoded RTC HV backscatter and biomass at stand level for four different minimum stand sizes: (a) 0.25 ha, (b) 0.5 ha, (c) 0.75 ha, and (d) 1 ha minimum stand size.

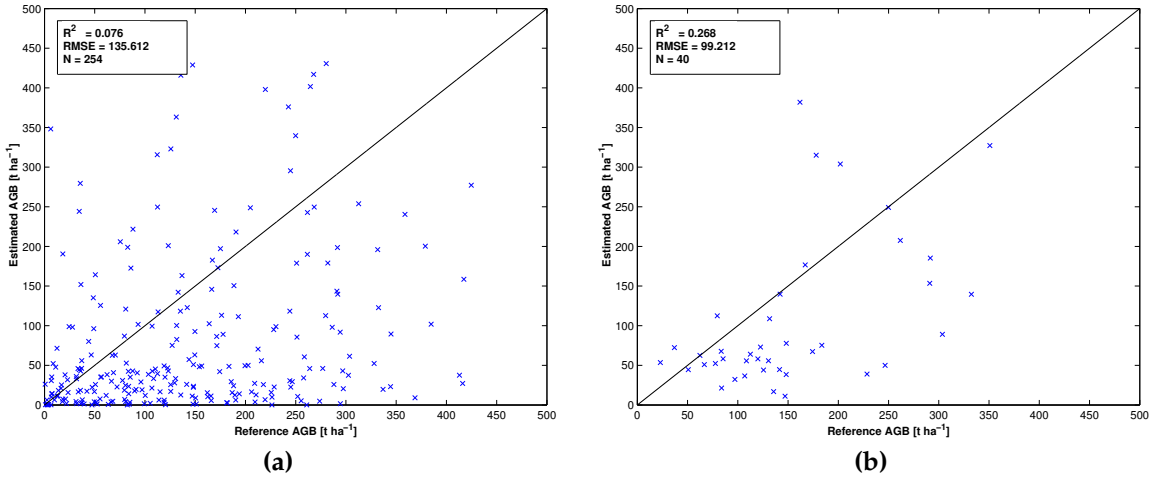


**Figure 5.17:** Estimated AGB from stand level HV RTC backscatter data vs. ALS reference biomass at stand level. (a) for all stands, (b) for stands with minimum size of 0.5 ha.

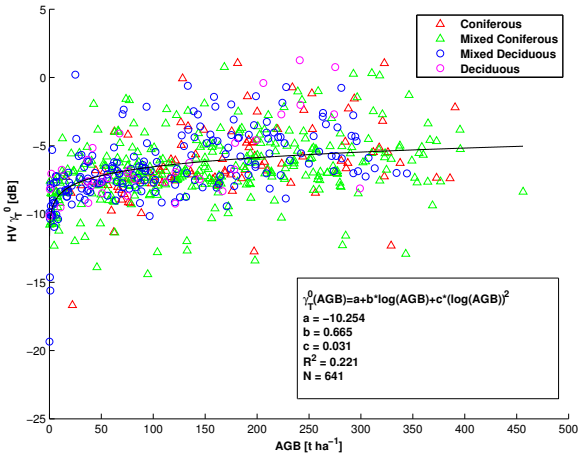


**Figure 5.18:** HV $\gamma_T^0$ backscatter sensitivity to biomass assessed for four forest types. Forest type information was taken from the WMG92 dataset.

### 5.5.2. Multiple polarization approach

Also for the multiple polarization approach, the model training was assessed first before using the retrieved model to assess the biomass estimation performance. As three independent backscatter values (HH-, VV-, and HV- channel) were available and one dependent (AGB) variable in this polynomial model, visualizing the model training results was difficult. The model training results are shown in tabular form in Table 5.2, where all model parameters as well as the model performance, declared with the $R^2$ are shown, for all analyzed backscatter products.

**Table 5.2:** Multi polarization approach training results at plot level for each processed E-SAR product (GTC DTM and DSM geocoded and RTC DTM normalized and DSM, DTM geocoded). Geoc = Geocoded, Norm = Normalized. Number of plots for model training = 55.

| SAR product | Parameters | | | | | | | Performance |
|---|---|---|---|---|---|---|---|---|
| | a0 | a1 | a2 | b1 | b2 | c1 | c2 | $R^2$ |
| GTC DTM Geoc | 0.634 | -1.401 | -0.120 | 0.081 | -0.002 | -0.047 | 0.093 | 0.721 |
| GTC DSM Geoc | 3.339 | -0.637 | -0.064 | 0.030 | 0.024 | -0.286 | -0.019 | 0.735 |
| RTC DSM Geoc DTM Norm | 1.847 | -1.117 | -0.095 | 0.271 | 0.088 | -0.242 | -0.040 | 0.760 |
| RTC DTM Geoc DTM Norm | -0.376 | -1.551 | -0.111 | 0.066 | 0.014 | 0.107 | 0.053 | 0.630 |

Here we see that the DSM geocoded products performed slightly better compared to the DTM geocoded products. The DSM geocoded RTC product performed also slightly better compared to the DSM geocoded GTC product.

In Figure 5.19, the performance of estimating biomass using the above retrieved models and the validation KSP plots are shown. We can clearly see, that the DTM geocoded products (Figures 5.19a and 5.19c) are not able to estimate biomass with an $R^2$ of 0.004 and 0.044 and an RMSE of 235.5 and 114.6 t ha$^{-1}$ for the GTC and RTC products respectively. The performance of the DSM geocoded products (Figures 5.19b and 5.19d) was much higher with an $R^2$ of 0.227 and 0.16 and an RMSE of 87.8 and 94.3 t ha$^{-1}$ for the GTC and RTC products respectively. Interestingly, the DSM geocoded RTC product showed less biomass estimation capability than the DSM geocoded GTC product. Although the estimation appears noisy, a clear increase in estimated biomass with increasing reference biomass is visible, especially in Figures 5.19b and 5.19d. It would be interesting to analyze this behavior with a larger number of validation plots to see if the behavior is consistent with more data points.

With the multiple polarization approach a stand level analysis was also carried out. The model training performance with the retrieved model parameters for the four analyzed E-SAR products is outlined in Table 5.3. Here we see that the model training performance was much weaker compared to the plot level training. The best performance was delivered by the DSM geocoded RTC product with an $R^2$ of 0.265. Note that no stand size filtering was applied here.

In Figure 5.20, a comparison of estimated and reference biomass from the stand level analysis is outlined for the two DSM geocoded products. While the DSM geocoded GTC product showed nearly no increase in estimated biomass given increasing reference biomass, the DSM geocoded RTC product registered at least small increases in estimated biomass given increasing reference biomass. Yet the noise level in the DSM geocoded RTC product appeared much higher compared to the DSM geocoded GTC product.

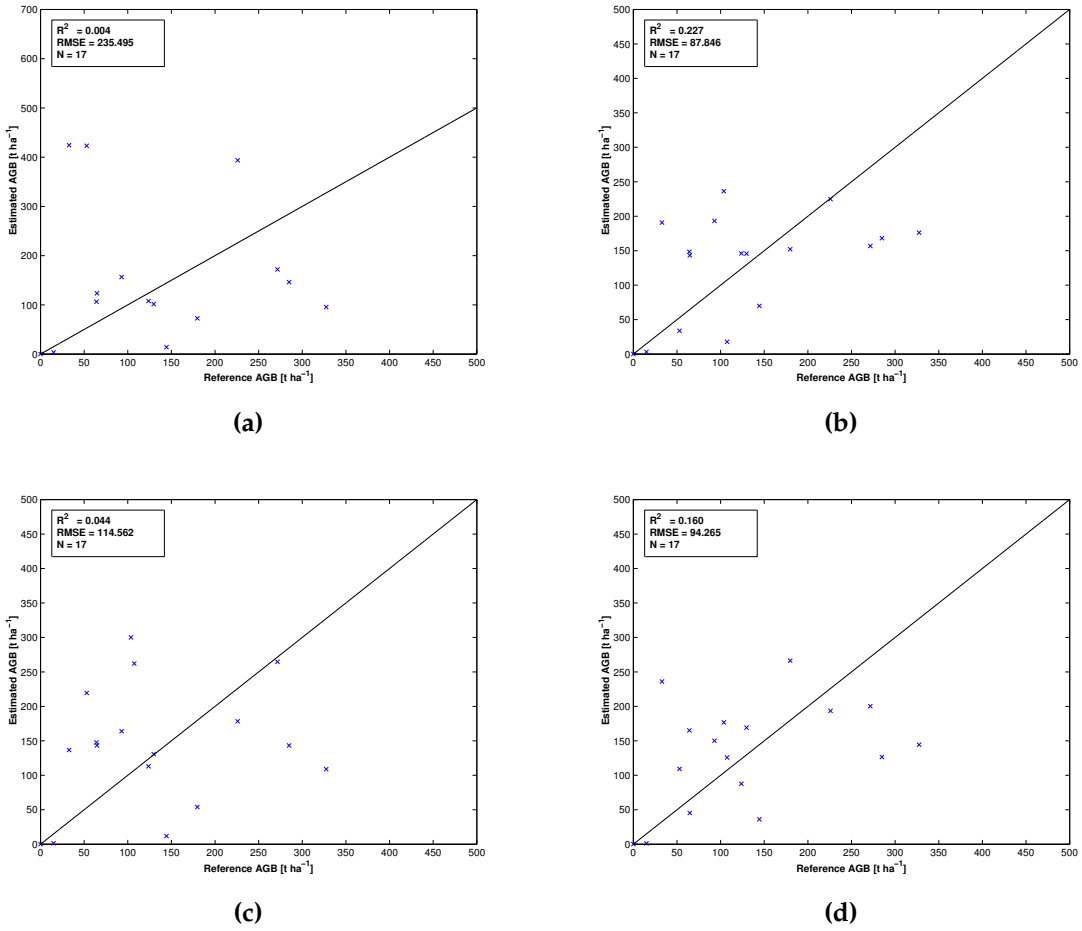


**Figure 5.19:** Reference AGB vs. estimated AGB for the multiple polarization approach and for the four different E-SAR products: (a) DTM geocoded GTC, (b) DSM geocoded GTC, (c) DTM geocoded RTC, and (d) DSM geocoded RTC.

Due to the high noise levels in the estimated vs. reference AGB at stand level shown in Figure 5.20b, the effect of filtering out smaller stands was analyzed. For this, the minimum stand size was set to 0.25, 0.5, 0.75 and 1 ha. The performance of the model training for the four different minimum stand sizes is shown in Table 5.4 and the estimated vs. reference AGB plots also for the four different minimum stand sizes are shown in Figure 5.21. The results for the model training were already significantly better when focusing only on stands larger than 0.25 ha (increase in $R^2$ from 0.265 to 0.31). The best model performance was achieved with 1 ha minimum stand size and an $R^2$ of 0.56. Also for the comparison between estimated and reference biomass (Figure 5.21), an increase in performance when only larger stands are analyzed was observed. The main cause was likely the reduced noise in the data, due to averaging over larger areas. The best result was achieved with a minimum stand size of 0.5 ha ($R^2$ 0.41 and RMSE of 74.3 t ha$^{-1}$) followed by the 1 ha minimum stand size ($R^2$ of 0.37 and RMSE of 77.4 t ha$^{-1}$). Interestingly, the model used for the 0.5 ha minimum stand size actually performed worst in the model training, compared to the other minimum stand size datasets. Note that after 150 t ha$^{-1}$ saturation, and therefore more noise, was observed in all analyzed minimum stand size datasets.

**Table 5.3:** Multi polarization approach training results at stand level for each processed E-SAR product (GTC DTM and DSM geocoded and RTC DTM normalized and DSM, DTM geocoded).
Geoc = Geocoded, Norm = Normalized. Number of stands for model training = 654.

| SAR product | Parameters | | | | | | | Performance |
|---|---|---|---|---|---|---|---|---|
| | a0 | a1 | a2 | b1 | b2 | c1 | c2 | $R^2$ |
| GTC DTM Geoc | 4.482 | -0.194 | -0.028 | 0.03 | 0.011 | 0.008 | 0.023 | 0.067 |
| GTC DSM Geoc | 3.666 | -0.514 | -0.056 | 0.007 | 0.017 | 0.084 | 0.038 | 0.145 |
| RTC DSM Geoc DTM Norm | 4.861 | -0.218 | -0.041 | 0.018 | 0.011 | -0.003 | 0.013 | 0.265 |
| RTC DTM Geoc DTM Norm | 3.974 | -0.373 | -0.043 | -0.007 | 0.01 | 0.068 | 0.03 | 0.117 |

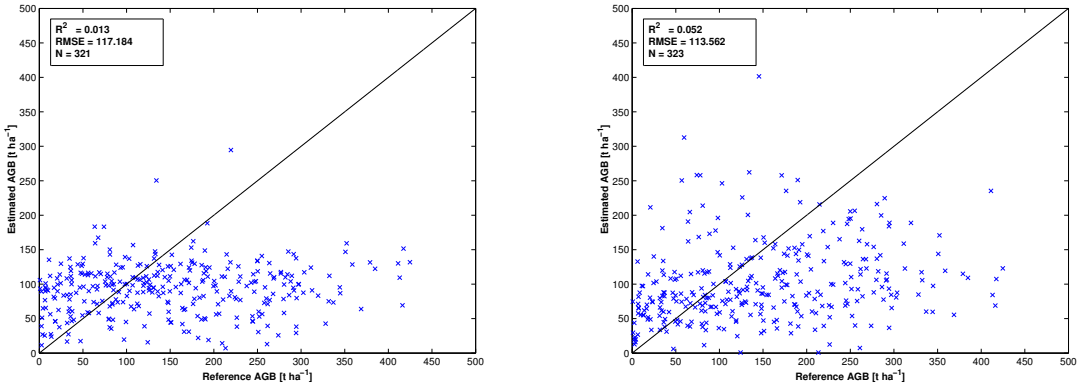


**(a)** **(b)**

**Figure 5.20:** Reference AGB vs. estimated AGB for the multiple polarization approach at the stand level and for the two different E-SAR products: (a) DSM geocoded GTC, and (b) DSM geocoded RTC.

**Table 5.4:** Multiple polarization approach model training results at the stand level for DSM geocoded RTC E-SAR product with different minimum stand sizes. The number of stands analyzed in model training is declared in the last column labeled as N.

| Minimum Stand Size [ha] | Parameters | | | | | | | Performance | |
|---|---|---|---|---|---|---|---|---|---|
| | a0 | a1 | a2 | b1 | b2 | c1 | c2 | $R^2$ | N |
| 0.25 | 5.073 | -0.044 | -0.005 | -0.036 | 0.014 | 0.172 | -0.026 | 0.31 | 167 |
| 0.5 | 5.2 | -0.028 | -0.004 | 0.012 | -0.011 | 0.112 | -0.019 | 0.245 | 97 |
| 0.75 | 3.368 | -0.555 | -0.036 | -0.068 | -0.099 | 0.275 | 0.037 | 0.287 | 55 |
| 1 | 1.848 | -0.923 | -0.043 | 0.577 | 0.135 | -0.209 | -0.18 | 0.565 | 41 |

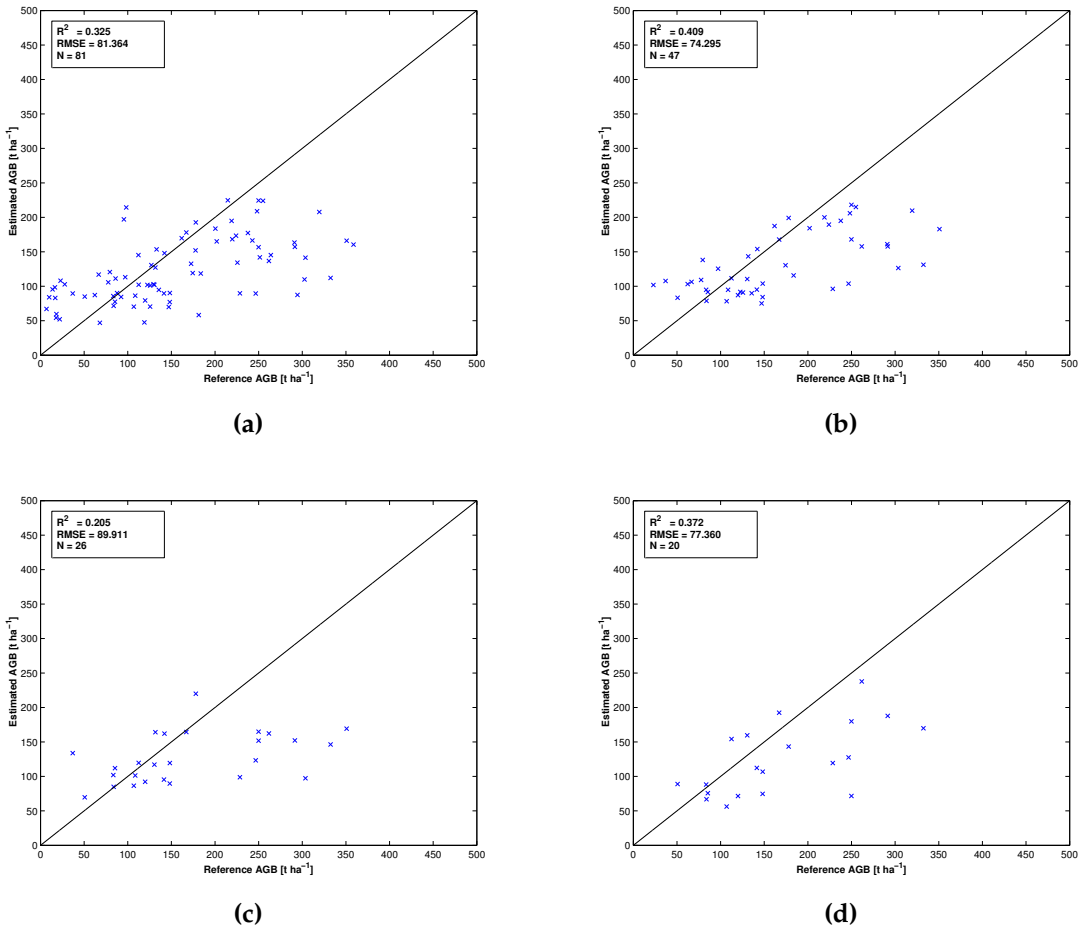


**Figure 5.21:** Reference AGB vs. estimated AGB for the multiple polarization approach at different minimum stand sizes using the DSM geocoded RTC E-SAR product. (a) minimum stand size of 0.25 ha, (b) minimum stand size of 0.5 ha, (c) minimum stand size of 0.75 ha and (d) minimum stand size of 1 ha.

### 5.5.3. Polarimetric decomposition approach

In Figure 5.22, the sensitivity of the three Pauli scattering mechanisms *surface*, *double bounce* and *volume* scattering vs. biomass is shown at the plot level. Only the results taken from the DSM geocoded RTC products are shown, as they showed the highest sensitivity to biomass. The third Pauli base, i.e. the volume scattering part (HV + VH) showed the highest sensitivity to biomass with an $R^2$ of 0.54, followed by the double bounce scattering (HH-VV with $R^2$ of 0.49) and the surface scattering (HH+VV with $R^2$ of 0.42). The model validation showed that the validation points could also be explained with the retrieved model (see Figure C.1 in Appendix C). In Figure 5.23a, the sensitivity of the scattering mechanism ratio $\frac{(HH-VV)*(HV+VH)}{(HH+VV)}$ to biomass at plot level for the DSM geocoded RTC product is shown. This ratio showed a slight increase in biomass sensitivity ($R^2$ of 0.55) compared to the single *volume* scattering channel ($R^2$ of 0.54). Yet also here, the saturation effect was apparent already at very low biomass levels, leading to difficulties in retrieving biomass information from this polarimetric decomposition data at the plot level, as seen in Figure 5.23. Here we see that, similar to the single polarization approach, the third pauli base and the scattering mechanism ratio are not capable of accurately estimating biomass at the plot level. Also the rotation of the Pauli scattering mechanisms as discussed in Section 2.1.4 did not improve this behavior as seen in Table 5.5. Here we see again that the first Pauli base is invariant to rotation. The performance was therefore the same as with unrotated data. For the double bounce scattering mechanism, the model training performance increased slightly and for the volume scattering mechanism, the model training performed even worse with the rotated data than with the unrotated. Only very small differences were found in model training for the rotated and unrotated Pauli scattering mechanism ratio. Yet the performance in estimating biomass at plot level, using the model fitted to the rotated data, increased slightly from an $R^2$ of 0.07 to 0.115 with a decrease in RMSE from 120.4 t ha$^{-1}$ in the unrotated case to 114.4 t ha$^{-1}$ in the rotated case. Yet still, the sensitivity and biomass estimation performance using polarimetric decompositions at plot level was very low, calling into question the applicability of this approach at least at this study site with the SAR data used.

Also at the stand level, the sensitivity of the scattering mechanisms to biomass was low as shown in Figure 5.24 for the unrotated and rotated volume scattering and Pauli scattering ratios taken from the DSM geocoded RTC Pauli products. The sensitivity of these two products was quite similar to the stand level sensitivity of the cross-polarized backscatter channel seen in Figure 5.15. As the increase

**Table 5.5:** Results from model training, validation and biomass estimation performance analysis with rotated E-SAR Pauli scattering mechanisms at the plot level. The model as described in single polarization approach was used to fit the data: $\gamma^0_T(AGB) = a + b * log(AGB) + c * (log(AGB))^2$.

| | Model Parameters | | | Performance | | | |
|---|---|---|---|---|---|---|---|
| | | | | Training | Validation | Prediction | |
| | a | b | c | $R^2$ (N=55) | $R^2$ (N=17) | $R^2$ (N=17) | RMSE [t ha$^{-1}$] |
| $\langle$HH+VV$\rangle(\theta)$ | -6.423 | 0.907 | 0.0032 | 0.417 | 0.702 | 0.001 | 110.22 |
| $\langle$HH-VV$\rangle(\theta)$ | -7.19 | 1.03 | 0.022 | 0.52 | 0.726 | 0.044 | 121.483 |
| $\langle$HV+VH$\rangle(\theta)$ | -12.129 | 1.01 | 0.0025 | 0.505 | 0.751 | 0.022 | 114.262 |
| P2($\theta$)*P3($\theta$)/P1($\theta$) | -11.736 | 1.12 | 0.01 | 0.55 | 0.775 | 0.115 | 114.383 |

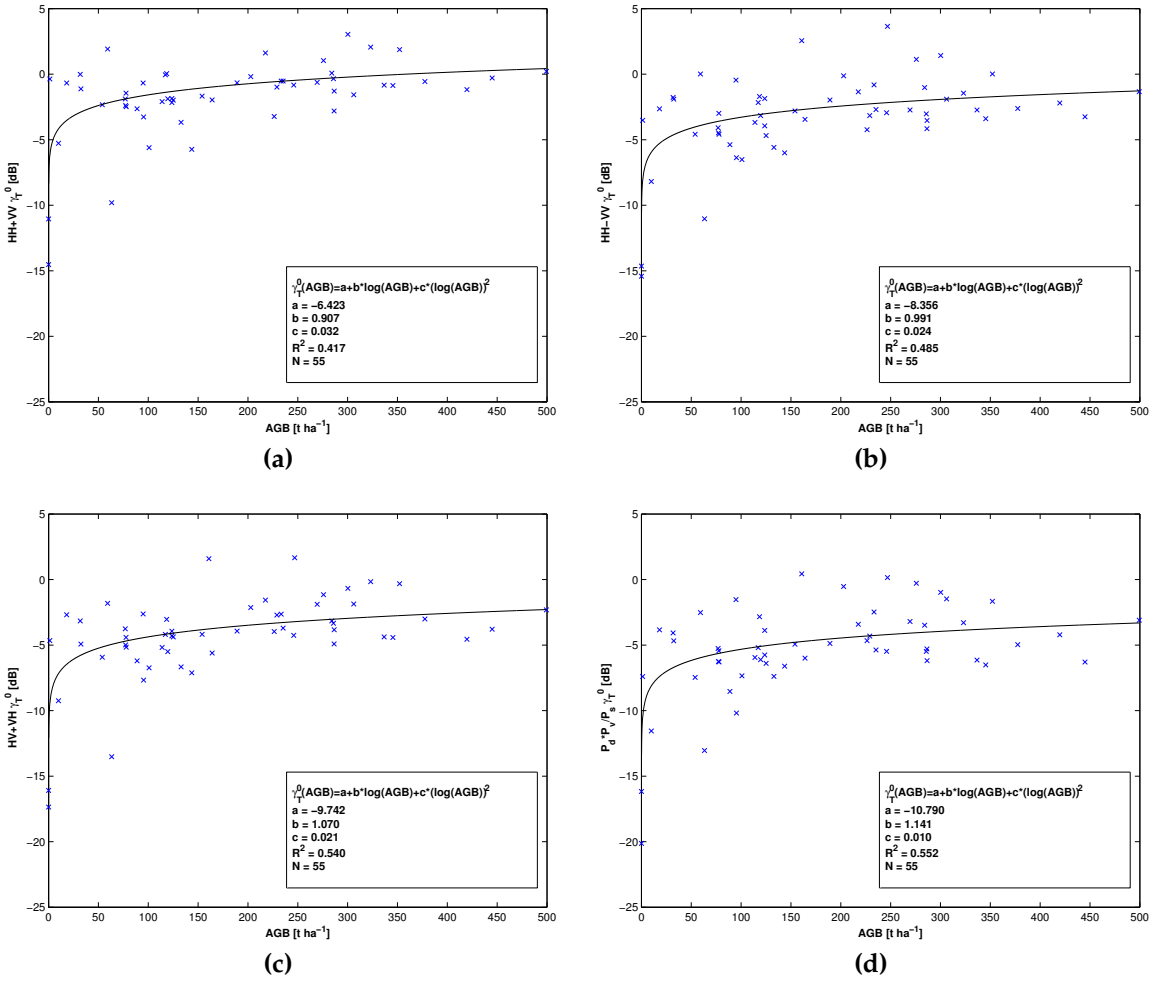


**Figure 5.22:** Pauli decomposition power sensitivity to biomass at plot level for fully polarimetric E-SAR data. (a) Model training for surface scattering term (HH+VV), (b) model training for double bounce scattering term (HH-VV), (c) model training for volume scattering term (HV+VH), and (c) model training for Pauli ratio $P_d * P_v / P_s$.

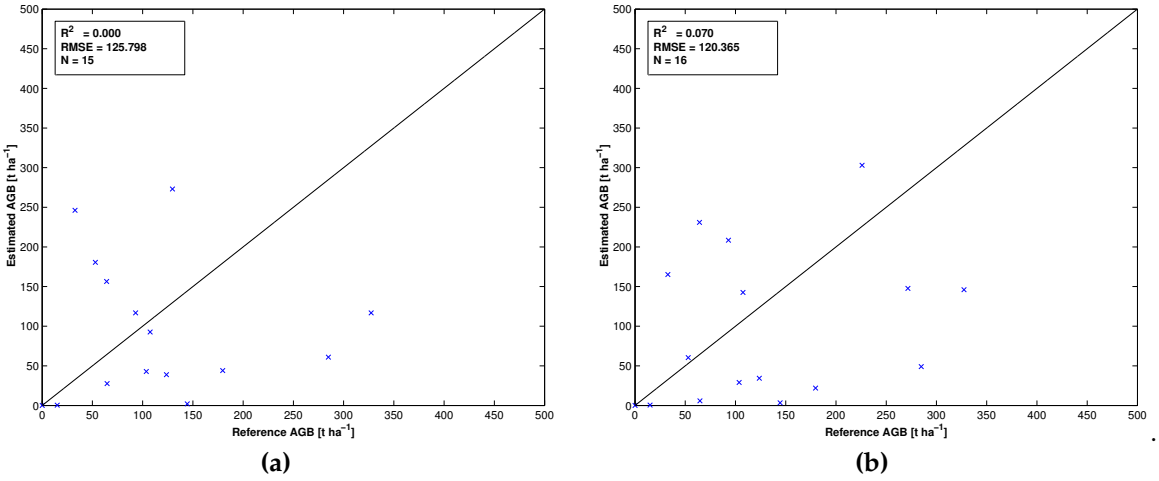


**Figure 5.23:** Biomass estimation at the plot level with DSM geocoded RTC Pauli products; (a) from volume scattering, (b) from the Pauli ratio $P_d * P_v / P_s$.

in minimum stand size did not result in much better correlation in the single polarization approach and due to the similarity of the unfiltered stand-level relation between the single polarization and polarimetric decomposition approach, no further analysis regarding different minimum stand sizes was performed here.

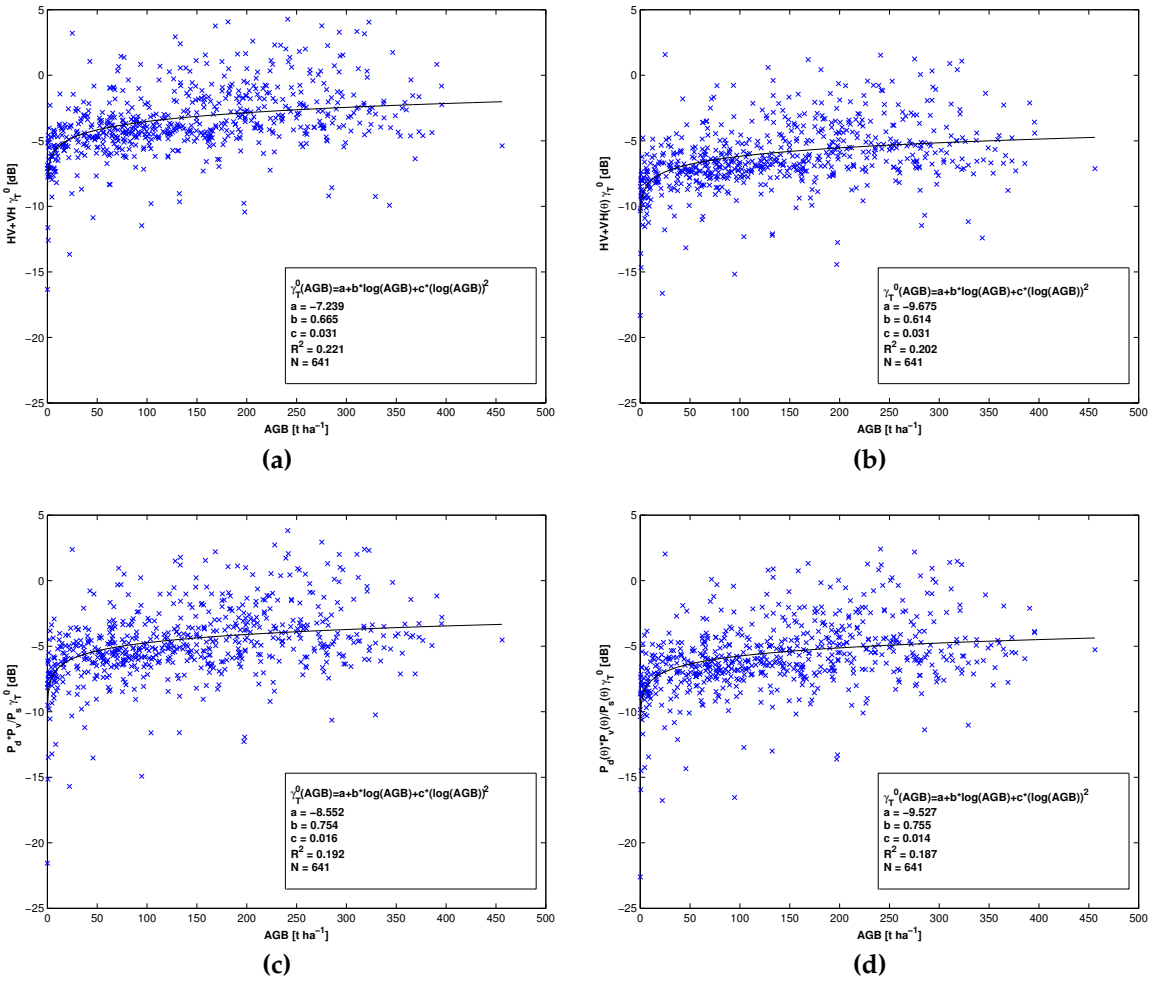


**Figure 5.24:** Unrotated and rotated volume scattering and Pauli ratio sensitivity to biomass at the stand level. (a) unrotated volume scattering, (b) rotated volume scattering, (c) unrotated Pauli ratio, (d) rotated Pauli ratio.

## 5.6. Biomass sensitivity of ALOS PALSAR backscattering data

At the beginning of this thesis, only spaceborne SAR data acquired by the ALOS PALSAR instrument had been available, and the initial goal was to estimate biomass only from this dataset covering most of the north-eastern part of Switzerland. Yet, already quite early in the process of this thesis it became apparent that the fully polarimetric ALOS PALSAR data showed only very weak sensitivity to biomass over the analysed heterogenous mixed forests at the two selected study sites at Hinwil

and Lägern. Due to this, the focus was then placed on the higher resolved fully polarimetric airborne SAR data acquired by the E-SAR instrument over the Hinwil study site. Nevertheless, some of the results of the analysis with ALOS PALSAR PLR data over the two study sites Hinwil and Lägern are shown here. As the PLR data showed weak correlation to biomass, only a sensitivity analysis without a later biomass estimation attempt was performed. Focus was placed on the cross-polarized channel in the single polarization approach and on the volume scattering channel as well as the Pauli ratio channel (see Equation 4.13) for the polarimetric decomposition approach, as these three channels showed the highest sensitivity to biomass in the analysis with E-SAR data. In several studies employing ALOS PALSAR data (mainly using the FBD mode) the cross polarized channel (e.g. in Mitchard et al., 2009) and the volume scattering mechanism (eg. in Chowdhury et al., 2013) showed the highest sensitivity to biomass or growing stock volume.

### 5.6.1. PLR sensitivity to biomass at Hinwil test site

In Figure 5.25, the relation between GTC (Figure 5.25a), RTC (Figure 5.25b) backscatter intensities and ALS retrieved biomass information at pixel scale (25 m pixel spacing) is shown for the PLR frame acquired on the 9th of May 2009 at an off-nadir angle of 23.1°. We see that neither the GTC nor the RTC backscatter values showed any correlation to biomass. The observed backscatter values showed a large variability stretching over 10 dB. This was probably accountable to the high noise level of the PLR dataset at 25 m pixel spacing. In order to reduce the noise in the data, both the PLR and ALS derived biomass maps were rescaled to 100 m pixel spacing. The result is shown in Figure 5.26. Due to the averaging over a larger area, the high variability in the backscatter values was successfully reduced. Yet, the correlation between backscatter intensity and biomass was not increased, neither in the GTC nor in the RTC case. Note that due to the large averaging window of 100 m, the number of samples in the lower biomass range (below 100 t ha$^{-1}$) decreased drastically. This hindered the potential of estimating biomass from the backscatter data, considering that L-band SAR is most sensitive to biomass variations below 100 t ha$^{-1}$. Not shown here are the backscatter

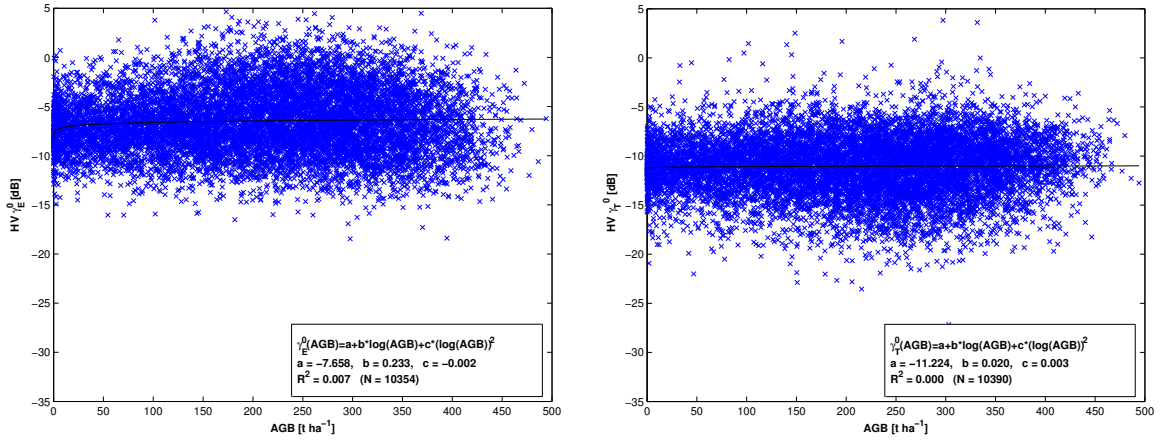


**(a)** **(b)**

**Figure 5.25:** GTC vs. RTC of PLR231 HV-polarization backscatter data acquired on 9th of May 2009 vs. biomass at 25 m pixel spacing over Hinwil study site. (a) GTC product, (b) RTC product.

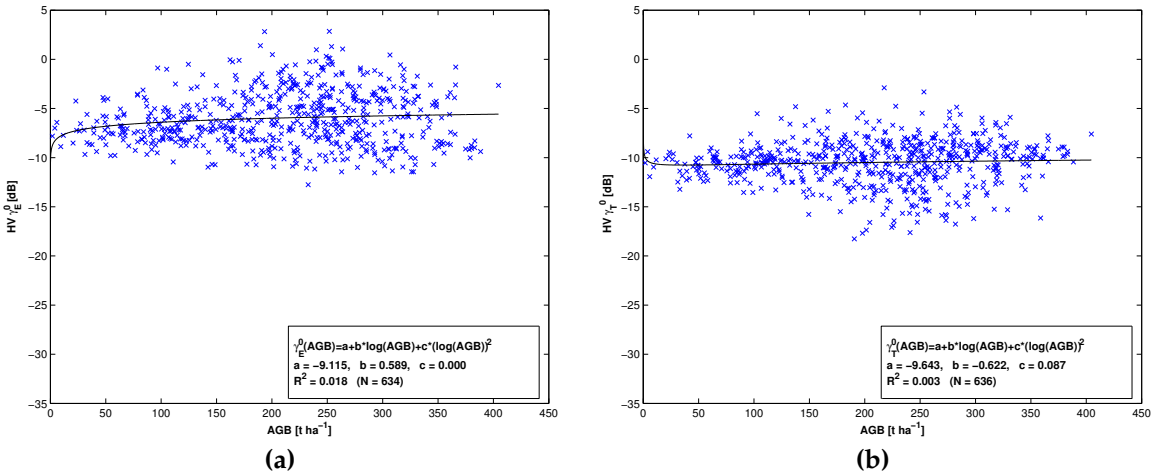


**Figure 5.26:** GTC vs. RTC of PLR231 HV-polarization backscatter data acquired on 9th of May 2009 against biomass at 100 m pixel spacing over Hinwil study site. (a) GTC product, (b) RTC product.

response to biomass from the available PLR frames at an off-nadir angle of 21.5°. Those frames also showed no correlation between backscatter and biomass (shown in Figure D.2 in Appendix D).

Similar to the results achieved with E-SAR data, polarimetric decomposition powers derived from the PALSAR data did not show any better correlation to biomass (see Figure D.4 in Appendix D). Also rotation of the coherency matrix did not improve the correlation.

The stand-level analysis showed that the noise could be reduced due to averaging of the backscatter and biomass data over a whole stand as shown in Figure 5.27. Nevertheless no correlation between biomass and backscatter was observable. Also considering the different forest types, no obvious relation between backscatter and biomass was visible.

As the backscatter intensity at all four polarizations was insensitive to biomass, no multiple polarization analysis was performed here (backscatter vs. AGB scatter plots for all four radiometrically normalized polarizations at 100 m resolution are shown in Figure D.1 in Appendix D).

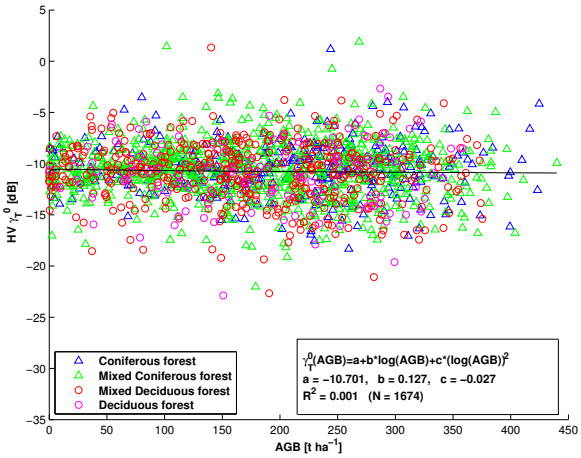


**Figure 5.27:** Stand level sensitivity of HV $\gamma_T^0$ backscatter vs. biomass based on PLR231 frame acquired on the 9th of May 2009 over Hinwil. The stands are labeled according to their respective forest type.

### 5.6.2. PLR sensitivity to biomass at Lägern test site

Also at the Lägern study site, no sensitivity of the backscatter signal to biomass for the PALSAR PLR data was observed. In Figure 5.28 the $\gamma^0_T$ backscatter sensitivity at HV-polarization at pixel (25 m and 100 m resolution) as well as stand level is shown. The backscatter and biomass values were further averaged into 10 t ha$^{-1}$ bins as shown in Figure 5.28b. Due to the averaging, the very low correlation between biomass and backscatter was even more pronounced, as the line fitted through the averaged data points was largely a straight horizontal line. At a pixel spacing of 100 m, the noise in the data could be reduced significantly again, yet a lot of information was lost in the lower biomass range as we see in Figure 5.28c. Also at the stand level, no correlation between backscatter and biomass was observable, even when analyzing individual forest types as shown in Figure 5.28d.

The analysis of Pauli decomposition powers relation to biomass did not result in any better results. As expected, also the compensation for polarization orientation angle shifts did not improve the relation between corrected decomposition powers and biomass (for some results see Figure D.5 in Appendix D).

Interestingly though, the sensitivity to biomass increased significantly if we did not mask out non-forest areas as shown in Figure 5.29. Due to this tactic more low biomass reference pixels were incorporated into the analysis. At least for the Lägern test site, most non-forest areas were related to agricultural land-cover; only very few were related to built-up areas (this is different from the Hinwil study site, where several larger villages were present), these low-biomass reference pixels exhibited lower backscatter values, increasing the correlation between biomass and backscatter significantly. Yet, this approach is not very useful for this study, as the goal is to estimate the biomass stored in the (a priory) known forests. There the relation between biomass and backscatter was still weak as shown in Figure 5.28.

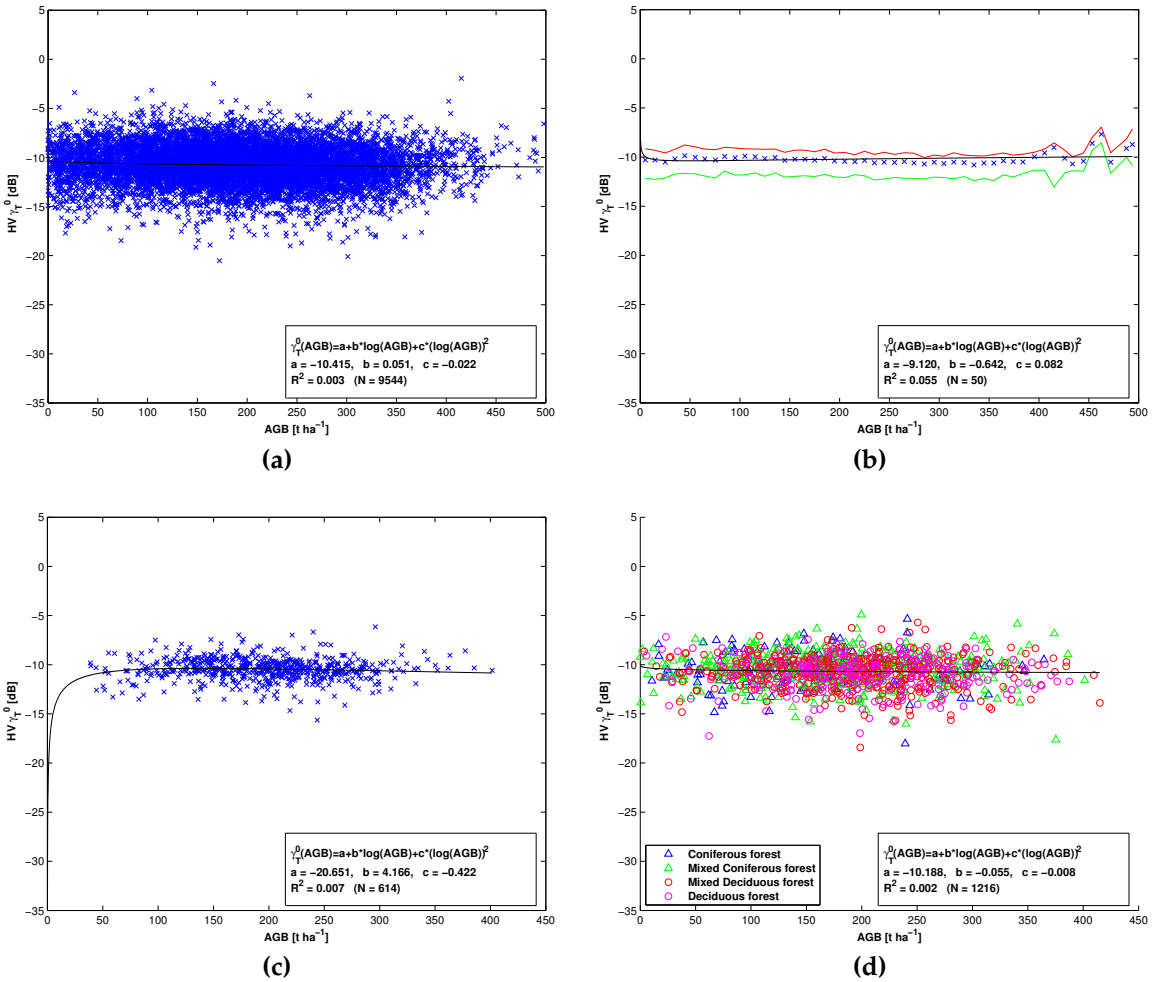


**Figure 5.28:** Sensitivity of PLR215 HV $\gamma_T^0$ backscatter to biomass over the Lägern study site. (a) Sensitivity at pixel-level with 25 m resolution, (b) Sensitivity at pixel-level with 25 m resolution, where the backscatter and biomass data was averaged in 10 t ha$^{-1}$ bins. The blue crosses denote the mean backscatter and biomass values, the black line is the function fit through these points, and the red and green lines denote the 75th and 25th percentile of each 10 t ha$^{-1}$ bin. (c) Sensitivity at 100 m sample-level. (d) Sensitivity at stand level regarding the different forest types. PLR frame was acquired at an off-nadir angle of 21.5°, the image was acquired on the 24th of March 2009 over the Lägern test site.

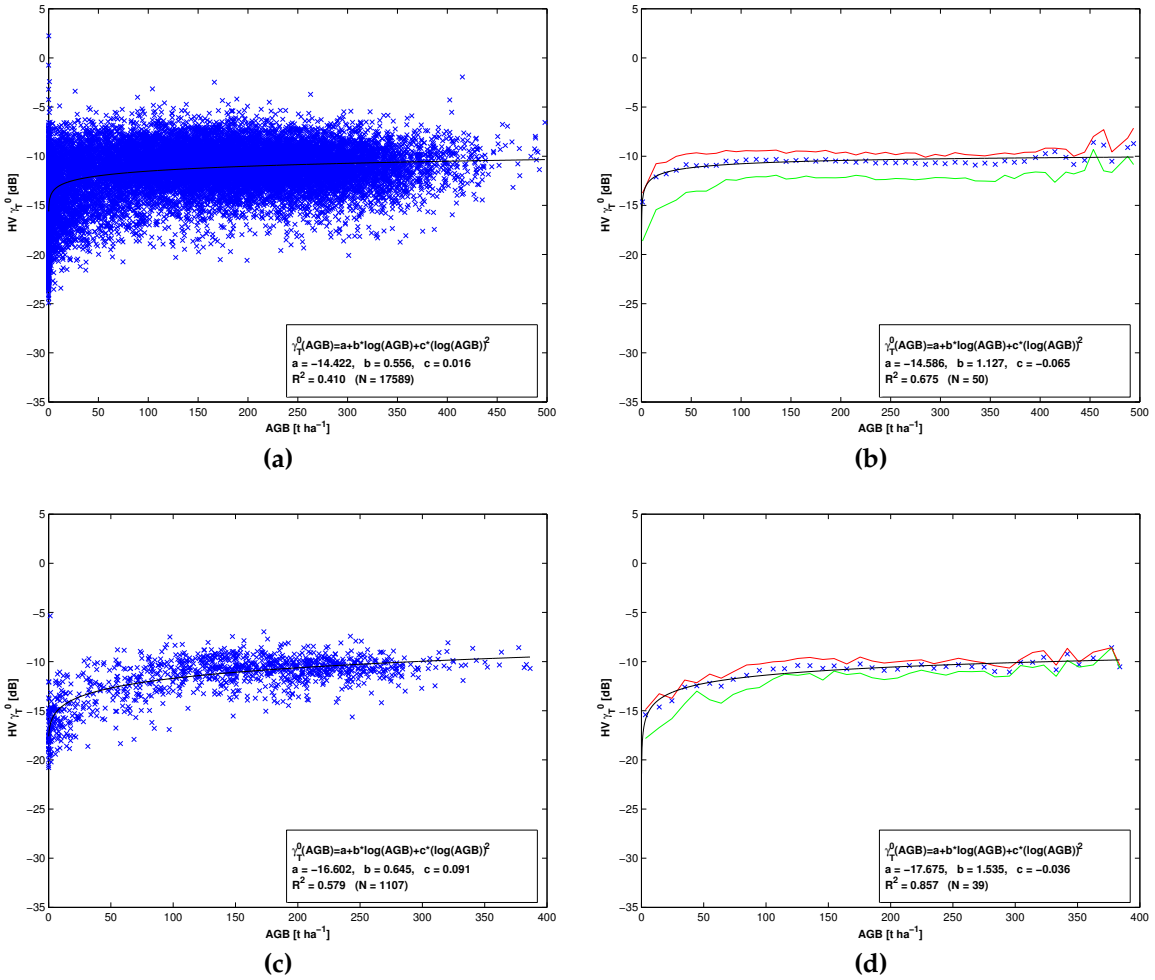


**Figure 5.29:** Sensitivity of PLR215 HV $\gamma_T^0$ backscatter to biomass over the Lägern study site when the non-forest areas were not masked out. PLR frame was acquired at an off-nadir angle of 21.5° acquired on the 24th of March 2009. (a) backscatter vs. biomass relation at 25 m pixel spacing, (b) backscatter vs. biomass relation at 25 m pixel spacing and averaged over 10 t ha$^{-1}$ bins, (c) backscatter vs. biomass relation at 100 m pixel spacing, (d) backscatter vs. biomass relation at 100 m pixel spacing and averaged over 10 t ha$^{-1}$ bins. In (b) and (d): The solid black line denotes the curve fit through the averaged backscatter points; the red and green lines denote the 75th and 25th percentile of the respective bins.

# 5.7. Biomass estimation through PolInSAR

Focus lies in this section on the performance of the different PolInSAR methodologies to estimate canopy height and biomass. First, the performance of estimating canopy height of the four different approaches outlined in the methodology section is assessed. The performance of estimating biomass from the retrieved canopy heights is then outlined.

## 5.7.1. Canopy height estimation with PolInSAR

In Figure 5.30, the CHMs derived from the PolInSAR forest height retrieval algorithms introduced in Sections 4.6.1 to 4.6.4 are shown. For comparison, the ALS CHM over the same region is shown in Figure 5.31. The CHMs derived from PolInSAR were produced by using DSM-flattened interferograms at HV-polarization for the volume dominated channel and HH-VV (double-bounce) polarization for the surface dominated channel. We see that most of the CHMs were able to depict the outlines of the forests. Yet in all products, a clear near-range to far-range effect was visible, resulting in tendencies to lower forest height estimates at near-range and higher height estimates at far range. The DEMDiff and RPI CHM mostly underestimated the canopy height when compared to the ALS CHM. The number of negative height estimates was highest for these two products. The CHM derived from coherence amplitude only (SINC inversion) showed a clear overestimation of the canopy height, especially at far range. On bare surfaces, the height was usually overestimated. As the PCI CHM shown in Figure 5.30d is a combination of the RPI and SINC inversion, it shows also a combination of effects seen in these two CHMs. The surface height over bare surfaces was often overestimated, yet not as much as in the SINC inversion case. Inside the forest, the heights seemed to be underestimated and several patches with negative height estimates were visible, yet not as dominant as with the RPI inversion. Due to these findings, we dismissed the CHMs derived from DEM differencing and RPI inversion for further analysis, as these two products would most probably lead to unsatisfying results for the subsequent biomass estimation. We therefore concentrated on the two CHMs derived from the SINC and PCI inversions. First, the two estimated CHMs were more closely compared to the ALS derived CHM by calculating the difference between the PolInSAR estimated CHM and the ALS derived CHM as shown in Figure 5.32. Here we see again that the CHM derived from the SINC inversion significantly overestimated the canopy height over forest as well as over bare ground. While the PCI CHM also slightly overestimated the canopy height over bare surface, it mainly underestimated the canopy height over forested areas. Also note that the forests located in the more topographic region in the east of the scene were underestimated in both PolInSAR derived CHMs. This suggests that these two PolInSAR procedures are highly affected by topography, leading to significantly underestimated canopy heights.

For a closer look into the two estimated canopy height products, an analysis over several transects covering a forested area was performed. In Figure 5.33, a subset of the ALS CHM is shown with the three transects highlighted. Transects were chosen to lie in the along track direction (transect 3) or the across track direction (transects 1 and 2) to analyze the effects of image acquisition geometry on the retrieved canopy height. In Figure 5.34, transects of the PCI and SINC inversion results compared to the ALS CHM transect are shown. Here we see that the two PolInSAR derived CHMs do not closely match the ALS derived CHM. Almost no features found in the ALS CHM could be distinguished in the two PolInSAR transects. We see that the SINC inversion usually overestimated the canopy height.

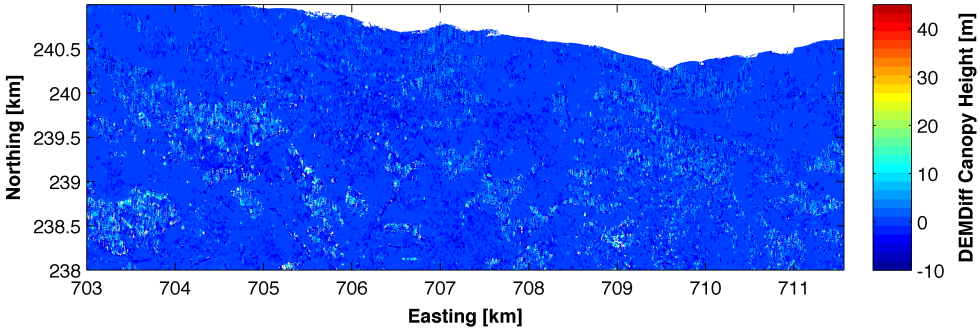


**(a)** DEM-Diff

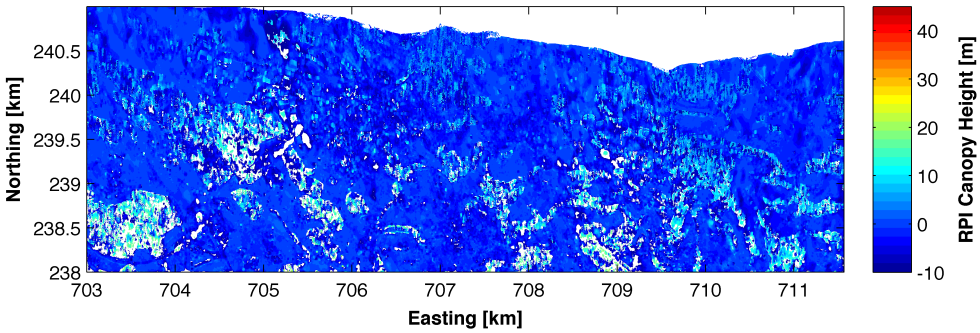


**(b)** RPI

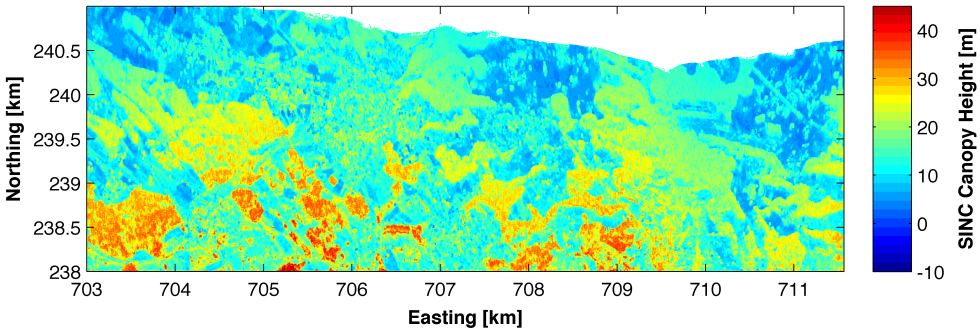


**(c)** SINC

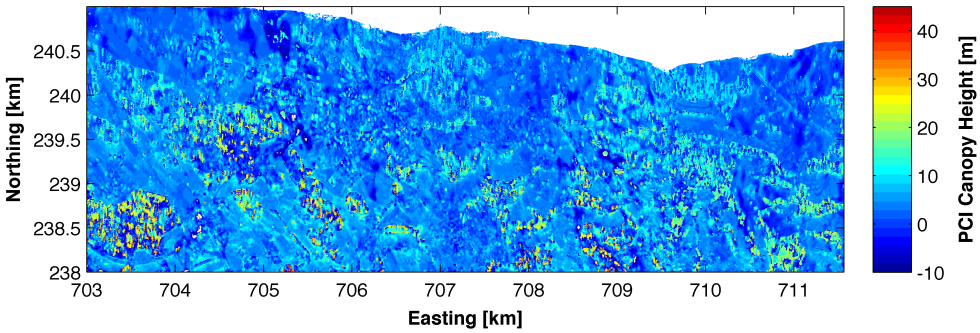


**(d)** PCI

**Figure 5.30:** Different CHMs derived from different PolInSAR methodologies. Interferograms were flattened with ALS DSM. HV polarization taken for the volume dominated interferogram and HH-VV (double-bounce) channel taken for the surface dominated interferogram. (a) DEM-Differencing CHM, (b) RPI CHM, (c) SINC CHM, (d) PCI CHM.

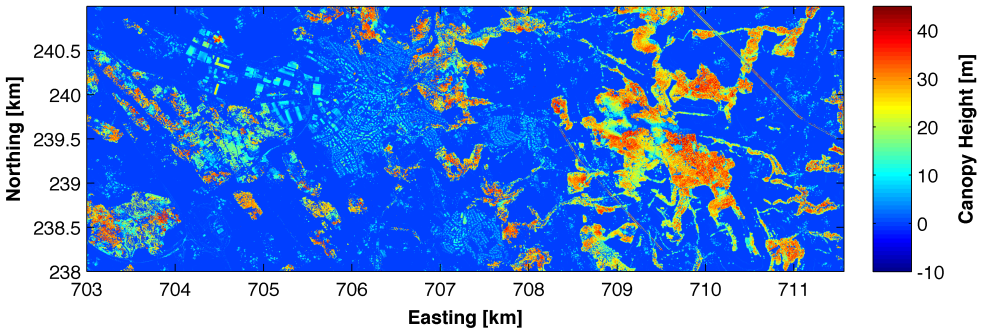


**(a)** ALS

**Figure 5.31:** ALS CHM for comparison to PolInSAR CHMs shown in Figure 5.30.

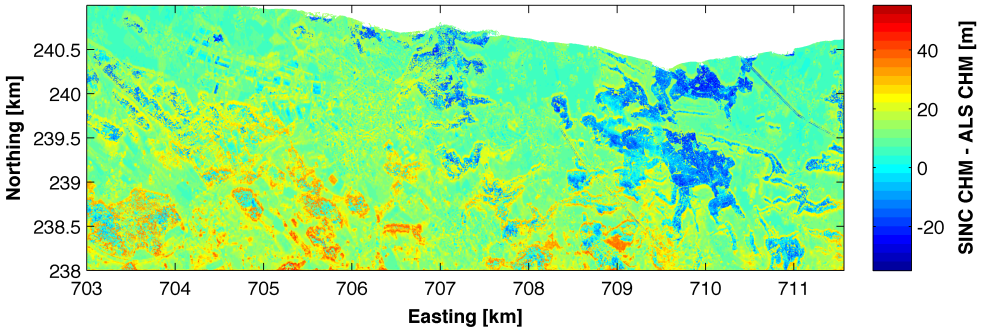


**(a)**

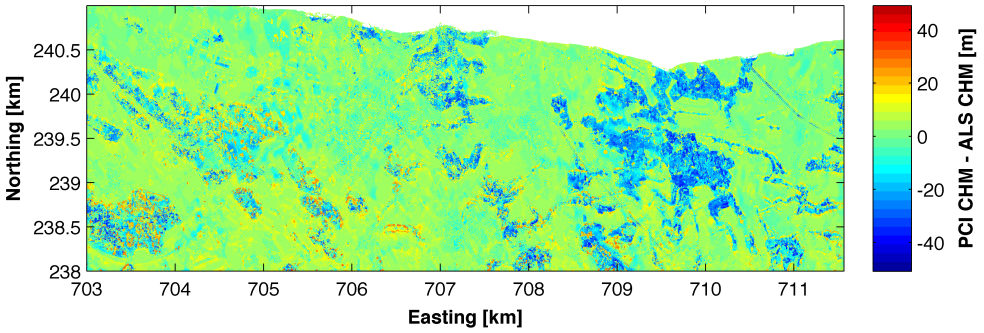


**(b)**

**Figure 5.32:** Difference image between PolInSAR derived CHMs and ALS derived CHM. (a) Difference between SINC CHM and ALS CHM, (b) Difference between PCI CHM and ALS CHM.

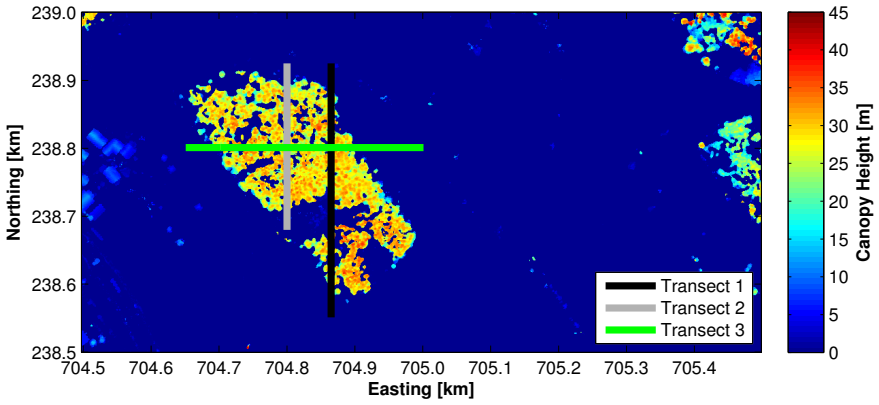


**Figure 5.33:** Subset of Hinwil ALS CHM over the forest Buelholz near Hinwil with highlighted transect locations for transect analysis with PolInSAR derived CHMs.

The SINC inversion was also not able to depict forest clearings e.g. in transect 1 at around 238700 m Northing. The PCI derived CHM transect showed at least a decrease in estimated forest height at this location. Yet the PCI derived CHM clearly showed a very high noise level, where high canopy height estimates were often followed by very small, or even negative height estimates. Also interesting is that for the north-south oriented transects (transects 1 and 2) derived from the PCI inversion, some clear forest border effects are visible. At the north end of the transects (at the right hand side of Figures 5.34b and 5.34d) large height estimates are derived already *before* the actual forest begins, enlarging the forest stand in the PolInSAR derived CHM estimate. At the south end, a clear drop in height estimate *before* the actual end of the forest is observed, after which the height estimates peak again approximately on the forest border. Such effects are not so distinct in the transect oriented east-west (along the flight track). On bare surfaces behind the forest borders, both PolInSAR derived CHMs overestimated the canopy height. This analysis shows that a height estimation from PolInSAR at very small scales did not produce satisfying results. At greater scales, averaging the estimated heights over a larger area, the PolInSAR derived height estimates could lead to acceptable results. This was shown in the average height over the analysed transects especially for the PCI derived CHM. While the SINC inversion derived CHM highly overestimated the mean transects height by up to 20 meters (for transect 1), the PCI derived mean transect heights only underestimated the ALS derived mean transect height by a maximum of 4 meters. Due to this observation, the subsequent PolInSAR analysis were based on the stand level, the most common scale for PolInSAR studies found in the literature (e.g. Chen et al., 2008 or Mette et al., 2004). Also note that the study site is further reduced to a smaller subset located at the western part of the scene in order to reduce the topographic effects found in the eastern part of the scene as discussed earlier and illustrated in Figure 5.32. The northernmost part was excluded from the analysis to minimize near range effects. The final study site size for the PolInSAR study was therefore roughly 2x4 km in the south-western corner of the E-SAR scene (Easting coordinates between 703 and 707 km, Northing coordinates between 238 and 240 km).

In Table 5.6, the performance of the PCI and SINC inversion to estimate forest height at the stand level for different minimum stand sizes and different interferogram flattening procedures are shown. The SINC inversion was clearly not able to predict forest height accurately even at the stand level. Only at a minimum stand size of 2 ha was the SINC inversion able to achieve an $R^2$ of over 0.1, even

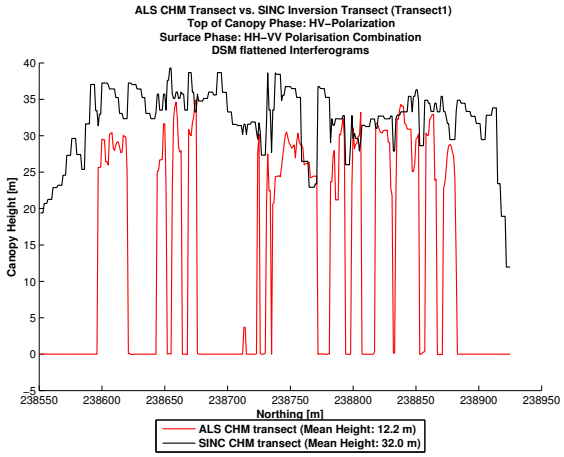


**(a)** SINC Transect 1

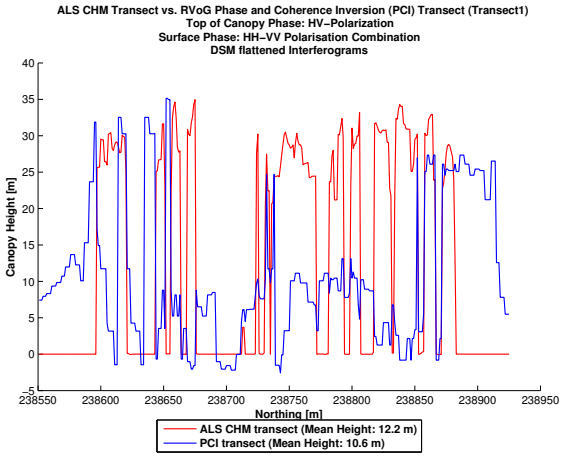


**(b)** PCI Transect 1

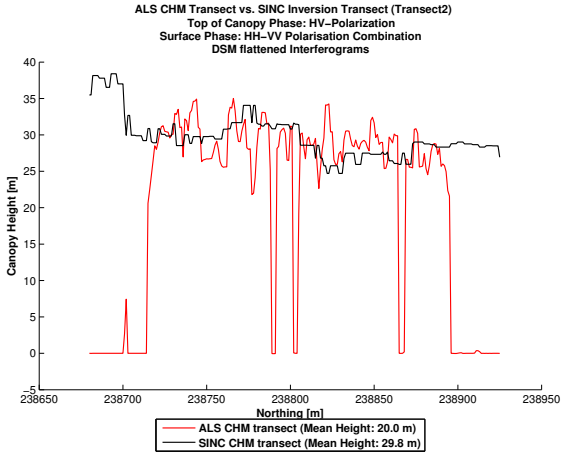


**(c)** SINC Transect 2

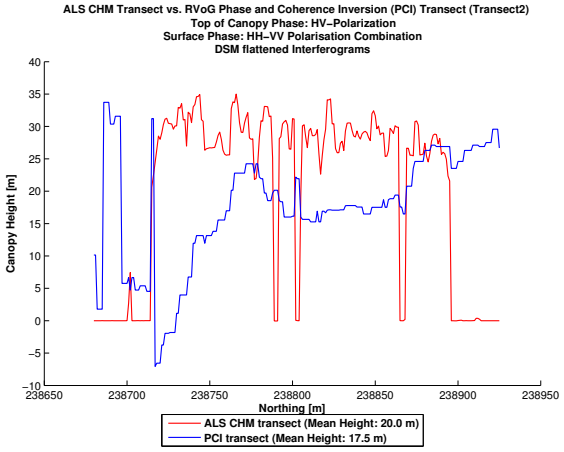


**(d)** PCI Transect 2

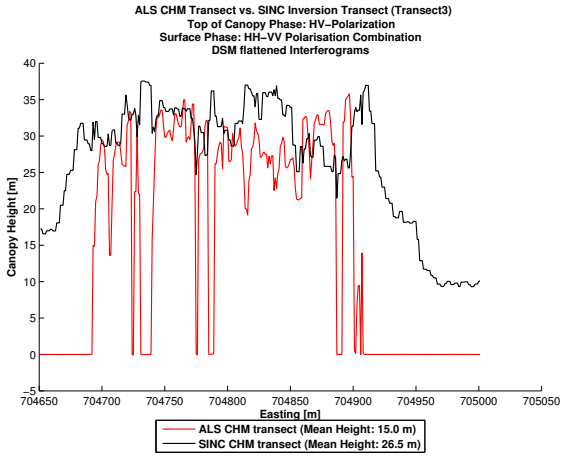


**(e)** SINC Transect 3

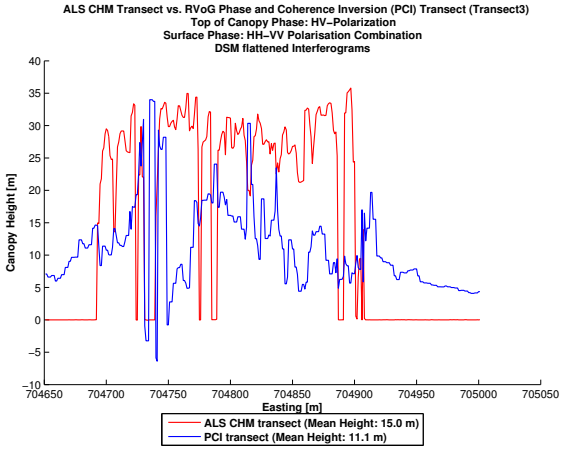


**(f)** PCI Transect 3

**Figure 5.34:** Transect analysis of SINC inversion derived CHM (left column) and of PCI inversion derived CHM (right column) compared to the ALS derived CHM. For the PolInSAR CHM estimation DSM flattened interferograms at HV-polarization for the volume dominated channel and HH-VV polarization for the surface dominated channel were used. ALS data was acquired April 2003 and E-SAR data was acquired in September 2006 (see Sections 3.3 and 3.5).

then with an RMSE of up to 15 m in the DSM flattened case, which is more than 100% of the mean ALS measured stand canopy height (12 m at 2 ha minimum stand size). The PCI inversion performed much better, especially when increasing the minimum stand size to at least approximately 1 ha. Better results were achieved when DSM flattened interferograms were employed than when DTM or ellipsoid flattened interferograms were used. The best results were achieved with a minimum stand size of 2 ha with an $R^2$ of 0.49 and an RMSE of 5.3 m. The mean ALS measured stand heights at 2 ha minimum stand size was about 12.3 m, resulting in relative errors in height estimates from the PCI inversion of 43% of the reference mean stand height. In Figure 5.35, ALS-measured and PolInSAR-derived mean canopy heights from the SINC and PCI inversions at the stand level are compared for the minimum stand size case of 2 ha. We see here again that while the PCI inversion detected the increase in canopy height, the SINC inversion failed across the line. The PCI inversion mainly underestimated the canopy height, while the SINC inversion significantly overestimated the canopy height.

**Table 5.6:** Performance of the PCI and SINC inversion in estimating forest heights at the stand level for different minimum stand sizes and different interferogram flattening procedures. For the volume dominated channel, the interferogram at HV-polarization was used and for the surface dominated channel, the interferogram at HH-VV polarization was used. $\overline{h}$ denotes the mean ALS measured canopy height.

| | PCI Inversion | | | | | | | | | |
|---|---|---|---|---|---|---|---|---|---|---|
| | unfiltered (N=336) $\overline{h}$ = 8.9m | | 0.5 ha (N=55) $\overline{h}$ = 10.4m | | 1 ha (N=28) $\overline{h}$ = 11.3m | | 1.5 ha (N=17) $\overline{h}$ = 12.4m | | 2 ha (N=14) $\overline{h}$ = 12.3m | |
| | $R^2$ | RMSE [m] | $R^2$ | RMSE [m] | $R^2$ | RMSE [m] | $R^2$ | RMSE [m] | $R^2$ | RMSE [m] |
| DSM flattened | 0.047 | 6.8 | 0.022 | 5.3 | 0.325 | 4.8 | 0.476 | 5.5 | 0.491 | 5.3 |
| DTM flattened | 0.088 | 6.9 | 0.05 | 5.2 | 0.096 | 5.2 | 0.177 | 5.2 | 0.227 | 4.8 |
| Ellipsoid flattened | 0.043 | 7.4 | 0.023 | 6.3 | 0.095 | 5.2 | 0.22 | 5.14 | 0.265 | 4.8 |
| | SINC Inversion | | | | | | | | | |
| | unfiltered (N=336) $\overline{h}$ = 8.9m | | 0.5 ha (N=55) $\overline{h}$ = 10.4m | | 1 ha (N=28) $\overline{h}$ = 11.3m | | 1.5 ha (N=17) $\overline{h}$ = 12.4m | | 2 ha (N=14) $\overline{h}$ = 12.3m | |
| | $R^2$ | RMSE [m] | $R^2$ | RMSE [m] | $R^2$ | RMSE [m] | $R^2$ | RMSE [m] | $R^2$ | RMSE [m] |
| DSM flattened | 0.039 | 17.9 | 0.036 | 16.1 | 0.057 | 14.8 | 0.076 | 14.2 | 0.172 | 15.2 |
| DTM flattened | 0 | 15.8 | 0.008 | 13 | 0.03 | 11.6 | 0.092 | 10.8 | 0.188 | 11.6 |
| Ellipsoid flattened | 0 | 15.8 | 0.009 | 13.1 | 0.025 | 11.7 | 0.087 | 10.8 | 0.182 | 11.6 |

## 5.7.2. Biomass estimation from PolInSAR-derived mean canopy height

With the canopy height estimate from PolInSAR established, the performance of the later biomass estimation can be assessed. As the PCI inversion with the DSM flattened interferograms achieved the best results in predicting canopy height, we focused on this dataset to assess the biomass estimation performance. In Figure 5.36, a scatterplot of PCI derived mean canopy height and the reference biomass derived from the ALS measurements is shown with the power law model fitted to the data points. Stand-wise comparisons for minimum stand sizes of 1 ha, 1.5 ha and 2 ha are shown. Note that due to the few stands that were large enough for this analysis, no separation of training and model validation stands could be performed. A model validation was therefore unfortunately not

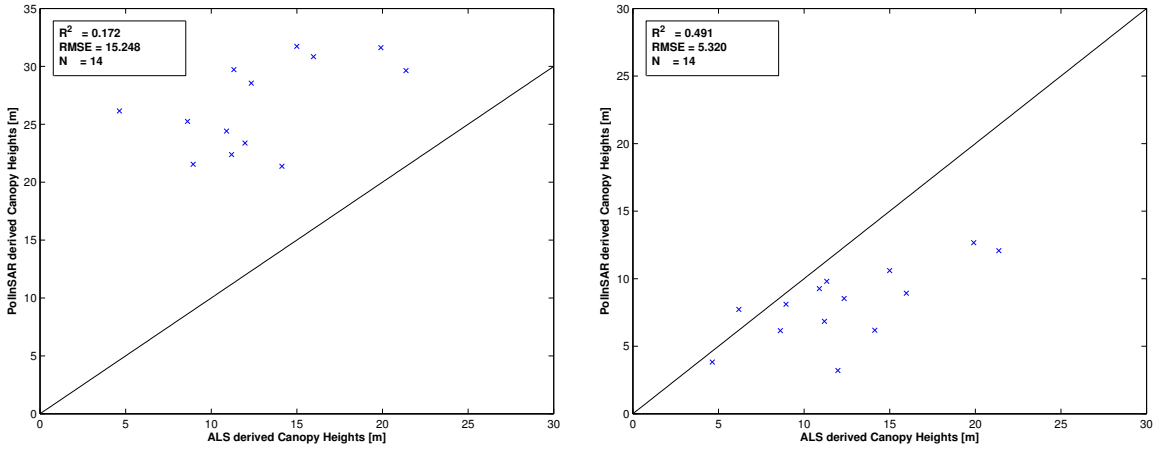


**(a)** **(b)**

**Figure 5.35:** ALS derived mean canopy height vs. PolInSAR derived mean canopy height at stand level with minimum stand size of 2 ha. Interferograms are DSM flattened. Volume dominated interferogram: HV, surface dominated interferogram: HH-VV. (a) ALS vs SINC mean canopy height, (b) ALS vs PCI mean canopy height.

possible in this case. Yet, we were still able to see that an increase in reference biomass is clearly accompanied with in increase in PCI derived mean stand height. Increasing the minimum stand size resulted in an increase in $R^2$ from 0.37 for the 1 ha minimum stand size case up to 0.56 for the 2 ha minimum stand size case. Yet the RMSE increased with increasing minimum stand sizes from 117.9 t ha$^{-1}$ for the 1 ha case up to 133.5 t ha$^{-1}$ for the 2 ha case. This is notably roughly 100% of the average ALS predicted reference AGB, as shown in Table 5.7.

**Table 5.7:** Model fitting performance between PCI derived mean stand canopy height and ALS derived reference AGB.

| | Parameters | | | Performance | | |
|---|---|---|---|---|---|---|
| minimum Stand Size | a | b | $R^2$ | RMSE [t ha] | rel. RMSE [% of mean AGB] | mean ALS AGB |
| 1ha | 20.956 | 0.831 | 0.366 | 117.9 | 102.3 | 115.2 |
| 1.5ha | 15.538 | 1.02 | 0.525 | 133.2 | 102.2 | 130.3 |
| 2ha | 11.595 | 1.139 | 0.564 | 133.5 | 103.2 | 129.4 |

In this section it was shown that all analyzed approaches to estimate biomass clearly showed some limitations and uncertainties. In the next section, these limitations and uncertainty sources are discussed and an attempt is made to explain why these approaches show difficulties in accurately estimating biomass for the analyzed study sites.

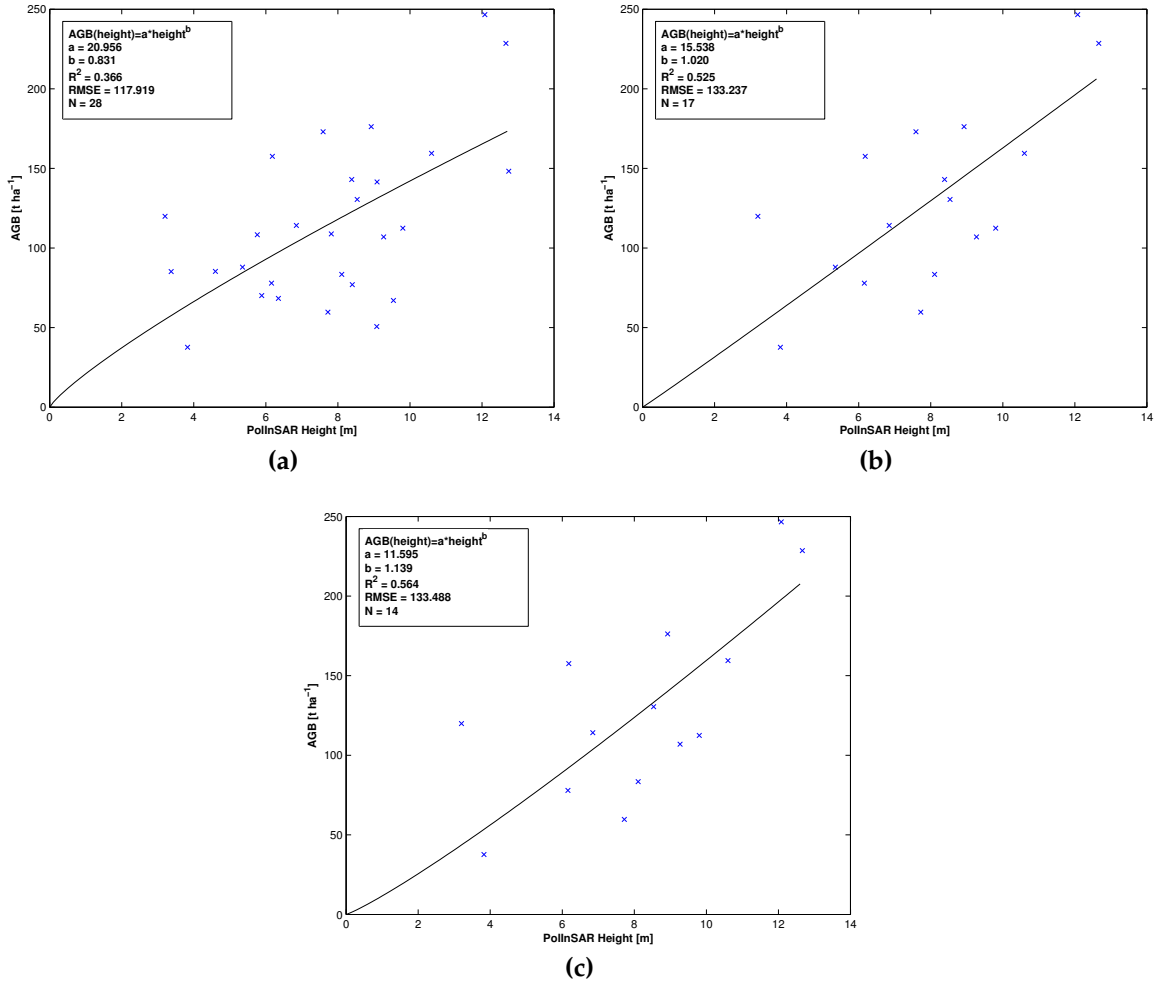


**Figure 5.36:** PCI derived mean canopy height vs. ALS derived reference AGB with fitted power model. (a) minimum stand size of 1ha, (b) minimum stand size of 1.5ha, (c) minimum stand size of 2ha.

# 6. Discussion

In this section, the results of the different biomass estimation approaches outlined in the previous section are discussed and compared to results found in the literature. An attempt is made to explain the reasons for the shown limitations of the different biomass estimation approaches. Finally, several sources of uncertainties are listed and discussed.

## 6.1. Comparison of the different biomass estimation approaches

As shown in the results section, none of the introduced approaches using fully polarimetric SAR data was able to estimate biomass accurately at a plot level. The best result at the plot level was achieved with the multiple polarization approach where the model was able to explain roughly 22% of the variability found in the reference biomass taken from the KSP plots with an RMSE of 88 t $ha^{-1}$. Both single polarization and polarimetric decomposition approaches were able to explain less than 10% of the variability found in the reference biomass at the plot level. Only when looking at the stand level, and filtering out smaller stands, it became possible to estimate biomass with better accuracies. Yet the estimation accuracy was still quite limited. For the single and multiple polarization approach a minimum stand size of 0.5 ha was needed to achieve the best results. Even larger minimum stand sizes did not result in better biomass estimation accuracies. Note that no minimum stand size analysis was performed using the polarimetric decomposition approach, as results based on this approach were very similar to those based on the single polarization approach. While the single polarization approach using the HV-polarization was able to explain roughly 27% of the variability in the reference biomass with an RMSE of 99 t $ha^{-1}$, the multiple polarization approach employing HH-,HV- as well as VV-polarization was able to explain roughly 41% of the variability in the reference biomass with an RMSE of 74 t $ha^{-1}$. The average stand-level biomass for the validation stands with stand sizes larger than 0.5 ha was 169 t $ha^{-1}$. The relative RMSE for the single and multiple polarization approach was therefore roughly 59% and 43% of the mean stand-level biomass in the validation stands.

The PolInSAR approach using phase as well as coherence information delivered the best results of all the analyzed PolInSAR approaches. Yet the minimum stand size required here was at least 1 ha. Best results were achieved with a minimum stand size of 2 ha. With a minimum stand size of 2 ha, the retrieved model relating PCI retrieved stand-level canopy height to biomass was able to explain roughly 56% of the variability found in the reference biomass with a RMSE of 133.5 t $ha^{-1}$. This is notably over 103% of the average stand-level biomass of all analyzed stands with at least 2 ha size (129 t $ha^{-1}$). Note that due to the very low number of suitable stands in the PolInSAR case study the retrieved model could not be independently validated, as was done in the backscatter approach. The stand dataset analyzed herein was therefore also different than the stand dataset analyzed in the backscatter approaches which limited the inter-comparability of the results from the different approaches.

Compared to these results, the very simple approach of estimating biomass from ALS, simply relating the mean canopy height to biomass, performed much better. The retrieved model was able to explain roughly 50% of the variability found in the reference biomass derived from the KSP field

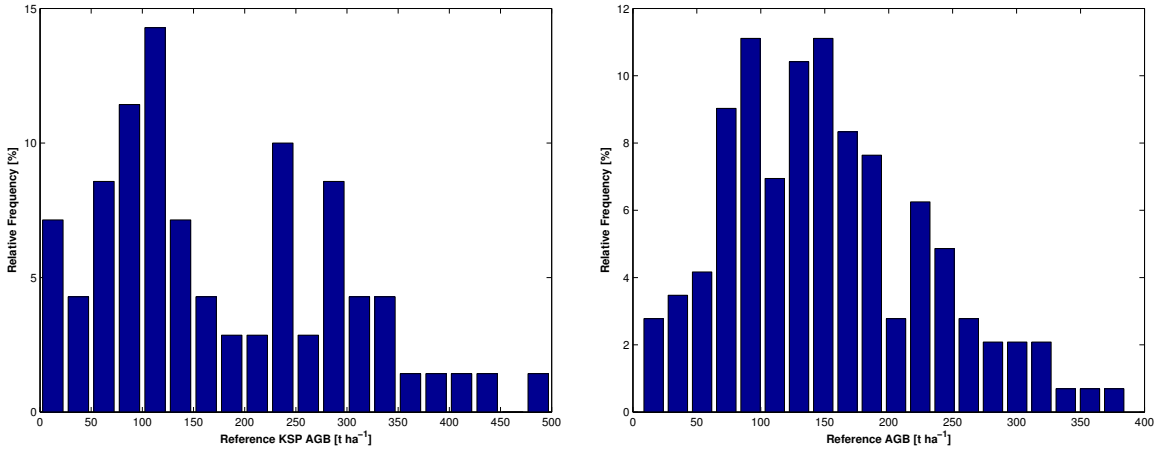


**Figure 6.1:** Histograms from reference AGB over Hinwil, (a) plot level KSP reference AGB, (b) stand level AGB reference retrieved from ALS measurements (0.5 ha minimum stand size).

measurements with an RMSE of 83.5 t ha$^{-1}$. The average biomass over all validation plots used for the model evaluation was 183 t ha$^{-1}$, resulting in a relative RMSE of 45%. Note that this performance is related at the plot level. The performance of the ALS based biomass estimation at the plot level was in the same range as the biomass estimation at the stand level using the multiple polarization approach. With a very simple approach based on ALS measurements it was possible to receive more accurate biomass estimations than the analyzed SAR based methodologies even at smaller scales.

Due to the small stands and the very low sensitivity of the ALOS PALSAR backscatter data, no biomass estimation was performed using the ALOS PALSAR data. A comparison of the biomass estimation performance using E-SAR vs. PALSAR data was therefore not performed.

## 6.2. Biomass estimation from fully polarimetric SAR backscatter data

The results have shown that no single polarization channel nor Pauli decomposition base from airborne or spaceborne measurement was sufficiently sensitive to biomass in order to accurately estimate forest biomass, neither at plot nor stand levels. Although there were a few plots and stands available for this study that covered the lower biomass range, a distinct increase in backscatter with increasing biomass at the lower biomass range was not observed (see also Figure 6.1 for E-SAR study site at Hinwil for plot and stand level AGB histograms, and Figure 6.2 for the Hinwil and Lägern AGB histograms of the study site extents analyzed by PALSAR PLR data at 25 and 100m resolution). This is somehow contradictory to the common findings reported in literature where especially the HV channel is reported to have high sensitivity to biomass changes in the lower biomass spectrum at L-band for airborne as well as spaceborne SAR instruments (typically ALOS PALSAR FBD data) (e.g. Mitchard et al., 2009, 2011; Saatchi et al., 2007a). This could be due to the different forest types analyzed in these studies compared to the forests analyzed in this study. Most studies reporting a high sensitivity of L-band HV-polarization to biomass were conducted in boreal or tropical forests

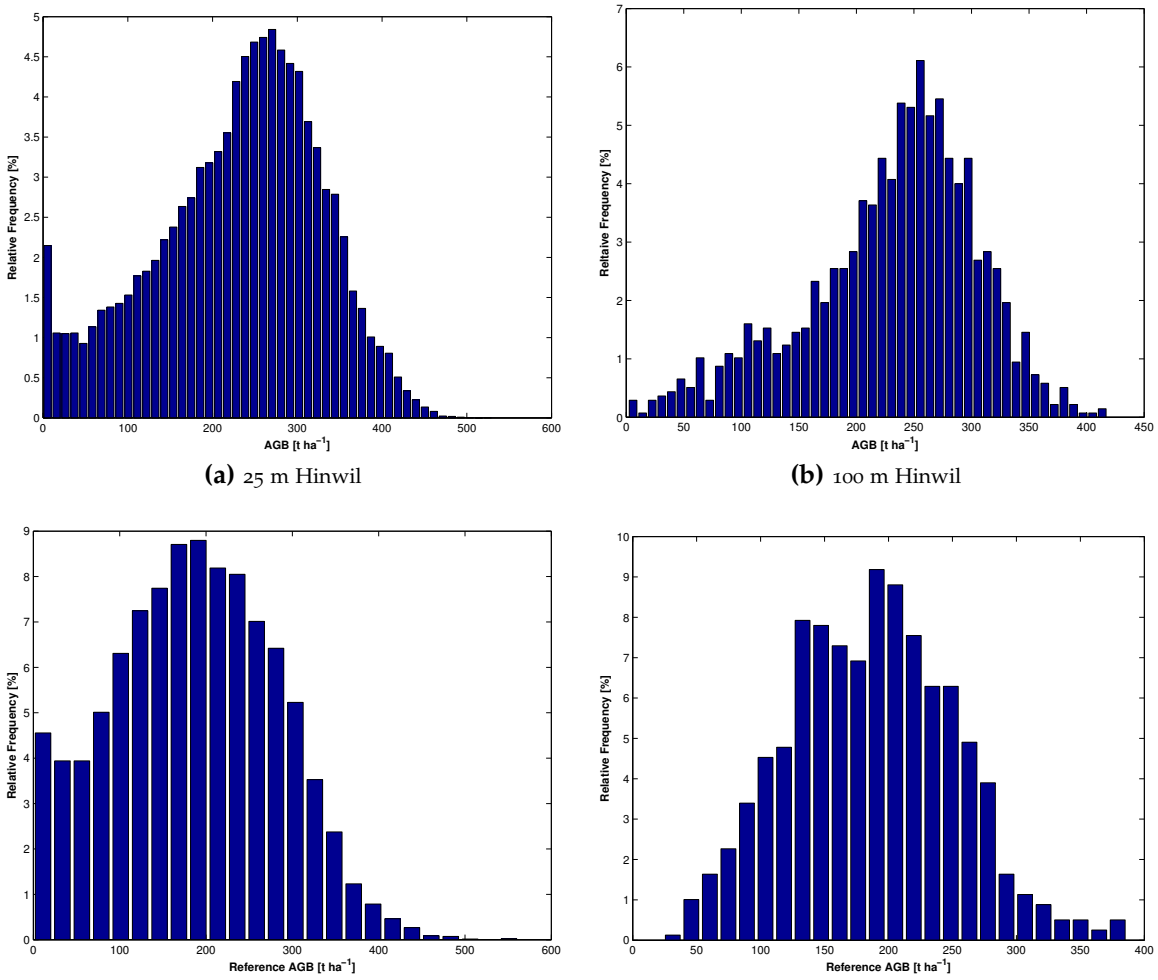


**(a)** 25 m Hinwil **(b)** 100 m Hinwil

**(c)** 25 m Lägern **(d)** 100 m Lägern

**Figure 6.2:** Histograms of AGB reference retrieved from ALS measurements for PALSAR analysis over Hinwil and Lägern study site. (a) AGB histogram over Hinwil study site at 25m resolution, (b) AGB histogram over Hinwil study site at 100m resolution, (c) AGB histogram over Lägern study site at 25m resolution, (d) AGB histogram over Lägern study site at 100m resolution.

(often in transition zones between savanna and tropical forests where many low biomass plots are found, e.g. in Mitchard et al., 2009), and where forest stands are usually characterized by a few dominant tree species and typically cover larger areas. The forests analyzed in this thesis are characterized as mixed-coniferous forests, covering a large variety of tree species. Furthermore, the forests are often highly managed, leading in a high variability in stand density. Ackermann et al. (2010) came to a similar conclusion that L-band SAR backscatter data at HV-polarization showed only very weak sensitivity to biomass in a study concerning ALOS PALSAR FBD data over the Thuringian forest in Germany.

Only by adding further low biomass plots to the regression analysis, was a higher correlation between reference biomass and measured backscatter intensity found. This is a common tactic also employed by Saatchi et al. (2007a). Yet, note that it does actually not fit one goal of this study which was to estimate the biomass stored in forests. As the biomass spectrum found in the analyzed forests

lays typically at 100 t ha$^{-1}$ and above, this tactic did not improve the biomass estimation capability inside the forests, as we were already usually in the saturated area of the model (also see Figure 6.3).

In Figure 6.3, a comparison between the AGB-backscatter model retrieved from E-SAR $\gamma^0_T$ data at HV-polarization at plot level, from PALSAR $\gamma^0_T$ data at HV-polarization with 100m resolution over Lägern study site, as well as two models established by Mitchard et al. (2009) and by Saatchi et al. (2007a), also at plot level, is shown. Note that while we employed $\gamma^0_T$ backscatter data, Mitchard et al. (2009) used $\sigma^0_E$ backscatter values, not compensated for terrain effects (yet, the study site did not show significant topography, Mitchard et al., 2009), and Saatchi et al. (2007a) used $\sigma^0$ backscatter values compensated for local incident angle effects. While Mitchard et al. (2009) used ALOS PALSAR FBD data over several African landscapes, Saatchi et al. (2007a) used airborne L-band SAR data from the AIRSAR instrument over the Yellowstone National Park in the United States to retrieve the models. The models shown do not differ extremely from each other. The $R^2$ values for the listed models are broadly similar. Interestingly though, the backscatter intensities from the E-SAR $\gamma^0_T$ case were several decibels higher than all other models. This could be evidence for erroneous radiometric calibration of the E-SAR dataset. Note that for both models established in this thesis, the saturation point was lower in comparison to the models established by Mitchard et al. (2009) and Saatchi et al. (2007a). This could be accountable to differences in site characteristics. The backscatter model taken from the PALSAR PLR data over the Lägern study site included also non-forest areas as low biomass reference data. When only *forested* areas were analyzed with ALOS PALSAR data, no correlation between biomass and backscatter was observed. The reference biomass for the PALSAR Lägern study site was taken from ALS canopy height measurements. When no forest masking was performed, also structures *not* related to vegetation (such as buildings) can be included in the biomass reference data as these structures also have a height value in the CHM. To overcome this problem, another filtering and masking approach should be used to filter out areas not related to vegetation. Yet, as the focus of this thesis lies on estimating biomass inside forests, no further efforts were undertaken to analyze this behavior.

The observed saturation in backscatter intensities with increasing biomass at L-band has been reported and discussed in literature at length. It limits the utility of L-band SAR data for estimating biomass at large scales and for different forest types. An attempt to explain this saturation effect was made by Woodhouse (2006a) and in Zuberbühler (2014) where the saturation of the backscatter intensities at higher biomass levels was explained with a *thinning* effect. With the growth of the forest over time, more dominant trees gain in size at the cost of fewer smaller trees, leading to fewer trees in a stand. Zuberbühler (2014) was able to relate the saturation to this *thinning* effect with fully-polarimetric E-SAR P-band SAR data and could therefore compensate the saturation effect by employing a correction factor based on the stand density. Yet, such an approach requires either extensive forestry record keeping on the stand density or high resolved LiDAR measurements from which the stand density could be derived via a single tree detection approach. Unfortunately, for most areas in the world, such data is not available and a robust estimation of the *thinning* factor requires further research. Although both reference datasets in order to estimate the stand density would have been available for this study (KSP field measurements and ALS measurements), no analysis of this *thinning* effect is performed here, as it would have gone beyond the scope of this thesis.

Several studies have shown that the average backscatter intensity shows better correlation to biomass at the stand level than at the plot level (e.g. Chowdhury et al., 2013; He et al., 2012; Saatchi et al., 2007a etc.). Also in this thesis it was found that the relation of backscatter intensities to biomass

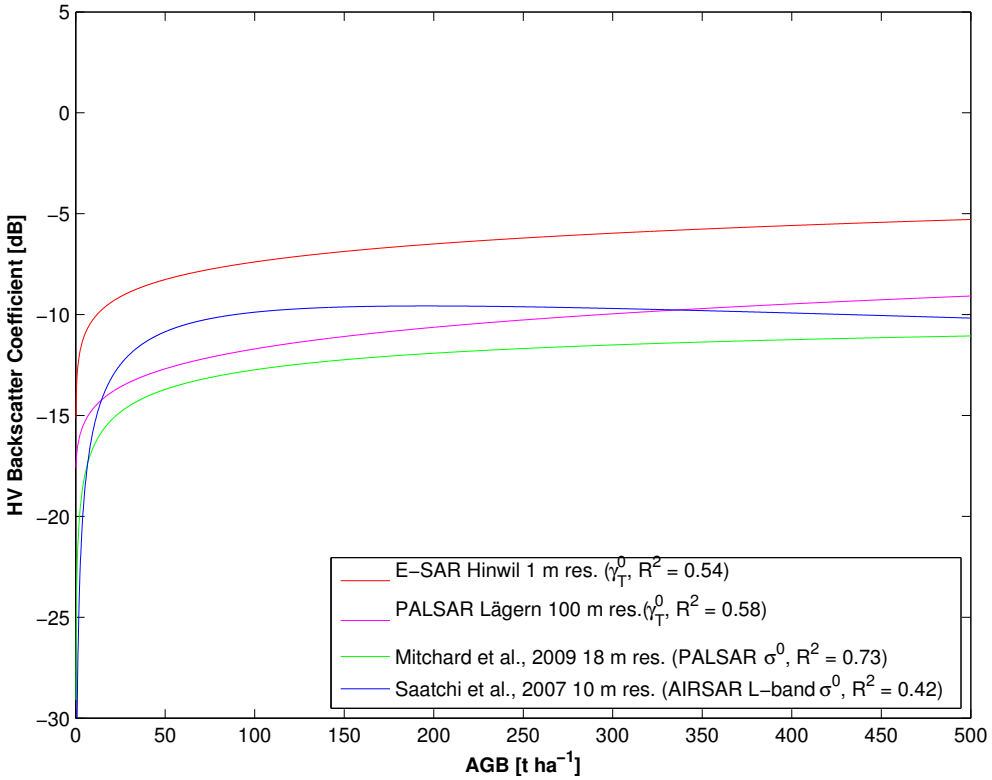


**Figure 6.3:** Comparison between models derived from E-SAR and PALSAR HV polarization against biomass over Hinwil and Lägern study site and the models retrieved by Mitchard et al. (2009) and Saatchi et al. (2007a). The model by Mitchard et al. (2009) was retrieved from PALSAR FBD data over 4 African low-biomass tropical woody vegetation. No radiometric normalization was performed. The model by Saatchi et al. (2007a) was retrieved over boreal forests in the Yellowstone National Park with airborne L-Band AIRSAR data. Radiometric normalization based on incident angle correction was applied. All shown models relate to plot level (or pixel level for PALSAR Lägern model). The $R^2$ values for the Mitchard et al. (2009) and Saatchi et al. (2007a) models were retrieved from the declared literature.

slightly increased when looking at larger stands of at least 0.5 ha. For smaller stands, noise in the SAR data often limited the sensitivity to biomass. The noise level was successfully reduced by averaging over larger stands. Yet, the backscatter values for the different stands tended to converge to a very small backscatter range, lacking any sensitivity to changes in biomass. Furthermore, due to averaging of larger stands, the number of stands in the lower biomass spectrum (lower than 100 t ha$^{-1}$) decreased significantly.

The best results from backscatter data was achieved when employing a combination of HH-, HV- and VV-polarization as introduced by Saatchi et al. (2007a). This could be partly accounted to the reduced noise when integrating data from several channels. The biomass estimation performance using this multiple polarization approach increased with increasing stand size, with best results found at 0.5 ha. Saatchi et al. (2011) came to a similar conclusion in their study on the influence of the spatial variability of tropical forest structure on radar estimation of AGB, where they also employed a combination of the three polarization channels at several stand sizes. Saatchi et al. (2011) concluded that the accuracy was optimal at 1 ha scale with a RMSE of 23.8 t ha$^{-1}$ for AGB<150 t ha$^{-1}$. The higher RMSE error found in this thesis can be accounted to the higher biomass range found in the

analyzed forests, as well as to the fact, that while Saatchi et al. (2011) only analyzed the biomass range up to 150 t $ha^{-1}$, the whole biomass range was analyzed in this thesis. Due to the good performance of the multiple polarization approach, this model became a reference model for predicting biomass, especially also with P-band SAR focusing on the upcoming ESA BIOMASS mission (Sandberg et al., 2011; Le Toan et al., 2011).

In the following subsections the benefits of the different normalization techniques are discussed as well as some further points specific to E-SAR and PALSAR data.

### 6.2.1. The use of different backscatter normalization procedures

Radiometrically normalized products were shown to typically exhibit higher sensitivity to biomass and perform better in estimating biomass than GTC products. This is accountable to the normalized radiometric distortions such as foreshortening and layover in the RTC products. Such topographic induced effects were present in both analyzed study sites. Especially in the E-SAR case, the RTC products performed better than the GTC products. In the PALSAR case, the high noise level in the data and the very low sensitivity to biomass inside the forests did not allow such a clear statement. Yet, it has to be mentioned that with 25 m resolution a rather poorly resolved Digital Height Model (DHM) was used to normalize the PALSAR product as compared to the 1 m resolved ALS derived DHM used to normalize the E-SAR products. To allow a better grounded conclusion concerning the difference between GTC and RTC products of ALOS PALSAR data, an analysis over larger areas with more topography should be performed as the two study sites used in this thesis did not show many radiometric distortions in the ALOS PALSAR data. Efforts towards reducing the high noise level in the PALSAR data would be needed, e.g. with a kind of speckle filter.

The employment of radiometric normalization of the SAR backscatter data for later biomass estimation procedures has not often been used in the published literature. He et al. (2012) reported that the employed PALSAR data showed higher sensitivity to biomass after correction for topography-induced distortion effects. Yet, often the study sites are selected to be flat and uncorrected $\sigma^0$ backscatter values were used (e.g. in Mitchard et al., 2009) or a local incident angle based correction approach when using airborne SAR data was performed (e.g. in Saatchi et al., 2007a). Especially for large scale and multi-temporal analysis an accurate radiometric normalization of the SAR data is important to ensure a robust backscatter vs. biomass relation.

In the E-SAR case also a radiometric normalization using the ALS derived DSM was performed, in order to compensate for radiometric distortions induced by the canopy topography inside the forests. It was found that such a normalization induced more noise and was therefore not feasible for forestry applications. This is mainly due to the very complex structure of the canopy with steep height changes. As the radiometric normalization software treats the passed DHM as a solid surface, impenetrable by the radar waves, the canopy surface was highly overcorrected, resulting in many shadow pixels where the radar was actually still able to retrieve reliable backscatter information. In order to correct for such canopy induced radiometric distortions a different procedure should be developed that treats the DSM not as an impenetrable surface, but employs a wavelength-dependent correction factor. Perhaps the use of a LiDAR derived point cloud dataset could lead to better corrections of such vegetation induced radiometric distortions, as vegetation density information from different canopy height levels could be retrievable from such laser measurements. Such an

analysis of radiometric normalization inside forested terrain using point cloud LiDAR metrics could be interesting for further studies.

Also a correction for terrain induced azimuth slope effects or polarization orientation angle correction was performed herein. Yet, contrary to the findings reported in Chowdhury et al. (2013), where a POA correction was applied to ALOS PALSAR data, the volume scattering channel or the scattering mechanism ratio $P_d * P_v / P_s$ did not show higher sensitivity to biomass when such an azimuth slope correction was applied. This was consistent when using PALSAR or E-SAR data. This was most probably due to the high noise level in the POA estimate over forested terrain. By rotation with the estimated POA around the LOS, further noise was likely added to the backscatter vs. biomass relation, leading to even worse biomass sensitivity or estimation performance. This was a more considerable problem with PALSAR data, as no robust estimate of the POA was possible due to the high noise level (see Figure 5.6c). Such an azimuth slope correction would be more feasible at longer wavelengths, such as P-band, where the radar waves are less affected by vegetation.

### 6.2.2. Geocoding using a DTM vs. DSM

As both an ALS-derived DTM and DSM were available for the Hinwil study site, the difference between geocoding with a DTM or a DSM was analyzed for the backscatter data from the E-SAR instrument. The results showed that the backscatter products geocoded with the DSM consistently had higher sensitivities to biomass than the products geocoded with DTM. This can be explained with the scattering phase center location. Several studies (e.g. Saatchi et al., 2007a; Cloude, 2005) reported that the scattering phase center height of the HV-polarization lies somewhere between the middle of canopy and the top of canopy. When geocoding with the DSM, the backscatter value is therefore mapped closer to the actual scattering location than when using the DTM. This should also be true for the co-polarized channels at L-band, as these channels will also not penetrate through the whole canopy and will therefore have their scattering phase center somewhere in the middle of the canopy. A more extensive analysis of where the actual backscatter information comes from is still missing in literature and should be the subject of future studies. The information received from LiDAR metrics, such as height percentiles, could be of benefit to such studies.

### 6.2.3. E-SAR vs. PALSAR backscatter sensitivity to biomass

It was shown that while E-SAR backscatter data showed some sensitivity to biomass, ALOS PALSAR backscatter data exhibited nearly no sensitivity to biomass. This can be accounted to some extent to the higher noise level in the PALSAR acquisitions. This is shown in Figure 6.4a, with a small subset over forested terrain taken from a PALSAR $\gamma^0_T$ frame at HV-polarization at the Hinwil study site. While the outlines of the forest can be made out due to increased backscatter compared to the surrounding non-forested areas, variability inside the forest caused by different biomass levels was not observable, mainly due to the high noise level. Compare also to the biomass map over the same area taken from ALS measurements shown in Figure 6.4e. After reducing the noise level with a 3x3 median filter, as shown in Figure 6.4b, no clear variability in the backscatter data was observed. The forest is mostly represented by a homogenous area with nearly the same backscatter intensities. The E-SAR backscatter $\gamma^0_T$ image at HV-polarization over the same area shows much higher variability in the forest, which can be related to biomass differences. This is of course also accountable to the

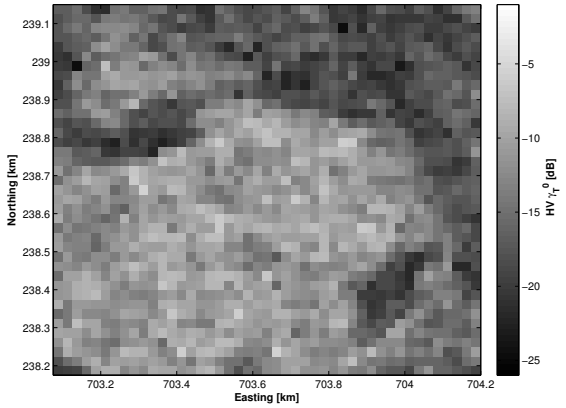


**(a)** PALSAR HV @ 25 m

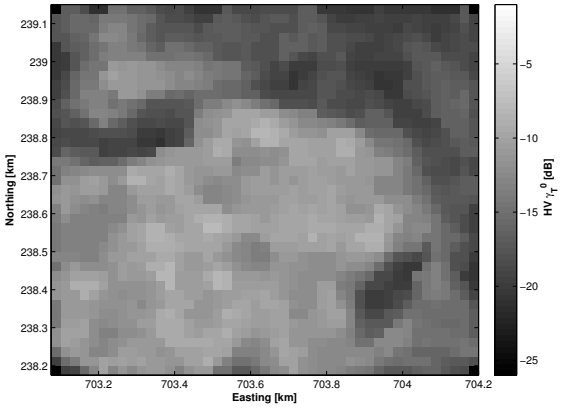


**(b)** PALSAR HV @ 25 m with 3x3 Median filter

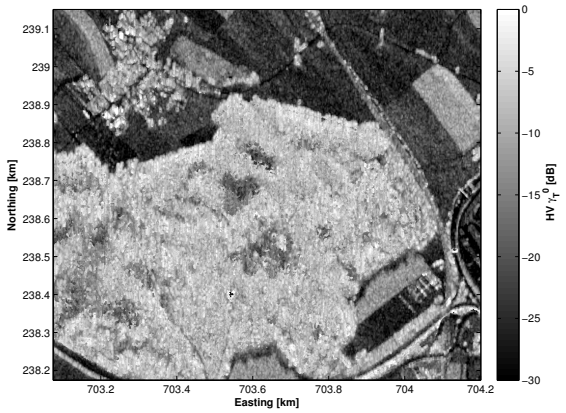


**(c)** E-SAR HV @ 1 m

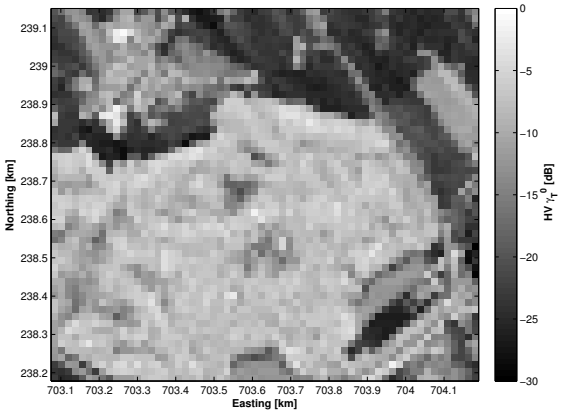


**(d)** E-SAR HV @ 25 m

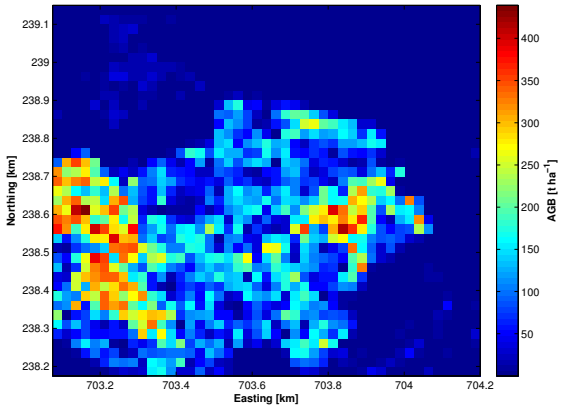


**(e)** ALS reference AGB map @ 25 m

**Figure 6.4:** PALSAR vs. E-SAR HV $\gamma_T^0$ over forested area (Sennwald) in Hinwil test site. (a) PALSAR HV $\gamma_T^0$ at 25m resolution, (b) PALSAR HV $\gamma_T^0$ with applied 3x3 pixel median filter, (c) E-SAR HV $\gamma_T^0$ at 1m pixel spacing, (d) E-SAR HV $\gamma_T^0$ at 25m pixel spacing, (e) reference AGB map over same area derived from ALS height measurements. E-SAR data acquisition was on the 12th of September 2006. PALSAR frame showed here was acquired on the 9th of May 2009 at an off-nadir angle of 23.1°.

much higher resolution. Yet, if the resolution of the E-SAR image is reduced to 25 m, matching the resolution of the PALSAR data as shown in Figure 6.4d, variations in the backscatter levels inside the forest remain visible and a much lower noise level is observed.

## 6.3. Forest height and biomass estimation from PolInSAR

Prerequisites for robust height inversions from PolInSAR measurements are a sufficient scattering phase center separation between the surface dominated and volume dominated interferograms and a low temporal decorrelation. The latter can decrease the coherence substantially, leading to a significant overestimation of forest heights, as was observed in the results from the height inversion using coherence amplitude only. As shown in Figure 6.5, both of these prerequisites were not given in our case. The coherence in both channels was low, with the peak between 0.1 and 0.2. In most studies reporting good results in forest height inversions, significantly higher coherence values were reported (e.g. in Cloude & Papathanassiou, 1998; Cloude, 2005). Yet these high coherence values often stem from simulated data without any temporal decorrelation. Cloude & Papathanassiou (1998) proposed a coherence optimization approach that increases the coherence also over forested terrain, allowing also for better scattering phase center separation. Also in Chen et al. (2008) such a coherence optimization was performed and a better height estimation performance using the optimized channels is reported. Yet, the problem with such coherence optimizations is that the actual scattering phase center is not known, it can stem from surface or the volume above it (Chen et al., 2008). Therefore, no analysis regarding coherence optimization was performed in the course of this thesis. The low coherence found in the E-SAR data may have been due to temporal decorrelation, as the two images were acquired 3 hours apart. A thorough analysis of the source of the low coherence was not performed here.

The second prerequisite concerning the separation of the scattering phase centers was also not sufficiently filled. In Figure 6.5d, the histogram of the volume-dominated and surface-dominated phases over the same highlighted forested area is shown. No large difference between the observed phases in the two channels is visible. This is mostly due to the fact that no polarization at L-band is unbiased from vegetation. A model-based ground phase estimate is required using the RVoG model (Cloude, 2005). The result of such a ground phase estimate is shown in Figure 6.5d (blue histogram), where a clear separation between the volume-dominated HV channel and the ground phase estimate is visible.

In comparison to the results published by Chen et al. (2008), where forest heights at a pre-alpine landscape in southeast Bavaria were estimated using similar algorithms, the results attained in the course of this thesis are similar. Yet, Chen et al. (2008) reported that the highest correlation between estimated and reference stand height were found using the coherence amplitude inversion (SINC inversion) with an $R^2$ of 0.78. But they also reported a high RMSE for this inversion with 13.76 m. For the phase and coherence inversion (PCI), the results reported in this thesis ($R^2$ = 0.49, RMSE = 5.3 m at minimum stand size of 2 ha) were even better then those reported in Chen et al. (2008) ($R^2$ = 0.15, RMSE = 7.99 m, stand sizes between 1 and 23 ha, dominated by spruce).

As the algorithms used for forest height inversions are based on several assumptions that simplify the height inversions, there is still high potential for improvement. For example, a full model

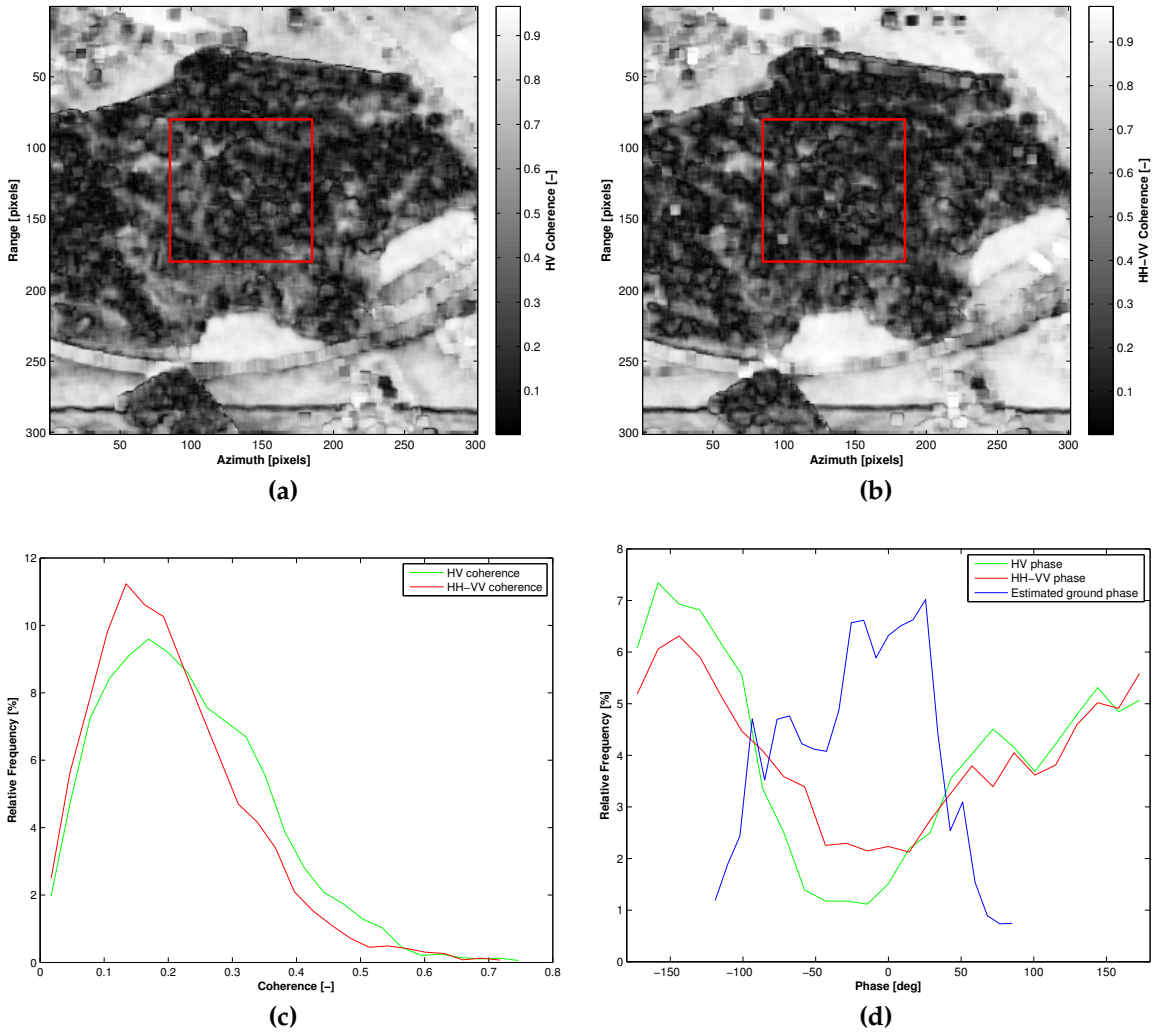


**Figure 6.5:** Coherence and phase over forested terrain in HV and HH-VV channels. (a) and (b) subset of coherence image over forested terrain at HV and HH-VV channels respectively. (c) coherence histogram for HV and HH-VV channel for the area highlighted in (a) and (b). (d) phase histogram for HV and HH-VV channel and the estimated ground phase over the same highlighted area. Coherence and phase measurements were taken from the DSM flattened interferograms. Horizontal baseline $B_h$ = 10 m. Perpendicular baseline $B_n$ = 2.5 m. Temporal Baseline 3 hours.

inversion, employing more than just two interferograms, where for each pixel it is determined which channel is volume- and which is surface-dominated, as proposed by Cloude & Papathanassiou (2003), could lead to greatly improved height estimates, as was also found by Chen et al. (2008).

Due to the still quite high inaccuracies in the forest height estimation, also the subsequent biomass estimation was affected by high noise levels and large uncertainties. Although the model fit the PolInSAR height vs. biomass data points quite well with a $R^2$ of 0.56 at 2 ha stand size, the error in biomass estimation was very high at 133.5 t ha$^{-1}$ which is notably over 100% of the average biomass stored in the analyzed stands. Yet, compared to the results of the backscatter based approaches, no obvious saturation effect was observed, making biomass estimation from PolInSAR forest height retrievals at sites with biomass levels beyond the saturation point of L-band SAR backscatter data (mainly below 100 t ha$^{-1}$) a viable option. Yet as shown in this thesis, topography can significantly affect the forest height estimation performance from PolInSAR. Due to those considerations, a smaller subset of the whole E-SAR scene was taken for the PolInSAR analysis. A correction for such effects in interferograms is therefore needed in order to retrieve robust forest height estimates in more rugged terrain.

## 6.4. Possible sources of uncertainties

There are numerous sources of uncertainties in the different biomass estimation procedures discussed in this thesis. Three major sources of uncertainties are discussed in the following: uncertainties in biomass reference information, uncertainties due to co-registration and geocorrection, as well as uncertainties due to erroneous radiometric calibration of the SAR backscatter data.

### 6.4.1. Uncertainties in biomass reference

An accurate biomass *reference* is crucial to the establishment of regressional models for biomass estimation from SAR or LiDAR signals. The most accurate biomass reference used in this thesis was the one retrieved from the KSP field measurements. As explained in Section 3.2, only the DBH is reported in the KSP field measurements as a proxy for biomass. The biomass reference had to be calculated first from this DBH measurement, using tree species-specific tariff functions and a biomass expansion factor (BEF) as described in Kaufmann (2001) and Thürig & Schmid (2008). Yet, this calculation of biomass from DBH only has a significant level of uncertainty. Kaufmann (2001) reported that by using these tariff functions, the standard deviation of the residuals still amounts to 26.3% of the mean bole volume. Furthermore, the KSP measurements can incorporate some amount of systematic and/or stochastic measurement errors, leading to an even higher inaccuracy in the biomass reference. Yet, inaccuracy in field-measured biomass is a common problem. Saatchi & Moghaddam (2000) compared biomass measurements of two individual field campaigns conducted by *Forestry Canada* and BOREAS (Boreal Ecosystem Atmospheric Study) in the same homogenous boreal forest stands in Canada. They reported differences in the two field-measured biomass references at the stand level of up to 90 t ha$^{-1}$ at a maximum biomass level of 200 t ha$^{-1}$.

These inaccuracies in biomass reference information taken from field measured DBH and allometry also propagate to the biomass reference derived from ALS measurements of mean canopy height at the plot level. A further source of inaccuracy in establishing a biomass reference map from

the ALS data is the large time gap between the ALS data acquisition over Hinwil in 2003 and the KSP field measurement campaign conducted in 2008. In these five years much can change inside the highly managed forests found in the Swiss midlands, leading to difficulties in retrieving a simple mean canopy height vs. biomass relation. This could also explain the large RMSE in the retrieved reference model with 83.5 t $ha^{-1}$. The retrieved model was able to explain roughly 50% in the variation found in the KSP biomass reference dataset. Also Nelson et al. (1988) reported that the average canopy height in a plot can only explain 53-65% of the variability in biomass, which puts the model retrieved in this thesis into the same order of magnitude, even though the study by Nelson et al. (1988) was conducted in a purely coniferous forest, whereas heterogenous mixed forests were analyzed in this thesis. More sophisticated biomass references based on ALS measurements is therefore needed. Approaches using single tree detection with tree height and crown dimension estimates show promising results (Popescu et al., 2003; Popescu, 2007). Yet, most of these studies were undertaken in homogenous coniferous forests, typically consisting of one single tree species. Applying such methods in more heterogenous mixed forests is more challenging and not yet common. Unfortunately, due to the rather low point density in the ALS dataset over Hinwil, as well as difficulties in matching the detected trees with the trees found in the KSP dataset, such an approach was not investigated in more depth. Over the Lägern study site such an approach would have been feasible due to the full-waveform system flown at very low altitude, yet the low resolution and high noise level of the PALSAR data over this study site would have made the cost-benefit ratio unfeasible for this approach. Unfortunately, no high resolution airborne SAR datasets exist yet over the Lägern test site.

### 6.4.2. Co-registration errors

As several datasets acquired by different measurement systems (SAR, LiDAR, field measurements etc.) were compared, an accurate co-registration of these datasets is of high importance. Yet, a perfect co-registration between all analyzed products cannot be assumed. Biases lead to uncertainties in the regression models retrieved later and the estimated biomass. The comparison of datasets at different resolutions also lead to inaccuracies as several datasets had to be resampled to lower or higher resolutions.

Mapping the SAR backscatter and derived PolInSAR height pixels to geocoded pixels using a DEM and the state-vectors of the satellite or airplane can lead to significant uncertainties. In the E-SAR case, the accurate geocoding proved to be a larger challenge and a small mis-registration of the SAR pixels could remain.

### 6.4.3. Inaccurate radiometric calibration

While the radiometric calibration of the PALSAR backscatter data used most probably shows high accuracies, this is not entirely certain in the E-SAR case. As shown in the methodology and results section, the generation of accurately radiometric calibrated GTC and RTC products was not trivial. The software applied had been originally developed for use with spaceborne sensors. Some inaccuracies in the backscatter data derived from E-SAR measurements could remain, leading to further inaccuracies in the later established statistical models for biomass estimation.

# 7. Conclusion

In this thesis, several approaches for estimating above ground biomass of heterogenous, temperate mixed forests with fully polarimetric airborne and spaceborne L-band SAR data were analyzed. The focus lay on approaches based on backscatter and PolInSAR data. In this section, the research questions stated in the introduction are answered.

1 *How sensitive are airborne and spaceborne fully polarimetric L-band SAR backscatter and Pauli decomposition data to biomass in heterogenous temperate mixed forests found in the Swiss north-eastern midlands?*

The backscatter at HV-polarization as well as the volume scattering term of the Pauli decomposition showed the highest sensitivity to biomass. Yet, it was shown that the sensitivity of the SAR backscatter data using a single polarization or Pauli decomposition term to biomass was limited to a very low biomass range below 50 t $ha^{-1}$ and was often not present at all. This reduces the applicability of backscatter based approaches for biomass estimation in the heterogenous, temperate forests found in the Swiss midlands, as the biomass levels are typically above 100 t $ha^{-1}$. The performance of backscatter-based biomass estimation was further limited by high noise levels in the data. This was successfully reduced by employing multiple polarizations in a regression analysis and by focusing on the stand level. It was found that a minimum stand size of 0.5 ha is needed to get more reliable biomass estimates from backscatter data.

While the backscatter information from the airborne E-SAR system showed some sensitivity to biomass, the spaceborne PALSAR PLR backscatter data proved nearly insensitive. This contradicts many findings in literature that report a high sensitivity to biomass of PALSAR backscatter data at HV-polarization up to 100 and 150 t $ha^{-1}$. The insensitivity of PALSAR PLR data to biomass found in this work is mainly accountable to the high noise level found at a resolution of 25 m. This noise could be reduced when resampling to 100 m resolution. Yet the number of low biomass pixels was reduced drastically by this resampling attempt. This is further evidence that the biomass levels in the two selected study sites are too high for accurate biomass estimation from L-band backscatter data.

2 *How do different SAR backscatter terrain normalization products impact on biomass estimation approaches?*

It was shown that the backscatter sensitivity to biomass increased when backscatter signals were corrected for topography-induced distortions. This shows the necessity of accurate radiometric normalizations when using backscatter data for forest structural studies, and gives the opportunity to move beyond the flat study sites often found in literature and focus also on more rugged terrain. The correction for orientation angle shifts due to azimuth slopes relative to the acquisition geometry proved not to be useful for the available L-band SAR data, as the derived Polarization Orientation Angle (POA) data over forested terrain was too noisy. Longer wavelengths are required to get useful POA estimates over forested terrain.

3 *Does the more complex approach of forest structure retrieval from PolInSAR measurements deliver more reliable biomass estimation in heterogenous temperate forests compared to backscatter based approaches?*

The limitation of backscatter based approaches due to saturation at already low biomass levels could be successfully overcome by inferring forest heights using PolInSAR methodologies. Yet the

estimation of forest heights at high resolution is very noisy. Only when analyzing stand level forest heights with a minimum size of 1 ha, could the errors in the height estimates be reduced to about 5 m. The retrieved PolInSAR forest heights could afterwards be related to stand level biomass, where a distinct increase in estimated forest height with increasing biomass could be observed. Yet, the errors in biomass estimation using such an approach are still too high, with relative RMSE of around 100% of the average biomass found in the analyzed stands. Also this PolInSAR based approach is highly influenced by topography which made estimation of forest height and biomass in more rugged terrain impossible. Methods to compensate for topography in interferometric measurements should therefore be investigated.

4 *How can LiDAR derived products improve biomass retrieval from SAR data?*

Due to the available high resolved ALS data also the effect of geocoding with a DTM or a DSM was contrasted. It was shown that sensitivity to biomass increased when geocoding with a DSM. This can be explained by the fact that the backscatter pixel is mapped closer to the actual scattering center. For L-band the scattering center of the HV-polarization is assumed to be somewhere between the middle and top of canopy. Yet a thorough investigation of where in the canopy the actual backscatter information comes from is still missing in the literature and should be part of future investigations.

In order to allow for accurate biomass estimation also in regions with high biomass levels mainly above 100-150 t $ha^{-1}$, alternative approaches are needed. P-band SAR backscatter data proved to be sensitive to biomass up to 200 t $ha^{-1}$ and could therefore be more appropriate for estimating biomass in high biomass regions. Yet, until now no spaceborne P-band SAR has been available. This will change with the forthcoming ESA BIOMASS mission, specifically designed for global biomass estimation using backscatter as well as PolInSAR and SAR tomography measurements (see Section 8). Also a multi-sensoral approach is highly recommended for accurate biomass estimations in regions with high biomass and significant topography. Especially synergies from LiDAR and SAR already proved highly effective (see Section 8.1) and should be further assessed to overcome the limitations of the SAR only approaches.

# 8. Outlook

This section should give an outlook to several promising biomass estimation approaches and upcoming satellite missions with a focus on forest monitoring and biomass quantification.

## 8.1. Some promising biomass estimation approaches

More and more promising approaches are being reported in the literature, that try to overcome the stated limitations of the approaches based on L-Band SAR data discussed in this thesis. Saatchi et al. (2007b) used multiple remote sensing products from different instruments (Normalized Difference Vegetation Index (NDVI) and Leaf Area Index (LAI) from the Moderate Resolution Imaging Spectroradiometer (MODIS), SAR backscatter data from the Japanese Earth Resources Satellite 1 (JERS-1) and data from the Shuttle Radar Topography Mission (SRTM) DEM to estimate above ground biomass in the Amazon basin using a decision-tree approach with an accuracy of over 80%. Santoro et al. (2011) estimated growing stock volume over large areas in boreal forests using hyper-temporal series of ENVISAT Advanced Synthetic Aperture Radar (ASAR) backscatter measurements without the estimation of prior *in-situ* measurements. Even though Santoro et al. (2011) employed even shorter wavelengths with the C-band ASAR instrument, the retrieved growing stock volume showed no saturation up to 300 $m^3$/ha. This sensitivity of C-band also at high biomass levels can be accounted to the combination and weighted averaging over multiple ASAR acquisitions with varying incident angles over the same area. The use of P-band backscatter data would also counteract the apparent limitation of backscatter saturation in high biomass regions. Yet also P-band saturates at biomass levels around 150 to 200 t $ha^{-1}$ and is therefore also not able to give reliable biomass estimates over the whole biomass range found in the two study sites discussed in this thesis. Indirect approaches using interferometric and polarimetric SAR data to retrieve forest heights can lead to biomass estimations without any apparent saturation. Yet, the methodology used in this thesis showed that also these PolInSAR approaches have obvious limitations and high noise levels and are therefore only applicable to large scale analysis.

Persson & Fransson (2014) proposed an approach that used a DSM extracted from TerraSAR-X stereo synthetic aperture radar images at X-band and a reference ALS DTM to calculate tree heights and biomass in boreal forests. Tree height estimation at the stand level showed a relative RMSE of just 9.4% and biomass estimation just 22.9%. Yet, also in that study, strong influences due to topography were reported where already 4 degrees in mean slope over a whole stand can significantly effect the DSM extraction. Promising results in forest height and stand structure extraction are reported from SAR-tomography (Tebaldini, 2010; Tebaldini & Rocca, 2012). With this approach, a real 3D image of the scene is obtained by creating an additional synthetic aperture in elevation, using a coherent combination of images acquired from multiple parallel flight tracks (Koch, 2010). This approach delivers highly resolved information about the three-dimensional forest structure, similar to the point cloud data derived from LiDAR measurements. Yet, until now mainly airborne tomography studies exist. This will change with the tomography mission phase of the upcoming BIOMASS mission (see Section 8.2) which will deliver spaceborne tomography measurements at P-band over selected study sites. Yet, the costs and time consumption as well as the small coverage of such tomography missions are a clear limitation of this technique.

## 8.2. New and future spaceborne missions for global biomass estimation

On the 24th of May 2014, the Advanced Land Observing Satellite-2 (ALOS-2) was successfully launched by JAXA on a H-IIA rocket from the Tanegashima Space Center (Japan Aerospace Exploration Agency (JAXA), 2014). ALOS-2 aimes to continue the successful land-observing mission carried out by ALOS. Compared to ALOS PALSAR, the L-band SAR instrument onboard ALOS-2 has the following improvements: higher resolution, lower Noise Equivalent Sigma Zero (NESZ), and higher signal to ambiguity ratio, as well as right- and left-looking capabilities. With a repeat-pass orbit of just 14 days, higher coherence needed for InSAR and PolInSAR studies (such as forest height inversions) will be achievable (Kankaku et al., 2009). The main mission aims of ALOS-2 are global land and disaster monitoring. The observation of global forest cover and deforestation is an important mission objective (Suzuki et al., 2009).

An ambitious satellite mission combining a L-band SAR with a LiDAR instrument was introduced with the mission proposal of the Deformation, Ecosystem Structure, and Dynamics of Ice (DESDynI) satellite by National Aeronautics and Space Administration (NASA). The focus of this mission would have been the measurement of forest height and structure, changes in carbon storage capabilities of vegetation, ice-shield deformation, as well as changes in Earth surface and volcanic magma flow (Freeman et al., 2009). Yet, although the launch of DESDynI was slated between 2010 and 2013, the outcome and actual launch of this satellite mission is still unclear. Due to the high cost of this ambitious mission and a budget cut ordered by the White House, NASA was told to come up with a more affordable approach to the mission (Turner, 2011). A recent idea was to launch only a radar instrument at L- and S-band, in a joint venture with the Indian Space Research Organisation (ISRO) (Thakur, 2014).

Tandem-L is a proposal for an interferometric and polarimetric SAR mission for global forest height and biomass inventories, large scale measurements of millimetric displacements due to tectonic shifts, and systematic observations of glacier movements. In this mission, two identical satellites would fly in close proximity to each other, allowing for single-pass interferometric measurements, reducing the limiting effects of temporal decorrelation on forest height estimation (Krieger et al., 2009).

A similar approach is pursued with the TanDEM-X (TerraSAR-X add-on for Digital Elevation Measurements) spaceborne radar interferometer that is based on two TerraSAR-X radar satellites flying in close formation. Launched on the 21st of June 2010, TanDEM-X delivers highly resolved elevation measurements of the Earth's surface in X-band (Krieger et al., 2007). Together with a highly resolved Digital Terrain Model (DTM), the TanDEM-X acquisitions can deliver highly accurate forest height estimates, allowing for biomass estimation on global scale.

ESA's highly anticipated forthcoming BIOMASS mission is going to be the first spaceborne P-band SAR instrument with launch planned in 2020. The BIOMASS satellite was chosen to be ESA's 7th Earth Explorer satellite as part of the Living Planet program in 2013 (ESA, 2013). The polarimetric P-band SAR mounted on BIOMASS will provide measurements of the full range of the world's above-ground biomass by combining backscatter as well as InSAR, PolInSAR and tomographic measurement techniques. Over the proposed five-year mission lifetime a unique archive of information about the world's forest and their dynamics will be built up (Le Toan et al., 2011).

The launch of the second generation of NASA's Ice, Cloud and Land Elevation Satellite (ICESat) is highly anticipated. Continuing the pioneering - though compromised - capabilities demonstrated by its predecessor, ICESat-2 will deliver precise, global laser surface height measurements. Although focused on the study of ice sheets and sea ice, the higher resolution of ICESat-2 compared to its predecessor will deliver new capabilities for large scale (1 km spatial resolution) vegetation height and biomass estimation (Abdalati et al., 2010). The launch of ICESat-2 is currently slated for launch in 2017 (NASA, 2014).

# Acknowledgment

I would like to thank a number of people for contributing to the success of my master's thesis. Thanks go out to various people at the RSL: Dr. David Small for the competent and dedicated supervision during the whole master's thesis. Dr. Felix Morsdorf for the assistance with the processing and analysis of the ALS datasets. Lukas Zuberbühler for the help in processing the E-SAR datasets. Dr. Adrian Schubert for the support in processing the ALOS PALSAR PLR data. Reik Leiterer for valuable inputs concerning ALS data processing. Furthermore I would like to thank the whole RSL staff, Christoph Rohner and Jonas Böhler for interesting inputs of any kind.

I would also like to thank several offices and departments: Armasuisse for providing E-SAR data flown by the German Aerospace Center (DLR ). The European Space Agency (ESA) for providing ALOS PALSAR data. The Swiss Federal Office for Topography swisstopo for providing the *DHM25* height model, the *Pixelkarte 25* dataset, and the SPOT mosaic. The Swiss Federal Statistical Office for providing the forest mixture dataset *Waldmischungsgrad 92*. The building department of Canton of Zurich for the field survey data and the Remote Sensing Laboratory for providing the ALS datasets.

Special thanks go out to Anja Kükenbrink, Fabian Schneider and Philipp Strahm for their great effort in proofreading the thesis and for their valuable inputs and suggestions. Furthermore I want to thank my family and Lona Meier for their patience and mental support during the whole thesis.

# 9. References

Abdalati, W., Zwally, H. J., Bindschadler, R., Csatho, B., Farrell, S. L., Fricker, H. A., Harding, D., Kwok, R., Lefsky, M., Markus, T., Marshak, A., Neumann, T., Palm, S., Schutz, B., Smith, B., Spinhirne, J., & Webb, C. (2010). The icesat-2 laser altimetry mission. *Proceedings of the IEEE*, *98*, 735–751. doi:10.1109/JPROC.2009.2034765.

Ackermann, N., Thiel, C., Borgeaud, M., & Schmullius, C. (2010). Potential of fusion of SAR and optical satellite imagery for biomass estimation in temperate forested areas. In *ESA Living Planet Symposium* (pp. 1–10). Bergen, Norway: ESA.

Albertz, J. (2007). Laserscanner. In *Einführung in die Fernerkundung* chapter 2.3.5. (pp. 53–55). Wissenschaftliche Buchgesellschaft, Darmstadt. (3rd ed.).

Askne, J., Santoro, M., Smith, G., & Fransson, J. (2003). Multitemporal repeat-pass SAR interferometry of boreal forests. *IEEE Transactions on Geoscience and Remote Sensing*, *41*, 1540–1550. doi:10.1109/TGRS.2003.813397.

Askne, J., Fransson, J., Santoro, M., Soja, M., & Ulander, L. (2013). Model-Based Biomass Estimation of a Hemi-Boreal Forest from Multitemporal TanDEM-X Acquisitions. *Remote Sensing*, *5*, 5574–5597. doi:10.3390/rs5115574.

Baker, J., & Luckman, A. (1999). Microwave observations of boreal forests in the NOPEX area of Sweden and a comparison with observations of a temperate plantation in the United Kingdom. *Agricultural and Forest Meteorology*, *98-99*, 389–416. doi:10.1016/S0168-1923(99)00111-2.

Balzter, H. (2001). Forest mapping and monitoring with interferometric synthetic aperture radar (InSAR). *Progress in Physical Geography*, *25*, 159–177. doi:10.1177/030913330102500201.

Balzter, H., Rowland, C., & Saich, P. (2007). Forest canopy height and carbon estimation at Monks Wood National Nature Reserve, UK, using dual-wavelength SAR interferometry. *Remote Sensing of Environment*, *108*, 224–239. doi:10.1016/j.rse.2006.11.014.

Bamler, R., & Hartl, P. (1998). Synthetic aperture radar interferometry. *Inverse Problems*, *14*, R1–R54. doi:10.1088/0266-5611/14/4/001.

Building Department Canton of Zurich (2009). *Aufnahmeanleitung Stichprobeninventur*. Technical Report Building Department Canton of Zurich.

Cartus, O., Santoro, M., Schmullius, C., & Li, Z. (2011). Large area forest stem volume mapping in the boreal zone using synergy of ERS-1/2 tandem coherence and MODIS vegetation continuous fields. *Remote Sensing of Environment*, *115*, 931–943. doi:10.1016/j.rse.2010.12.003.

Chen, E., Li, Z., Cloude, S., Papathanassiou, K. P., & Pottier, E. (2008). Comparison of Methods to derive Forest Height from Polarimetric SAR Interferometry. In *Proc Dragon I Programme Final Results 2004-2007* (pp. 1–8). Beijing, P.R. China.

Chowdhury, T., Thiel, C., Schmullius, C., & Stelmaszczuk-Górska, M. (2013). Polarimetric Parameters for Growing Stock Volume Estimation Using ALOS PALSAR L-Band Data over Siberian Forests. *Remote Sensing*, *5*, 5725–5756. doi:10.3390/rs5115725.

Clark, S. (2011). Japan ends land observing mission after satellite trouble. Available online at http://www.spaceflightnow.com/news/n1105/12alos/ last accessed: 15-Jun-2014, 12:00.

Cloude, S., & Pottier, E. (1996). A review of target decomposition theorems in radar polarimetry. *IEEE Transactions on Geoscience and Remote Sensing*, *34*, 498–518. doi:10.1109/36.485127.

Cloude, S., & Papathanassiou, K. (1997). Polarimetric optimisation in radar interferometry. *Electronics Letters*, *33*, 1176–1178. doi:10.1049/el:19970790.

Cloude, S., & Papathanassiou, K. (1998). Polarimetric SAR interferometry. *IEEE Transactions on Geoscience and Remote Sensing*, *36*, 1551–1565. doi:10.1109/36.718859.

Cloude, S., & Papathanassiou, K. (2003). Three-stage inversion process for polarimetric SAR interferometry. *IEEE Proceedings - Radar, Sonar and Navigation*, *150*, 125–134. doi:10.1049/ip-rsn:20030449.

Cloude, S. (2005). PoL-InSAR training course. Available online at https://earth.esa.int/polsarpro/Manuals/1_Pol-InSAR_Training_Course.pdf last accessed: 15-Feb-2014 09:45.

D'Errico, J. (2006). Polynomial model in 1 or n dimensions *polyfitn*. Available online at http://www.mathworks.com/matlabcentral/fileexchange/34765-polyfitn last accessed: 23-May-2014 22:30.

DLR (2000). E-SAR, The Airborne SAR System of DLR. Available online at http://www.dlr.de/hr/desktopdefault.aspx/tabid-2326/3776_read-5679/ last accessed: 11-Jun-2014 14:45.

Dobson, M., Ulaby, F. T., Le Toan, T., Beaudoin, A., Kasischke, E. S., & Christensen, N. (1992). Dependence of radar backscatter on coniferous forest biomass. *IEEE Transactions on Geoscience and Remote Sensing*, *30*, 412–415. doi:10.1109/36.134090.

ESA (2011). PolSARPro v4.2. Available online at http://earth.eo.esa.int/polsarpro/default.html last accessed: 15-Jun-2014 15:30.

ESA (2013). Future missions, earth explorers. Available online at http://www.esa.int/Our_Activities/Observing_the_Earth/The_Living_Planet_Programme/Earth_Explorers/Future_missions/About_future_missions last accessed: 15-Jun-2014 12:15.

FAO (2010). Global Forest Resources Assessment 2010 Main Report. *FAO Forestry Paper*, *163*, 378.

Ferretti, A., Monti-Guarnieri, A., & Prati, C. (2007). *InSAR Principles-Guidelines for SAR Interferometry Processing and Interpretation*. Noordwijk: ESA Publications, ESTEC.

Freeman, A., Rosen, P., Jordan, R., Johnson, W., Scott, H., Sweetser, T., Loverro, A., Smith, J., Sprague, G., & Shen, Y. (2009). DESDYNI - A NASA Mission for ecosystems, solid Earth, and cryosphere science. In *Proc. Pol-InSAR Workshop* (pp. 26–30). Frascati, Italy.

Garestier, F., Dubois-Fernandez, P., Guyon, D., & Le Toan, T. (2009). Forest Biophysical Parameter Estimation Using L- and P-Band Polarimetric SAR Data. *IEEE Transactions on Geoscience and Remote Sensing*, *47*, 3379–3388. doi:10.1109/TGRS.2009.2022947.

Ghasemi, N., Sahebi, M. R., & Mohammadzadeh, A. (2013). Biomass Estimation of a Temperate Deciduous Forest Using Wavelet Analysis. *IEEE Transactions on Geoscience and Remote Sensing*, *51*, 765–776. doi:10.1109/TGRS.2012.2205260.

Hagberg, J., Ulander, L., & Askne, J. (1995). Repeat-pass SAR interferometry over forested terrain. *IEEE Transactions on Geoscience and Remote Sensing*, *33*, 331–340. doi:10.1109/36.377933.

He, Q.-S., Cao, C.-X., Chen, E.-X., Sun, G.-Q., Ling, F.-L., Pang, Y., Zhang, H., Ni, W.-J., Xu, M., Li, Z.-Y., & Li, X.-W. (2012). Forest stand biomass estimation using ALOS PALSAR data based on LiDAR-derived prior knowledge in the Qilian Mountain, western China. *International Journal of Remote Sensing*, *33*, 710–729. doi:10.1080/01431161.2011.577829.

Hoffmann, C. (1982). Die Berechnung von Tarifen für die Waldinventur. *Forstwissenschaftliches Centralblatt*, *101*, 24–36.

Horn, R., Scheiber, R., & J., F. (2007). *E-SAR Image Data Description*. Technical Report DLR.

Hyyppä, J., Hyyppä, H., Yu, X., Kaartinen, H., Kukko, A., & Holopainen, M. (2009). Forest Inventory Using Small Footprint Airborne LiDAR. In J. Shan, & C. Toth (Eds.), *Forest Inventory Using Small Footprint Airborne Topographic Laser Ranging and Scanning Principles* chapter 12. (pp. 335–370). Boca Raton: CRC Press.

IPCC (2007). *Climate change 2007: The Physical Science Basis. Contribution of Working Group I to the Fourth Assessment Report of the Intergovernmental Panel on Climate Change*. Cambridge, United Kingdom and New York, NY, USA,: Cambridge University Press.

Japan Aerospace Exploration Agency (JAXA) (2014). Launch Result of H-IIA Launch Vehicle No. 24 with "DAICHI-2" (ALOS-2) onboard. Available online at http://global.jaxa.jp/press/2014/05/20140524_h2af24.html last accessed: 08-Jun-2014 23:15.

Kaartinen, H., Hyyppä, J., Yu, X., Vastaranta, M., Hyyppä, H., Kukko, A., Holopainen, M., Heipke, C., Hirschmugl, M., Morsdorf, F., Næ sset, E., Pitkänen, J., Popescu, S., Solberg, S., Wolf, B. M., & Wu, J.-C. (2012). An International Comparison of Individual Tree Detection and Extraction Using Airborne Laser Scanning. *Remote Sensing*, *4*, 950–974. doi:10.3390/rs4040950.

Kankaku, Y., Osawa, Y., Suzuki, S., & Watanabe, T. (2009). The overview of the L-band SAR onboard ALOS-2. In *Proceedings of Progress in Electromagnetics Research Symposium* (pp. 735–738). Moscow, Russia.

Kasischke, E., Christensen, N., & Bourgeau-Chavez, L. (1995). Correlating radar backscatter with components of biomass in loblolly pine forests. *IEEE Transactions on Geoscience and Remote Sensing*, *33*, 643–659. doi:10.1109/36.387580.

Kaufmann, E. (2001). Estimation of Standing Timber, Growth and Cut. In P. Brassel, & H. Lischke (Eds.), *Swiss national forest inventory: methods and models of the second assessment* chapter 3.2. (pp. 162–196). Birmensdorf: WSL Swiss Federal Research Institute.

Kellndorfer, J., Walker, W., Pierce, L., Dobson, C., Fites, J. A., Hunsaker, C., Vona, J., & Clutter, M. (2004). Vegetation height estimation from Shuttle Radar Topography Mission and National Elevation Datasets. *Remote Sensing of Environment*, *93*, 339–358. doi:10.1016/j.rse.2004.07.017.

Koch, B. (2010). Status and future of laser scanning, synthetic aperture radar and hyperspectral remote sensing data for forest biomass assessment. *ISPRS Journal of Photogrammetry and Remote Sensing*, *65*, 581–590. doi:10.1016/j.isprsjprs.2010.09.001.

Krieger, G., Moreira, A., Fiedler, H., Hajnsek, I., Werner, M., Younis, M., & Zink, M. (2007). TanDEM-X: A Satellite Formation for High-Resolution SAR Interferometry. *IEEE Transactions on Geoscience and Remote Sensing*, *45*, 3317–3341. doi:10.1109/TGRS.2007.900693.

Krieger, G., Hajnsek, I., Papathanassiou, K., Eineder, M., Younis, M., De Zan, F., Prats, P., Huber, S., Werner, M., Fiedler, H., Freeman, A., Rosen, P., Hensley, S., Johnson, W., Veilleux, L., Grafmueller, B., Werninghaus, R., Bamler, R., & Moreira, A. (2009). The tandem-L mission proposal: Monitoring earth's dynamics with high resolution SAR interferometry. In *IEEE Radar Conference* (pp. 1–6). Pasadena, California: IEEE. doi:10.1109/RADAR.2009.4977077.

Le Toan, T., Beaudoin, A., Riom, J., & Guyon, D. (1992). Relating forest biomass to SAR data. *IEEE Transactions on Geoscience and Remote Sensing*, *30*, 403–411. doi:10.1109/36.134089.

Le Toan, T., Quegan, S., Davidson, M. W. J., Balzter, H., Paillou, P., Papathanassiou, K. P., Plummer, S., Rocca, F., Saatchi, S. S., Shugart, H., & Ulander, L. M. H. (2011). The BIOMASS mission: Mapping global forest biomass to better understand the terrestrial carbon cycle. *Remote Sensing of Environment*, *115*, 2850–2860. doi:10.1016/j.rse.2011.03.020.

Lee, J.-S., Schuler, D., & Ainsworth, T. (2000). Polarimetric SAR data compensation for terrain azimuth slope variation. *IEEE Transactions on Geoscience and Remote Sensing*, *38*, 2153–2163. doi:10.1109/36.868874.

Lee, J.-S., Schuler, D., Ainsworth, T., Krogager, E., Kasilingam, D., & Boerner, W.-M. (2002). On the estimation of radar polarization orientation shifts induced by terrain slopes. *IEEE Transactions on Geoscience and Remote Sensing*, *40*, 30–41. doi:10.1109/36.981347.

Lee, J.-S., & Ainsworth, T. L. (2011). The Effect of Orientation Angle Compensation on Coherency Matrix and Polarimetric Target Decompositions. *IEEE Transactions on Geoscience and Remote Sensing*, *49*, 53–64. doi:10.1109/TGRS.2010.2048333.

Lee, S.-k., Kugler, F., Hajnsek, I., & Papathanassiou, K. P. (2009). The impact of temporal decorrelation over forest terrain in polarimetric SAR interferometry. In *Proceedings of the International Workshop on Applications of Polarimetry and Polarimetric Interferometry (Pol-InSAR)* (pp. 1–6). Frascati, Italy.

Lefsky, M. A., Harding, D., Cohen, W., Parker, G., & Shugart, H. (1999). Surface Lidar Remote Sensing of Basal Area and Biomass in Deciduous Forests of Eastern Maryland, USA. *Remote Sensing of Environment*, *67*, 83–98. doi:10.1016/S0034-4257(98)00071-6.

Lefsky, M. A., & Cohen, W. (2002). Lidar remote sensing of above-ground biomass in three biomes. *Global Ecology and Biogeography*, *11*, 393–399. doi:10.1046/j.1466-822x.2002.00303.x.

Li, Z., & Guo, M. (2012). A new three-stage inversion procedure of forest height with the Improved Temporal Decorrelation RVoG model. *2012 IEEE International Geoscience and Remote Sensing Symposium*, *2*, 5141–5144. doi:10.1109/IGARSS.2012.6352453.

Lim, K., Treitz, P., Baldwin, K., Morrison, I., & Green, J. (2003). Lidar remote sensing of biophysical properties of tolerant northern hardwood forests. *Canadian Journal of Remote Sensing*, *29*, 658–678. doi:10.5589/m03-025.

Lim, K. S., & Treitz, P. M. (2004). Estimation of above ground forest biomass from airborne discrete return laser scanner data using canopy-based quantile estimators. *Scandinavian Journal of Forest Research*, *19*, 558–570. doi:10.1080/02827580410019490.

Means, J., Acker, S., & Harding, D. (1999). Use of large-footprint scanning airborne lidar to estimate forest stand characteristics in the Western Cascades of Oregon. *Remote Sensing of Environment*, *67*, 298–308. doi:10.1016/S0034-4257(98)00091-1.

MeteoSwiss (2010). CLIMAP. Available online at http://www.meteoschweiz.admin.ch/web/en/services/data_portal/climap-net.html last accessed: 11-Jun-2014 14:45.

MeteoSwiss (2014a). *Normwerte 1981-2010: Lufttemperatur 2m*. Technical Report Federal Office of Meteorology and Climatology MeteoSwiss Zürich. Available online at http://www.meteoschweiz.admin.ch/files/kd/normwerte/norm8110/nvrep_tre200mo_de.pdf last accessed: 20-Jan-2014 15:30.

MeteoSwiss (2014b). *Normwerte 1981-2010: Niederschlagssumme*. Technical Report Federal Office of Meteorology and Climatology MeteoSwiss Zürich. Available online at http://www.meteoschweiz.admin.ch/files/kd/normwerte/norm8110/nvrep_rre150mo_de.pdf last accessed: 20-Jan-2014 15:30.

Mette, T., & Papathanassiou, K. (2004). Applying a common allometric equation to convert forest height from Pol-InSAR data to forest biomass. In *International Geoscience and Remote Sensing Symposium IGARSS* (pp. 269–272). Anchorage, Alaska: IEEE.

Mette, T., Papathanassiou, K., & Hajnsek, I. (2004). Biomass estimation from polarimetric SAR interferometry over heterogeneous forest terrain. In *International Geoscience and Remote Sensing Symposium IGARSS* (pp. 511–514). Anchorage, Alaska: IEEE. doi:10.1109/IGARSS.2004.1369076.

Mitchard, E. T. A., Saatchi, S. S., Woodhouse, I. H., Nangendo, G., Ribeiro, N. S., Williams, M., Ryan, C. M., Lewis, S. L., Feldpausch, T., & Meir, P. (2009). Using satellite radar backscatter to predict above-ground woody biomass: A consistent relationship across four different African landscapes. *Geophysical Research Letters*, *36*, 1–6. doi:10.1029/2009GL040692.

Mitchard, E. T. A., Saatchi, S. S., Lewis, S. L., Feldpausch, T., Woodhouse, I. H., Sonké, B., Rowland, C., & Meir, P. (2011). Measuring biomass changes due to woody encroachment and deforesta-

tion/degradation in a forest-savanna boundary region of central Africa using multi-temporal L-band radar backscatter. *Remote Sensing of Environment*, *115*, 2861–2873. doi:10.1016/j.rse.2010.02.022.

Moisy, F. (2014). *ezyfit* a free curve fitting toolbox for matlab. Available online at http://www.fast.u-psud.fr/ezyfit/ last accessed: 23-May-2014 08:15.

Morsdorf, F., Meier, E., Kötz, B., Itten, K. I., Dobbertin, M., & Allgöwer, B. (2004). LIDAR-based geometric reconstruction of boreal type forest stands at single tree level for forest and wildland fire management. *Remote Sensing of Environment*, *92*, 353–362. doi:10.1016/j.rse.2004.05.013.

Naesset, E. (2002). Predicting forest stand characteristics with airborne scanning laser using a practical two-stage procedure and field data. *Remote Sensing of Environment*, *80*, 88–99. doi:10.1016/S0034-4257(01)00290-5.

NASA (2014). Icesat-2: Mission overview. Available online at http://icesat.gsfc.nasa.gov/icesat2/mission_overview.php last accessed: 22-Jun-2014 11:00.

Nelson, R., Krabill, W., & Tonelli, J. (1988). Estimating forest biomass and volume using airborne laser data. *Remote Sensing of Environment*, *24*, 247–267. doi:10.1016/0034-4257(88)90028-4.

Papathanassiou, K., & Cloude, S. (2001). Single-baseline polarimetric SAR interferometry. *IEEE Transactions on Geoscience and Remote Sensing*, *39*, 2352–2363. doi:10.1109/36.964971.

Papathanassiou, K., & Cloude, S. (2003). The effect of temporal decorrelation on the inversion of forest parameters from PoI-InSAR data. In *International Geoscience and Remote Sensing Symposium IGARSS* (pp. 1429–1431). volume 3.

Penman, J., Gytarsky, M., Hiraishi, T., Krug, T., Kruger, D., Pipatti, R., Buendia, L., Miwa, K., & Ngara, T. (2000). Intergovernmental Panel on Climate Change Good Practice Guidance for Land Use , Land-Use Change and Forestry. In J. Penman, M. Gytarsky, T. Hiraishi, T. Krug, D. Kruger, R. Pipatti, L. Buendia, K. Miwa, & T. Ngara (Eds.), *IPCC Good Practice Guidance for LULUCF* chapter Annex 3A.1. (pp. 151–186). Kamiyamaguchi Hayama, Kanagawa, Japan: Institute for Global Environmental Strageties (IGES) for the IPCC.

Peregon, A., & Yamagata, Y. (2013). The use of ALOS/PALSAR backscatter to estimate above-ground forest biomass: A case study in Western Siberia. *Remote Sensing of Environment*, *137*, 139–146. doi:10.1016/j.rse.2013.06.012.

Persson, A., Holmgren, J., & Söderman, U. (2002). Detecting and measuring individual trees using an airborne laser scanner. *Photogrammetric engineering and remote sensing*, *68*, 925–932.

Persson, H., & Fransson, J. (2014). Forest Variable Estimation Using Radargrammetric Processing of TerraSAR-X Images in Boreal Forests. *Remote Sensing*, *6*, 2084–2107. doi:10.3390/rs6032084.

Pitkänen, J., & Maltamo, M. (2004). Adaptive Methods for Individual Tree Detection on Airborne Laser Based Canopy Height Model. *International Archives of Photogrammetry, Remote Sensing and Spatial Information Sciences*, *36*, 187–191.

Popescu, S. C., Wynne, R. H., & Nelson, R. F. (2003). Measuring individual tree crown diameter with lidar and assessing its influence on estimating forest volume and biomass. *Canadian Journal of Remote Sensing*, *29*, 564–577. doi:10.5589/m03-027.

Popescu, S. C. (2007). Estimating biomass of individual pine trees using airborne lidar. *Biomass and Bioenergy*, *31*, 646–655. doi:10.1016/j.biombioe.2007.06.022.

Pyysalo, U., & Hyyppä, H. (2002). Reconstructing tree crowns from laser scanner data for feature extraction. *International Archives of Photogrammetry, Remote Sensing and Spatial Information Sciences*, *34*, 218–221.

Rahman, M. M., & Tetuko Sri Sumantyo, J. (2013). Retrieval of tropical forest biomass information from ALOS PALSAR data. *Geocarto International*, *28*, 382–403. doi:10.1080/10106049.2012.710652.

Raney, R., & Freeman, T. (1994). A Plea for Radar Brightness. In *Proc. IGARSS 1994* (pp. 1090–1092). Pasadena, CA, USA.

Rosenqvist, A., Shimada, M., Ito, N., & Watanabe, M. (2007). ALOS PALSAR: A Pathfinder Mission for Global-Scale Monitoring of the Environment. *IEEE Transactions on Geoscience and Remote Sensing*, *45*, 3307–3316. doi:10.1109/TGRS.2007.901027.

Rosenqvist, A. k., Milne, A., Lucas, R., Imhoff, M., & Dobson, C. (2003). A review of remote sensing technology in support of the Kyoto Protocol. *Environmental Science & Policy*, *6*, 441–455. doi:10.1016/S1462-9011(03)00070-4.

Saatchi, S., & Moghaddam, M. (2000). Estimation of crown and stem water content and biomass of boreal forest using polarimetric SAR imagery. *IEEE Transactions on Geoscience and Remote Sensing*, *38*, 697–709. doi:10.1109/36.841999.

Saatchi, S., Halligan, K., Despain, D. G., & Crabtree, R. L. (2007a). Estimation of Forest Fuel Load From Radar Remote Sensing. *IEEE Transactions on Geoscience and Remote Sensing*, *45*, 1726–1740. doi:10.1109/TGRS.2006.887002.

Saatchi, S. S., Houghton, R. A., Dos Santos Alvalá, R. C., Soares, J. V., & Yu, Y. (2007b). Distribution of aboveground live biomass in the Amazon basin. *Global Change Biology*, *13*, 816–837. doi:10.1111/j.1365-2486.2007.01323.x.

Saatchi, S. S., Marlier, M., Chazdon, R. L., Clark, D. B., & Russell, A. E. (2011). Impact of spatial variability of tropical forest structure on radar estimation of aboveground biomass. *Remote Sensing of Environment*, *115*, 2836–2849. doi:10.1016/j.rse.2010.07.015.

Sandberg, G., Ulander, L. M. H., Fransson, J., Holmgren, J., & Le Toan, T. (2011). L- and P-band backscatter intensity for biomass retrieval in hemiboreal forest. *Remote Sensing of Environment*, *115*, 2874–2886. doi:10.1016/j.rse.2010.03.018.

Santoro, M., Beer, C., Cartus, O., Schmullius, C., Shvidenko, A., McCallum, I., Wegmüller, U., & Wiesmann, A. (2011). Retrieval of growing stock volume in boreal forest using hyper-temporal series of Envisat ASAR ScanSAR backscatter measurements. *Remote Sensing of Environment*, *115*, 490–507. doi:10.1016/j.rse.2010.09.018.

Schubert, A., & Small, D. (2012). *PALSAR Instrument Processing Facility : Geometric and Radiometric Verification*. Technical Report Remote Sensing Laboratories, University of Zurich.

Schuler, D. L., Lee, J.-S., Ainsworth, T. L., & Grunes, M. R. (2000). Terrain topography measurement using multipass polarimetric synthetic aperture radar data. *Radio Science*, *35*, 813–832. doi:10.1029/1999RS002266.

Shimada, M., Isoguchi, O., Tadono, T., & Isono, K. (2009). PALSAR Radiometric and Geometric Calibration. *IEEE Transactions on Geoscience and Remote Sensing*, *47*, 3915–3932. doi:10.1109/TGRS.2009.2023909.

Shimada, M., & Ohtaki, T. (2010). Generating Large-Scale High-Quality SAR Mosaic Datasets: Application to PALSAR Data for Global Monitoring. *IEEE Journal of Selected Topics in Applied Earth Observations and Remote Sensing*, *3*, 637–656. doi:10.1109/JSTARS.2010.2077619.

Small, D., Jehle, M., Meier, E., & Nüesch, D. (2004). Radiometric terrain correction incorporating local antenna gain. In *Proc. of EUSAR* (pp. 929–923). Ulm, Germany.

Small, D., Jehle, M., Schubert, A., & Meier, E. (2008). Accurate geometric correction for normalisation of PALSAR radiometry. In *Proc. ALOS 2008 Symposium* (pp. 1–7). Rhodes, Greece.

Small, D., Miranda, N., & Meier, E. (2009). A revised radiometric normalisation standard for SAR. In *2009 IEEE International Geoscience and Remote Sensing Symposium* (pp. 566–569). doi:10.1109/IGARSS.2009.5417439.

Small, D. (2011). Flattening Gamma: Radiometric Terrain Correction for SAR Imagery. *IEEE Transactions on Geoscience and Remote Sensing*, *49*, 3081–3093. doi:10.1109/TGRS.2011.2120616.

Suzuki, S., Osawa, Y., Hatooka, Y., Kankaku, Y., & Watanabe, T. (2009). Overview of Japan's Advanced Land Observing Satellite-2 Mission. In R. Meynart, S. P. Neeck, & H. Shimoda (Eds.), *SPIE* (pp. 1–10). Berlin, Germany. doi:10.1117/12.831340.

Swiss Federal Statistical Office (2004). *Waldmischungsgrad der Schweiz*. Technical Report Swiss Federal Statistical Office.

Swisstopo (2005). *DHM25 Das digitale Höhenmodell der Schweiz*. Technical Report Swiss Federal Office of Topography swisstopo. Available online at http://www.swisstopo.admin.ch/internet/swisstopo/de/home/products/height/dhm25.html last accessed: 11-Jun-2014 11:45.

Swisstopo (2006). Spot Mosaic. Available online at http://www.swisstopo.admin.ch/internet/swisstopo/de/home/products/images/ortho/spot.html last accessed: 11-Jun-2014 15:45.

Swisstopo (2007). Die Laser Höhenmodelle DTM-AV und DOM. *geodata-news*, (pp. 1–4). Swiss Federal Office of Topography swisstopo.

Swisstopo (2012). *Pixelkarte 25*. Technical Report Swiss Federal Office of Topography swisstopo. Available online at http://www.swisstopo.admin.ch/internet/swisstopo/de/home/products/maps/national/digital.html last accessed: 15-Jun-2014 14:00.

Tebaldini, S. (2010). Single and Multipolarimetric SAR Tomography of Forested Areas: A Parametric Approach. *IEEE Transactions on Geoscience and Remote Sensing*, *48*, 2375–2387. doi:10.1109/TGRS.2009.2037748.

Tebaldini, S., & Rocca, F. (2012). Multibaseline Polarimetric SAR Tomography of a Boreal Forest at P- and L-Bands. *IEEE Transactions on Geoscience and Remote Sensing*, *50*, 232–246. doi:10.1109/TGRS.2011.2159614.

Thakur, K. V. (2014). Nasa-isro synthetic aperture radar radar satellite (ni-sar). Available online at http://isp.justthe80.com/space-applications/cartography-mapping-surveillance-satellites/nasa-isro-radar-satellite last accessed: 21-Jun-2014 13:40.

Thiel, C., Thiel, C., & Schmullius, C. (2009). Operational Large-Area Forest Monitoring in Siberia Using ALOS PALSAR Summer Intensities and Winter Coherence. *IEEE Transactions on Geoscience and Remote Sensing*, *47*, 3993–4000. doi:10.1109/TGRS.2009.2021469.

Thürig, E., & Schmid, S. (2008). Jährliche CO 2 -Flüsse im Wald: Berechnungsmethode für das Treibhausgasinventar | Annual CO 2 fluxes in forests: calculation method for the Greenhouse Gas Inventory. *Schweizerische Zeitschrift fur Forstwesen*, *159*, 31–38. doi:10.3188/szf.2008.0031.

TopoSys (2003). *TopoSys Porjekt-Bericht ALS Befliegung Hinwil leaf-off*. Technical Report TopoSys.

TopoSys (2010a). *Projekt-Bericht Uni Zürich, Auftragsnummer A09-20*. Technical Report TopoSys.

TopoSys (2010b). *Projekt-Bericht Uni Zürich Lägeren, Auftragsnummer A10-070*. Technical Report TopoSys.

Treuhaft, R. N., Madsen, S. r. N., Moghaddam, M., & van Zyl, J. J. (1996). Vegetation characteristics and underlying topography from interferometric radar. *Radio Science*, *31*, 1449–1485. doi:10.1029/96RS01763.

Treuhaft, R. N., & Siqueira, P. R. (2000). Vertical structure of vegetated land surfaces from interferometric and polarimetric radar. *Radio Science*, *35*, 141–177. doi:10.1029/1999RS900108.

Turner, B. (2011). NASA Cuts 2 Earth Science Missions on White House Orders. Available online at http://www.space.com/11050-white-house-nasa-earth-science-cuts.html last accessed 10-06-2014 20:30.

Ulaby, F., Moore, R., & A.K., F. (1982). *Microwave Remote Sensing: Active and Passive, Volume II: Radar Remote Sensing and Surface Scattering and Emission Theory*. Norwood, MA, USA: Artech House.

Woodhouse, I. (2006a). Predicting backscatter-biomass and height-biomass trends using a macroecology model. *IEEE Transactions on Geoscience and Remote Sensing*, *44*, 871–877. doi:10.1109/TGRS.2006.872356.

Woodhouse, I. H. (2006b). *Introduction to Microwave Remote Sensing*. Boca Raton, FL, USA: Taylor & Francis Group.

Yamaguchi, Y., Moriyama, T., Ishido, M., & Yamada, H. (2005). Four-component scattering model for polarimetric SAR image decomposition. *IEEE Transactions on Geoscience and Remote Sensing*, *43*, 1699–1706. doi:10.1109/TGRS.2005.852084.

Zebker, H., & Villasenor, J. (1992). Decorrelation in interferometric radar echoes. *IEEE Transactions on Geoscience and Remote Sensing*, *30*, 950–959. doi:10.1109/36.175330.

Zhou, Y., Hong, W., Cao, F., Wang, Y.-p., & Wu, Y.-r. (2008). Analysis of Temporal Decorrelation in Dual-Baseline PolInSAR Vegetation Parameter Estimation. In *Proceedings of IGARSS 2008* (pp. 473–476). Boston, USA.

Zuberbühler, L. D. (2012). Radar-Polarimetrie (PolSAR) Part 2 (Presentation).

Zuberbühler, L. D. (2014). *Einflüsse der Waldstruktur auf die Messparameter voll polarimetrischer abbildender Radarsysteme*. Ph.D. thesis University of Zurich.

# A. ALOS PALSAR specifications

**Table A.1:** ALOS PALSAR Instrument Characteristics (after Rosenqvist et al., 2007).

| | |
|---|---|
| Antenna size | 8.9 m x 3.1 m |
| Center frequency | 1270 MHz /23.6 cm |
| Chirp band width | 28 MHz (FBS, ScanSAR long burst)<br>14 MHz (FBD, POL, ScanSAR short burst) |
| Transmission peak power | 2 kW |
| Pulse Repetition Frequency | 1500 - 2500 Hz (discrete stepping |
| Image modes | |
| Fine beam mode (FBS, FBD) | Single polarization (HH or VV)<br>Dual polarization (HH/HV or VV/VH) |
| Polarimetric mode (POL) | Quad-pol. (HH,HV,VH,VV) |
| ScanSAR mode | Single polarization (HH or VV)<br>No. sub-beam: 3, 4 or 5<br>Short (14 MHz) or long (28 MHz) burst |
| Direct Transmission mode (DT) | FB single pol (14 MHz)<br>ScanSAR (14 MHz) |
| Bit quantisation | 5 bits |
| Swath width | 70 km (FBS, FBD @ 34.3°)<br>30 km (POL @ 21.5°)<br>360 km (ScanSAR 5-beam) |
| Off-nadir angle | Variable: FBS/FBD: 9.9° - 50.8°<br>POL: 9.7°-26.2°<br>Fixed: ScanSAR: 20.1° - 36.5° (beam 1-5) |
| Look direction | Right |
| Ground resolution | 10 m x 10 m (FBS @ 34.3°) |
| Rg (1 look) x Az (2 looks) | 20 m x 10 m (FBD @ 34.3°)<br>31 m x 10 m (POL @ 21.5°)<br>71-157 m (4 look) x 100 m<br>(2 look) (ScanSAR 5-beam) |
| Yaw steering | near-zero Doppler |

**Table A.2:** Frame listing of ALOS PALSAR data in fully polarimetric mode (PLR) at two off-nadir angle (21.5° and 23.1°). If interferometric processing is possible, the corresponding baseline (perpendicular) for the two frames are listed (only combination with temporal baselines of 46 days are considered).

| PLR215 | | | | |
|---|---|---|---|---|
| Track | Frame | Acquisition Date | Baseline [m] | Contained Study Sites |
| T638 | F930 | 5. April 2009 | | |
| | F940 | 5. April 2009 | | |
| | | 16. November 2007 | | |
| | F950 | 5. April 2009 | | |
| T639 | F930 | 17. April 2007 | | Hinwil, Eschenberg (partial) |
| | F940 | 15. Octobre 2006 | 408,274 | Hinwil, Eschenberg (partial) |
| | | 30. November 2006 | | Hinwil, Eschenberg (partial) |
| | | 17. April 2007 | 480.517 | Hinwil, Eschenberg (partial) |
| | | 2. June 2007 | | Hinwil, Eschenberg (partial) |
| | | 3. December 2007 | | Hinwil, Eschenberg (partial) |
| | F950 | 15. October 2006 | 410.695 | Eschenberg (partial) |
| | | 30. November 2006 | | Eschenberg (partial) |
| | | 17. April 2007 | | Eschenberg (partial) |
| T640 | F930 | 24. March 2009 | | |
| | F940 | 24. March 2009 | | Lägern |
| | F950 | 24. March 2009 | | Lägern |
| PLR231 | | | | |
| Track | Frame | Acquisition Date | Baseline [m] | Contained Study Sites |
| T639 | F930 | 7. June 2009 | | |
| | F940 | 7. June 2009 | | |
| | F950 | 7. June 2009 | | |
| T640 | F930 | 9. May 2009 | | |
| | F940 | 9. May 2009 | | Hinwil, Eschenberg |
| | F950 | 9. May 2009 | | Eschenberg |

# B. Field survey data information

**Table B.1:** Parameters stored in the KSP dataset that were used for analyzation purposes in this thesis.

Parameters describing each KSP sample plot

| Parameter | Further Description | Example |
|---|---|---|
| Sample plot number | Identification of the plot | 702426 |
| Easting coordinate of plot center [m] | Swiss LV03 Coordinates | 703200 |
| Northing coordinate of plot center [m] | Swiss LV03 Coordiantes | 238250 |
| Survey date | in DDMMYY format | 251108 |
| Forest Mixing Factor | 1 = pure coniferous forest<br>(91 - 100 % coniferous trees)<br>2 = mixed coniferous forest<br>(51 - 90 % coniferous trees)<br>3 = mixed deciduous forest<br>(11 - 50 % coniferous trees)<br>4 = pure deciduous forest<br>(0 - 10 % coniferous trees) | 1 |

Parameters describing each tree in a KSP sample plot

| Parameter | Further Description | Example |
|---|---|---|
| Sample plot number | Key for assignment of tree to corresponding plot | 702426 |
| Azimuth angle [gon] | Angle between tree and plot center | 88 |
| Radius [m] | Distance to plot center | 5.55 |
| Tree species | Character code for tree species | TA = fir |
| Diameter at breast height (DBH) [cm] | Diameter at 1.3 meters above ground | 17 |

# C. Additional plots to polarimetric decomposition approach for E-SAR data

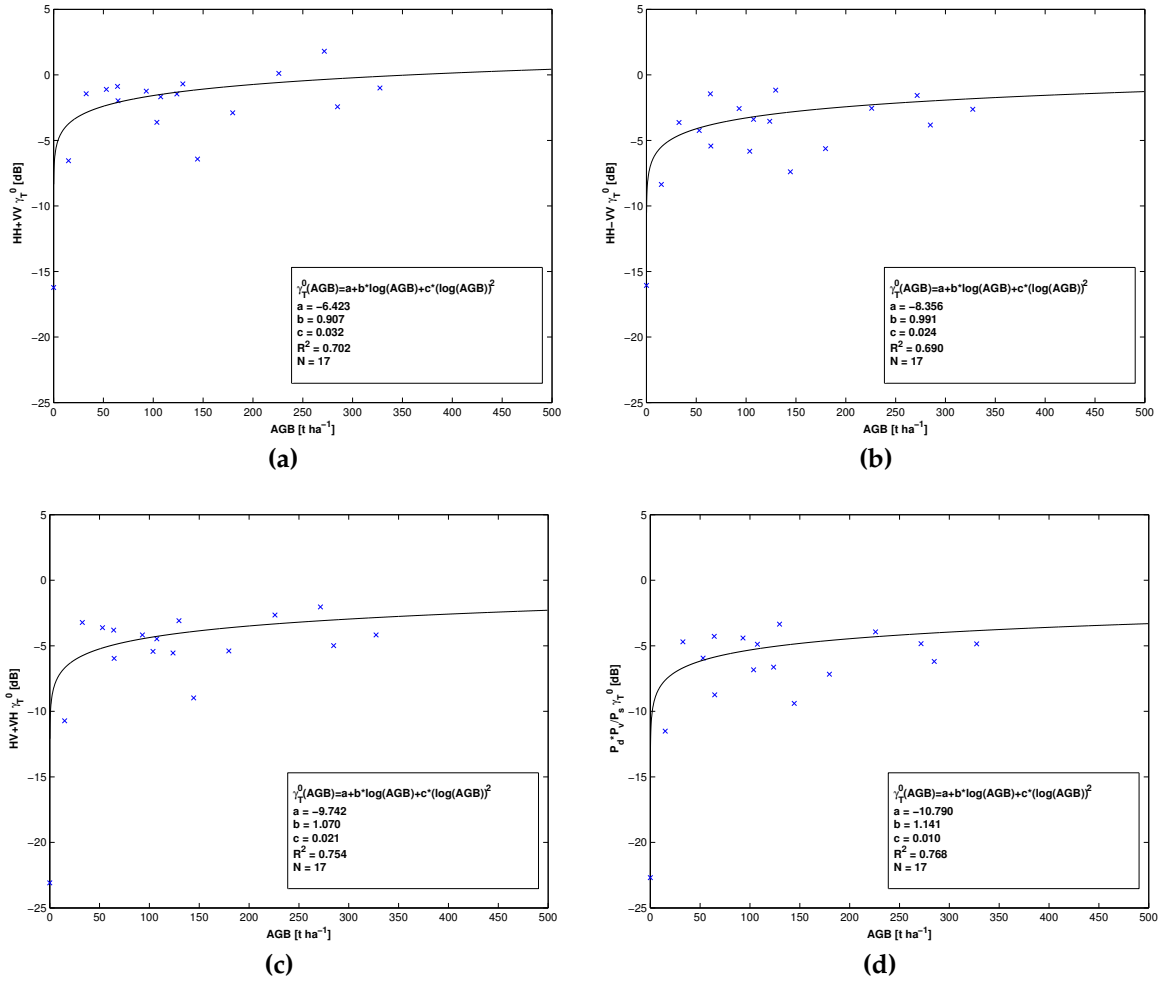


**Figure C.1:** Model validation for the Pauli decomposetion approach using E-SAR derived DSM geocoded $\gamma_T^0$ Pauli scattering powers. (a) Model validation for 1st Pauli base (HH+VV), (b) Model validation for 2nd Pauli base (HH-VV), (c) Model validation for third Pauli base (HV+VH), and (c) Model validation for Pauli ratio $P_d * P_v / P_s$.

# D. ALOS PALSAR backscatter sensitivity to biomass additional plots

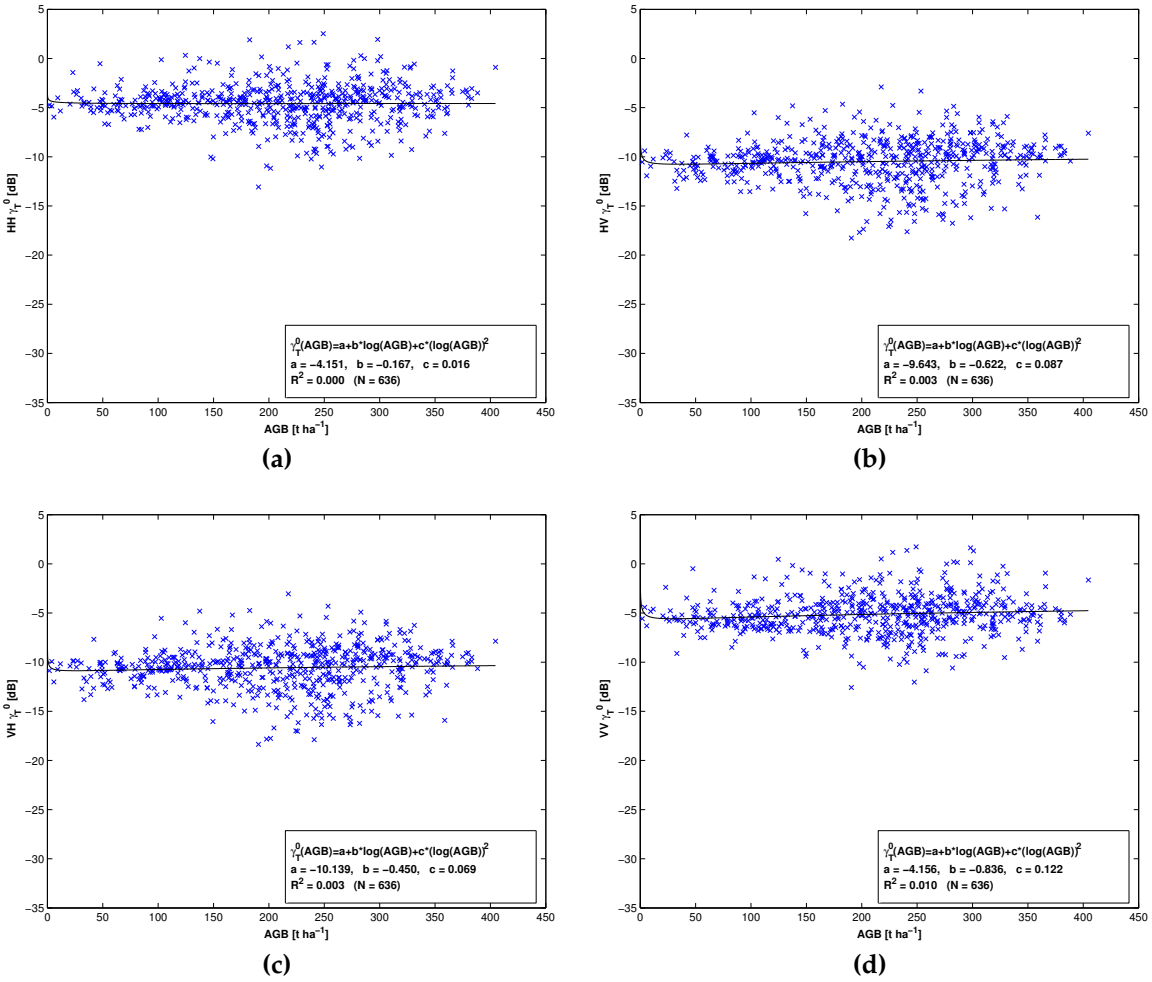


**Figure D.1:** Backscatter sensitivity to AGB of the radiometrically normalized $\gamma_T^0$ backscatter channels at HH-, HV-, VH-, and VV-polarization over Hinwil. PLR frame was acquired at an off-nadir angle of 23.1° and the image was taken on the 9th of May 2009. (a) HH, (b) HV, (c) VH, (d) VV.

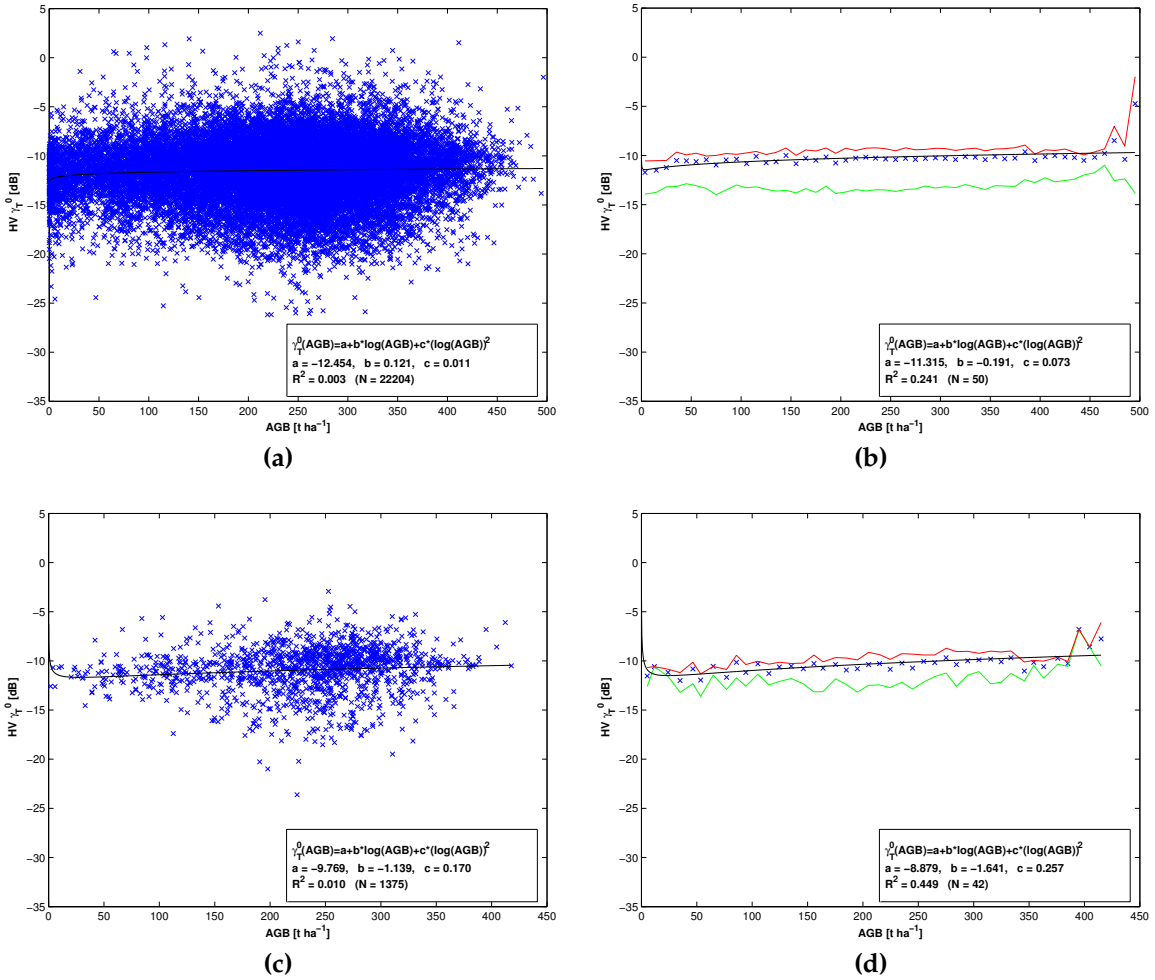


**Figure D.2:** PLR215 RTC backscatter at HV-polarization acquired at the 15th of October 2006 over Hinwil against biomass at 25m resolution (top row) and at 100 m resolution (bottom row). Right column: averaged backscatter in 10 t ha$^{-1}$ bins with outlined 75th (red line) and 25th percentile (green line).

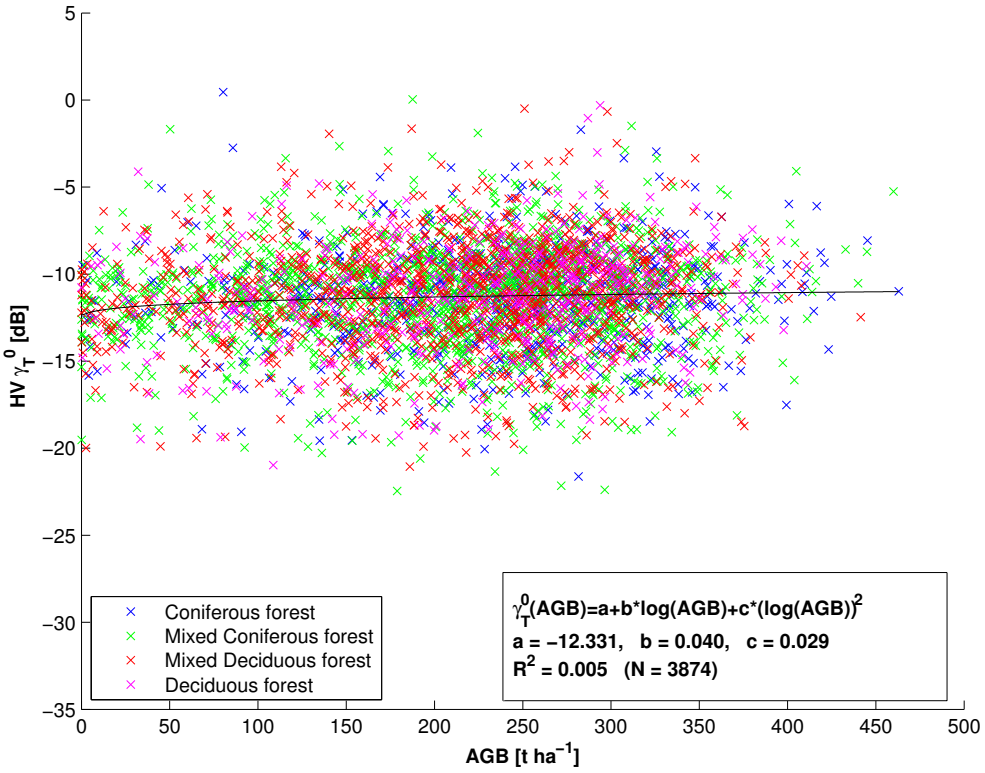


**Figure D.3:** PLR215 RTC backscatter at HV-polarization vs. AGB at stand-level over the Hinwil study site. SAR image was acquired on the 15th of October 2006.

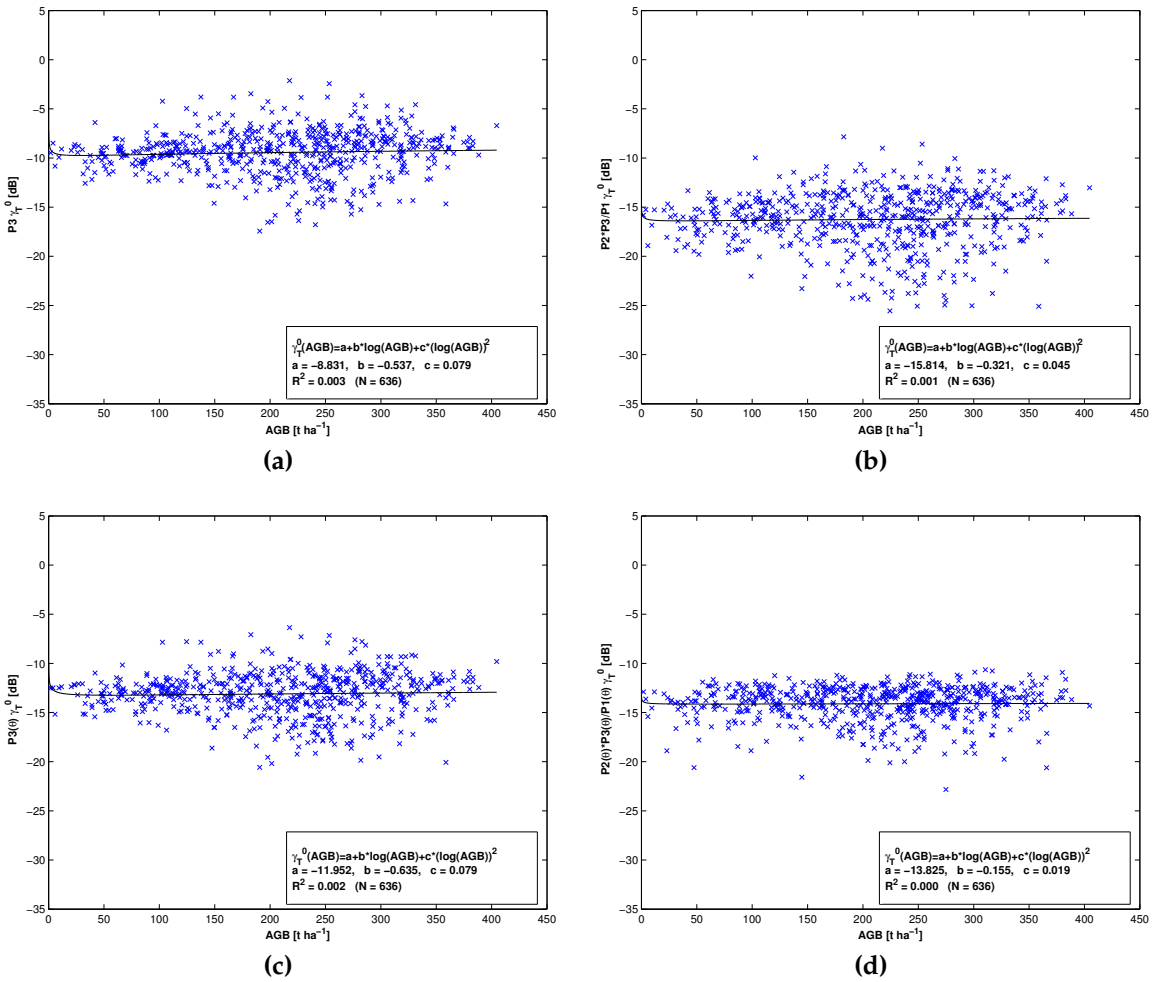


**Figure D.4:** Volume scattering and Pauli ratio ($\frac{(HH-VV)*(HV+VH)}{(HH+VV)}$) radiometrically normalized vs. biomass at 100 m resolution over Hinwil study site. (a) Volume scattering, (b) Pauli ratio, (c) rotated volume scattering, (d) rotated Pauli ratio. Data taken from frame PLR231-T640F940, image acquisition on the 9th of May 2009.

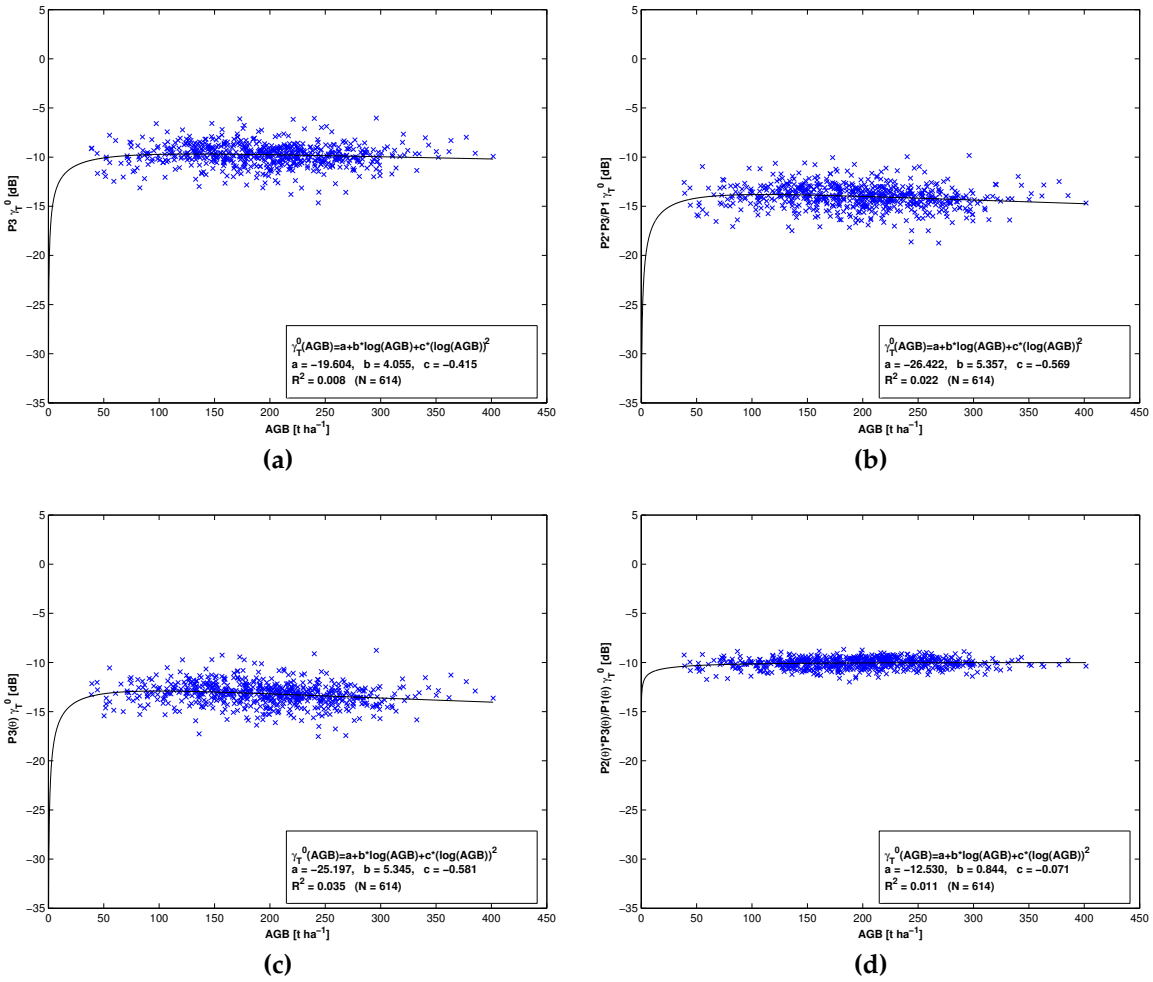


**Figure D.5:** Sensitivity of PLR215 Pauli volume scattering and Pauli ratio ($\frac{(HH-VV)*(HV+VH)}{(HH+VV)}$) against biomass at 100 m pixel spacing over the Lägern study site. (a) unrotated volume scattering vs. AGB, (b) unrotated Pauli ratio vs. AGB, (c) rotated volume scattering vs. AGB, (d) rotated Pauli ratio vs. AGB. Pauli channels are all radiometrically normalized. PLR frame was acquired at an off-nadir angle of 21.5° and the image was taken on the 24th of March 2009.

# E. ALOS PALSAR Mosaics

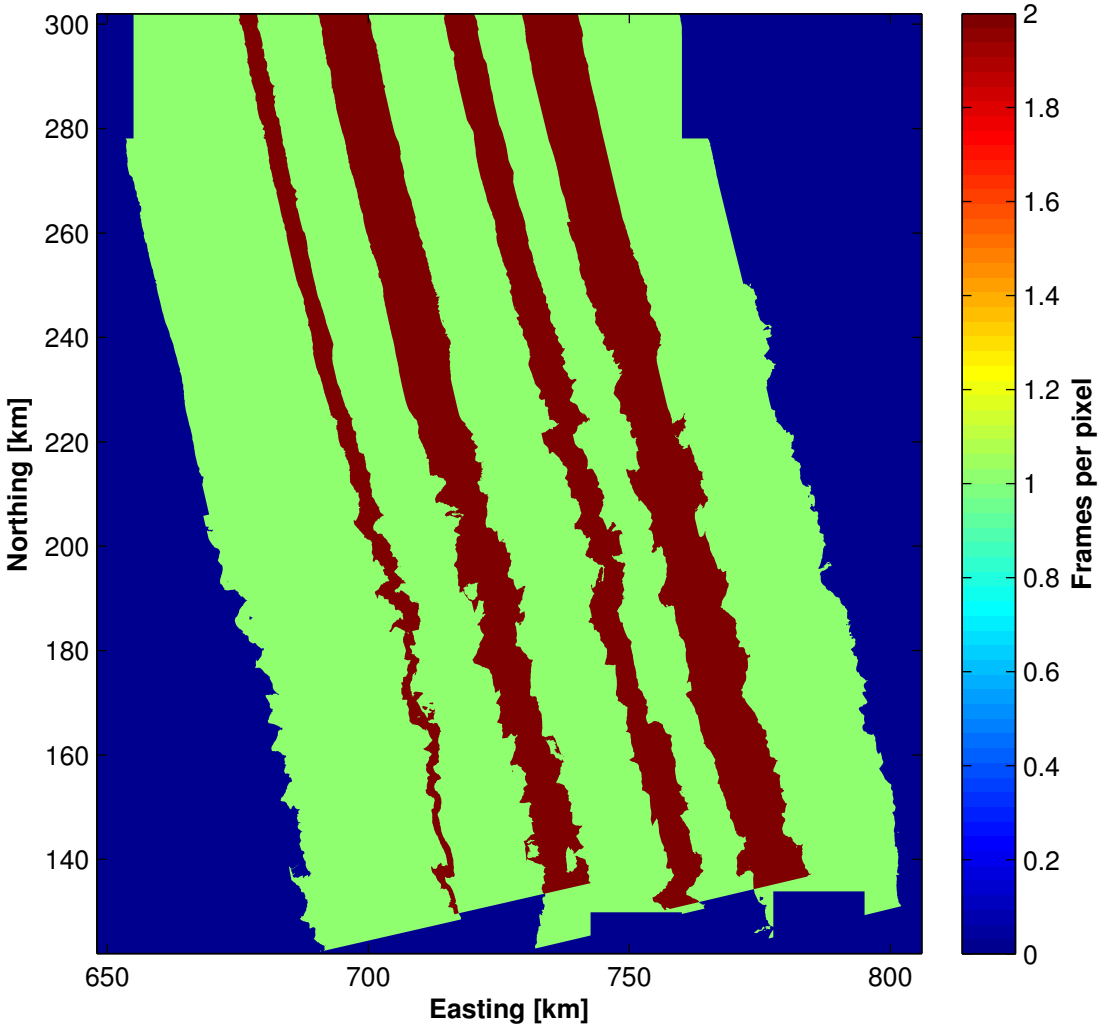


**Figure E.1:** Frame coverage of the mosaic. The number of frames covering each pixel in the mosaic (maximum 2).

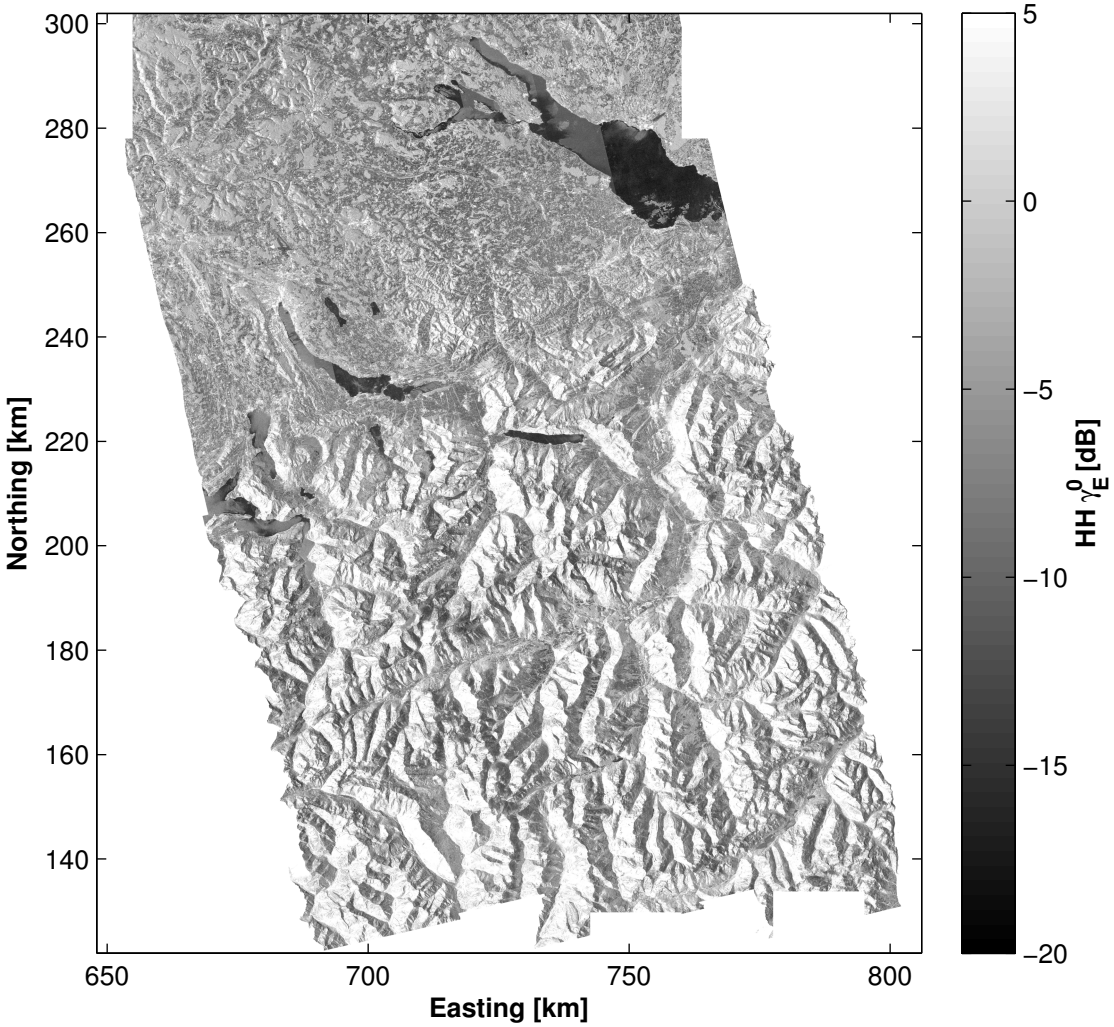


**Figure E.2:** PLR GTC mosaic at HH polarization.

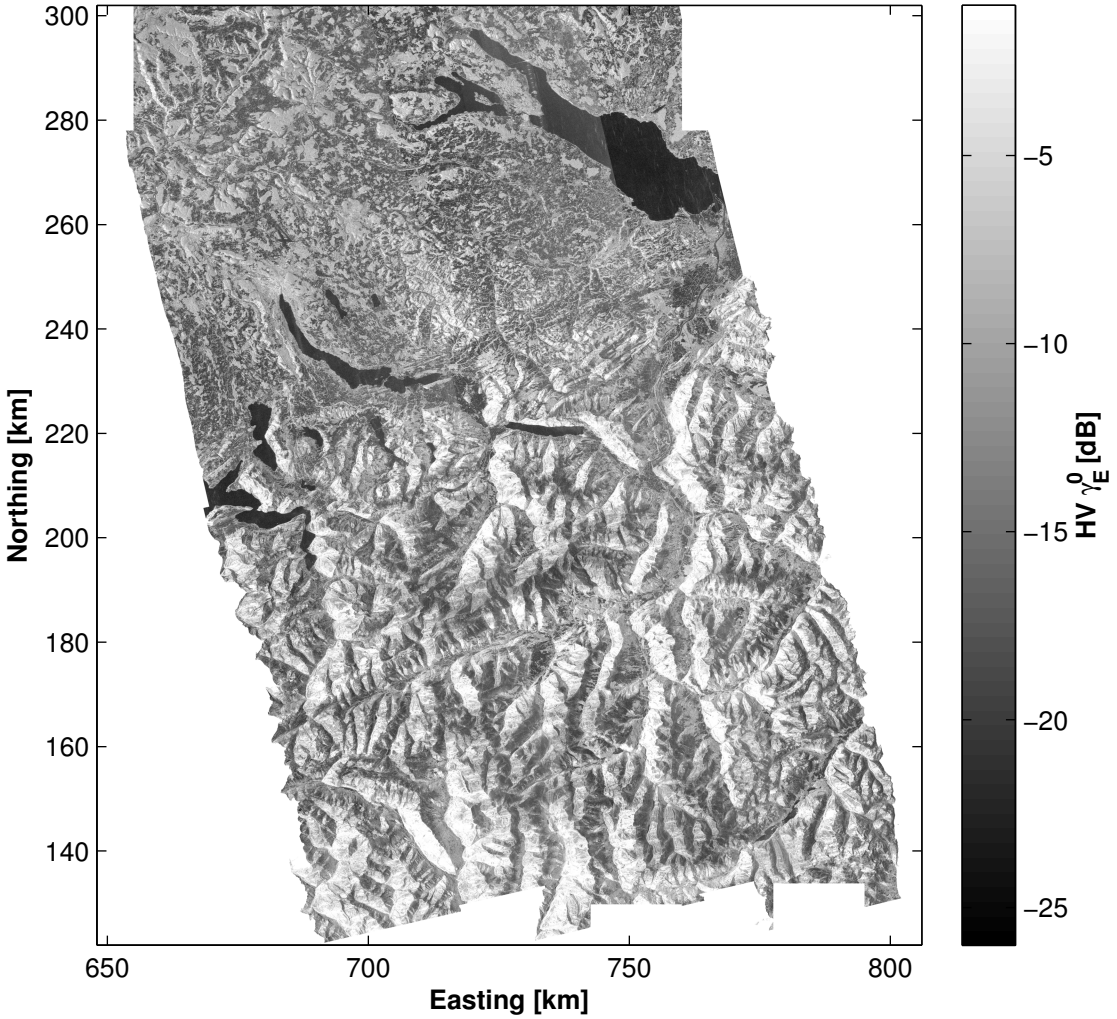


**Figure E.3:** PLR GTC mosaic at HV polarization.

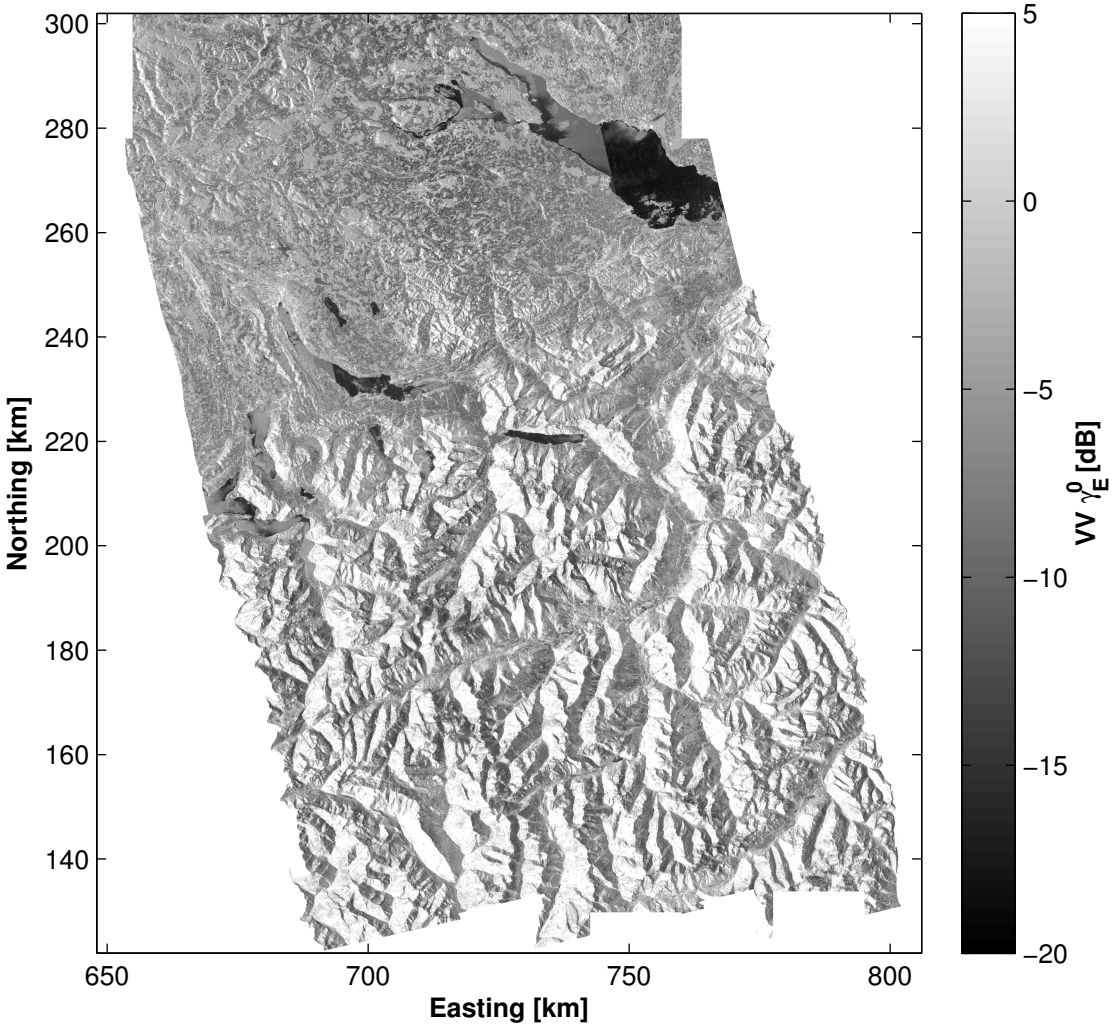


**Figure E.4:** PLR GTC mosaic at VV polarization.

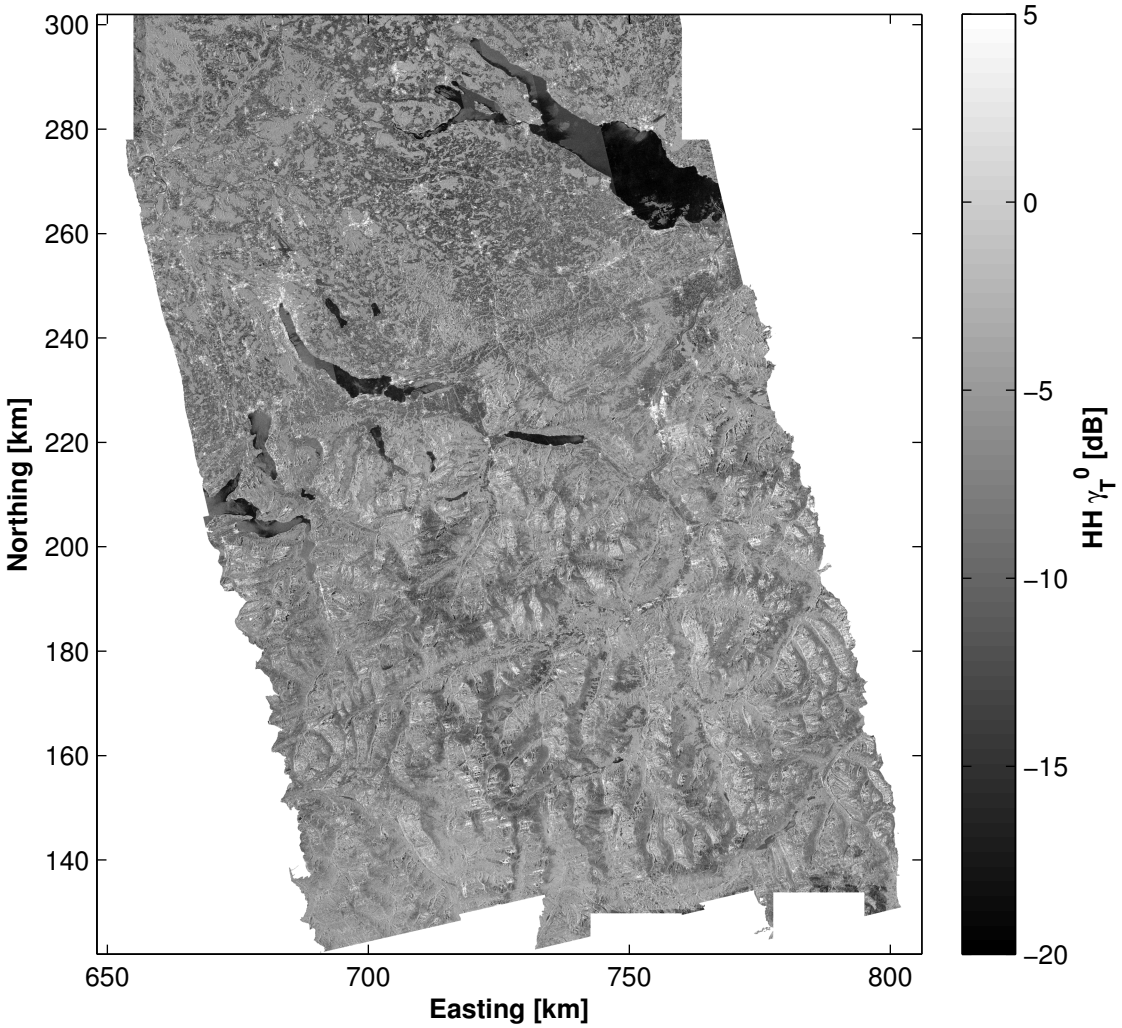


**Figure E.5:** PLR RTC mosaic at HH polarization.

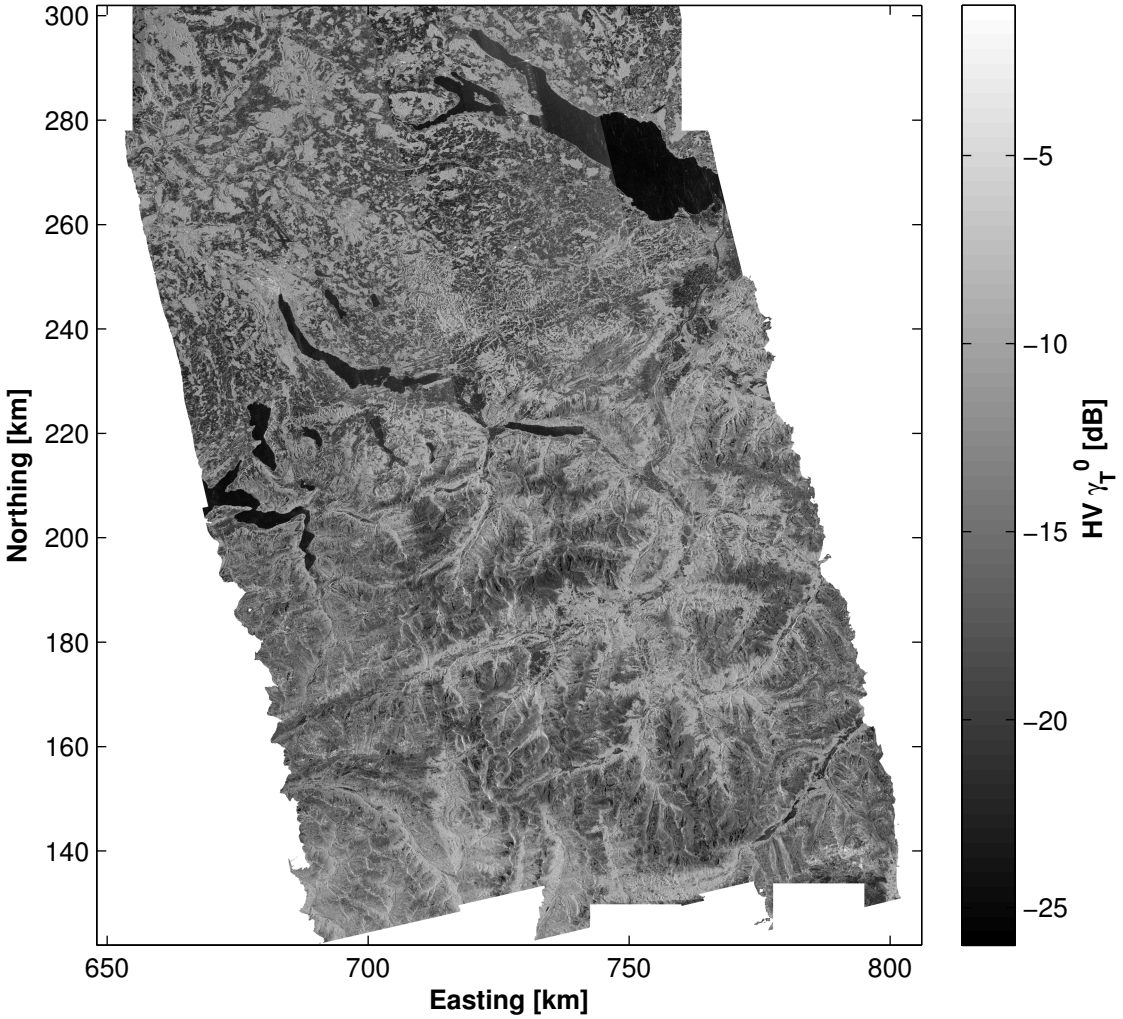


**Figure E.6:** PLR RTC mosaic at HV polarization.

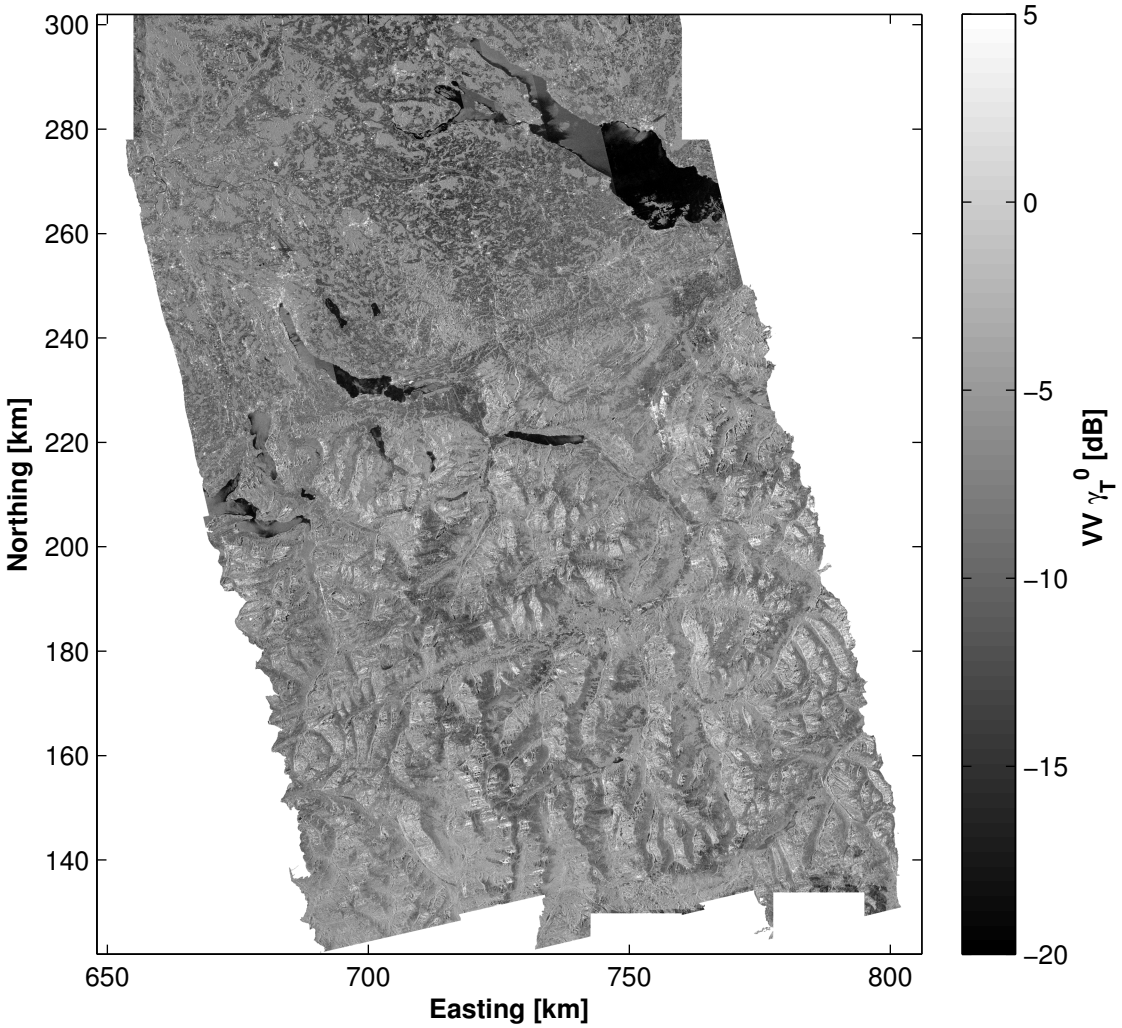


**Figure E.7:** PLR RTC mosaic at VV polarization.

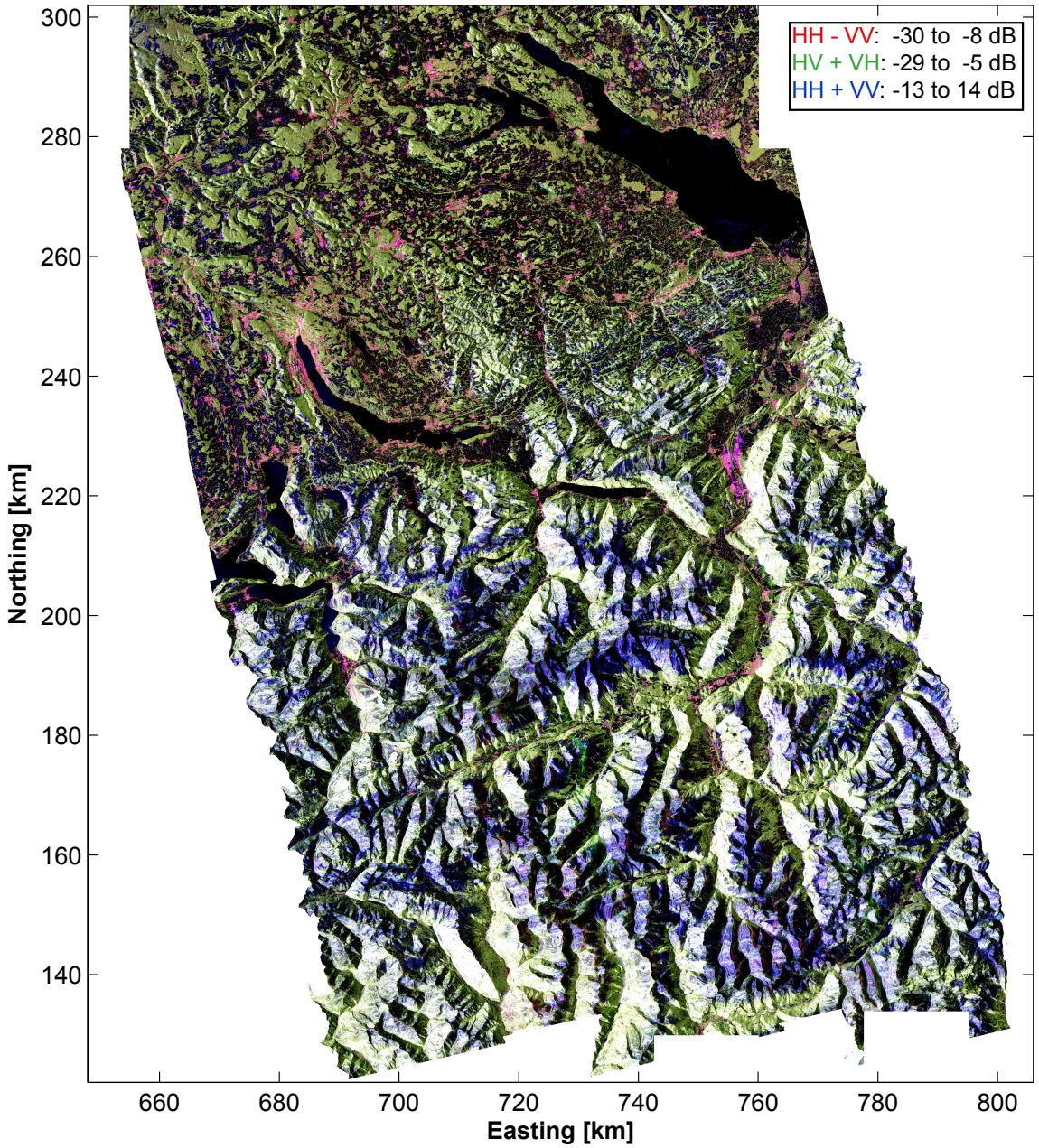


**Figure E.8:** PLR Pauli GTC mosaic.

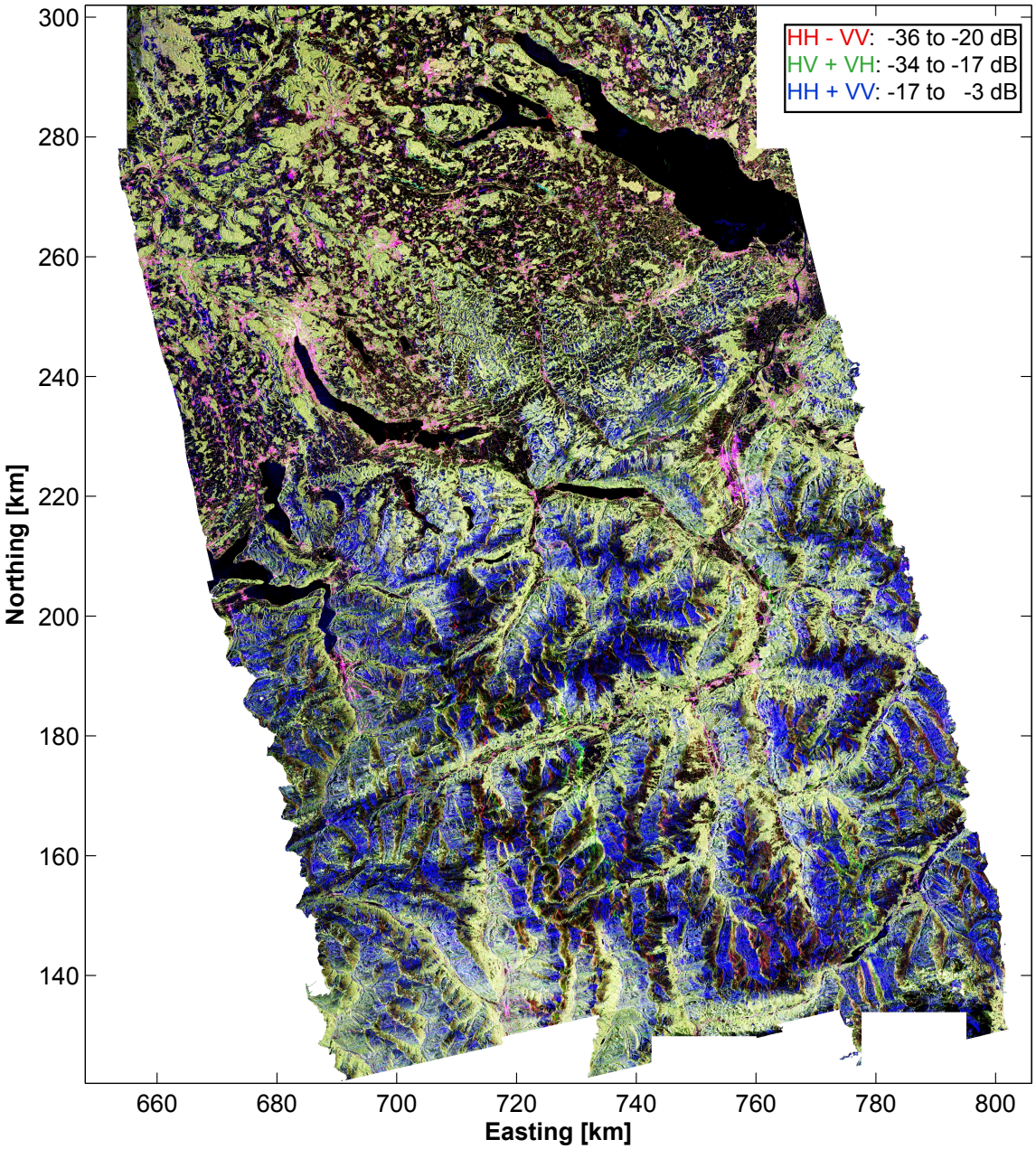


**Figure E.9:** PLR Pauli RTC mosaic.

# Personal declaration

Personal declaration: I hereby declare that the submitted thesis is the result of my own, independent work. All external sources are explicitly acknowledged in the thesis.

---

Place, Date

Signature